Investigation of the Cell Membrane Architecture by Single-Molecule Tracking of Peptidic Toxins

Silvan Türkcan

▶ To cite this version:

HAL Id: tel-00608124

https://pastel.hal.science/tel-00608124v2

Submitted on 25 Jul 2011

Silvan Türkcan
PhD Thesis

Investigation of the Cell Membrane Architecture by Single-Molecule Tracking of Peptidic Toxins
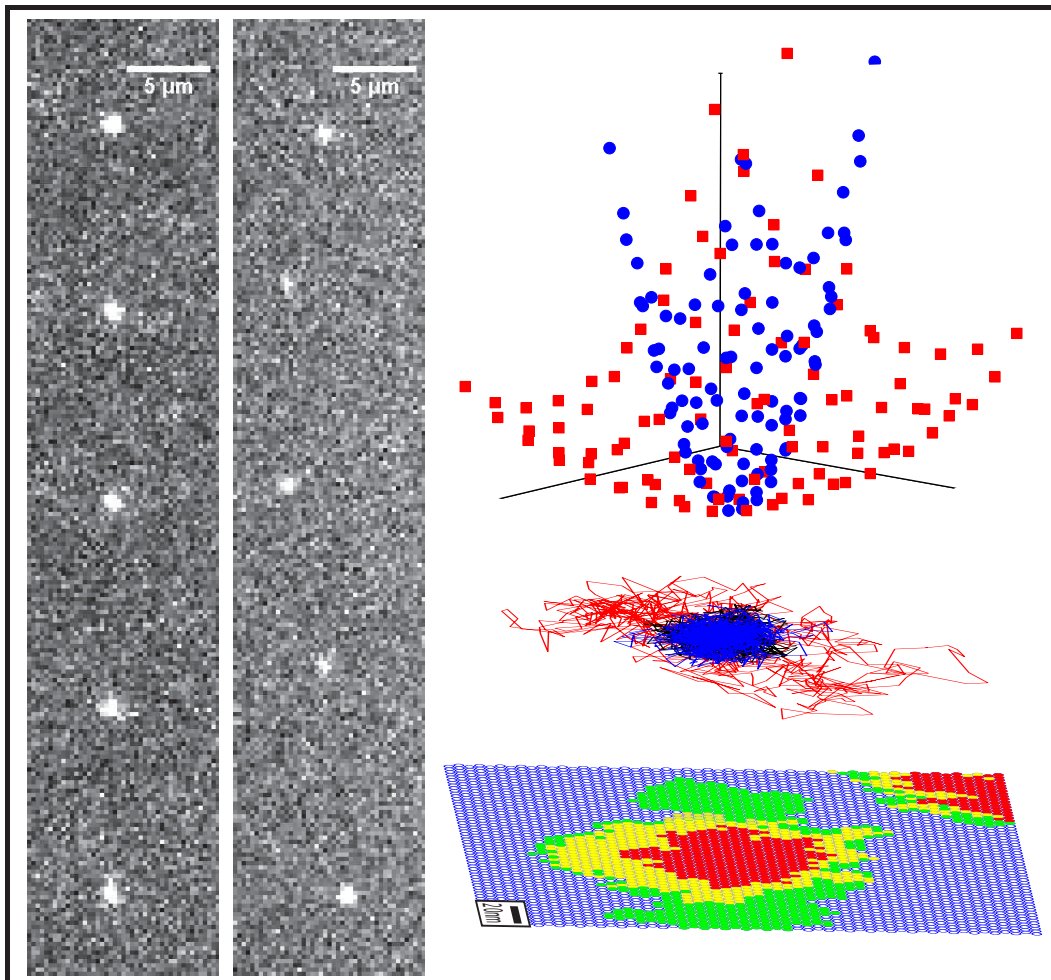
Laboratoire d'Optique et Biosciences
Ecole Polytechnique

PhD Thesis

presented by

Silvan Türkcan

on the subject of

Investigation of the Cell Membrane Architecture by Single-Molecule Tracking of Peptidic Toxins

**Laboratoire d'Optique et Biosciences
Ecole Polytechnique**

Defense on December 7th, 2010

Jury Members

Dr. Bernard Poulain	President
Dr. Didier Marguet	Reviewer
Dr. Pierre-Emmanuel Milhiet	Reviewer
Dr. Laurent Cognet	Examinator
Dr. Jean-Baptiste Masson	Examinator
Dr. Jean-Louis Viovy	Examinator
Dr. Antigoni Alexandrou	Advisor

To my father

Acknowledgements

Over the past three years, I used a beautiful microscope, an amazing camera and a laser to watch molecules move a few nanometers over from where they were and back again. I would like to thank and acknowledge all the people that helped and motivated me. I could not have done this without you and furthermore, you made it very pleasant.

I am grateful to the members of the Jury, Laurent Cognet, Jean-Baptiste Masson, Bernard Poulain and Jean-Louis Viovy and, on particular, to the reviewers, Didier Marguet and Pierre-Emmanuel Milhiet, for their work, evaluation and helpful feedback on my work.

I thank Jean-Louis Martin for having me in the Laboratoire d'Optique et Biosciences.

I was generously funded by the Direction des Relations Extérieures (DRE) de l'Ecole Polytechnique and the Bayer Science and Education foundation.

Foremost, I would like to thank Antigoni Alexandrou for bringing me into the Laboratoire d'Optique et Biosciences and for supervising my work, for all the discussions and the help and for being a perfect mentor. But also for her easy going personality, the freedom she gave me and the laughs, even when they were directed at my interest in a particular subset of the french student body. Thank you Antigoni.

I would also like to thank all the collaborators that made the many projects possible, such as Michel Popoff for his help with the toxins, Jean-Baptiste Masson and Massimo Vergassola for their statistical physics contribution, Geraldine Dantelle, Blaise Fleury, Geneviève Mialon for providing me with nanoparticles and the help during experiments, Thierry Gacoin, Jean-Pierre Boilot, and Jean-Marc Allain, who experimented with me and furthermore invited me to join him with his group for some work at the Académie de la Bière.

Contents

Foreword

Confinement of biomolecule diffusion in the cell membrane has often been observed since 1990, but there is still an ongoing debate about the underlying reason for it. Different models compete and, in some cases, the confinement of the same biomolecule has been attributed to different mechanisms. Overall, the answer to how the membrane is structured has significant impact on our understanding of cell biology. Virtually all processes that involve signaling and trafficking, such as immune response and endocytosis, rely on the peculiar membrane architecture.

The work presented in this thesis lies at the interface of physics and cell biology. The starting point was previous work by Didier Casanova, who showed in his thesis *"Nanoparticules d'oxyde: développements et applications comme sondes biologiques"* that rare-earth doped nanoparticles are attractive labels for tracking single molecules due to their photostability and absence of blinking. He observed that the receptors of a peptidic bacterial toxin were confined in the cell membrane and the simple question: *"What causes the confinement?"*, became the motivation of the work presented here. This work benefited from many different collaborations. The nanoparticles were synthesized by the group of Thierry Gacoin and Jean-Pierre Boilot in the Laboratoire de Physique de la Matière Condensée at Ecole Polytechnique and based on work that was developed during the thesis of Domitille Giaume and Geneviève Mialon. Michel Popoff from the Anaerobe Bacteria and Toxins unit at the Institut Pasteur proposed studying pore forming toxins and supplied all the toxins used in this work. The first demonstration of the analysis of experimental single-molecule trajectories using the inference approach was done in the beginning of the thesis in collaboration with Jean-Baptiste Masson, Guillaume Voisinne and Massimo Vergassola at the Physics of Biological Systems Unit at Institut Pasteur [1]. All further developments regarding bias, type of potential and comparison with other techniques were performed in the framework of this thesis and in collaboration with Jean-Baptiste Masson. Finally, the application of an external force using a microfluidic flow was realized in collaboration with Jean-Marc Allain at the Laboratoire de mécanique des solides at Ecole Polytechnique.

Outline

The goal of this manuscript is to explain why the receptors of the peptidic α & ϵ-toxin synthesized by the anaerobic bacteria, *Clostridium septicum* and *Clostridium perfingens*, respectively, are confined in zones, much smaller than the cell surface:

- Chapter 1 is an introduction to current models of the cell membrane architecture and the microscopy techniques that are used to investigate it.

- Chapter 2 introduces the single-molecule experiments. First, it introduces the toxins, their receptors and the rare-earth doped nanoparticle labels. The chapter also introduces important considerations for choosing the appropriate conditions for single-molecule tracking experiments.

- Chapter 3 discusses a new technique based on Bayesian inference and its application to single-molecule trajectories to infer values for diffusion coefficients and forces acting on the biomolecule.

- Chapter 4 describes the motion of the toxin receptors and shows that they move in a confining potential.

- Chapter 5 investigates the origin of the confinement and proposes a new model that predicts the potential confining the receptors.

- Chapter 6 presents the unexpected motion of the toxin receptors under an external force that is generated by a microfluidic flow.

- Chapter 7 summarizes the results and gives an outlook on experiments that can provide further insight.

Chapter 1

Introduction

Just like the human's skin is one of its vital organs, the cellular membrane is an integral part of the cell, with an architecture, which plays a crucial role in many cellular processes and pathologies. The aim of this work is to study the membrane architecture by investigating the movement of molecular species within it. The species we will follow are toxin receptors. They are observed by a particle tracking technique that uses fluorescence microscopy.

Since the experiment lies at the interface of physics and biology, both aspects of the project are introduced. The first section presents an introduction to the importance of the membrane and its nature. The second section is an overview over current microscopy techniques that are used to investigate the cell membrane including the single-particle tracking technique that is used for this study. The microscopy techniques are followed by an introduction to the different diffusion modes and the corresponding diffusion equations. Finally, four biologically relevant membrane models are discussed that could lead to the different diffusion modes.

1.1 The cell membrane

About four billion years ago, compartmentalization of early RNA complexes along with some transcription machinery took place. This can be seen as the birth of the first cells. There are now more than 10 million different types of living organisms, all composed of cells [2, 3]. Three steps were crucial in the evolution of life: formation of large and complex organic molecules, emergence of the cell and finally multi-cellular organisms. Whereas it is easier to explain the differentiation into multi-cellular organisms, by considering the increase in fitness and thus the better performance in Darwinian evolution, it is more difficult to find the source of the RNA precursors, but the 1953 publication of Urey and his student Miller

showed that it was possible to create amino acids from the early atmosphere [4]. The origin of the first cell was probably due to an emerging process involving self-organization of a lipid bubble [3]. In the 1960s, it was shown that lipids from egg yolk spontaneously form lipid vesicles in water. Evolution chose cells with water permeable membranes despite the huge cost in energy of constantly pumping ions across the membrane to avoid bursting the cell. Unselective permeability of the membrane often means the death of the cell.

The cell membrane separates the inside of the cell from the outside, keeping ions, proteins and other molecules where they are needed. The actual barrier is the phospholipid bilayer, which is flexible, water impermeable and only a few nanometers thick. Phospholipids are the constituent molecules of the lipid bilayer and have a hydrophilic head and two hydrophobic tails. The bilayer is spontaneously assembled due to hydrophilic interactions between the lipid head groups with water and the hydrophobic interactions of the tail groups, which will hide from the water at the inside of the bilayer [5]. The cellular membrane harbors many different types of lipids and proteins, to perform tasks such as signaling, trafficking, ion pumping, adhesion, force sensing and even apoptosis. Furthermore, the entire lipid membrane is supported by an underlying cytoskeleton made up of spectrin and actin. This structure supports the membrane like the beams in a tent and links it to the microtubules, which give the cell its shape.

The notion that cells are surrounded by a semipermeable membrane appeared by the early twentieth century after work done by Traube, who determined that salts migrate slower into cells than water [6]. Gorter and Grendel proposed in an article in 1924 that *"chromocytes of different animals are covered by a layer of lipoids just two molecules thick"* and thus determined that the structure is the bilayer as it is known today [7]. Initially, following observations by Frey, Edidin and Cone [8,9], all the proteins and lipids were thought to diffuse homogeneously in the membrane. The viscosity of the membrane was found to be 100 times larger than that of water. *"The commonplace view now is that the average bilayer lipid viscosity is similar to that of olive oil − a more exotic standard is the viscosity of crocodile fat on a warm summers day "* [10]. These observations led to the notion that proteins and lipids diffuse freely according to the fluid mosaic model proposed by Singer and Nicolson [11]. The image of the authors' model is shown in figure 1.1. Here the large black complexes display proteins that are integrated into the bilayer of phospholipids, which are shown as small spheres together with their fatty chain tail groups. The proteins can diffuse freely in the membrane and can form clusters. However, subsequent experiments, pushed forward by a drastic improvement in microscopy techniques, fluorescent labeling and camera technology, proved that lateral diffusion of the proteins in the membrane was not free after all.
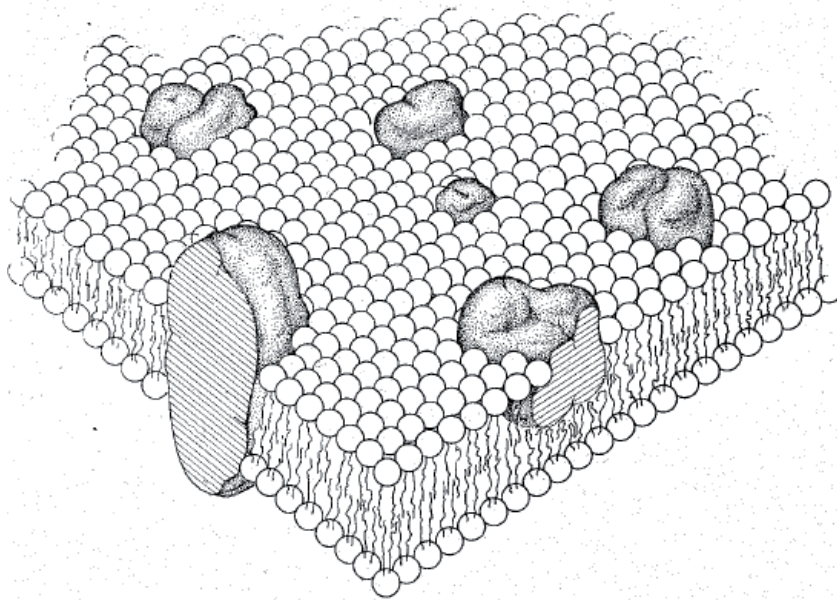
Figure 1.1: The fluid mosaic model of the membrane as shown in a publication in 1972 by Singer and Nicholson [11]. Here the large black complexes display proteins that are integrated into the bilayer of phospholipids, which are shown as small spheres together with their fatty acid chain tail groups. The proteins can diffuse freely in the membrane.

1.2   Microscopy tools for the investigation of the cell membrane

An early microscope was built in 1590 by the Dutch lens grinders Hans and Zacharias Janssen by placing two lenses in a tube. In 1644 Giambattista Odierna first gave a detailed description of living tissue, a fly's eye, in L'ochio della mosca. Just a few decades later in 1675, Anton van Leeuwenhoek first describes microorganisms, cells and bacteria, seen through his simple microscope with only one lens. He also described blood cells and spermatozoa. Hundred years later, Ernst Abbe formulated his description of the diffraction limit of light. Due to the Rayleigh limit, based on Abbe's formulation, the resolution of optical microscopy is limited to about the wavelength of the light and it is often at these length scales where the current unsolved questions of membrane architecture lie. However, many developed tools have been able to shed light onto the architecture of the membrane.

Different types of microscope exist: Optical Microscopes, Electron Microscopes (TEM, SEM) and Scanning Probe Microscopes (AFM, STM, SNOM). Electron microscopy provides a tool for studying the membrane with very high resolution below the nanometer. However, cells that are imaged must be freeze-dried beforehand and thus electron microscopy cannot be used to image live cells. Optical microscopy techniques allow imaging of membrane molecules on living cells. Working with live cells is of interest because dynamic processes can be filmed as they unfold. Furthermore, the natural order of the membrane will be disturbed once the cell is dead. Optical techniques include tagging of molecules of interest with fluorescent labels that render them visible by means of fluorescence microscopy, detection of surface plasmon resonance, light scattering or absorption. Using light limits their resolution to the wavelength of the light, but techniques exist to overcome this limit. The following sections will briefly introduce optical techniques used to measure ensembles or single molecules. The techniques that are introduced here, can image the motion of molecules on membranes of live cells. Optical scanning probe techniques are often not limited by the diffraction limit and increase the optical resolution by working in the near-field. However, these techniques can only scan a small area in a given time.

1.2.1   Ensemble measurements

Due to advances in fluorescent molecules and molecular labeling techniques, it is possible to render membrane proteins or lipids fluorescent by coupling fluorescent molecules to them or by using genetically encoded fluorophores and to track their movement [12]. Due to the high number of genetically expressed fluorescent tagged molecules, this will often lead to a high concentration of labeled molecules in the

membrane. Due to the high number and density of labeled molecules, it will be impossible to distinguish single molecules from each other by most techniques. However, the behavior of the ensemble of molecules is still accessible.

Fluorescence Recovery After Photobleaching (FRAP) is a technique that can be give access to the behavior of the ensemble of molecules. All molecules in a small area on the membrane are photobleached by an excitation laser beam or flash lamp [13]. After the bleaching process, the time required by the fluorescent molecules to diffuse from the outside into the bleached area is measured. Assuming a circular photobleaching spot, the diffusion coefficient can be calculated from the following equation:

$$D = \frac{w^2}{4t_{1/2}} \tag{1.1}$$

Here the radius of the beam w has to be carefully determined, as it enters quadratically into the value for the diffusion coefficient. The time $t_{1/2}$, for which the emission of the spot has recovered half of its initial value can be obtained from the recovery of fluorescence vs. time.

The FRAP technique is an excellent choice for measuring the bulk diffusion coefficient of membrane molecules. The technique was actually designed to prove that certain molecules are mobile while others are immobile in the cell membrane. It is also possible to measure binding kinetics of complex formation in the membrane [14]. However, this technique fails to differentiate between multiple subpopulations, which diffuse with different coefficients.

A more versatile technique than FRAP is **fluorescence correlation spectroscopy (FCS)**, which was first demonstrated by Elson, and Webb in 1972 [15] for fluorescence. It can also measure diffusion coefficients and binding kinetics, but it can furthermore be used to determine multiple diffusion coefficients, concentrations in a calibration-free manner and complex stochiometry.

FCS is a technique that creates an autocorrelation spectrum that is a time spectrum and not a frequency spectrum as the word spectroscopy might suggest. The technique is the fluorescent equivalent to the dynamic light scattering technique. For both techniques, fluctuations in emitted or scattered intensity due to molecules entering and leaving a certain zone are directly related to the diffusion coefficient. The technique requires the fluctuations to be frequent and large enough with respect to the total intensity of the fluorescence signal.

The autocorrelation function, which is an expression for the fluctuations $\delta I(t)$ from the mean intensity $\langle I(t) \rangle$ from one time point to a time point shifted by τ is given in equation 1.2.

$$G(\tau) = \frac{\langle \delta I(t)\, \delta I(t+\tau) \rangle}{\langle I(t) \rangle^2} = \frac{\langle I(t)\, I(t+\tau) \rangle}{\langle I(t) \rangle^2} - 1 \qquad (1.2)$$

This correlation function $G(\tau)$ is then fitted to extract the quantities of interest, such as the diffusion coefficient. Models are reported for normal [15], anomalous [16], polydisperse diffusion [17] and for diffusion with flow [18]. A variation of the FCS technique, fluorescence cross-correlation spectroscopy (FCCS), measures differences in diffusion times to quantify molecular interactions [19].

Förster resonant energy transfer (FRET) is a technique that takes advantage of resonant energy transfer via non-radiative dipole-dipole interaction between a donor and an acceptor particle. A donor may transfer its energy, while in its excited state to an acceptor through non-radiative dipole-dipole interaction. This effect was first described by Theodor Förster, after whom it was named [20]. However, for this process to occur, the donor-acceptor pair has to be carefully chosen to ensure energy transfer. The emission range of the donor has to overlap with the absorption region of the acceptor in order to exchange a virtual photon [21–23]. Although it cannot be used to measure diffusion coefficients, is often used in the investigation of the membrane to measure complexing of species in the bilayer, which in turn could cause anomalous diffusion.

The FRET efficiency depends on the overlap of the emission and absorption band of donor and acceptor, respectively, the distance of the two molecules and the relative orientation of the dipole moments of the fluorophore. The efficiency decreases with the distance to the sixth power, making this technique very appropriate for measuring small distances between two proteins. It has been used to investigate the signal transduction from the epidermal growth factor receptor (EGFR) in A431 carcinoma cells to show that the mechanism of dimerization involves the formation of a cell-surface complex of one EGF molecule and an EGFR dimer, followed by the direct binding of a second EGF molecule [24]. The data indicated that the dimer had been formed before the binding of the second molecule. With respect to membrane architecture, this technique has been used to study lipid rafts in model membranes [25].

With the advent of superresolution techniques, such as **stimulated emission depletion microscopy (STED)**, it is possible to use techniques such as FCS in the single molecule regime to study the membrane. A recent example is the de-

termination that the maximum lipid raft size that confines glycosylphosphatidyli-nositol (GPI)-anchored proteins in PtK2 cells is 20 nm [26]. As the frame rate of these techniques increases, single particle tracking with very high resolution will become possible.

1.2.2   Single molecule techniques

In the single molecule regime, the concentration of labeled molecules in the micro-scope field of view is low enough so that single labels can be localized with high precision. The localization, trajectories and behavior of single molecules can be observed to study their behavior in the membrane. Mean values can be built from the bottom up to create histograms that are more informative than just the mean value. The advantage is that the full distribution can be determined, which would otherwise be masked by the ensemble techniques like FRAP and FCS. The means of label detection can be fluorescence, light scattering, absorption or surface plas-mon resonance. Single-molecule labels will be discussed in the following section.

Nanometer-scale single particle tracking can be achieved because it is possible to determine the center of a small particle with a precision well below the diffrac-tion limit [27–30]. Although the particle label is much smaller than the wavelength of the light, it creates a Frauenhofer diffraction pattern, the Airy disk, whose size d is determined by the objective's numerical aperture NA and the wavelength of the light λ in equation 1.3.

$$d = 0.61 \frac{\lambda}{NA} \tag{1.3}$$

According to the Rayleigh criterion, two particles cannot be resolved if they are closer than this distance. This criterion, however does not impede localizing the position of the peak with a higher accuracy than the size of the diffraction limit by fitting it to a Gaussian as shown in figure 1.2. A Gaussian fit is chosen since it is a good approximation to the Airy function, yet the optimization pro-cedure for the fitting is fast. The fit is the reason why single molecule tracking is performed with a low density of labeled target molecules. Once molecules get too close, they cannot be precisely distinguished. By determining the position at subsequent time points, the particle trajectory is reconstituted. A least-squares fit with a Gaussian is not the optimal scheme to find the location of the particle. Instead, a maximum likelihood estimation with the real point spread function can be used gain precision with respect to the here used simple technique that wastes

one-third of the available information [31].
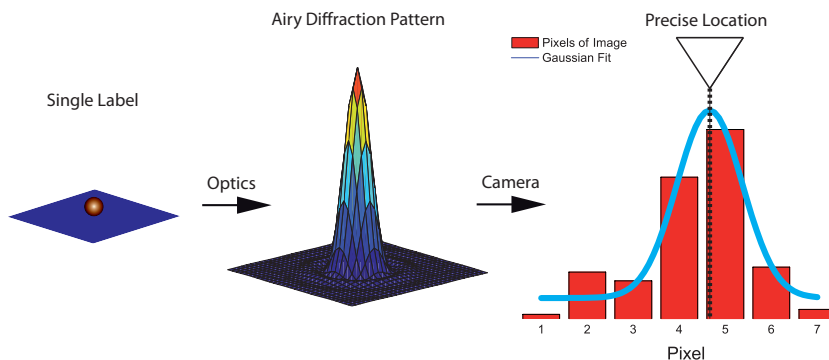
Figure 1.2: Localization of a single emitter with sub-diffraction resolution. Imaging of the nanometer size label creates a diffraction pattern of size d, which depends on the numerical aperture of the objective and on the wavelength of the light. The camera acquires a pixilated image of the diffraction pattern. This data can be fitted with a Gaussian to obtain the localization of the label with sub-pixel and sub-diffraction precision as indicated by the arrow.

The optics, camera and mechanical stability of the apparatus determine the minimal spatial accuracy. Furthermore the acquisition time plays a role by affecting the signal to noise ratio. The speed of motion of the diffusing particle is also important as it decreases the spatial accuracy [29].

1.2.3 Probes for single-molecule tracking

Probes used in single-particle or single-molecule tracking (SPT or SMT) are fluorescent molecules or nanometer particles such as latex spheres, gold colloids or nanocrystals. These particle-labels are commonly attached to the molecule of interest via antibodies or fragments of antibodies. For SPT, the label is not expressed genetically as it is often done in the previously introduced ensemble techniques. However, it is possible to express specific tags, such as avidin, the Halo or Snap tag, to which the label will bind [32, 33]. Since the goal is to track a single target, the stochiometry of labels bound to targets should be one to one [34]. Chemically this is very difficult to achieve and it is an active field of research to produce labels that only have one attachment site. For small labels, where the surface is carefully controlled, it is possible to use gel electrophoresis to select labels that have one attachment site from a sample that has a Poissonian distribution of functional sites on their surface [35].

Fluorescent molecules are small and can be engineered to bind monovalently to the target molecule. Experiments with a labeled lipid investigated lipid

microdomains or rafts in the plasma membrane of human coronary artery smooth muscle (HASM) cells with the marked lipid Dimyristoyl-sn-glycero-3- phospho-ethanolamine (DMPE) [36]. The epidermal growth factor receptor (EGFR) was then tracked by fluorophore labeling [24]. One of the first implementations of the green fluorescent protein (GFP) and yellow fluorescent protein (YFP) in SMT, was demonstrated for E-Cadherin cell-cell adhesion protein and the L-Type Ca^{2+} channels in live cells [37,38]. A review summarizing fluorophore SPT can be found in reference [39]. The advantage of fluorophore labels is their small size of 1 to 4 nm, which reduces their perturbation to the movement and function of the tracked species. Furthermore, protein monomers and multimers can be distinguished by using stepwise photobleaching [39]. Although new breakthroughs in minimizing photobleaching and blinking of fluorescent dyes have been made by designing reducing and oxidizing systems [40], fluorophores cannot be tracked for very long under excitation conditions for single-molecule observation due to photodestruction. Furthermore, the buffer system used to stabilize the fluorophore can interfere with live cells.

Another class of labels are colloidal semi-conductor **quantum dots (QDs)**. Due to the underlying physics that governs their emission, the emission spectrum depends on the diameter of the crystals. Generally, smaller dots will localize the exciton more strongly, generate greater spacing between energy levels and create an emission that is further in the blue. The size of the single crystals can be precisely controlled by the duration, temperature and ligand molecules used during the synthesis [41]. QDs are normally capped with shells of a crystal with a larger bandgap that create a barrier for the exciton. Another difference with respect to organic fluorophore is the broad band absorption peak due to photons that can be absorbed with energies higher than the barrier bandgap. Due to very high absorption coefficients, excitation with lamps, which is easy to implement, becomes possible. The lifetime of the quantum dot emission is also longer (10 ns), which allows for the implementation of gated detection schemes [42]. Quantum efficiencies of these core-shell QDs can reach close to 90 % [43]. The first application of these markers as single molecule probes was the measurement of the diffusion of glycine receptors on the neuronal membrane [44]. On the other hand, these labels commonly exhibit blinking, due to surface defects that can temporarily trap an electron or hole and stop the quantum dot from emitting light [45]. ANother concern is target molecule crosslinking. More recent work has lead to suppression of blinking by growing multiple thicker or graded shells around the QDs, giving hope that these very bright labels can be used to collect trajectories of molecules without intermittency [46,47]. Multiple species can be tracked simultaneously by using QDs of different colors. Quantum dots are also good candidates for two-photon microscopy because they have a very large two-photon absorption cross section [48]. Current research in the field focuses on narrower fluorescence emission, smaller

sizes, extension to the near infrared spectrum, suppression of blinking, quantum yield enhancement and built-in on-off switches [49].

Although **gold nanoparticles** do not fluoresce under normal circumstances, they can be used as labels using scattering as a detection method. Here the labels are light sinks rather than light sources. The minimal detectable diameter by scattering for these labels is 15 nm, but $30 - 40$ nm are typically used [50, 51]. Typical acquisition rates are around the standard video rate of 30 ms, but they have been imaged at up to 25 μs per frame [52, 53]. Although these particles are perfectly stable and there are no problems with photobleaching, target molecule crosslinking represents a difficulty due to their large size.

Due to surface plasmon effects, smaller gold nanoparticles can also be used to create third harmonic generation at 500 nm [54]. They can also be used in techniques that exploit the heat and resulting refractive index change generated by the surface plasmon absorption and the interference between a reference beam and the scattered field due to the refractive index change [55, 56].

Another class of labels include **rare-earth-doped oxide nanoparticles**, which show very high photostability without blinking. Another advantage is their long radiative lifetime (~ 1 ms), which can be used for gated detection. Their main drawback is their relatively low quantum efficiency and their low absorption cross section outside the UV regime. The first application with respect to visualizing live cells was the labeling of sodium ion channels with Eu-doped nanoparticles [57]. Recently, two-photon excitation in the infrared has been achieved using Er,Yb-doped nanoparticles [58–60] and has the potential for detection without background from cell fluorescence. Rare-earth-dope oxide nanoparticles are used as labels of the membrane receptors in this work. The nanoparticles are described in more detail in chapter 2.

Other labels also include dye-doped silica nanoparticles [61, 62], fluorescent microspheres, nano-diamonds [63, 64] and fluorescently labeled viruses.

Bigger gold nanoparticles and **latex beads** that are linked to molecules in the membrane can also be dragged by **optical tweezers** [65–71]. Here the position of the nanoparticle is determined by analyzing the four quadrant photodiode of the optical tweezers set-up or by video tracking. A force can be applied to investigate the architecture of the membrane, such as tethering of the molecule to the cytoskeleton or the length of the molecule barrier-free path.

1.3   Single molecule data analysis

The goal of single molecule tracking on cell membranes is to classify the motion of the tracked species and to find the distribution of the variables that describe the motion. To this end it is useful to look at the displacement of the molecule. **The mean square displacement (MSD)** $\langle r^2 \rangle$ is a measure of the displacement squared that a molecule underwent per time interval t, averaged over the whole trajectory. The basic mode of displacement a particle can undergo in two dimensions is a random 2D Brownian motion with a diffusion constant D, as described by equation 1.4. Diffusion in a more complicated environement can lead to anomalous diffusion as in equation 1.5, where $\alpha < 1$. Here the particle does not travel as far as during pure Brownian motion for the same time interval. Another form of motion, which is described by equation 1.6 is generated by active transport in the membrane and is known as directed motion, where v is the speed of the active transport [51]. Here the random walker is directed in a specific direction. Corralled motion, described by equation 1.7 [72,73] is of high interest since experiments suggest that many groups of molecules are confined in small domains or corrals of size L on the membrane [73,74]. Thus, the MSD $< r^2(t) >$ plot reveals the signature of the different modes of motion for the four mentioned cases by their deviation or non deviation from the straight line for free Brownian diffusion (see figure 1.3). The plateau of the green MSD trace for the corralled motion case is determined by the size of the confining domain.

$$\langle r^2 \rangle = \qquad\qquad 4Dt \qquad\qquad\qquad (Brownian) \qquad (1.4)$$

$$\langle r^2 \rangle = \qquad\qquad 4Dt^\alpha \qquad\qquad\qquad (Anomalous) \qquad (1.5)$$

$$\langle r^2 \rangle = \qquad\qquad 4Dt + (vt)^2 \qquad\qquad (Directed) \qquad (1.6)$$

$$\langle r^2 \rangle = \quad \frac{L^2}{3} - \frac{32L^2}{\pi^4} \sum_{n=1(odd)}^{\infty} \frac{1}{n^4} exp\left\{ -\frac{1}{2}\left(\frac{n\pi}{L}\right)^2 2Dt \right\} \quad (Corralled) \qquad (1.7)$$

Another way to describe the diffusion is the **probability density** $p(r,t)$, that describes the probability for a particle that was at the origin at time 0, to be at a distance $\mathbf{r}$ at time t. For normal Brownian diffusion with diffusion coefficient D, the probability is given by equation 1.8 and the solution for directed motion and motion in corrals is given in reference [51].

$$p(\mathbf{r},t)d\mathbf{r} = \frac{1}{4\pi Dt} exp\left(-\frac{r^2}{4Dt}\right) 2\pi r \, dr \qquad\qquad (1.8)$$
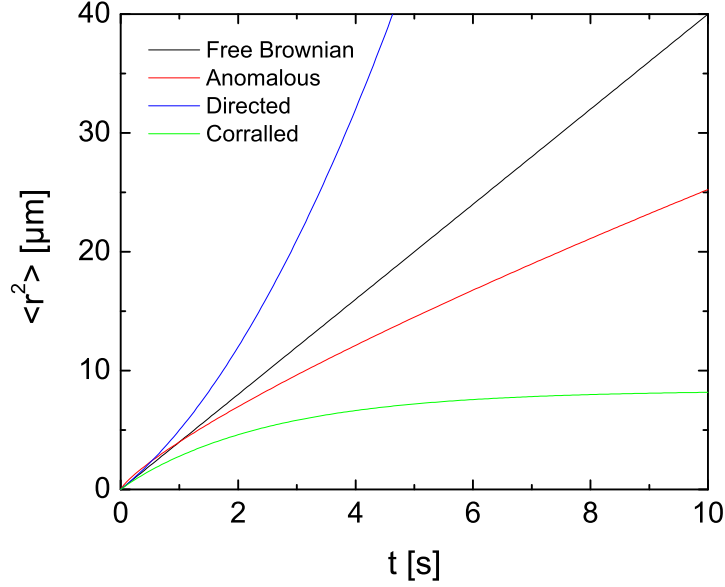
Figure 1.3: Mean square displacement for the four different types of diffusion that are often encountered in the membrane and described by equations 1.4 to 1.7. Normal two-dimensional Brownian diffusion with a diffusion coefficient of $1\,\mu m^2/s$ is shown in black. Anomalous subdiffusion with $\alpha = 0.8$ is shown in red. Directed motion with a speed of $1\,\mu m/s$ is given in blue. Corralled diffusion in a corral with a length L of $5\,\mu m$ is shown in green.

The diffusion coefficient in the description for the probability density $p(r,t)$ can be time dependent, as used by Webb and collaborators [75]. This definition allows for the re-interpretation of the diffusion equation, where an anomalous behavior is contained in the time-dependent diffusion coefficient $D(t)$ as shown in equation 1.9 & 1.10. The MSD distribution obeys a power law in this definition with transport coefficient Γ and can account for the presence of potential energy traps that vary in space and time. The underlying hypothesis is that the membrane is a random array of continuously changing traps. Since the distribution of trapping energies is very broad, there is no average residence time.

$$\left\langle r^2 \right\rangle = 4D(t)t = \Gamma t^\alpha \tag{1.9}$$
$$D(t) = 1/4\,\Gamma t^{\alpha-1} \tag{1.10}$$

The challenge in describing the motion of the molecule lies in matching the behavior to one of the discussed models. One path is the construction of the MSD plot followed by a comparison with different models to decide which model best fits the data. Anderson et al. calculated both the MSD and probability density plots when measuring the motion of the influenza virus receptor [76]. Kusumi et al. use the deviation from the straight line of free Brownian motion to classify the trajectories. The diffusion coefficient for the free motion is obtained by fitting only the first three points of the MSD plot with a straight line [73]. If the relative deviation from pure Brownian motion is larger than one, the motion is classified as directed, while if it is smaller than one, it is classified as anomalous or confined. The technique's advantage is that there is only one parameter, the relative deviation that describes the behavior of the curves. Other groups choose to use the anomalous diffusion coefficient α to classify the trajectory by measuring the initial slope of $\log \langle r^2 \rangle$ versus $\log t$ [75].

Often the trajectory of a molecule displays multimodal diffusion including a few of the introduced modes of diffusion. In such cases, it is important to develop a method to distinguish between them. Simson et al. have developed a method to detect the portion of a trajectory that is confined using the probability that a free random Brownian walker would spend a certain time in an area and comparing it to the analyzed trajectory [77].

1.4 Membrane Models

As already introduced, in the fluid mosaic model of the membrane [11] species diffuse freely in the lipid bilayer. However, subsequent experiments, mainly guided by more advanced microscopy techniques, fluorescent labeling and camera technology, proved that lateral diffusion in the membrane was not purely free Brownian diffusion [78]. Observations from FRAP experiments suggested membrane domains, based on lipid compartments, which would lead Simons and coworkers to articulate their raft hypothesis [79, 80]. Thereafter, additional models were proposed to explain membrane organization.

Single molecule experiments in artificial bilayers are another aproach to understand fundamentals of bilayer architecture. Since the content of artificial bilayers can be chosen, these experiments tend to be much better controlled. However, in live cells, the membrane is not in thermal equilibrium, as artificial lipid bilayers are, and this can lead to very different observations. Recent tracking experiments have even indicated that the behavior of diffusing species in living vertebrates is different from the behavior on the same cell type in cell culture [81].

The toxin receptors that are investigated in this thesis exhibit confined mo-

tion. For this reason, biological models that seek to explain confined motion are introduced below. These models are not exclusive. Confined motion can be due to a combination of more than one situation [82, 83].

1.4.1　Tethered proteins

The simplest model that would give a stationary or a strongly confined membrane protein trajectory is tethering of proteins to the actin cytoskeleton. In this model, a protein is either directly or via another protein attached to the actin filaments that lie underneath the cell membrane. Transmembrane proteins are typically held in place by such attachment points. However, the attachment is not entirely rigid. Most biologically important filaments are semiflexible, with changes in the length of a filament due to thermal fluctuations being comparable to the filament length in an extended conformation [84, 85]. Such filaments can act like springs, holding attached proteins in a fixed central position. The trajectory of such a protein would reveal motion confined to a domain, whose size is determined by the effective spring constant of the attached filaments and the thermal energy. The domain can drift following the changes of the actin filament attachment point.

One such receptor is the epithelial cystic fibrosis transmembrane conductance regulator (CFTR) Cl^- channel. Jin et al. showed that the receptor is confined by a spring potential with a spring constant of $2.6 \pm 0.8 \, \text{pN/µm}$ [86]. The spring constant was reduced by treatment with Latrunculin, a toxin that depolimerizes actin. This led to the conclusion that the receptor is tethered to the cytoskeleton. Other membrane proteins that bind or can bind to the cytoskeleton are receptors for transferrin, epidermal growth factor and α-2-macroglobulin, E-cadherin, T-cadherin, and the band 3 anion channel in erythrocytes [73, 87–89]. These receptors exhibit a variety of types of motion while still being attached to the cytoskeleton, including stationary behavior, oscillations about a fixed point, and long range diffusion. Experiments with optical tweezers determined a spring constant of $2.4 - 8.4 \, \text{pN/µm}$ for the LFA-1 adhesion protein after binding to ICAM-1 ligand [69] and $10 \, \text{pN/µm}$ for the δ-receptor in the membrane of Escherichia coli bacteria [71]. During these experiments, the receptors were labeled by latex or gold beads, which were pulled on by the trap.

1.4.2　Picket and fence model

The picket and fence model is an extension of the earlier conceived fence model, that could explain confinement of only larger proteins that protrude from the membrane into the cytosol [87, 90–94]. In the picket and fence model, tethered immobile

transmembrane proteins provide obstacles in the cell membrane, as shown in figure 1.4. Steric hindrance is the key concept to explain how even smaller proteins and molecules are confined in this model. It was proposed by Kusumi and is a model that could also extend the effects of the cytoskeleton from only acting on transmembrane molecules to smaller molecules that reside only in the outer leaflet of the membrane.

Theoretical modeling of diffusion through immobile obstacles predicts that the dependence of the diffusion coefficients of tracer molecules on the density of immobilized obstacles is highly nonlinear. When the density of obstacles is as low as 25 %, freely diffusion species can be slowed down drastically or stopped. The membrane proteins can escape from one domain and move to adjacent compartments as a result of the dynamic reorganization of the membrane skeleton. The distance between the membrane and the skeleton may fluctuate over time, or may dissociate or form. These effects will cause the constant restructuring of the compartments and allow for proteins to change domains. Furthermore, if the thermal energy of the protein is high enough, it can also simply hop over the fence. This model has been used to explain the diffusion barrier set up by the initial segment of the axon (AIS) [95]. Nakada et al. showed that even phospholipid phosphatidylethanolamine is immobilized by the barrier and that the level of immobilization depends on the assembly of ankyrin G.

It is argued that this hop diffusion is often not seen by experiments that use an acquisition time that is too long to observe the particle localized in its domain before the next hop. This is a valid argument for DOPE phospholipids, where measured hopping times are $1 - 17 \, \text{ms}$ [53,96]. In such a case, the apparent diffusion coefficient that is measured is a combination of the free diffusion coefficient in the small corrals and the hopping probability. However, confined motion is also detected with residence times that are substantially longer than the residence times in the dynamic corrals. Such confinement can be easily detected with longer acquisition times and it is often attributed to another effect, the crowding effect, which will be introduced in the next section.

Table 1.1 summarizes a selection of molecules whose confinement type is attributed to the picket and fence model. The results show rather low diffusion coefficients for large transmembrane proteins that are tethered to the cytoskeleton, such as E-Cadherin and EGF-R. This is because the experiment measured the apparent diffusion coefficient D_{macro}, which mainly depends on the boundary hopping frequency and not on the discussion inside the domain. Later the group defined the diffusion coefficient inside the picket and fence domain as the microscopic diffusion coefficient D_{micro}, which was not accessible at the moment of the experiments due to experimental limitations. Nevertheless, the range of ex-
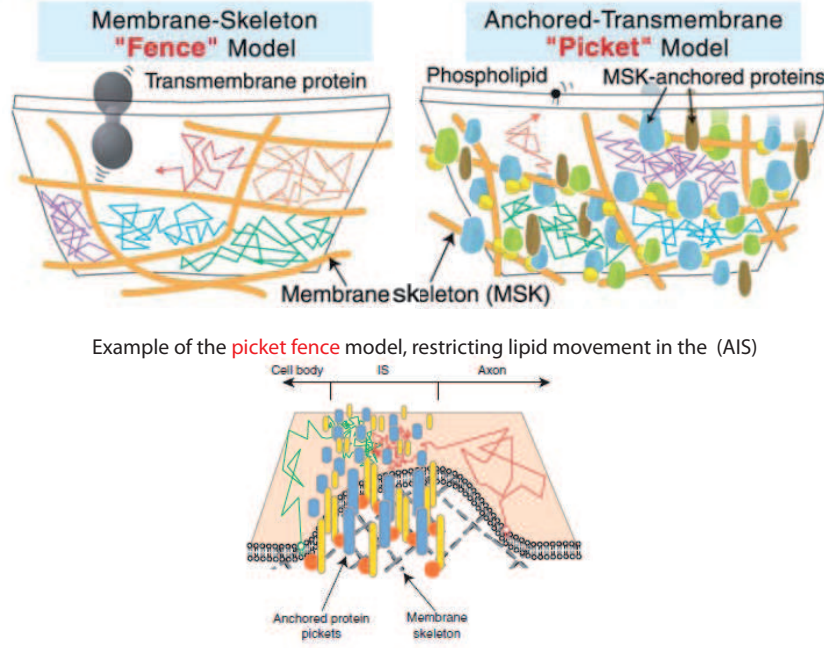
Figure 1.4: In the picket and fence model, the movement of transmembrane proteins is restricted by the membrane skeleton. Acting as percolation barriers, they can also confine the movement of smaller molecules. This image has been proposed by Kusumi et al. [96]. The model has been used to describe the diffusion barrier in the neuron between the cell body and the axon. Bottom figure reproduced from [95].

perimentally determined diffusion coefficients for the transmembrane Transferrin (Tf-R) receptor is very large, depending on the experimental method. A strong proponent of this picket and fence model is the Kusumi group that is able to track gold particles at very high acquisition times down to 25 μs per image and can thus observe domains with very small residence times.

1.4.3   Crowding effects

Crowding effects are thought to be responsible for anomalous diffusion, but they are nevertheless discussed here since strongly anomalous diffusion may lead to protein confinement. When the size of a solute is larger than or similar to the size of the solvent, its diffusion is governed by Fick's law of diffusion and the diffusion constant D depends on the size and shape of the solute. This process will lead to normal Brownian diffusion. In inhomogeneous environments, in crowded environments, or when the solute is smaller than the solvent, the diffusion coefficient is no longer simply Brownian [97]. In this case it can be described as subdiffusion with α in equation 1.5 being smaller than 1, as described in the work of Bouchaud & Georges [98]. A similar argument is used in the picket and fence model, where

small lipids are confined due to barriers. The difference between the models is that crowding does not necessarily require interactions with the cytoskeleton. Experiments suggesting confinement or anomalous diffusion due to crowding effects are summarized in table 1.2.

1.4.4   Lipid rafts

Advances in ultrasensitive mass spectrometry have shown that the lipid composition of the plasma membrane of living eukaryotic cells consists of up to 500 different lipid species that can be classified according to their head and tail structure [99–101]. Cells can sort their lipids and proteins to generate order in the membrane [102, 103]. Regions where certain lipids are sorted to, have come to be known as lipid rafts [79]. As the name suggests, lipid rafts consist of a more ordered, more tightly packed phase of lipids. Initially, the only proof for the existence of rafts was provided by biochemical studies in artifical bilayers. In 1978, the proposed model for lipid rafts had changed from quasicrystalline lipid clusters [104] to lipids in an ordered state [105]. The first phase seperation in a model lipid bilayer was shown by Lentz et al. in 1980 [106]. Formally, the concept of lipid domains was introduced by Karnovsky et al. in 1982, who observed multiple phases in a lipid membrane [78].

Two approaches are followed to proof the existence of rafts and to gain information about their properties: artificial model membranes where the composition can be carefully controlled and cell membranes.

In artificial membranes, it has been shown that, when glycosphingolipids and less saturated lipids are present, the glycosphingolipids will spontaneously assemble into small domains [79, 107–109]. The driving force includes line tension [110–112], hydrophobic interactions [112] and lipid-lipid interactions of various types, such as van der Waals and weak dipolar interactions [99]. Often the packing is mediated via cholesterol, which allows the lipid tail groups to move together more closely. The densely packed or more ordered raft phase is referred to as the lipid ordered phase (L_o). The more fluid, unordered phase is named lipid disordered phase (L_d). Furthermore, experiments have shown that GM1 glycospingolipids also form clusters, rich in glycosphingolipids and cholesterol [113]. Such rafts scale from nanometers [114, 115] to mircometers [116].

Experiments in model membranes repeatedly showed these domains and the question remains why these domains are much more difficult to observe in cells [117]. Furthermore, all the proofs for the existence of lipid rafts in model membranes are obtained at thermal equilibrium, whereas living cells are not in equilibrium. Thus, these domains have to be observed in live cells to prove their existence.

In live cells, certain lipids and proteins were found to be in a detergent-insoluble fraction, which is sometimes referred to as detergent resistant membrane (DRM) domains or detergent-insoluble glycolipid-rich (DIG) domains [118,119]. Biochemical experiments also showed that glycosylphosphatidylinositol (GPI)-anchored proteins are recruited into these rafts. Indeed they were found to be constituents of the insoluble phase after Triton-X-100 detergent extraction [102,120–123]. Antibody crosslinking of receptors can co-patch certain lipids and raft proteins while excluding others [120,124]. These observations led Simons and co-workers to articulate their raft hypothesis [79,80]. However, clusters of proteins were not observed until single molecule experiments by Sheets et al. [125], that confirmed clusters for C3H 10T1/2 cells with sizes of $260 - 330$ nm. The authors also showed that GM1 glycospingolipids were also confined to these zones. Varma et al. [74] confirmed this finding by FRET measurements on a folate receptor bound to a fluorescent analogue of folic acid and showed that depletion of cholesterol led to disaggregation. This disaggregation was also observed in different biochemical studies [123]. Further experiments by Pralle et al. [126] and Sharma et al. [127] on GPI-anchored proteins also showed domains in live cells and determined these rafts to be on the order of 50 nm. With the advent of superresolution techniques, Eggeling et al. [26] could show with FCS measurements that sphingolipids can get trapped in zones no larger than 20 nm. GPI-anchor rich rafts were also directly observed by near field techniques [128]. The interaction of these rafts with actin is debated, as their formation was shown to be both actin-dependent [129] and independent [130].

Perhaps the most striking difference between model membranes and cell membranes are results obtained for the association of transmembrane proteins. In model membranes, they have found to be excluded from the lipid ordered raft phase [131–133], while they have been shown to localize into lipid rafts in live cells [126]. This points towards an effect where proteins would interact strongly with the lipids and thereby influence the environment. The concentration of protein in model membranes is typically very low when compared to the concentration of 32000 proteins / μm^2 in caveolae [118]. The question remains if it is the proteins that form the rafts or if proteins get recruited to already existing rafts. Membrane proteins recruit lipids, which is referred to as wetting [134] or lubricating [135]. In the picture of the shell model, proteins are addressed to lipid rafts via the nature of the lipids that they recruit in a small shell around themselves [136].

Rafts have been correlated with a variety of signaling and sorting properties of membrane components. In parallel, sphingolipid depletion has also been shown to perturb sorting and signaling properties of many membrane proteins. Recent strong evidence for lipid rafts in live cells comes from the lipidome of the HIV virus, which was found to be enriched in cholesterol, sphingolipids, phosphatidylserine,

and plasmenylethanolamine, similar to components found in lipid rafts [137]. It has been proposed that budding of the HIV virus occurs from lipid rafts [138]. The special lipid composition of the virus suggests that the composition was already present in the live cell before the budding occurred.

In recent years the lipid raft definition has been changing. They are no longer strictly associated with DRMs because the credibility of the DRMs has been challenged. Indeed, a study has shown that extraction with Triton X-100 detergent from tertiary artificial bilayer dramatically altered the lipid composition of the pre-existing domains [108, 140]. These and other experiments suggest that the spontaneous demixing of lipids is likely to be sensitive to the incorporation of detergent molecules. For different detergents, different lipids are found in DRMs [141]. Additional difficulties in classifying rafts come from their heterogeneity. For example, experiments have shown that a GPI-anchored prion protein and a GPI-anchored Thy-1 protein reside in lipid rafts of different lipid composition [142].

Another point of conceptual importance is that lipid segregation in artificial bilayers is achieved at thermal equilibrium. However, the cell membrane bilayer is far from being in thermal equilibrium as indicated by the transbilayer lipid and protein asymmetry and lateral compositional heterogeneity. New models build upon the previously described classical lipid raft model and predict the existence of small ($\sim 4 - 5$ nm) high-density clusters of proteins and lipids with cholesterol [74, 127]. These small clusters have also been shown to contain GPI-anchored proteins. They are actively maintained by the cell and can then be merged to form rafts that function as a signaling platform [123, 143, 144]. The different scenarios are summarized in figure
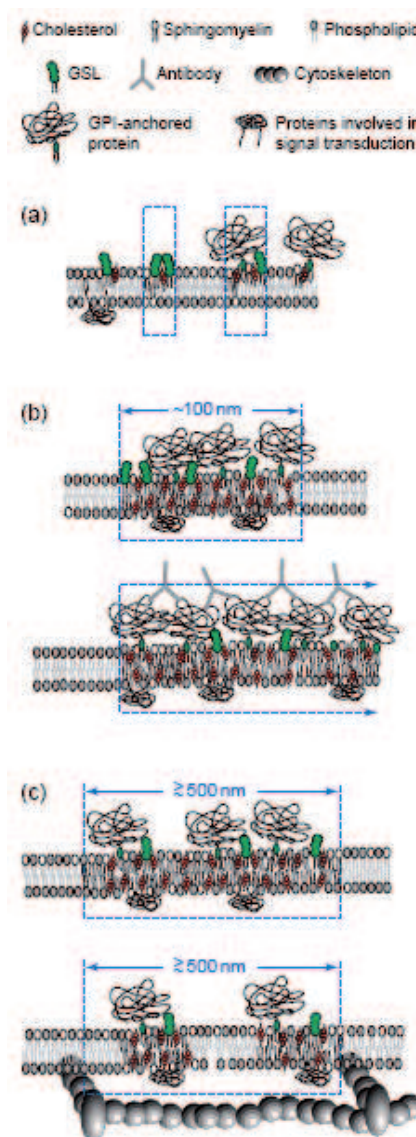
Figure 1.5: Summary of the raft models as seen by Jacobson and Dietrich (Ref. [139]).

1.5, which appeared in an article by Jacobson and Dietrich [139]. Figure 1.5 a) shows nano-rafts that only contain a few lipids and proteins as proposed in [127]. These clusters will disaggregate upon cholesterol extraction. Figure 1.5 b) shows the formation of larger rafts by accumulation of small entities. This could be induced actively by the cell or by ligand binding or by antibodies [99]. Such rafts could contain up to 600 proteins. Macro-rafts are shown in figure 1.5 c). These rafts can interact with the cytoskeleton, which could also control the raft size. Some experiments that were interpreted with rafts being the confining elements are summarized in table 1.4. A major problem of the lipid raft picture is the raft size variability. Experiments find a very large range of results as shown in table 1.4 (see quoted values for domain area).

In the 2006 Keystone Symposium of Lipid Rafts and Cell Function, a consensus definition of lipid rafts taking into account recent research developments was proposed: *"Lipid rafts are small (10−200 nm), heterogeneous, highly dynamic, sterol- and sphingolipid-enriched domains that compartmentalize cellular processes"* [111].

1.4.5   Protein clusters

Analogous to clustering lipids, proteins are also suspected to cluster due to protein-protein interactions, which are of the order of $k_B T$ [145, 146]. The size of such clusters depends on the ratio of attractive and repulsive force between the proteins. It is important to note that unlike in the above mentioned lipid raft model, the raft formation in this model is driven by the proteins and not by the lipids. Evidence that lipid-lipid interactions are not enough to stabilize proteins in rafts is given by a study of Sieber et al., that considered the clustering of syntaxin 1 and syntaxin 4 [147].

In a model by Destainville [146], the diffusion coefficient in the clusters depends on the concentration of proteins in the cluster. This means that as the cluster grows in terms of number of proteins n, the diffusion coefficient will decrease as $D \propto 1/n$. In reconstituted proteoliposomes, the number of proteins per cluster grows with protein concentration according to an electron microscopy study [148]. In the proposed model, the attractive short-range forces between the proteins have a range of a few nm and an energy of $k_B T$ and include osmotic pressure and hydrophobic mismatch with the lipids. The long-range repulsive forces are due to elastic deformation of the membrane.

Protein clusters have been observed for the Kv2.1 channel, where a few GFP-tagged channels were labeled with quantum dots in HEK cells [149]. Dual-color imaging revealed that receptors were confined within the micrometric clusters and they could be recruited or escape. The actin cytoskeleton, however, was shown to play a role in cluster maintenance.

In terms of function of protein clusters, experiments by Mossman et al. and Lillemeier et al. have shown to activate the immunological synapse of T-cells [150,151]. Furthermore, it was shown that if cluster formation of EphA2 receptors was prohibited, the cell could activate a immunoresponse [152].

Receptor	Type	Cell line	Diffusion coefficient [$\mu m^2/s$]	Domain size	Temperature [$°C$]	Notes	Reference
TM-I-E^k	transmembrane, MHC II	CHO	0.15 ± 0.12	$0.018\,\mu m^2$	37	-	[153]
GPI-I-E^k	GPI-Anchor	CHO	0.33 ± 0.3	$0.0011\,\mu m^2$	37	-	[153]
Thy-1	GPI-Anchor	3T3	0.1	$1-4\,\mu m^2$	37	speculate on cytoskeleton	[154]
Various GPI	GPI-Anchor	COS-7, NRK, BHK-21	$0.4-0.7$	-	37	-	[155]
HLA-DR	cell surface receptor, MHC II	M1DR1	$0.13-1.9 \times 10^{-4}$	$0.14 \pm 0.003\,\mu m^2$	21	no reason for confinement	[156]
Tf-R	transmembrane	NRK	0.1	$0.25\mu m^2$	37	-	[87]
Tf-R	transmembrane	F7p	0.0078 ± 0.0081	$0.04-0.24\,\mu m^2$	37	-	[73]
Tf-R	transmembrane	PtK2	0.55 ± 0.04	$0.002\,\mu m^2$	37	apparent D	[157]
Tf-R	transmembrane	PtK2	2.2 ± 0.2	$0.002\,\mu m^2$	37	D micro	[157]
α2M-r	transmembrane	NRK	0.1	$0.25\mu m^2$	37	-	[87]
EGF-R	transmembrane	F7p	0.011 ± 0.015	$0.04-0.24\,\mu m^2$	37	-	[73]
E-Cadherin	transmembrane	F7p	0.0065 ± 0.079	$0.04-0.24\,\mu m^2$	37	-	[73]
µOR	G-protein coupled receptor	CHO	$0.032-0.25$	-	37	-	[158]
µOR	G-protein coupled receptor	NRK	0.14 ± 0.1	$-$	37	-	[158]
DPP	transmembrane	COS-7	FCS: diff time vs. spot area	-	37	Actin meshwork	[83]
Tf-R	transmembrane	COS-7	FCS: diff time vs. spot area	-	37	Actin meshwork	[83]
FcϵR		RBL-2H3	0.074	-	37	-	[159]
IgG+Bead		DRG	viscosity measurement	$-$	37	Tether force: 6.7 pN	[88]*
Tf-R	transmembrane	NRK	0.1 ± 0.2	$0.40-0.67\,\mu m^2$	37	Holding force: 0.25 pN 2 fractions elastic boundaries	[66]*
E-Cadherin	tethered	L-cells	0.005	$0.13\,\mu m^2$	37	Holding force: 0.8 pN	[67]*
E-Cadherin	(Catenin-minus mutant)		0.01	$0.52\,\mu m^2$	37	spring constant	
E-Cadherin	(Short-tailed)		0.02	$0.52\,\mu m^2$	37	$k_r = 5$ pN/µm	
H-2D^b	transmembrane	L-cells	0.13 ± 0.02	$0.6\,\mu m$ (BFP)	22	D independent of Temp	[68]*
Qa2^b	transmembrane	L-cells	0.13 ± 0.02	$1.7\,\mu m$ (BFP)	22	D independent of Temp	[68]*
DOPE	Lipid	HASM	$0.15-0.3$	-	37	free motion	[36]
DOPE	Lipid	NRK, CHO-B1, T24, FRSK	$0.2-0.53$	$0.0009-0.053\,\mu m^2$	37	-	[53, 96]
DOPE	Lipid	HEK293, HEPA-OVA, HeLa	$0.2-0.53$	$0.0009-0.053\,\mu m^2$	37	-	[53, 96]

Table 1.1: Selected experimental results for molecules whose confinement was attributed to localization in domains defined by the cytoskeleton in live cells. *: Optical tweezers measurement. (BFP) = Barrier free path

Receptor	Type	Cell line	Diffusion coefficient [µm^2/s]	Domain size	Temperature [°C]	Notes	Reference
TM-I-E^k	transmembrane, MHC II	CHO	0.59 ± 0.04	-	37	D reduces after cholesterol extraction	[160, 161]
GPI-I-E^k	GPI-Anchor	CHO	1.1 ± 0.06	$0.16\,\mathrm{µm}^2$	37	D reduces after cholesterol extraction	[160, 161]
AQP1^k	transmembrane	COS-7	0.072 ± 0.012	$0.0576 \pm 0.0004\,\mathrm{µm}^2$	37	D reduces after cholesterol extraction	[162]
AQP1^k	transmembrane	MDCK	0.020 ± 0.003	$0.0128 \pm 0.0001\,\mathrm{µm}^2$	37	and cytoskeleton has no effect	[162]

Table 1.2: Selected experimental results for molecules whose confinement has been attributed to crowding effects.

Receptor	Type	Cell line	Diffusion coefficient [µm^2/s]	Domain size	Temperature [°C]	Notes	Reference
H-Ras	inner leaflet	tsA201	0.53 ± 0.02	$0.063 \pm 0.001\,\mathrm{µm}^2$	22	-	[163]
H-Ras	inner leaflet	3T3-A14	1.13 ± 0.07	$0.042 \pm 0.001\,\mathrm{µm}^2$	37	-	[163]
Lck	inner leaflet	3T3-A14	0.26 ± 0.13	$0.049 \pm 0.002\,\mathrm{µm}^2$	37	-	[164]
H-Ras	inner leaflet	3T3-A14	0.29 ± 0.12	$0.04\,\mathrm{µm}^2$	37	-	[164]
K-Ras	inner leaflet	3T3-A14	0.15 ± 0.05	$0.048\,\mathrm{µm}^2$	37	-	[164]
HLA-DR	cell surface receptor, MHC II	HT29	0.2	-	-	-	[165]

Table 1.3: Selected experimental results for molecules that are confined to domains due to an undetermined origin.

Receptor	Type	Cell line	Diffusion coefficient [$\mu m^2/s$]	Domain size	Temperature [$^\circ$C]	Notes	Reference
Thy-1	GPI-Anchor	C3H 10T1/2	$0.0035 - 0.081$	$0.12\,\mu m^2$	37	-	[125]
GM1	GSL	C3H 10T1/2	$0.0035 - 0.081$	$0.12\,\mu m^2$	37	-	[125]
GFP-GPI	GPI-Anchor	COS-7	FCS: diff time vs. spot area	-	37	Dynamic partition	[83]
GFP-Thy1	GPI-Anchor	COS-7	FCS: diff time vs. spot area	-	37	Dynamic partition	[83]
Av-GPI	GPI-Anchor	HeLa	0.038	$0.33 - 0.5\,\mu m^2$	27	Colocalization with:	[166]
Av-GPI	GPI-Anchor	HeLa	0.00091	-	27	GM1 & Caveolin	
PLAP	GPI-Anchor	BHK-21	-	$0.0007\,\mu m^2$	37	Holding force: $0.1\,pN$	[126]*
HA	transmembrane	BHK-21	-	$0.0007\,\mu m^2$	37	Measured viscosity	[126]*
						D increased after	
						cholesterol extraction	
DMPE	Lipid (ordered phase)	HASM	0.60 ± 0.04	$0.04 - 4\,\mu m^2$	37	D did not decrease in raft	[36]

Table 1.4: Selected experimental results for molecules that are confined to domains attributed to lipid rafts. *: Optical tweezers measurement.

1.5   Summary

This introduction begins with an overview over some imaging techniques that are currently applied to the problem of membrane architecture, which is important with respect to signaling, trafficking and transport mechanisms in cell biology. The techniques can be separated into ensemble measurements and single molecule experiments, which can reveal subpopulations. Single molecule tracking will be used in this work to investigate the motion of toxin receptors, which can be viewed as probes of the membrane architecture.

Tracking with sub-pixel and sub-diffraction resolution was introduced as it is used in this work to localize and track the motion of toxin receptors. It allows determining the position of the receptor with an error that lies below the diffraction limit of the optical microscope. A short introduction of the different modes of motion, including free Brownian motion, anomalous diffusion, guided or directed motion and motion in corrals was given. The respective signatures in the MSD plots were presented.

Since the toxin receptors are confined to small domains, this chapter introduced only models that can explain such motion. The first of the five introduced models was the tethering of molecules to the cytoskeleton. The second model was the picket and fence model, where actin acts as a fence and fixed transmembrane proteins as barriers. Then it was discussed how crowding of proteins can cause smaller molecules to undergo anomalous diffusion and even localize them. The fourth model was the lipid raft model, which is based on the clustering of lipids providing zones that recruit proteins and other molecules. The last introduced model concerns confined motion of proteins due to protein clustering. Selected experiments were summarized in tables to give an overview of experimental results on diffusion coefficients and domain sizes for molecules that are confined and their interpretation in terms of the various models. However, some experiments showed that, depending on the tracked molecule, multiple types of confinement could coexist [83].

Chapter 2

Single Molecule Tracking of Peptidic Toxins with Luminescent Nanoparticles

Single-molecule tracking using luminescent nanoparticles has developed into an indispensible tool to study proteins. It started with first demonstrations on neurons [44] to current applications, such as tracking of coated QDs on cancer cells in living mice [167]. It is a powerful method used to investigate a plethora of biological processes, such as diffusion and interaction.

2.1 Action of peptidic toxins

The goal of this study is to gain insight into the architecture of the cellular membrane, as introduced in the previous chapter 1. To this end, we monitor single toxin molecules, as they diffuse on the membrane, coupled to their receptor. We monitor the receptor motion of the pore-forming α-toxin of *Clostridium septicum* (C. septicum) [168, 169] and the receptor of the pore-forming ϵ-toxin of *Clostridium perfingens* (C. perfingens) types B and D [170, 171] on epithelial cells. The interest in these receptors is twofold. For one, *C. Septicum* and *C. Perfingens* cause a variety of enteric infections in both animals and humans that can be fatal and cause economic damage. The second interest is to understand the mechanism used for achieving their relatively high toxicity.

*C. Septicum* infections cause, in humans and animals, symptoms like edema and gangrene, which are rapidly fatal if untreated. The bacterium is often found in soil and has also been isolated from feces of domestic animals and humans [172,173]. It is also a common postmortem invader. The bacterium can directly infect wounds, leading to as malignant edema [174]. In the case of enteric infections, production

of toxins in the gut by bacteria initiate enterotoxaemia when the toxins produced in the gut enter the blood [175], causing a disease also known as braxy or bradshot in lambs and older sheep [176]. In later stages, *C. Septicum* causes local lesions in the stomach lining, edema, hemorrhages and sometime necrosis. The disease has been observed in sheep and calves. The bacteria also causes fatal enteric infections such as necrotic enteritis, which has a mortality rate between 5 to 50 % in poultry. Alpha toxin was first described by Alan Bernheimer in 1944, who injected the toxin into mice and observed lethal and hemolytic activity [177]. The α-toxin is the only known lethal factor of *C. septicum*.

C. perfingens is the most widely occurring pathogenic bacterium [178] and is thus the most important cause for enteric disease in domestic animals. The bacterium lives in the intestinal tracts of animals and also in the environment. It is also a common post mortem invader. The bacterium is known to produce 17 exotoxins, while ϵ-toxin is most important virulence factor of *C. perfingens* [169]. In fact, ϵ-toxin is the most potent clostridial toxin known after botulinum and tetanus neurotoxins [179] and has been classified as a possible bioterrorism agent of the category B (moderately easy to disseminate; result in moderate morbidity and low mortality rates) by the U.S. Center for Disease Control and Prevention.

To understand the high toxicity of the toxins one has to consider the interaction at the molecular level. Pore-forming toxins assemble a complex from small monomeric subunits that pierces the membrane. Structures of both toxins are known [168, 180] and they show strong homology to the pore-forming toxin aerolysin [169, 180]. Figure 2.1 a) shows the structure of the alpha toxin of *C. Septicum* with its three domains. The toxin binds to a GPI-Anchored receptor via domain 1. Domain 3 plays a role in the oligomerization of the monomers. Domain 2 folds out and pierces the cell membrane with a beta-barrel. Figure 2.1 b) shows the pore of the toxin α-Hemolysin with the beta-barrel that pierces the cell membrane.

The steps of the toxin action are secretion, activation, coupling to the cellular membrane, formation of a pre-pore form, insertion of the β barrel and cell lysis [183]. After secretion by the bacterium, both toxins undergo enzymatic cleavage to transform into an activated form [169,184]. The uncleaved form, the prototoxin, cannot form pores but attaches nevertheless to its receptor. Once secreted and activated by cleavage, the monomers attach to receptors in the membrane. It has been shown that the hijacked receptor of the α-toxin is a glycophosphatidylinositol-anchored protein (GPI)-anchor [185,186], as is the case for aerolysin. The receptor of the ϵ-toxin has yet to be determined, but has been determined to be of similar molecular weight (34 kDa) [170, 187]. Once coupled to the membrane, the toxins diffuse laterally to find other activated monomers. For the ϵ-toxin it has been shown that seven 29 kDa monomers assemble into $155 - 210$ kDa complexes after
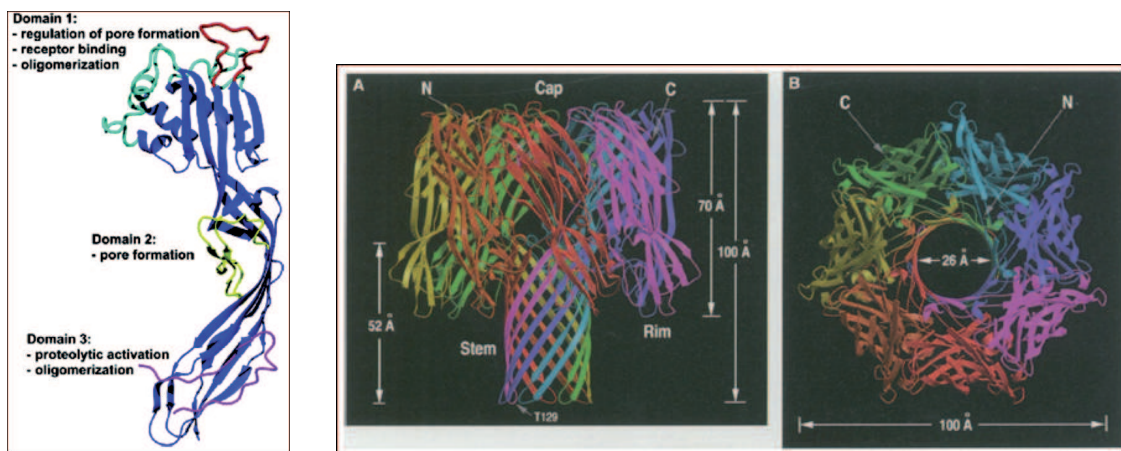
(a) Structure of the α toxin of *C. Septicum*, reproduced from ref. [181].

(b) Pore of the α-Hemolysin toxin, reproduced from ref. [182].

Figure 2.1: Structure of the α-toxin, which shows a strong homology to the pore-forming toxin aerolysin and α-Hemolysin. The α-toxin binds to a GPI-Anchored receptor via domain 1. Domain 3 plays a role in the oligomerization of the monomers. Domain 2 folds out and pierces the cell membrane with a beta-barrel.

30 minutes [170,188]. The activated monomers of the α-toxin have a size of 48 kDa and form complexes of 210 kDa [175]. When enough monomers oligomerize, they form a large pre-pore complex. The complex is coined pre-pore, since actually no pore has yet formed and there are no transmembrane regions. It is actually possible to trap the complex in this state at 4 °C [189]. Upon insertion of the β barrel that pierces the membrane, cells will lose K^+ ions, which leads to cell death.

The striking feature of the toxin activity is that, although it goes through a complex mechanism of self assembly of many monomers to build up the pore, it maintains an extremely high lethality of $10\,\mu g\,kg^{-1}$ and $100\,ng\,kg^{-1}$ for α-toxin and ϵ-toxin, respectively [175, 180]. For high toxicity, one would expect that the required dose of monomers would also be high but this is not the case.

Obviously the toxins take advantage of a mechanism, implemented by the cell they are attacking, that groups receptors together in close proximity to concentrate them onto a smaller surface, increasing the number of monomers per surface area. These toxins are thus excellent probes for the membrane architecture. Using receptors that do not diffuse all over the membrane surface, but are somehow localized, increases the chance of successful pore formation and enhances the potency of the toxin. It has already been shown that GPI-anchored proteins, which are the α toxin receptor, localize into detergent resistant membrane do-

mains (DRMs) [74, 79, 121, 122, 190]. Furthermore, the ϵ-toxin receptors were also shoawn to localize into DRMs.

The Madin-Darby Canine Kidney (MDCK) epithelial cell line, to which these toxins have been shown to bind [170, 191], is an epithelial cell line that exhibits membrane polarization, thus expressing different proteins on different sides of the cell [192, 193]. We are using this cell line as a model cell line to study the toxins. These cells connect to each other through their lateral membranes to form epithelial sheets that line cavities and surfaces in the body. It is thus one of the first cell types encountered by the infecting bacterium. The cells in the sheet are bound to each other via adherent junctions formed by the adhesion molecule E-cadherin, linking the actin skeleton of neighboring cells. How exactly the polarization between apical, basal and lateral membranes is maintained is not fully understood but might involve principles such as positive feedback, segregation of polarity determinants by an active mechanism or directed exocytosis [194–196].

2.2   Experimental set-up and sample

This section introduces the specific system that is used to investigate the organization of the cell membrane by investigating trajectories of single nanoparticle-labeled toxin monomers. First the label is described, followed by a description of the experiment.

Toxins, which hijack the cell's receptors, are coupled to a fluorescent label to render them visible. As discussed in chapter 1, there are many different fluorescent markers, such as fluorescent molecules, fluorescent microspheres [197], low-density lipoprotein with carbocyanine lipid analogs (diI-LDL) [27, 198], fluorescent viruses [76], quantum dots [44] or other nanocrystals and polymers [59]. We chose rare-earth doped nanoparticles, because these markers are highly photostable and do not exhibit blinking. The $30 - 60$ nm nanoparticles also display good photo stability and are synthesized directly in water. The particles were synthesized, functionalized with APTES, coated with a silica layer in the group of T. Gacoin and J.-P. Boilot [199]. The coupling reaction was first realized by D. Casanova [200].

The excitation and emission spectra of the $Y_{1-x}Eu_x VO_4$ nanoparticles are shown in figure 2.2 a and b, respectively. The nanoparticles can be excited either by direct excitation of the Eu^{3+} ions ($^5D_2 - ^7F_{0,1}$ transition at 466 nm and $^5L_6 - ^7F_{0,1}$ transition at 396 nm) or by excitation of the vanadate matrix in the UV (absorption peak centered at 280 nm) followed by excitation transfer to the Eu^{3+} ions. In both cases, the emission spectrum is dominated by the $^7F_2 - ^5D_0$ transition

consisting of two narrow lines at 615 and 619 nm. Even though the vanadate matrix extinction coefficient in the UV (410×10^6 $M^{-1}cm^{-1}$ for a 30 nm 40 %-doped nanoparticle) is much higher than that for direct excitation ($24000\,M^{-1}cm^{-1}$ at 466 nm for a 30 nm 40 %-doped nanoparticle), we chose to excite the nanoparticles in the visible to avoid photoexcitation-induced toxicity to the cells. We therefore used the 465.8 nm-line of the Argon-ion laser which coincides with the $^5D_2 - {}^7F_{0,1}$ Eu^{3+} transition to excite the nanoparticles. The lifetime of the $^7F_2$ Eu^{3+} excited state depends on the Eu^{3+} doping concentration [201] and is 340 μs for 40 % doping. The lifetimes were measured as explained in appendix A.6 and are shown in figure 2.2. For the doping range, where Eu-Eu energy transfer is not very important, higher dopant concentration will lead to a higher number of emitted photons. Thus 40 % doped YVO_4^-:Eu nanoparticles are coupled to toxins to maximize the signal-to-noise ratio. With the exception of a decrease in quantum efficiency, the optical properties of the nanoparticles do not change upon functionalization [202].

The current coupling reaction to proteins, summarized in appendix A.1, leads to a decrease in quantum efficiency. For a specific coupling reaction, the efficiency was observed to drop from 8 % to 3 % after the completed reaction. This is also visible from the lifetime evolution, where the characteristic lifetime of the exponential emission decay of the particle is 340 μs before the coupling (blue data points) and 237 μs after the BS_3 coupling reaction (red data points), as can be seen in figure 2.2 c). This is probably caused by the appearance of additional non-radiative de-excitation pathways due to the cross-linker molecules coupled to the nanoparticle surface.

Much work has been invested in the Laboratoire de Physique Condensée to increase the quantum efficiency of the nanoparticles. To this end, an annealing process was developed to improve the crystallinity of the nanoparticles. Since energy transfer from ion to ion is possible in the particles, if there is an ion close to a defect. Indeed, crystal line defects are an efficient route for non radiative decay. A better crystallinity will cause two competing effects that have to be considered to determine the optimal doping concentration of the nanoparticles. A better crystal structure of the particle will reduce bulk defects and thus leave fewer sites for non-radiative transitions and increase the number of emitted photons, as desired. However, on the other hand, the inter-ion energy transfer will increase as the crystallinity is improved. Due to the long lifetime of the radiative transition, relaxation via non-radiative surface defects is a major energy decay pathway. The evolution of the total number of emitted photons and relative quantum efficiency is shown in figure 2.3 a) & b), respectively for crude (black) and annealed (red) nanoparticles. The evolution of the decay contributions and their effect on the quantum efficiency is explained in more detail in references [201, 203]. So far, these annealed nanoparticles have been functionalized with APTES but have not
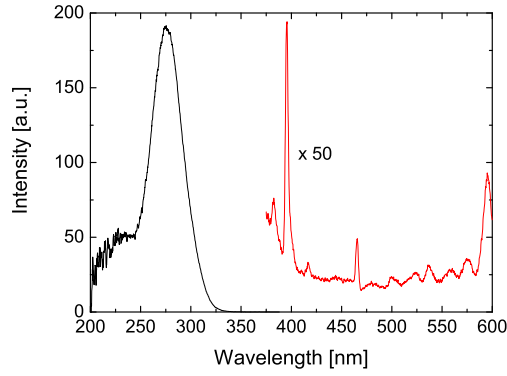
(a) Excitation spectrum. The emission is detected at 617 nm.
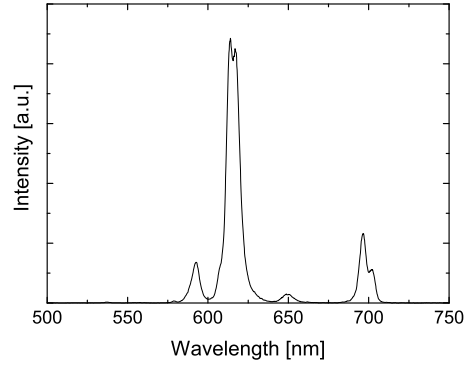
(b) Emission spectrum for excitation at 280 nm.
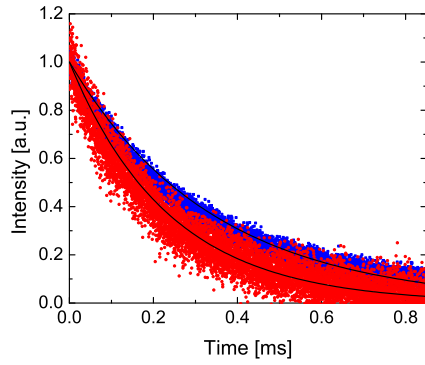
(c) Lifetime of NPs in observation medium. The emission decay at 617 nm of APTES functionalized NPs is given in blue and the decay of protein and BS$_3$ coupled NPs is shown in red. The black lines are the exponential fits to the decays that are used to extract the lifetime.
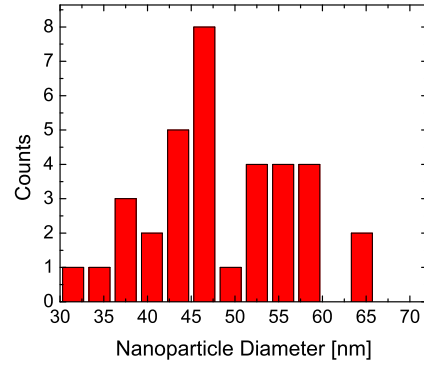
(d) Size dispersion of NPs during tracking experiments.

Figure 2.2: Spectral properties of of 40% doped Eu^{3+} YVO$_4^-$ nanoparticles with a diameter of 30 to 60 nm. During cell experiments, the particles are excited in the visible, using an Ar-ion laser at 465.8 nm, while fluorescence is recorded for the $^7F_2 - ^5D_0$ transition at 615 and 619 nm.

(a) Total emitted intensity form NPs.

(b) Relative quantum efficiency of NPs. Crude NPs in black and annealed NPs in blue.
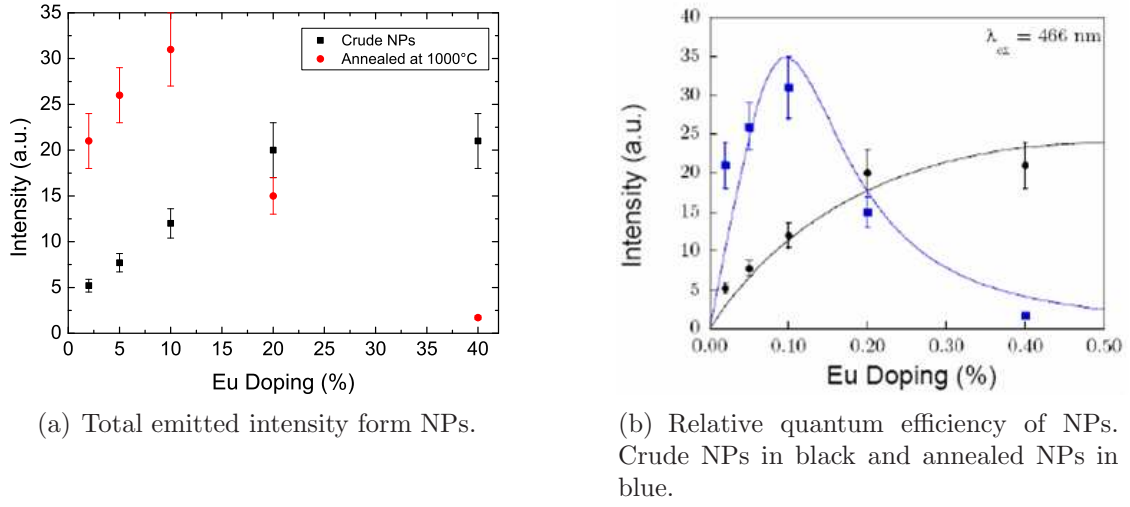
Figure 2.3: Quantum efficiency of nanoparticles with respect to dopant concentration. For the non annealed case, the number of crystal defects remains constant for all dopant concentrations, leading to the effect that more europium ions will give more photons. For annealed particles two effects compete. Better crystal structure increases the quantum efficiency at a constant rate for all doping concentrations. Easier energy transfer from ion to ion will increase the chance of relaxation at a defect for a higher concentration, actually lowering the photon emission at higher doping concentrations.

yet been coupled to biomolecules. They will certainly lead the way to improved photostability and signal-to-noise ratio. All experiments presented in this thesis make use of non-annealed nanoparticles.

For the experiments that are presented in this work, $Y_{0.6}Eu_{0.4}VO_4$ nanoparticles were prepared as described in [57, 202, 204, 205]. Briefly, the nanoparticles were prepared from an aqueous solution of sodium orthovanadate by drop-wise adding an aqueous solution of yttrium and europium nitrate with the desired europium content ($[Y^{3+}] + [Eu^{3+}] = [VO_4^-]$). The solution was then purified by dialysis against pure water. The particles were coated by a thin silica layer by absorption of silicate ions onto the surface from an added tetramethylammonium silicate solution. The nanoparticles were further functionalized with a silicon alkoxysilane bearing amino groups (3-aminopropyltriethoxysilane, APTES), which is polymerized around the particles through a hydrolysis / condensation reaction. The final thickness of the amino silane shell is about 2.6 nm, with 1.4 reactive amino groups per nm^2. We then coupled the APTES-coated europium-doped nanoparticles to α and ϵ toxins produced by the *C. septicum* and *C. perfringens* bacteria, respectively via the amine-reactive cross-linker bis (sulfosuccinimidyl) suberate (BS_3) [205]. After removing excess unbound toxins by centrifugation, the NP-toxin complexes were stored at $-80\,°C$. The coupling ratio can be adjusted by varying the ratio of

the toxin concentration to the nanoparticle concentration. To speed up the reaction high nanoparticle concentrations are used. A BCA test showed that we have achieved a coupling ratio of 1 : 1 for the ϵ-toxin to nanoparticles [202]. Since the distribution is Poissonian peaked at one, the fraction of NPs bound to zero, one and two or more toxins are 37 %, 37 %, and 26 %, respectively. Nanoparticles without toxins do not bind to the cells and are rinsed away. Given the size of the NPs, it is improbable that more than one toxin is present on the same area of the NP surface allowing simultaneous binding to more than one receptor. Furthermore, the binding ability of a fraction of the toxins may be impaired by the coupling to the NPs. We therefore estimate that the fraction of NPs bound to more than one receptor is less than 10 %.

The endothelial cells used in all experiments are Madin-Darby canine kidney (MDCK) cells. MDCK were cultured in culture medium (CM) (DMEM, 10 % fetal calf serum (FCS), 1 % penicillin-streptomycin) at 37 °C. For tracking experiments, cells were trypsinated (1x) two days before an experiment and transferred onto acid bath treated glass coverslips and grown until confluent. The medium was replaced by an observation medium (OM) (HBSS + 10 mM HEPES, 1 % FCS) just before the tracking experiment. Cells were not used for longer than 10 weeks for culture and not longer than 1.5 hours for experiments.

Tracking experiments were performed with a wide-field inverted microscope (Zeiss Axiovert 100) equipped with a 63x, NA = 1.4 oil-immersion objective. Images were recorded with an EM-CCD (Roper Scientific QuantEM:512SC). The nanoparticles were excited with an Ar^+-ion laser using the 465.8 nm line. The emission of the NPs was collected through a 617/8M filter (Chroma). Confluent cells on coverslips were incubated with 0.04 nM labeled α or ϵ-toxin (can form oligomers) or ϵ-prototoxin (cannot form oligomers) for 20 minutes at room temperature. The sample was then rinsed three times with observation medium to remove non bound nanoparticles (see appendix A.2). We recorded images at a frame rate of 20 Hz and an excitation intensity of $0.25 \, \text{kW/cm}^2$ at room temperature or 37 °C. The concentration of nanoparticle-toxin complexes was chosen such that single molecules can be easily distinguished.

2.3   Considerations for tracking experiments

Microscopes are extremely powerful tools, however, as Henry Baker already warned us about the use of microscopes in his book *The Microscope Made Easy* in 1742: *"When you employ the microscope, shake off all prejudice, nor harbor any favorite opinions; for, if you do, 'tis not unlikely fancy will betray you into error, and make you see what you wish to see"* [206]. This section will thus discuss potential pitfalls

in image acquisition and analysis, as well as in sample preparation, as suggested in [207].

2.3.1   Control experiments to test the sample

Observed experimental trajectories of labeled ϵ toxin monomers are confined to small domains with diameters smaller than 600 nm, as evident from their shape in figure 2.4 a and exhibit jumps rarely. The confining domain's dimensions are only a fraction of the entire cell surface of about 200 µm². Control experiments were performed to show that the observed trajectories of the labeled toxins reflect the natural behavior of the toxins.

In figure 2.4 a), the motion of the ϵ toxin receptor (black) is compared to the motion of the receptor in fixed cells (red) at room temperature. The image analysis of the single-molecule data is introduced in the next section. Fixing the cell with 4 % paraformaldehyde freezes out, although not completely [208], the motion of the proteins in the cell membrane. This experiment gives a measure of the lowest accessible and sensible values for diffusion coefficients and domain sizes. Applying the mean squares analysis (MSD) analysis, as described in appendix B.1, yields values for the diffusion coefficient D_{MSD} and domain size L_{MSD}, where the MSD subscript indicates the use of the MSD analysis. We obtain 0.004 µm²/s for D_{MSD} and 100 nm for L_{MSD} from experiments. These values are in agreement with minimal values from performance tests of our image analysis algorithms for similar signal-to-noise ratios of around 25. These minimal values are superior to those determined by evaluating the movements of immobilized nanoparticles on a glass substrate because of the large difference in signal-to-noise ratio due to the presence of cell fluorescence. Figure 2.4 a) shows that the movement we are detecting is not just noise, but the actual movement of the receptor.

Large nanoparticles could impede the motion of the receptor, causing a confinement or slower diffusion coefficients [209, 210]. Therefore, as a control experiment, the nanoparticle was substituted with a small organic fluorophore (Cy3) with a coupling ratio of ($\sim 3 : 1$). In both cases, the ϵ toxin receptor motion is confined to a small domain in the cell membrane of average length $\langle L_{MSD} \rangle = 350 \pm 230$ nm as shown in figure 2.4 c). The obtained average diffusion coefficients are $\langle D_{MSD}^{NP} \rangle = 0.05 \pm 0.06$ µm²/s and $\langle D_{MSD}^{FF} \rangle = 0.05 \pm 0.05$ µm²/s for nanoparticle labels and fluorophore labels, respectively. Furthermore, the overlay of the obtained histograms for D_{MSD} and L_{MSD} show no significant difference between the cases of nanoparticles and organic fluorophore labels. We are therefore allows us to be confident that the confinement is not due to the nanoparticle size and furthermore, that the motion is not perturbed.

(a) Typical trajectory of a nanoparticle coupled to its receptor (black) via ϵ toxin in a live MDCK cell and a trajectory on a fixed cell (red).

(b) Comparison of the diffusion coefficients D_{MSD} between NP (red) and fluorophore (blue) labeled ϵ-toxin receptors.

(c) Comparison of the domain size L_{MSD} between NP (red) and fluorophore (blue) labeled ϵ-toxin receptors.
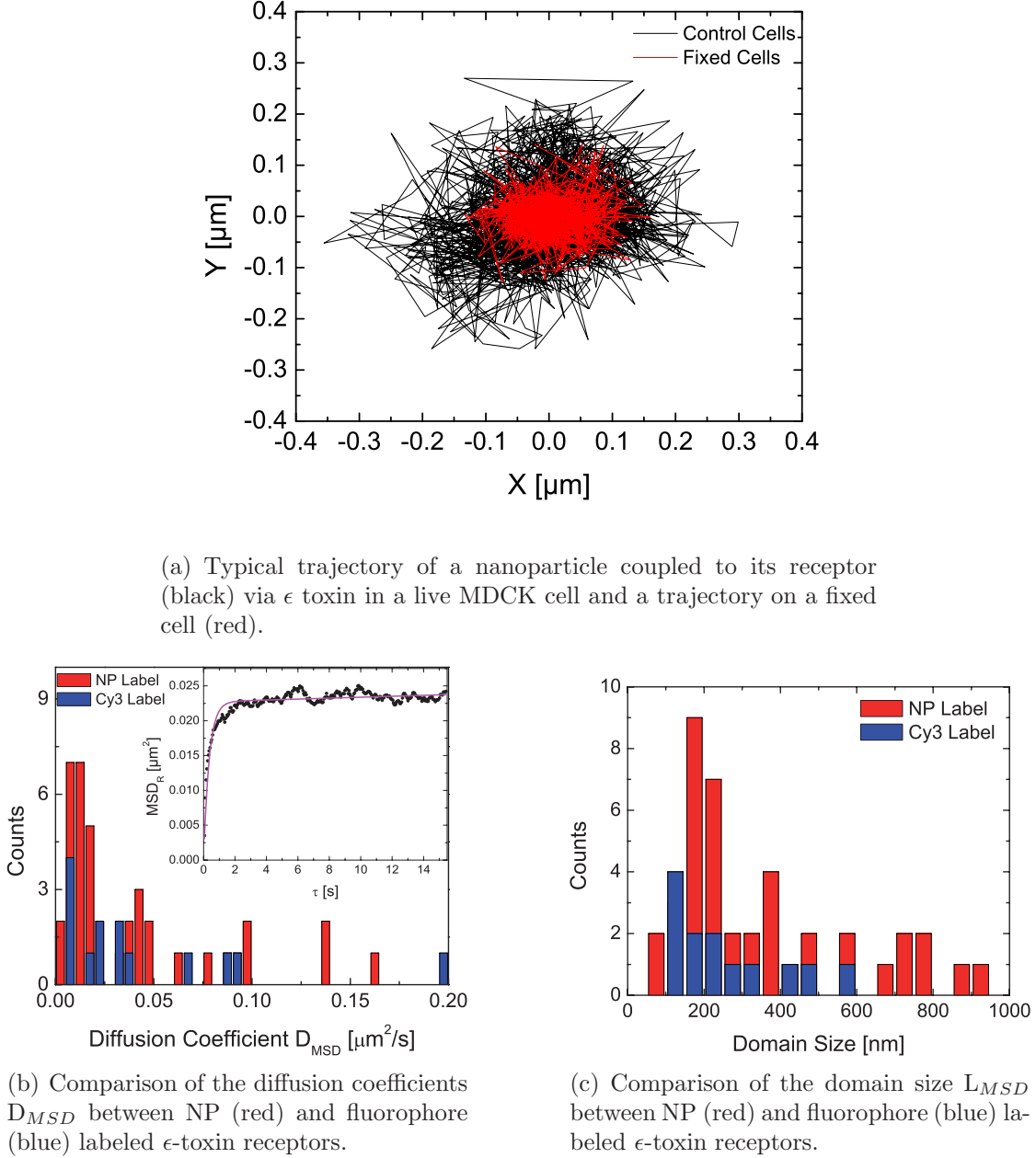
Figure 2.4: Comparison of he behavior of nanoparticle- and fluorophore-labeled ϵ-toxin receptors at room temperature. a) The black trajectory shows a typically observed trajectory in live cells, while the red trajectory is obtained after fixing and thus immobilizing the motion of proteins in the cell membrane. This gives an experimental estimate of the lowest accessible values for diffusion coefficients and domain sizes ($0.004\,\mu m^2/s$ for D_{MSD} and $100\,nm$ for L_{MSD}). Figures (b) and (c) show the distribution of results for diffusion coefficients and domain sizes from the MSD analysis of toxins labeled with nanoparticles (red) and with a fluorescent molecule Cy3 (blue). The determined mean values are $\langle D_{MSD}^{NP}\rangle = 0.05 \pm 0.06\,\mu m^2/s$ and $\langle D_{MSD}^{FF}\rangle = 0.05 \pm 0.05\,\mu m^2/s$ for diffusion coefficients and $\langle L_{MSD}\rangle = 350 \pm 230\,nm$ for both types of labels for domain sizes.

Further control experiments were performed to address the question, whether the toxin is actually coupled specifically to its receptor, or if it is just interacting non-specifically with the membrane. To this end, we incubated the ϵ-toxin functionalized NPs with an antibody against the toxin. Figure 2.5 a) shows that the number of bound nanoparticles to the cell membrane decreases to 16 % of the initial value if the NP-toxin conjugates are incubated with an antibody before addition to the cells, giving a measure of the specificity of the introduced label. This result also confirms that the toxin uses a receptor to couple to the membrane, rather than directly interacting with the lipid membrane.
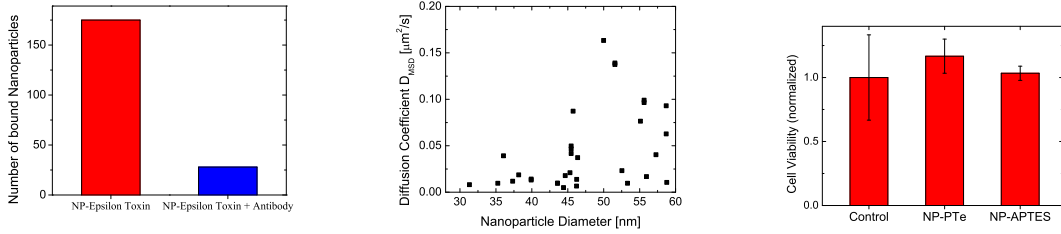
(a) Effect of an antibody specific to the toxin on the nanoparticle reduces the attachment of the NP-labeled toxins to the membrane.

(b) Measures diffusion coefficients D_{MSD} for different nanoparticles of different sizes.

(c) Toxicity test of NPs shows no reduction of cell viability.

Figure 2.5: Control experiments for nanoparticle labels. a) Prior incubation with an antibody reduces binding to only 16 %. This means that the NP-labeled toxins attach in a specific manner. b) The diffusion coefficient D_{MSD} does not vary systematically with nanoparticle size. c) An MTT assay shows that the cells are not perturbed by the nanoparticles.

The nanoparticle labels have different sizes that follow the previously shown size dispersion (figure 2.2 d). This size polydispersity allows the investigation of a potential relationship between measured diffusion coefficients (D_{MSD}) of labeled receptors and the diameter of the label, which is shown in figure 2.5 b. The process used to determine the size of the NP from the number of emitted photons is given in appendix A.4. The diffusion coefficients obtained for receptors, which are labeled with larger nanoparticles, is not lower, which implies an absence of a significant drag force on the receptor due to the nanoparticle label.

Since we use a toxin to label the receptors in the membrane, we have to consider side effects due to toxicity on the cell. Furthermore, the nanoparticles themselves without any toxins may induce toxic effects. An MTT assay reveals that the labels do not perturb the cell viability beyond the assay precision. The MTT as-

say procedure is explained in A.6. The viability of control cells was compared to
cells that were incubated with nanoparticles functionalized with APTES and with
nanoparticles that were functionalized with APTES and the ϵ-prototoxin at typical
conditions for SMT experiments of 0.04 nM in vanadate concentration. It is visi-
ble from figure 2.5 c) that the labels do not have a negative impact on cell viability.

2.3.2   Image analysis

Single molecule observation of dynamic processes relies on video microscopy and
became feasible only with the advent of cameras that were capable of taking se-
quences of images of faint objects, such as single molecule labels. Due to the
recent development of electron multiplication charge-coupled devices (EM-CCD),
it is now possible to rapidly image faint objects at lower acquisition times and to
observe the often rapid biological processes, such as diffusion or protein-protein
interaction.

The use of a camera to observe a diffusion process can lead to artifacts. Very
much like the eye, the camera is not a perfect imaging instrument. Here I will first
discuss how we analyze our images to obtain the localization of our biomolecule
with nanometer precision, as well as two important practical limitations with re-
spect to the minimal molecule displacement that can be meaningfully interpreted.

We employ a localization algorithm that automatically finds the position of
the nanoparticle label with subpixel resolution. The entire process is depicted in
figure 2.6. The algorithm loads an image series and filters the raw data with a
Laplacian filter of size 5 x 5 pixels^2 to enhance the contrast of the edge of the
label emission and further by a 3 x 3 low-pass filter to smooth out the raw data
(figure 2.6 c). Thresholding then allows the algorithm to built a binary mask from
the raw data, marking the position of pixels that belong to the signal and pixels
that belong to the background (figure 2.6 d). A cycle of eroding and dilating the
mask, leads to discarding pixels that belong to the background, but were above
the threshold. The background is smoothed once more via a 3 x 3 pixel^2 low-pass
filter and extrapolated into the zone of the signal. In this way, the algorithm
constructs a smooth background signal for the entire raw image, which can then
be subtracted from the filtered data to yield an image without background. One
pixel corresponds to 0.254 μm, which is comparable to the standard deviation of
the Airy diffraction pattern, which is 0.143 μm. It has been shown that the op-
timal image magnification for most cases should yield a pixel size about equal to
the standard deviation of the point spread function [211].

The precise localization of the label is then achieved by fitting the processed
image without background with a 2D Gaussian, to simulate the point spread func-

(a) Raw image

(b) Raw image in 2D

(c) Filtered image

(d) Binary mask obtained by thresholding

(e) Binary mask after eroding and dilation

(f) Extrapolated background

(g) Filtered image without background
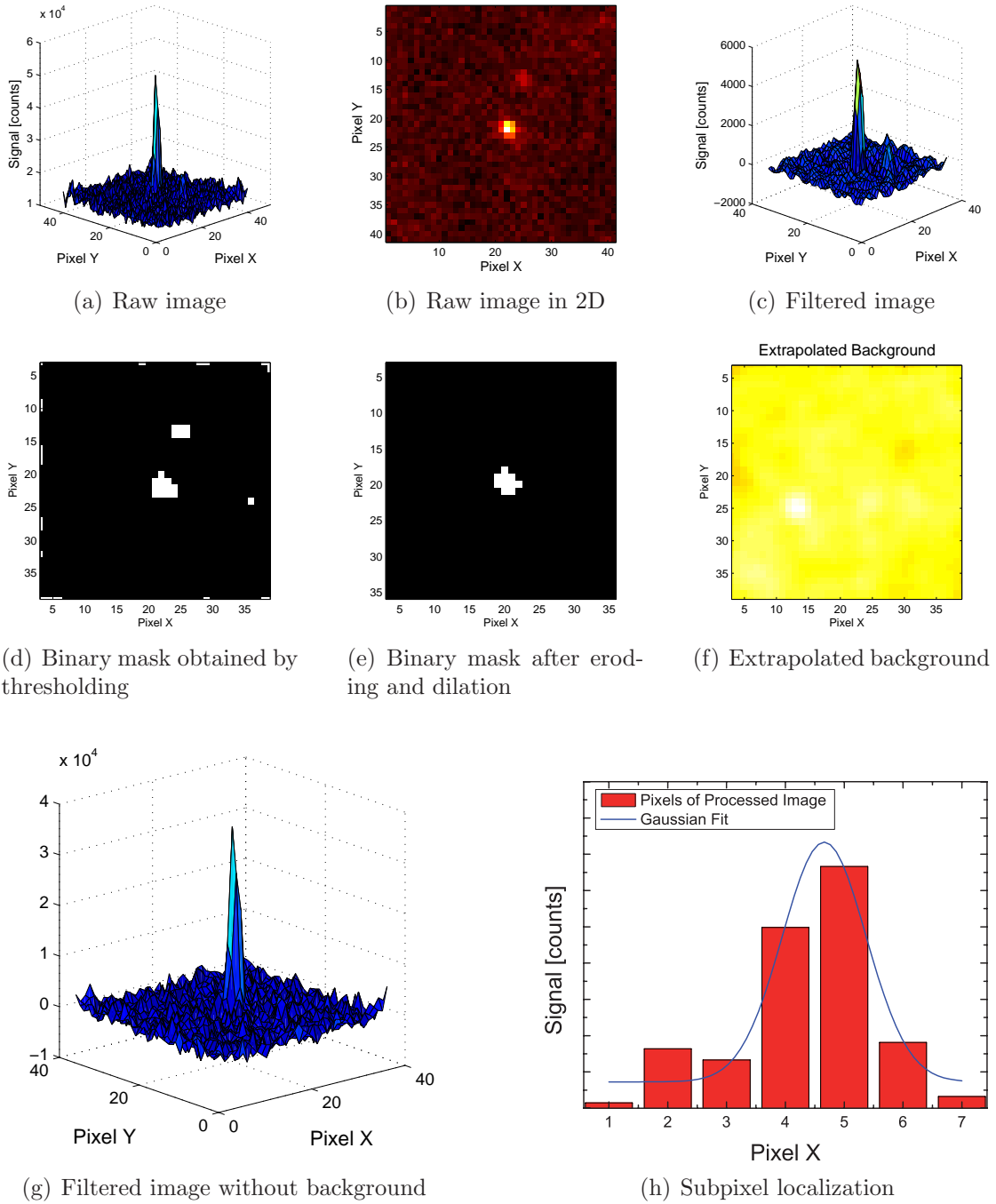
(h) Subpixel localization

Figure 2.6: Steps of the image treatment algorithm that is used to locate the position of a label with a higher resolution than the width of a single pixel of the imaging camera.

tion of a point emitter that emits photons at visible wavelengths. A Gaussian fit rather than a fit by an Airy function is used because the Gaussian fitting procedure is faster while it is a good approximation to the Airy function. The Gaussian function will find the center of the Airy disk, which is the diffraction pattern that is created by the objective lens. The spot diameter depends on the wavelength of the label emission and on the numerical aperture but also on the distance of the label from the focal plane of the objective lens.

Thus, a trajectory can be reconstructed from the positions of the label in each recorded image of the acquired video. However, before the trajectories are analyzed to determine diffusion parameters, domain sizes and interaction times one must stop and verify if the acquired trajectory is compatible with the physical limitations of the imaging set-up and image analysis process.

2.3.3 Limitations due to the signal-to-noise ratio

Background photons will add intensity fluctuations to the signal, which can, if large enough, cause a shift of the peak found by the Gaussian fit in figure 2.6. A stationary emitter would then appear to be moving. It is therefore crucial to investigate the performance of the tracking algorithm with respect to the signal-to-noise ratio (SNR). The SNR of the image is given in equation 2.1 and depends on the amplitude of two different noise forms, background variation σ_{BG} and shot noise $\sqrt{N}$ due to the signal of N photons.

$$SNR = \frac{N}{\sqrt{\sigma_{BG}^2 + (\sqrt{N})^2}} \tag{2.1}$$

We have considered that other sources of noise like thermal or readout noise are negligible. The background noise is then due to the shot noise of the background fluorescence N_{BG}. Equation 2.1 can then be rewritten

$$SNR = \frac{N}{\sqrt{N_{BG} + N}} \tag{2.2}$$

To accurately measure a displacement of the label, it is obvious that the measured displacement should be greater than the apparent displacement introduced by noise fluctuations, which is determiend by the so-called localization precision.

The localization precision under certain experimental conditions can be predicted using simulations. The Airy disk pattern of a nanometric label that is imaged through an objective lens can be described by the Fourier transform of the circular aperture of the lens:

$$I(\theta) = I_0 \left(2\frac{J_1(x)}{x} \right)^2 \tag{2.3}$$

$$x = kr\sin(\theta) = \frac{2\pi r}{\lambda}\frac{NA}{n} \tag{2.4}$$

Here, the intensity of the pattern at angle θ is given by the first-order Bessel function J_1, whose node locations are given by the radius of the lens r, the wavelength of the emitted light λ, the numerical aperture of the objective NA and the refractive index n. Such an Airy pattern is shown in figure 2.7.

Artificially generated images, where the signal-to-noise ratio is an input parameter, are a tool to access the localization precision of an imaging set-up and algorithm. A description of how noise degrades the localization precision is given in reference [211] and can be used to optimize imaging parameters depending of the expected number of photons from a particular label. For our set-up and algorithm, we can predict a theoretical limit on the smallest measurable displacement for various signal-to-noise ratios. To this end, we create artificial diffraction patterns of a point source based on the parameters of our optical system and label. This pattern is then mapped onto a camera chip to simulate the imaging process as shown in figure 2.7 b). Then shot noise is added to the signal and background and the SNR is varied to obtain an estimate of the positioning accuracy as a function of SNR. From the resulting images, which are displayed in figure 2.7 c) & d), one can already guess that a small SNR ratio of 5, which is often defined as the limit of detection, will lead to a much higher positioning error than a SNR of 20, where a peak is easily discernable.

The results of the analysis are given in Figure 2.8. The SNR is varied for a label that always emits a fixed number of photons by changing the noise fluctuations. Here the black line gives the error in position for various signal to noise ratios. The dashed lines indicate the diffusion length of a random walker in 2D for two different diffusion coefficients, which are typical for proteins in biological membranes. The lower the diffusion coefficient, the smaller is the step length. It is therefore more difficult to accurately measure small diffusion coefficients due to the positioning error. For example, measuring diffusion coefficients of 0.01 µm^2/s requires a SNR higher than 8.
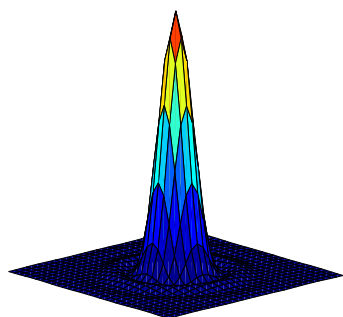
(a) Airy diffraction pattern
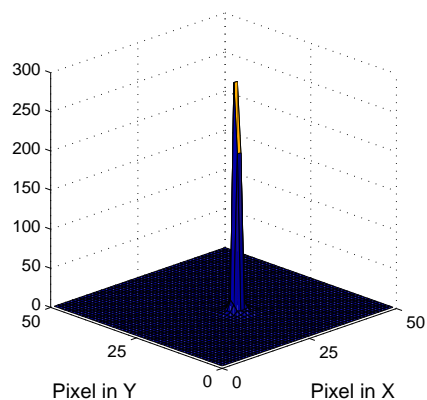
(b) Airy pattern mapped onto a camera chip with 50 x 50 pixel
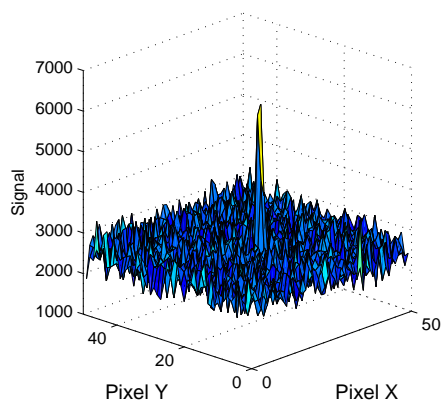
(c) Image with a SNR of 20
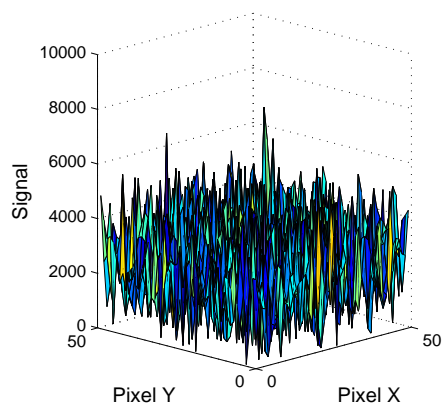
(d) Image with a SNR of 5

Figure 2.7: Artificially generated images of a nanometric label with a 63x objective and a 50 x 50 squarepixels camera with pixel size of 0.250 µm after magnification
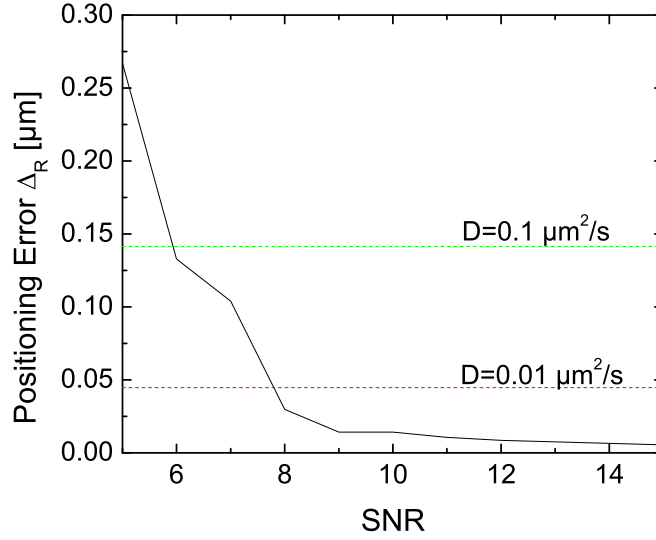
Figure 2.8: Noise gives rise to localization error. Therefore, it has to be verified if measured variables are actually meaningful. The black line gives the localization error for our labels under typical experimental conditions for various SNRs (acquisition time: 50 ms, N: 80). The dashed lines indicate the diffusion lengths of a Brownian 2D walker for two different and relevant diffusion coefficients during a theoretical acquisition time of 50 ms.

The simplest solution to decrease the localization error is to maximize the signal-to-noise ratio by prolonged integration during image acquisition. However, as we will see in the next section, increasing the acquisition time can lead to new problems and to the loss of information in the measured trajectories.

2.3.4   The acquisition time in video microscopy

The acquisition time is another important parameter whose choice can lead to measurement artifacts. Motion of biomolecules is continuous and not discretized in time. An image stack of this process is not continuous in time, but discretized. More importantly, each image of a stack is an average of the continuous observed process that unfolds within the time window of image acquisition. It is thus extremely important to select an acquisition time that allows the correct observation of the investigated biological process. The easiest solution to overcome this problem would be to choose an extremely short acquisition time. However, limited signal from the fluorescent label imposes a minimal limit on the acquisition time. Indeed, if the signal-to-noise ratio is too small, no meaningful data can be collected

as was shown in section 2.3.3.

Let us now consider the special case of a labeled random walker in 2D that is confined in a square domain. This is an important scenario for some types of membrane molecules and it is known that a long acquisition time will wash out information in recorded trajectories [157]. In addition, long exposure times will lead to an apparent quadratic trapping potential as shown in figure 2.9. As the acquisition time of this random walker in its 200-nm square domain with reflecting walls is increased, the determined position of the label will be biased and shifted inwards to the center of the domain. If the particle has explored the entire domain within one acquisition time, then the mean position of the particle is the center. This apparent concentration of detected positions at the center induces a density gradient, which is peaked at the center of the square domain, leading to the apparent observation of a confining potential, which is very different from the initial box-shaped potential. Such an effect, caused by an acquisition time that is too long, has been used to disprove work that have found confining potentials of parabolic shape in cell membranes [212].
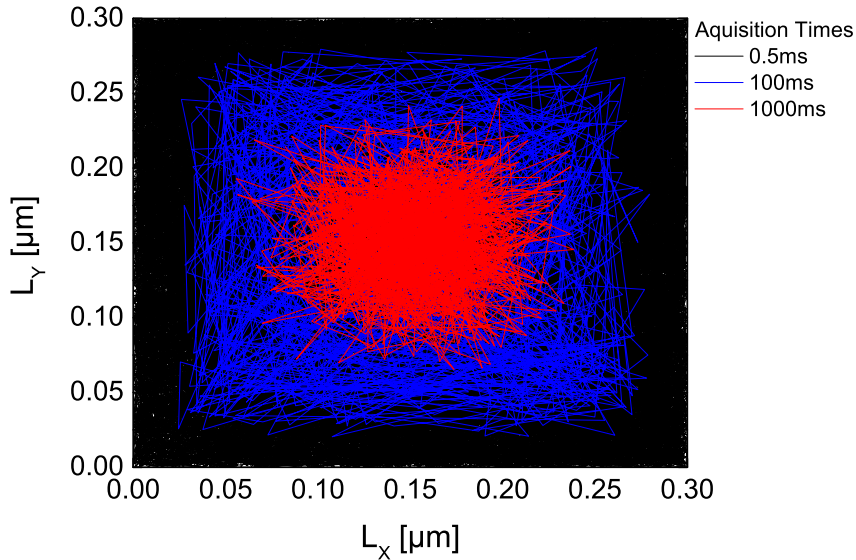
Figure 2.9: The effect of acquisition time averaging on a moving label. As the acquisition time increases, the positions found for the label are no longer homogeneously distributed in the square domain. The parameters for the random Brownian walker are a diffusion coefficient of $0.1\,\mu m^2/s$ and a domain length of $300\,nm$. The points appear to be concentrated in the center of the domain giving the impression of a domain that is smaller than the square box.

A reduction in confining area can certainly be observed, considering that sub-pixel resolution tracking relies on finding the maximum of a Gaussian fit of the diffraction pattern of a label. However, bias can be detected by noting that the Airy disk pattern moves too and creates a very different pattern on the final acquired image. Assuming that the pixel size of the camera is similar to the diameter of the magnified diffraction-limited spot, the movement will result in a smeared out diffraction pattern, that is potentially wider in the direction of motion of the label as depicted in figure 2.10. The resulting diffraction pattern will thus have different waist sizes than the pattern of a stationary label. It is thus easy to construct criteria to check if the acquisition is indeed biased by the acquisition time. For example, in the case of bias, as the acquisition time increases, the FWHM of the Gaussian fit should grow. In an extremely biased case, and provided that the domain size is larger than the magnified stationary diffraction pattern, the extent of the smeared out diffraction pattern will be equal to the domain size, creating a relationship between the domain size and the FWHM of the Gaussian fit. If the previous effects are not observed, one can rule out a bias due to the acquisition time.
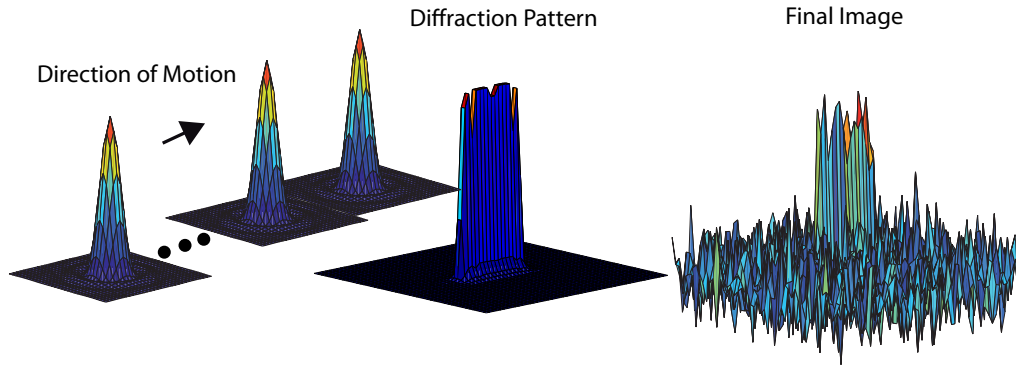
Figure 2.10: When a moving nanometric emitter is imaged with a finite acquisition time, its diffraction pattern is smeared out in the direction of motion. The center of a 2D Gaussian fit will locate the label at the center of the elongated pattern, giving rise to effects as those shown in figure 2.9 for long acquisition times. However, if the magnified diffraction pattern of a stationary spot is of the order of the camera pixel size, it will be obvious from the diffraction pattern that the acquisition time is too long and this effect can be used as a criterion to determine whether or not the acquisition time induces a bias on the measured position.

It is possible to determine an appropriate range of acquisition times from simulations of a trapped Brownian walker. The input parameters should match experimental conditions and we chose accordingly domain sizes of 500 nm and a diffusion coefficient of $0.1 \, \mu m^2/s$. Image analysis of simulated trajectories shows a broadening in FWHM of the diffraction pattern with increasing acquisition time above
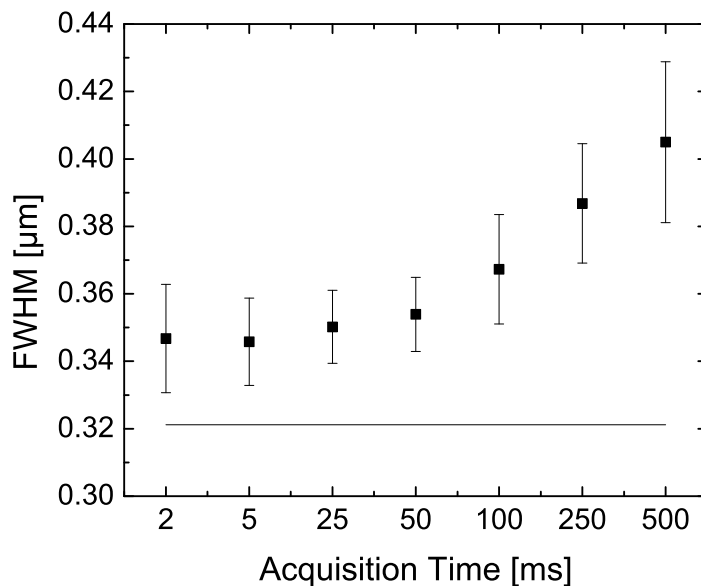
Figure 2.11: The diffraction pattern broadens with acquisition time for a random walker with a diffusion coefficient of $0.1\,\mu m^2/s$. This effect can be seen with normal cameras, when a photographer is trying to take an image of a fast moving object with a shutter time that is too slow. The straight line is the FWHM of a stationary particle and experiences no broadening.

values of about 50 ms in figure 2.11. The straight line shows, as a reference, the theoretical FWHM evolution of a particle that is fixed and thus experiences no diffraction pattern broadening.

2.4   Conclusion

This chapter introduces our single-molecule experiments to investigate the membrane architecture. The peptidic toxins α and ϵ of C. septicum and C. perfingens, are excellent candidates to gain insight into the intrinsic membrane organization. Indeed, they exploit the membrane architecture to concentrate their monomers on the cell membrane to more efficiently oligomerize and from pores that pierce through the membrane.

This chapter explains how these toxins were coupled to luminescent europium-doped oxide nanoparticles which are the labels we chose for the single-molecule tracking experiments. Warned by the words of one of the first great microscopists Henry Baker, this chapter also investigates typical pitfalls arising from sample preparation and image analysis since seeing is not always believing, as suggested in reference [207]. Control experiments with much smaller organic fluorophores show that the confinement of the trajectories does not arise from the labels, but from the cell membrane organization (figure 2.4). Further control experiments show that the toxin-particle conjugates bind specifically to a receptor in the membrane, that the motion is not impeded by the label and that there is no cell viability decrease due to the nanoparticles (figure 2.5). The image analysis and sub-pixel localization algorithm is reviewed in figure 2.6 and its performance, mimicking experimental conditions, is tested regarding parameters such as signal-to-noise ratio and camera acquisition time to show that the studied toxin receptor motion is not only noise (figures 2.8 and 2.10).

Chapter 3

Inferring Variables from Single Molecule Trajectories

Once images from single-molecule experiments have been analyzed and trajectories for molecules have been determined, quantitative measurements of variables, such as diffusion coefficients, domain sizes, speed of directed motion, trapping times, hopping frequencies, interaction times, are extracted. This chapter will introduce a new method to extract the diffusion coefficient and the forces acting on the molecule. This method exploits the full information stored in the trajectories and thus performs better at quantifying the motion of a receptor in a membrane.

In human cells, there are about $10\,000$ different proteins that constitute a large fraction of the membrane [3]. Therefore, the membrane can be considered an extremely crowded environment that influences lateral diffusion. Since there is also a strong interaction with the molecules below the membrane, the receptor motion is not a simple two dimensional Brownian walk. These receptors undergo diffusion, but are confined to a small domain, as we have already seen in the previous chapter in section 2.3.1. This confining domain might be a fenced-off zone, a lipid island or an aggregate. A better understanding of the confining potential will lead to a better understanding of the membrane architecture and related biological processes, especially in trafficking and signaling.

This chapter will introduce a novel inference technique that can be used to extract diffusion coefficients, force maps and confining potentials for confined 2D motion in a membrane. Simulations will give a measure of the quality of the inferred variables. The technique is then compared to other techniques currently used.

3.1 Means Square Displacement (MSD) technique

Mean Square Displacement (MSD) analysis is the most common technique to extract parameters, such as diffusion coefficients and domain sizes from single-molecule tracking experiments. The MSD is calculated and plotted against elapsed time using equation 3.1:

$$MSD(n\delta t) =$$
$$\frac{1}{N-1-n}\sum_{j=1}^{N-1-n}[x(j\delta t + n\delta t) - x(j\delta t)]^2 + [y(j\delta t + n\delta t) - y(j\delta t)]^2 \quad (3.1)$$

In the case of confined motion in a square corral of length L, the MSD plot is fitted with the following formula, derived in references [72, 213, 214].

$$MSD(n\delta t) = \frac{L_{MSD}^2}{3} - \frac{32 L_{MSD}^2}{\pi^4} \sum_{n=1(odd)}^{\infty} \frac{1}{n^4} exp\left\{ -\frac{1}{2}\left(\frac{n\pi}{L_{MSD}}\right)^2 2Dn\delta t \right\} \quad (3.2)$$

Often, the fit with equation 3.2 is only used to determine the domain length L_{MSD} and the diffusion coefficient D_{MSD} is obtained from a linear fit to the first three points of the MSD plot. The assumption used is that the elapsed time for the first three time steps is too short for the particle to feel the effects of the boundary. Thus, the slope will be proportional to the diffusion coefficient of the free Brownian motion. However, the use of only three points greatly reduces the amount of exploited information. More importantly, the analysis of the *mean* square displacement wipes out a large amount of information stored in the trajectory. It is only in the case of free Brownian motion without boundaries that the MSD extracts the full available information [215].

The MSD model for confined motion in equation 3.2 makes two strong assumptions. It assumes that the receptor is moving freely in a Brownian fashion in a square box, which is defined by rigid, reflecting walls. This analysis will give biased results if the region is not a square box and if there are forces acting within the box. Moreover, it is expected that confining regions in a cell will not be simple square boxes. The choice of the square-box confining potential is dictated by mathematical simplicity rather than by an attempt to correctly describe the reality. A more general description of the motion and domain can offer less biased results.

3.2   Inference technique

We propose a new technique, which was developed by Jean-Baptiste Masson, to infer parameters from confined single molecule data that is less biased, i.e. does not impose free motion and a square domain. This technique uses all the information that can be extracted from a data set and converges very quickly onto the input values for numerical simulations [1]. The inference technique assumes only that the receptor is moving in the membrane according to the Langevin equation of motion.

$$\frac{d\mathbf{r}}{dt} = \mathbf{v} \qquad m\frac{d\mathbf{v}}{dt} = -\gamma\mathbf{v} - \nabla V(\mathbf{r}) + \sqrt{2D\gamma^2}\xi \tag{3.3}$$

With respect to the equation of motion that leads to the model for the MSD fit of confined trajectories, we add an additional term for an arbitrary potential. In the Langevin equation of motion, velocity changes for the receptor with mass m are generated by three terms. The first term, $\gamma\mathbf{v}$ accounts for friction where the friction coefficient γ is assumed to be constant. The second term, $\nabla V(\mathbf{r})$, is the force created by an *arbitrary* potential. In the simple model for the motion in a box, discussed in the previous section, the potential is assumed to have a box shape, a major assumption. By allowing the potential to take an arbitrary form, the new method is much more versatile. The last term, $\sqrt{2D\gamma^2}\xi$, is the noise term that can be assimilated to a force leading to Brownian motion with diffusion coefficient D. However, the increased number of force terms leads to the difficulty of correctly attributing an observed displacement to the individual sources. The quality of the inferred variables must be tested under various scenarios and conditions, as shown in section 3.3.

For the case of motion inside the membrane, we can safely assume that steady-state conditions are rapidly reached, i.e. $dv/dt = 0$ ($\tau = m/\gamma \approx 10^{-16}$). The velocity is then given by

$$\mathbf{v} = -\frac{\nabla V(\mathbf{r})}{\gamma} + \sqrt{2D}\xi \tag{3.4}$$

The associated Fokker-Planck equation, which governs the evolution of the transition probability over time, is given in equation 3.5 [216]. Here, $F = -\nabla V$.

$$\partial_t P = -\frac{1}{\gamma}\nabla \cdot (\mathbf{F}P) + D\Delta P \tag{3.5}$$

Solving this equation will lead to an expression called the likelihood function,

$$P(\mathbf{r}_2, t_2 | \mathbf{r}_1, t_1) = \frac{exp(-\frac{(\mathbf{r}_2 - \mathbf{r}_1 - \mathbf{F}(t_2 - t_1)/\gamma)^2}{4D(t_2 - t_1)})}{4\pi D(t_2 - t_1)} \tag{3.6}$$

which is an expression for the probability of going from one space-time co-ordinate (r_1, t_1) to the next (r_2, t_2) supposing that the variables D and F are known. The overall probability of a trajectory T consisting of N space-time points (r_n, t_n) due to a certain set of variables is then computed by multiplying all the probabilities between all the individual points in the dataset because the process is Markovian:

$$P_{(T|D,\mathbf{F})} = \prod_{all\ transitions} P(\mathbf{r}_{n+1}, t_{n+1} | \mathbf{r}_n, t_n) \tag{3.7}$$

The derived likelihood function in equation 3.6 is not directly applicable. We rather aim at measuring the probability that a variable takes a particular value. For this purpose, we invoke Bayes' theorem:

$$P(Q|T) = \frac{P(T|Q)P_0(Q)}{P_0(T)} \tag{3.8}$$

Bayes' theorem updates our prior knowledge $P_0(Q)$ about the variables Q (in our case D & F) via the just derived likelihood $P(r_2, t_2 | r_1, t_1)$ for all transitions or $P(T|Q)$, given by equation 3.7, to obtain the posteriori probability $P(Q|T)$ that the variables Q take a particular value given the observation of the trajectory T. $P(Q|T)$ is also known as the conditional probabilities. The posteriori probability $P(Q|T)$ provides a criterion for a variable matching a trajectory T. This formula relates the two conditional probabilities. Here, $P_0(T)$ is simply a normalization constant and is set to 1 when a trajectory was recorded. The prior knowledge $P_0(Q)$ is assumed to be constant for a reasonable range and is set to zero elsewhere. The process is visualized schematically in figure 3.1.

The maximum value of the posteriori probability (MAP) is the inferred value for the variable. It is simply the most likely value. The optimization of the parameters
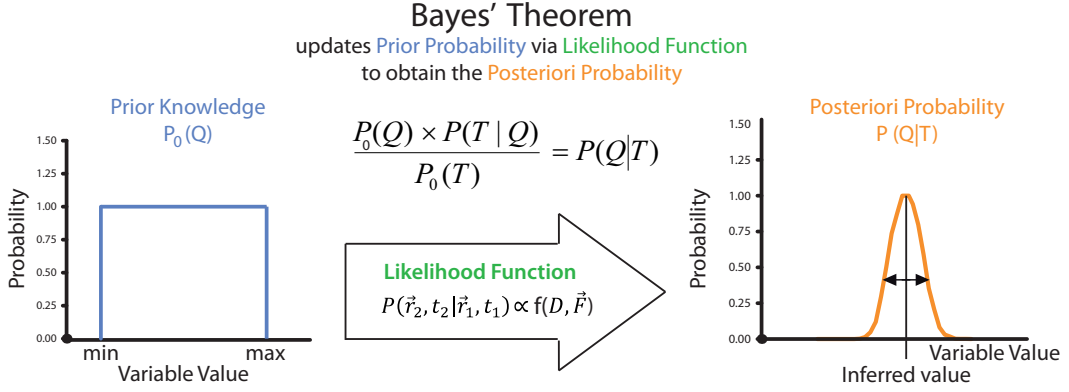
Bayes' Theorem
updates Prior Probability via Likelihood Function
to obtain the Posteriori Probability

Figure 3.1: The Inference technique. Invoking Bayes' theorem, the prior information about a variable Q, $P_0(Q)$ can be updated via the likelihood function $P(r_2, t_2|r_1, t_1)$ or $P(T|Q)$ (see eqn. 3.6 & 3.7). The calculated posteriori probability $P(Q|T)$ is a criterion for variable matching a trajectory assuming that the particle motion is governed by the Langevin equation of motion (see eqn. 3.3). The peak of the posteriori probability $P(Q|T)$ yields the most likely value for the variable Q and its width represents the uncertainty of this inferred value for the variable.

maximizing the posteriori probability is performed first with a Quasi-Newtonian optimization using the Broyden-Fletcher-Goldfarb-Shanno (BFGS) algorithm, explained in more detail in the appendix section B.2. A Monte Carlo simulation around the maximum values yields a value for the inferred variable and its uncertainty through its standard deviation as explained in more detail in section B.3. Numerical trajectories are used to determine a systematic bias and to correct for it.

The inferred variables can of course be chosen according to the features under investigation. In this work, the diffusion coefficient D_{Inf} is evaluated globally for the trajectory. It is assumed to be constant over the entire domain. The validity of this assumption will be addressed in chapter 4.

For the inference of forces two methods are applied. For the first, the domain is divided up into subdomains using a grid and the points of the trajectory are attributed to their respective grid-subdomains. Then the forces are considered constant in each subdomain and are optimized independently. This method is used in this work to extract the force maps. The forces are typically calculated on a 8 x 8 grid and are calculated in x and y direction independently. Overall, this method has to optimize $64 \times 2 + 1$ independent variables.

For the second method, instead of inferring independent forces in a subdomain grid dividing up the confining zone, we directly infer the parameters of a confining potential. The inference procedure optimizes the parameters of the potential, the resulting forces being still evaluated in each subdomain during the optimization

operation. This method is used to obtain a map of the potential and in the case of a parabolic potential, the associated spring constant. This does not only cut down computation time due to the reduction in the number of free variables that need to be optimized, but also leads to results that can be more easily compared between trajectories. The most general fashion of modeling the experimental potential is by a polynomial of high order. Then the order can be reduced until only a meaningful polynomial order is left, according to the Occam's razor principle, whose result is described in section 4.2. It turns out that a second order polynomial is good enough to accurately describe the confining potential of our experimental trajectories. When the potential is described by a second order polynomial, this optimization method only has to optimize $5 + 1$ independent parameters, since the forces are governed by a global equation and is thus much faster than the previous method. Moreover, the linear terms of the inferred polynomial are relatively small. This means that a simple parabolic potential is sufficient to model the confining potential of our experimental trajectories. Having just one variable, the radial spring constant k_r, to describe the confining potential is a great advantage.

3.3   Quality of extracted variables

In the case of confined diffusion in a flat potential with infinite barriers at the domain boundaries, it was shown that the inference method reaches the best performances theoretically achievable [215]. In the case of non-zero forces inside the confinement domains, the extra terms added to the model that describes the motion of the receptor gives rise to a difficulty in correctly attributing a displacement to one of the source terms, i.e. the potential or the Brownian motion. We therefore tested the performance of the implemented inference algorithm with numerical simulations. In principle, the technique should be less biased than the MSD analysis with respect to the true values of trajectory variables due to the less restrictive conditions posed by the model. However, the new model also has more degrees of freedom due to the added term $\nabla V(\mathbf{r})$. First of all, these extra dimensions could lead to mistakes in the optimization process. Moreover, the performance of the technique may suffer due to perturbations from the acquisition-time averaging for each frame and from the positioning error that depends on the SNR and the image analysis software. Furthermore, these extra degrees of freedom have to be justified, as will be done in section 3.3.4. It will be shown that the technique can detect the correct confining potential, and more importantly, that it can correctly infer that there are no forces if there are none present. All these issues have to be addressed before any concrete inference of variables describing the motion of the toxin receptors can be performed with confidence.

The choice of acquisition time with respect to the motion parameters of the

membrane receptor plays an important role in the quality of the measured parameters because for longer acquisition times, more information is scrambled due to more interaction with the boundary. This section will thus analyze the performance with respect to the choice of acquisition time. For generality, a dimensionless factor u is introduced, relating the total area covered by the diffusing molecule during the acquisition time Δt to the total area of the confining domain:

$$u = \frac{D\Delta t}{(\pi r)^2} \tag{3.9}$$

This dimensionless factor has been termed confinement factor [215]. However, one should keep in mind that it also contains the experimental parameter of acquisition time. Thus, the factor u can be reduced by reducing the acquisition time. Clearly, as u grows, the difficulty of extracting the correct diffusion coefficient increases, because the area covered by the diffusing particle becomes comparable or even larger than the confining zone and the particle interacts with the boundaries.

3.3.1 Inferred diffusion coefficient D_{Inf}

The most commonly extracted and calculated variable, describing the motion of molecules on the cell surface, is the diffusion coefficient. It will be shown that the newly implemented inference technique finds the correct values for numerical trajectory simulations.

The numerical trajectories can be generated in different ways, taking or not taking into account the influence of position averaging due to the acquisition time and of the positioning noise due to the signal-to-noise ratio, the tracking algorithm and other noise sources such as mechanical instability of the microscope. Numerical trajectories are also a tool that allows these contributions from different scenarios to be switched on and off separately to single out the major driving forces in bias generation. The bias is always taken to be the inferred value of the variable divided by the input value of that variable. Simulations were performed using conditions, reproducing experimental conditions: diffusion coefficient of $0.075\,\mu m^2/s$, parabolic confining potential (Spring like, $k = 0.002 - 0.64\,pN/\mu m$), acquisition time of $51.3\,ms$, positioning noise of $40\,nm$ and video length of 1000 frames. It should be noted that the number of data points N of the trajectory is proportional to the inverse of the standard deviation of the inferred value for free Brownian motion.

Numerical trajectories are calculated under 4 different conditions. The first condition neglects experimental noise completely. Here the generator considers a moving molecule and picks its position at time points spaced by the acquisition time, while the particle takes 1000 smaller steps in-between each frame.

The second case are trajectories that include the positioning error. Here the generator adds or subtracts a distance to the particle's final position, following a Gaussian statistics, which is peaked at the value of the radial positioning noise of 40 nm.

The third case simulates the effect of the position averaging due to the acquisition time. The trajectory generator simply determines the average position for all the 1000 smaller steps in-between each frame. This average position will be the position for that frame.

Trajectories that best mimic experimental conditions are those calculated in the fourth case. The generator first takes the average position for all frames corresponding to the smaller sub-steps and then adds or subtracts the positioning noise to determine the final position of the particle. This case is equivalent to combining the noise and error in cases two and three.

The algorithm for the generator is discussed in the appendix section and the same trajectory is displayed for the different cases in figure 3.2. The domain size is defined as the radius of the circular area that comprises 95 % of all data points.
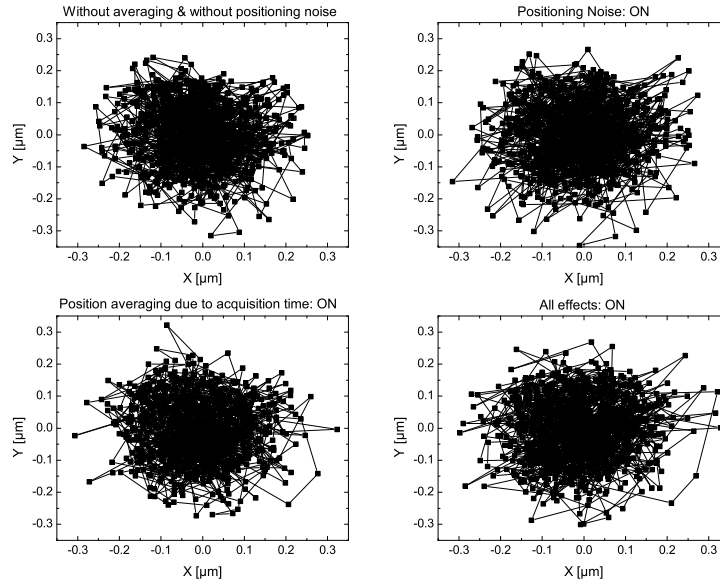
Figure 3.2: The displayed trajectory was generated at the same time, taking or not into account the positioning noise and/or the position averaging due to the acquisition time. It is difficult to discern a difference between the cases by eye.

The overall results of the analysis on the bias of the inferred diffusion coefficient as a function of the confinement factor u are shown in figure 3.3, where 1 indicates no bias. The four curves represent the case, without any influence

from noise (black), the results from trajectories taking into account the positioning noise (green), simulations taking into account the position averaging due to the acquisition time (blue) and the bias considering both effects (red). As the factor u increases, by means of stiffening the potential, there is a tendency for the algorithm to underestimate the real diffusion coefficient of $0.075\,\mu m^2/s$. For higher confinement u, the bias is stronger.

There are two striking features about these results. First, in all of the four scenarios, the shape or tendency of the bias evolution with the confinement remains unchanged, the slopes for the four cases are simply offset. The offset can be seen as an additional diffusion coefficient that either increases or decreases the input diffusion coefficient, which is added to the inferred diffusion coefficient. Strikingly, the noise does not simply increase the standard deviation of the inferred value, but it shifts the inferred value away from the correct input value.

For the case of the positioning noise, for example, the offset with respect to the scenario without any noise is 0.103 ± 0.009. This means that the positioning noise creates an increase in the measured diffusion coefficient of $10\,\%$. If random motion due to the positioning noise of $40\,nm$ per frame is considered by itself, the apparent diffusion coefficient, just due to the positioning noise, is $0.0078\,\mu m^2/s$. If this diffusion coefficient is divided by the input diffusion coefficient, the bias, solely due to the noise turns out to be 0.104, which is equal to the offset found in the figure. The positioning noise thus creates an extra apparent diffusion, which is added to the normal diffusion of the particle. The argument is summarized in the following equation and has been described before in [213].

$$Bias = \frac{D_{Total}}{D_{Input}} = \frac{D_{w/o\,noise}}{D_{Input}} + \frac{D_{Noise}}{D_{Input}} = Bias_{w/o\,noise} + \frac{D_{Noise}}{D_{Input}} \qquad (3.10)$$

A similar argument holds for the bias due to acquisition-time averaging, which induces a reduction of the diffusion coefficient. Surprisingly, the combined effect of positioning noise and acquisition-time position averaging roughly compensate each other for our experimental conditions.

The simple shape of the bias raises the issue of removing the bias to obtain the correct experimental results. However, in order to find a model for the evolution of the bias with u, the reason for the bias has to be determined. Because the simulated trajectories have been calculated using the simple spring potential $V = -kr^2$, a relationship between the spring constant and the domain size is expected. However, the diffusion coefficient should be strictly independent of the domain size in this model. This is not the case, as can be seen in figure 3.4. The
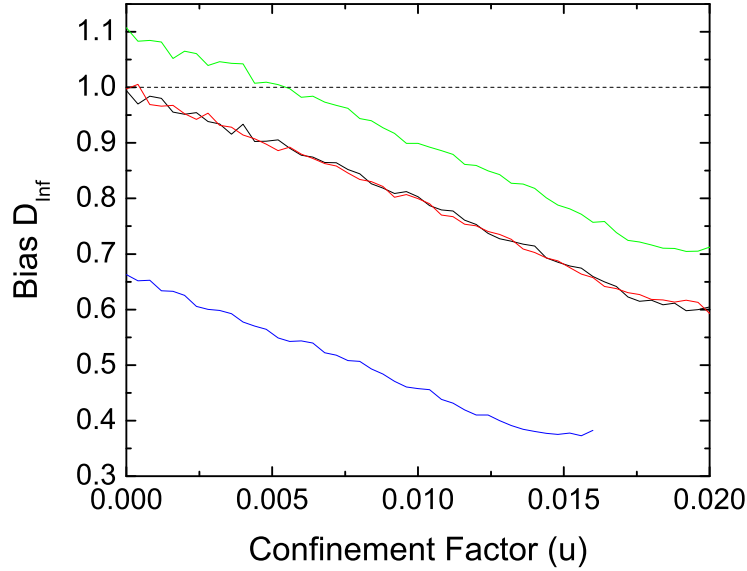
Figure 3.3: Numerical trajectories can be used to determine the quality of inferred diffusion coefficients. Here the bias was determined for 4 different scenarios. Trajectories without noise (black), trajectories with positioning noise of 40 nm (green), trajectories with position averaging due to the acquisition time (blue) and trajectories that contain both sources of error (red). Trajectories contain 1000 points, the spring constant is varied from $k = 0.002 - 0.64$ pN/µm and the acquisition time is set to 51.3 ms. It is clear that, as confinement increases, the algorithm underestimates the real input diffusion coefficient of 0.075 µm^2/s. The different scenarios show different bias. However, the biases are only offset with respect to each other and the evolution of the bias with the confinement remains constant. The MSD analysis is even more strongly biased with respect to the input value than the inference technique. This subject is discussed in section 3.4.

apparent relationship between the diffusion coefficient and the domain area is the key to the origin of the bias. Given the fact that for both techniques, MSD and inference, the parameter optimization takes place for more degrees of freedom than only the diffusion coefficient, there is a relationship between these parameters. If, for example, the spring constant are increased during the optimization, the diffusion coefficient is lowered automatically as the same total force can be created by a stiffer potential and lower diffusion coefficient, than the input ones, according to the Langevin equation 3.3. The next section will examine the behavior of the other parameters, namely the potential.
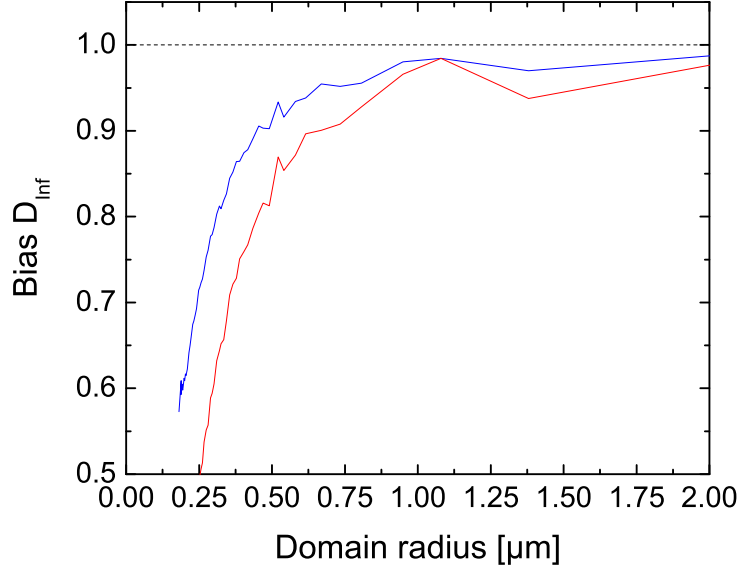
Figure 3.4: Bias of the inferred diffusion coefficient with respect to the domain radius for trajectories in the case without any error source. The used input parameters are: diffusion coefficient of $0.075 \, \mu m^2/s$, 1000 data points, acquisition time of $51.3 \, ms$ and the domain size is adjusted by varying the spring constant from $k = 0.002 - 0.64 \, pN/\mu m$. There is a clear relationship between the domain radius and the diffusion coefficient. This bias is present both for the inference method (blue) and the diffusion coefficient from the linear fit of the first three points of the $MSD(t)$ curve (red). There is no such relationship in the input model.

3.3.2 Inferred potential

As we have seen in the previous section, there is a bias in the inferred diffusion coefficient. The fact that there is an apparent relationship between the diffusion coefficient D and the domain area, which is controlled by the spring constant k_r of the simulation's input potential, hints towards a connection between the bias in D and a possible bias in k_r. The connection stems from the difficulty of correctly attributing the relative role the terms in the Langevin equation play on the total force that is exerted on the receptor.

In this light, this section will investigate the quality of the inferred spring constant. The bias of the inferred spring constant is given in red in figure 3.5 for the case of simulated trajectories without taking into account any error sources (positioning error, error related to acquisition time averaging). The bias in diffusion coefficient is also given in blue. The trend is clear: while the spring constant

is overestimated, the diffusion coefficient is underestimated by the optimization process. Since the spring constant also governs the radius R of the domain via $R \propto 1/\sqrt{k_r}$, it is this effect that creates the apparent relationship between the domain radius and the diffusion coefficient, observed in figure 3.4.
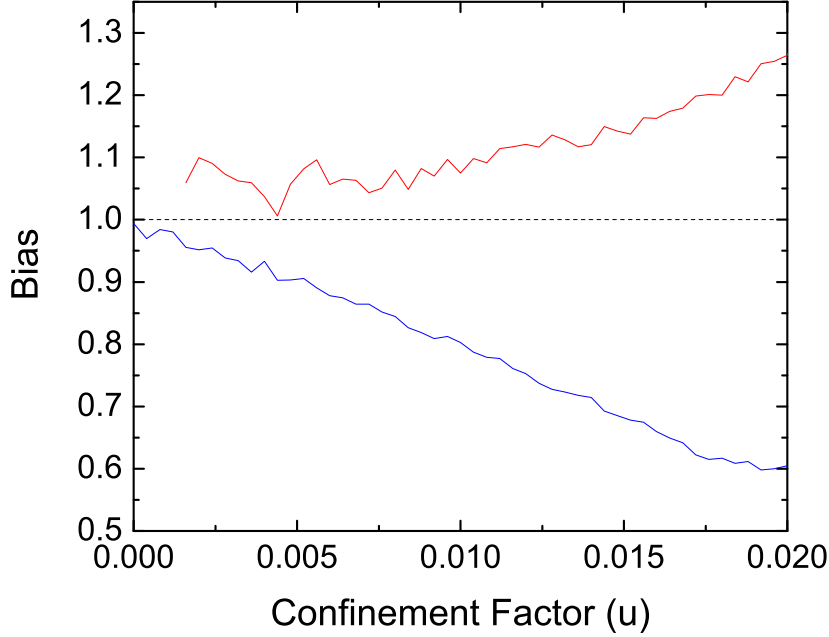
Figure 3.5: Numerical trajectories can be used to determine the quality of the inferred radial spring constant (red). The used input parameters are: diffusion coefficient of $0.075\,\mu\mathrm{m}^2/\mathrm{s}$, 1000 data points, acquisition time of $51.3\,\mathrm{ms}$ and u is adjusted by varying the spring constant from $k = 0.002 - 0.64\,\mathrm{pN}/\mu\mathrm{m}$. It is clear that as confinement increases, the algorithm overestimates the real spring constant. The bias of the inferred diffusion coefficient is given in blue. While the spring constant is overestimated, the diffusion coefficient is underestimated by the optimization process.

3.3.3   Compensating for the bias in inferred parameters

We now know that the bias of the diffusion coefficient and the spring constant are connected. We can therefore develop a model to compensate for it. It is the optimization process that overestimates one parameter at the expense of underestimating the other. The expression that is being optimized is equation 3.6 and is based on the model 3.3. In the Langevin equation two terms contain the variables that we are optimizing. The spring constant is contained in the expression for the potential $V = kr^2$, which in turn is contained in the force generated by the potential $-\nabla V(\mathbf{r})$. The diffusion coefficient enters directly in the expression of the thermal noise under the square root $\sqrt{2D\gamma^2}\xi$. The total force on the receptor can

thus be held constant when changing the force due to the potential linearly while compensating via the diffusion coefficient in a quadratic fashion. In other words, if the diffusion coefficient is changed by a factor a, this can be compensated for by adjusting the force due to the potential and thus the spring constant by the square root of that value. We thus have the relationship $aD \propto -\sqrt{a}k$ between the two variables. The two parameters, which are independent in the input model, are now linked due to the optimization process, which gives rise to the bias. We now know the relationship between the relative biases of the variables and we can find an expression for correcting for it:

$$\Delta D \qquad = -A\,u \qquad\qquad\qquad (3.11)$$

$$\Delta k_r \qquad = B\,u^2 \qquad\qquad\qquad (3.12)$$

$$with: \quad A = 21.4 \pm 0.2 \quad B = 570 \pm 15 \qquad\qquad (3.13)$$

The result of the correction is given by figure 3.6 for the diffusion coefficient and the spring constant. The resulting values closely match the values of input parameters and a bias is no longer observed. We can thus be confident in the inferred values, for the range of investigated confinement factors u from 0 to 0.02. If the diffusion coefficient is now plotted against the domain radius, there is no longer a dependency, as the one shown in 3.4.

Now, that we can be confident in the inferred values, we will examine in the next section if we can distinguish between different scenarios. It should be mentioned that, although we identified the relationship between the biases and we can compensate for them, the reason for the exact shape and sign of the correction in equations 3.11 & 3.12 was not found. In particular, the reason why it is D that is underestimated is not clear but it is most likely related to the optimization process.
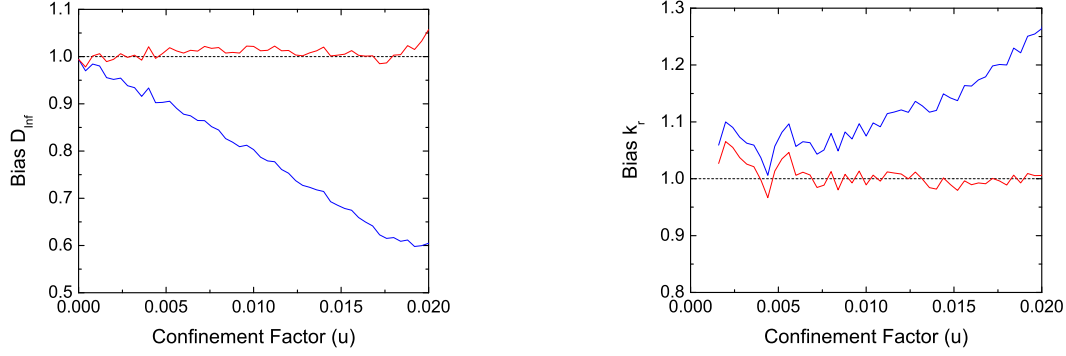
(a) Bias of the diffusion coefficient without (blue) and with the linear correction of eqn. 3.11 (red)

(b) Bias of the spring constant without (blue) and with the correction of eqn. 3.12 (red)

Figure 3.6: Bias of inferred parameters without and with the correction of equations 3.11 & 3.12. The used input parameters are: diffusion coefficient of $0.075\,\mu m^2/s$, 1000 data points, acquisition time of $51.3\,ms$ and u is adjusted by varying the spring constant from $k = 0.002 - 0.64\,pN/\mu m$. The diffusion coefficient correction has a linear term in u, and the corrected bias is shown in red. The correction for the spring constant is quadratic in u (red). After the bias correction operation, we obtain the correct results.

3.3.4 Forces are not inferred artifacts

The advantage of the inference technique is that it can not only extract the diffusion coefficient, but also the confining potential, since we suppose that the particle is moving accordingly to the Langevin equation 3.3, which contains a term due to a potential $V(r)$. But as already mentioned before, these extra degrees of freedom have to be justified. Two critical questions have to be examined. Does the algorithm find the correct input potential and can the technique distinguish between a case with and without forces? The first question, pertaining to the accuracy of the inferred potential has been discussed in the previous sections 3.3.2 and 3.3.3, whereas here it will be shown that the technique does not artificially find forces within the domain if none are present.

A trajectory is generated, where a random 2D Brownian walker with a diffusion coefficient of $0.075\,\mu m^2/s$ moves in a square box of 600 by $600\,nm$. Again the values were chosen to be close to experimental values. The length of the trajectory is 1000 frames and the acquisition time is $51.3\,ms$. Figure 3.7 shows the results of the inference technique.

Within the confining box, the inferred force map in figure 3.7 b) shows forces
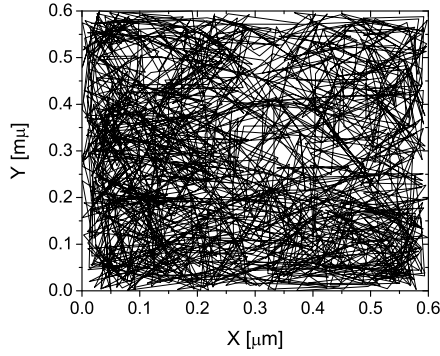
(a) Trajectory of a Brownian walker confined the box. No forces are present inside the box.
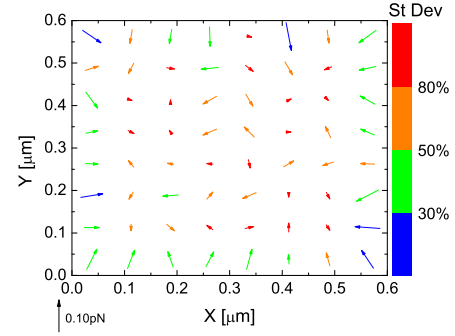
(b) Inferred force map.
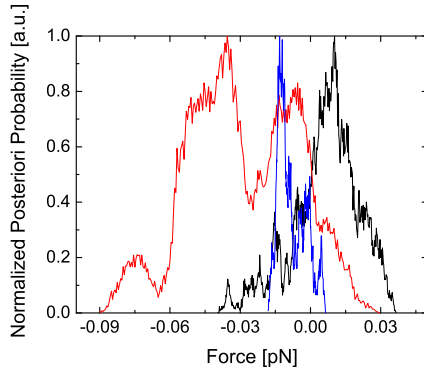
(c) Posteriori probabilities of inferred forces.
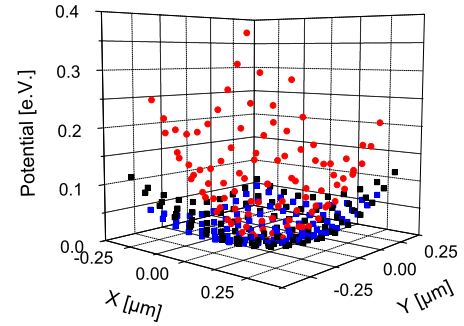
(d) Inferred potential (blue) compared to an experimental potential (red).

Figure 3.7: Can the inference technique determine that there are no forces within the domain? This numerical control experiment shows that the technique is able to extract the correct potential. A random 2D Brownian walker with a diffusion coefficient of $0.075\,\mu\mathrm{m}^2/\mathrm{s}$ moves in a square box of length $600\,\mathrm{nm}$. The inferred force map shows small forces with random orientations. The posteriori probabilities of the forces are very broad, which means that the error bar is large and they always include zero force. The inferred potential (blue), shown in d), is almost flat, with respect to a typical potential inferred from experimental data (red). The inferred potential, taking into account the errors due to image acquisition and positioning noise, is also almost flat (black).

that are small with respect to inferred forces from experimental trajectories. Furthermore, the inferred forces have a random orientation. These forces are characterized by a large error as can be seen from the color code in figure 3.7 b) and the posteriori probability plots in figure 3.7 c). The posteriori probability distributions for the forces in the domain are very broad and always include zero force. Forces at the boundaries point towards the center of the domain and are higher. They represent the force exerted by the boundary on the Brownian walker, when it is reflected. The inferred potential in figure 3.7 d) (blue) is almost flat with respect to a typical potential inferred from experimental data (red). When the influence of the acquisition-time averaging of position and of the positioning noise is turned on in simulated trajectories, the resulting potential is still flat (black potential in figure 3.7 d). We are thus confident that we can distinguish between the case of no forces and real forces within the domain. This in turn means that, if inference from experimental data shows forces within the domain, these forces are real and not artifacts created by the extra degrees of freedom or the acquisition-time averaging of position.

3.4   Performance of inference vs MSD analysis

The inference technique outperforms the commonly used MSD analysis in the case of a square box with no forces inside the domain, as shown in reference [215], using a different expression for the posteriori probability for the inference technique. Estimators based on the MSD analysis were shown to be either biased or less efficient for the same number of data points. It was also shown that the inference estimator reaches the best achievable theoretical performance according to the Cramér-Rao limit in [217]

$$\sigma(D) \geq \ \ J^{-1/2}(D) \tag{3.14}$$

This limit states that the minimal standard deviation σ of an unbiased estimator is lower-bounded by the Fisher information $J(D)$ for the diffusion coefficient D as follows:

$$J(D) = \ \ \left\langle (\partial_D ln P(D|\mathbf{R}))^2 \right\rangle \tag{3.15}$$

The advantage of the inference technique is that the receptor is considered to move according to the Langevin equation of motion 3.3. This equation is much less restrictive in terms of assumptions than the model used to fit the mean square

displacement in the case of confined motion (eqn. 3.2 or linear fit of first three points), where the assumptions are that the receptor moves in a Brownian fashion in a square box. Clearly, the MSD analysis cannot find forces within the domain, simply because it starts with the assumption that there are none. The Langevin equation of motion can find forces, if they are present. This will clearly lead to a difference in performance of the two methods in the case of a Brownian walker, which is constrained by an attractive potential as shown in figure 3.8. This graph compares the results from both techniques for the same trajectory over a range of confinement factors u.

D_{Inf} is extracted via the inference technique and its bias is shown in blue for the case of no added noise. The corrected values of D_{Inf}, using eqn. 3.11, are given in red. The diffusion coefficient of the MSD analysis D_{MSD} is obtained by fitting the first three points of the MSD plot with a straight line. The slope s is proportional to the diffusion coefficient via the equation $D_{MSD} = s/4$, as often used in the field of single-molecule tracking. It is one of the most widespread methods for determining the diffusion coefficient of molecules that move in a plane. The bias of D_{MSD} is shown in black. The third bias curve is obtained by fitting the entire MSD plot with eqn. 3.2 and is shown in green.

Both, inference and MSD techniques, show no bias at very low confinement u. When the confinement is virtually nonexistent, the molecule undergoes pure Brownian diffusion in two dimensions. The Fisher information for the diffusion coefficient for N one-step realizations is given by

$$J_N(D) = \ N J_1(D) \ = \ \tfrac{N}{2D^2} \tag{3.16}$$

and is a measure of the information that the trajectory carries about D. The equation for the confined motion 3.6, simplifies, as the spring constant k or the force F tend to zero, to the solution of the Fokker-Plank equation for a process where the transition probability only depends on the diffusivity D and not on force. It turns out that the maximum of the posteriori probability for the free-motion case is given by the formula that is used to determine D_{MSD} [215, 218]. This explains that both techniques work equally well for the extremely low or zero confinement limit. The standard deviation of both techniques also converges to the limit predicted by the Fisher Information 3.16 and decreases with the square root of the number of data points in the trajectory N.

However, as confinement becomes stronger, both techniques show a bias. The uncorrected inference however always outperforms the MSD analysis. The bias in the MSD analysis comes from the increase of the potential's impact on the trajectory. As forces play a larger role in the motion of the receptor, fitting the first
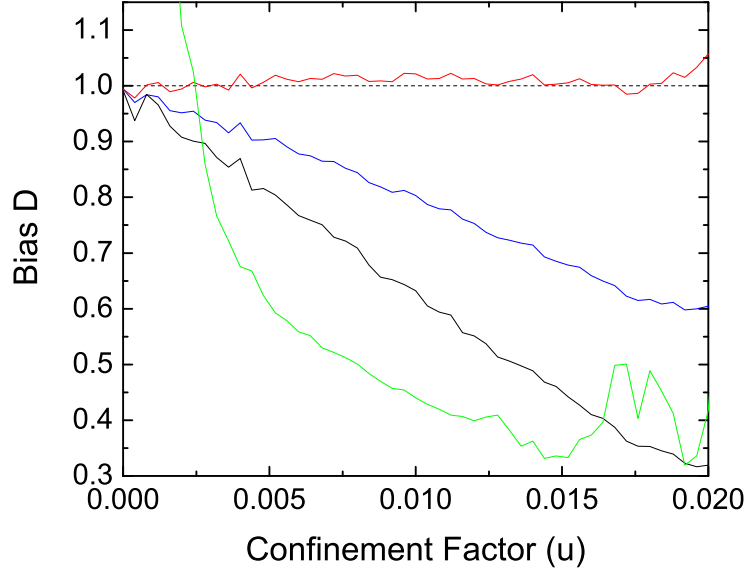
Figure 3.8: Bias of D_{Inf} and D_{MSD} for numerical trajectories, confined by a spring potential. The used input parameters are: diffusion coefficient of $0.075\,\mu m^2/s$, 1000 data points, acquisition time of $51.3\,ms$ and u is adjusted by varying the spring constant from $k = 0.002 - 0.64\,pN/\mu m$. The blue curve gives the uncorrected bias for the extracted diffusion coefficient from inference D_{Inf}, while the black curve is the bias of the diffusion coefficients found by the MSD analysis, D_{MSD}, by fitting the first three points of the data by a straight line. The green curve is the bias of $D_{MSD}^{(2)}$, obtained by fitting the entire MSD data with equation 3.2. The red curve shows the bias of the corrected inferred diffusion coefficients.

three MSD data points with a straight line to extract the free diffusion coefficient is no longer valid. It is clear that the extracted diffusion coefficients from the MSD technique cannot give the correct diffusion coefficients, since they do not account for forces from a potential acting on the receptor. As discussed before, the bias in the inference technique can be corrected for, to give a high-quality estimator for the case a biomolecule diffusing in a potential.

3.5   Performance of inference vs. residence time

The inference technique is not the only method to determine a confining potential, as it is also not the only method to determine a diffusion coefficient. The previous section highlighted the fact that inference method outperforms the MSD technique in extracting the diffusion coefficient D. Here the inference technique will be compared to the residence time method to quantify the technique's performance in extracting the potential. The residence time technique has recently been used in single-molecule tracking experiments to show that the confined diffusion of cystic fibrosis transmembrane conductance regulator (CFTR) Cl^- channels is due to a spring potential caused by the binding of the channels to actin filaments [86]. The authors used an intermediate step, where they calculated a radial density distribution first and then applied the residence time technique.

The residence time or inversion-of-fraction technique is based on Boltzmann statistics. Kramers has studied the escape kinetics of a trapped particle that undergoes Brownian motion to calculate rates of chemical reactions [219]. The underlying concept is that the number of times a random Brownian walker will visit a position is related to the confining potential. In fact, the probability of visiting a spot in an arbitrary potential is governed by Boltzmann statistics and given by the following equation:

$$N_{ij \in n} = N_0 \, e^{\frac{-V_{ij}}{k_B T}} \tag{3.17}$$

Here, the number of times a spot is visited in a grid of $n \times n$, $N_{ij \in n}$, is exponentially proportional to the potential V_{ij} and the temperature T. The resulting potential in that grid point can then be determined via the expression:

$$V_{ij} = -k_B T \, ln \left(\frac{N_{ij}}{N_0} \right) \tag{3.18}$$

Figure 3.9 shows a comparison between the potentials extracted with this residence time technique and with the inference technique for a numerical trajectory of 1000 points with a diffusion coefficient $0.075 \, \mu m^2/s$ and a spring constant of $0.36 \, pN/\mu m$. The input potential (black) is shown together with the extracted potential (red) for the case of inference and residence time in figure 3.9 a) and b), respectively. To visualize the performance of both techniques we show the difference of extracted and real input potential in blue. The first observation is that the deviation between the potentials is larger for the residence time analysis. The calculated mean deviation per grid-square from the input potential is

$0.000 \pm 0.003\,\text{eV}$ and $0.004 \pm 0.015\,\text{eV}$ for the inner most zone of 4×4 squares for the inference and residence time analysis, respectively. The mean deviation values over the entire mapped zone are $0.002 \pm 0.007\,\text{eV}$ and $0.015 \pm 0.018\,\text{eV}$ for the inference and residence time analysis, respectively.
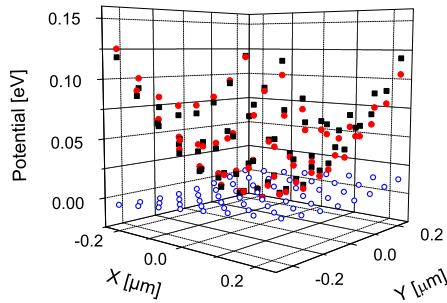
(a) Performance of the inference technique in extracting the confining potential.
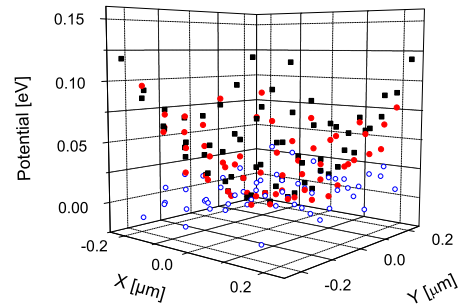
(b) Performance of the residence time technique in extracting the confining potential.

Figure 3.9: Difference in performance of inference vs. residence time techniques in extracting a confining potential. (a) gives the extracted potential from inference in red, the input potential in black and their difference in blue. (b) shows the potential determined from residence time analysis in red, the input potential in black and their difference in blue. The inferred potential follows the input potential more closely.

The residence time technique seems to overestimate the potential in regions that were visited less frequently. This problem arises from the fact that a fit with the Boltzmann equation assumes that the particle has explored all the accessible points often enough, i.e. it assumes a steady state. Steady state, however, may not have been achieved if the trajectory is too short. The inference analysis, on the other hand, does not systematically over- or underestimate the potential. The error becomes larger at the border of the confinement domain, i.e. where the forces were not accurately determined due to fewer data points in the outer subdomains. The posteriori distribution of the inferred forces on the outside of the domain is also broader. Overall, the inference technique is a valuable tool to evaluate the confining potential of a biomolecule and outperforms the residence time technique for short trajectories, which are typical for single-molecule tracking. The reason is that the inference technique extracts more information from the trajectory than the residence time analysis.

3.6   Conclusion

The technique introduced for inferring parameters from single-molecule trajectories, based on the Langevin equation of motion and using Bayes' Theorem, produces highly accurate results. An extra term that allows the confining potential to take an arbitrary form makes this model less constraining in terms of assumptions. In fact, the technique can be applied to other cases of motion, where the receptor is not confined, by replacing the Langevin equation of motion by a different equation that would contain terms for active transport or drift for example. Furthermore, terms can be added that model experimental parameters, such as the localization precision and the response of the detector.

Numerical simulations were used to investigate the bias for the extracted parameters of diffusivity D and spring constant k_r in figures 3.3 and 3.5. The systematic bias of the inferred values can then be corrected by taking the noise sources into consideration and by correcting the intrinsic bias through equations 3.11 & 3.12.

The inference is also capable of correctly distinguishing between a scenario with and without forces, as demonstrated in figure 3.7. Therefore, the developed tool is appropriate for finding forces in membrane micro domains.

The comparison between the inferred values for the diffusion coefficient with the values obtained from the commonly applied MSD analysis by fitting the first three points of the MSD curve (figure 3.8) shows that the MSD technique is more strongly biased. It cannot account for the presence of forces within the domain, since it assumes free motion within a confining box. Applying the MSD technique in the presence of a confining potential results in underestimating the diffusion coefficient.

The inference technique is also shown to outperform the residence time technique in determining the confining potential as shown in figure 3.9. The reason for the poorer performance of the residence time technique is that it relies on Boltzmann statistics and therefore requires a steady-state system, which is not necessarily true for experimental trajectories of a finite length.

One of the most important advantages of the inference technique is that it exploits the full information stored in the trajectory, which is not the case for any of the alternative techniques.

The inference technique can easily be extended to three dimensions making it suitable for tracking molecules within the cell. Furthermore, the length scales are not fixed and the sample can be a small molecule that moves on an organelle or a cell that moves within an animal. Because the potential is not imposed but inferred instead, this approach is very general.

Chapter 4

Diffusion Coefficients, Force Fields and Confinement Potentials of Receptors

After localization of the nanoparticle in each frame with sub-diffraction resolution and after reconstitution of trajectories, as explained in chapter 2, the trajectories can be analyzed to give insight into the motion of the toxin receptor and thus the membrane structure. As already shown, the receptors are confined in domains from which they rarely escape. Initially we will only consider the confined parts of trajectories without drift, without hopping or escape. In this chapter we will use the inference technique as explained in chapter 3 to determine the diffusion coefficient of single receptors and the confining potential.

The experimental wide-field fluorescence microscopy set-up used to collect the data presented here has been described in section 2.2. Briefly, all trajectories in this section have been obtained for receptors of the α-toxin of *C. septicum* and the ϵ-toxin and prototoxin from *C. perfringens* at room temperature or at $37\,^{\circ}\mathrm{C}$. The receptors were labeled by $Y_{0.6}Eu_{0.4}VO_4$ nanoparticles, which were coupled to the toxin in an average stoichiometry of one to one. The advantage of these nanoparticles for single-molecule tracking is their photostability and the absence of blinking, which allows for the acquisition of long uninterrupted trajectories. The length of a trajectory directly influences the quality and the precision of extracted variables, as demonstrated in reference [215].

This chapter will show how the inference technique can be applied to experimental data to obtain unbiased results for diffusion coefficients and how the technique can be used to quantify the shape of the confining potential. Inference can also be used to verify if the diffusion coefficient changes within a domain. From a more biological point of view, this chapter will investigate the difference in motion between the α- and ϵ-toxin receptor in MDCK cells.

The goal of this study is to track *single* toxin receptors and not multimers, which behave differently. The concentration of toxin used is very low with respect to the concentration needed to induce any toxic effects. This low concentration, along with the steric hindrance of the nanoparticles attached to the receptor ensures that only single receptors are tracked. In addition, in the case of ϵ-toxin, we have access to the inactive form of the toxin, the prototoxin, which cannot oligomerize. For this chapter, ϵ-prototoxin is used, rather than ϵ-toxin to further ensure tracking of single receptors. All the toxins that are used in this work were isolated and supplied by Michel Popoff from the Anaerobe Bacteria and Toxins unit at the Institut Pasteur. The isolation process is explained in reference [170].

4.1 The diffusion coefficient of the α- and ϵ-toxin receptors and the confinement domain size

The α-toxin of *C. septicum* couples to a GPI-anchored receptor in the membrane of MDCK cells. Experiments with a mutant CHO cell line (BAG15) that cannot synthesize GPI-anchored receptors was shown to be resistant to α-toxin [220]. The receptor of the *C. perfringens* ϵ-toxin was shown to be a membrane protein of molecular weight 34 kDa by cleaved by proteinase K or trypsin, but its exact nature remains unknown [170, 187]. Typical trajectories for both toxin receptors are shown in figure 4.1. The trajectories were recorded at 21 °C with a peak laser intensity of 0.25 kW/cm^2 at an acquisition time of 51.3 ms, where 50 ms are used for photon accumulation and 1.3 ms for camera readout. Confinement of the receptor motion means that the motion is confined to a domain that is significantly smaller than the entire apical cell surface of about 50 µm^2. From inspection of both trajectories it is already possible to confirm the receptor's confinement to small, round domains of about 0.15 µm^2. It is through this effect that the toxin increases its toxicity. By targeting receptors that are either already pre-clustered or in close proximity to each other, the toxin monomers drastically increase the probability of oligomerization and pore formation. It should be noted that the clustering of receptors or formation of a confinement zone can be caused as a response to the binding to the toxin receptor.

The mean square displacement (MSD) plots of both trajectories confirm the confinement. The MSD does not grow linearly with τ, as would be expected for free Brownian diffusion, but it levels off at 0.03 µm^2. This behavior is what is expected for a confined Brownian walker that exhibits Brownian diffusion in a confining domain. Here, the receptors undergo diffusion of the type $MSD_R = 2nDt^\alpha$, where $\alpha = 1$ and n is 2. The red line is the fit of the MSD plot with equation 3.2, which
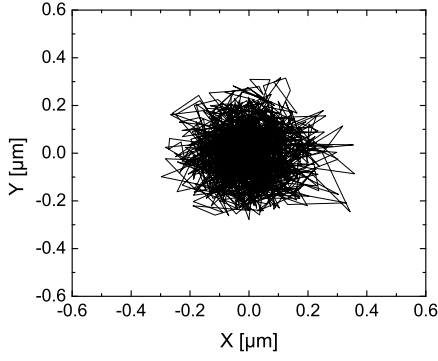
(a) Trajectory of a *C. septicum* α-toxin receptor.
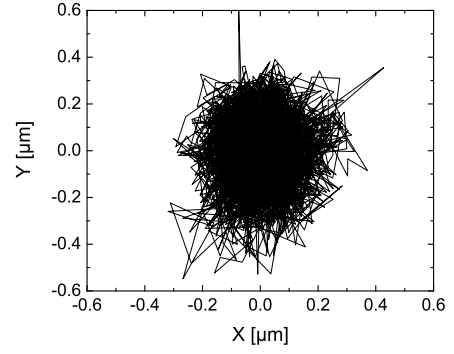
(b) Trajectory of a *C. perfringens* ϵ-toxin receptor.
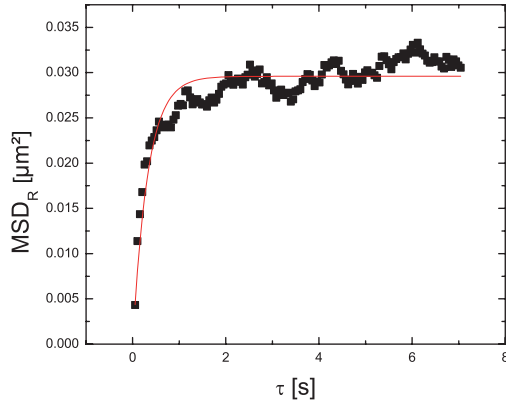
(c) MSD corresponding to the trajectory in a).
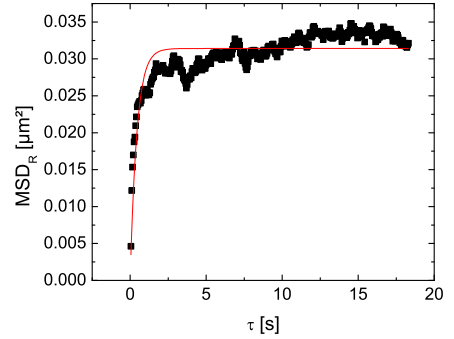
(d) MSD corresponding to the trajectory in b).

Figure 4.1: Trajectories of a *C. septicum* α-toxin ($N = 1281$ points) and a *C. perfringens* ϵ-toxin ($N = 3561$ points) receptor at 21 °C. Both toxin receptors are confined to zones that are drastically smaller than the apical surface of the cell. The confinement is visible in the MSD plots, where plateaus are observed, whereas straight lines are expected for a freely diffusing receptor.

is commonly used to calculate the domain size.

Assuming a quadratic potential, the inferred and corrected diffusion coefficient D_{Inf} for the α-toxin receptor shown in figure 4.1 a) is $0.124 \pm 0.007\,\mu\text{m}^2/\text{s}$ while the calculated domain area A, defined as the area encompassing $95\,\%$ of the trajectory's points was calculated to be $0.15\,\mu\text{m}^2$. The values for the ϵ-toxin receptor are $0.210 \pm 0.007\,\mu\text{m}^2/\text{s}$ and $0.15\,\mu\text{m}^2$, for D_{Inf} and A, respectively. However, to better compare the two receptor motions we will now consider the distribution of measured variables for many trajectories. The mean inferred diffusion coefficient $\langle D_{Inf}\rangle$ of the α-toxin receptor at room temperature is $0.16 \pm 0.09\,\mu\text{m}^2/\text{s}$, while the mean inferred diffusion coefficient of the ϵ-toxin receptor is $0.16 \pm 0.14\,\mu\text{m}^2/\text{s}$. There is no difference in the mean values of the diffusion coefficients. The mean values for the domain area A are $0.4 \pm 0.4\,\mu\text{m}^2$ both for the α-toxin and ϵ-toxin receptor. Again, the domain areas of the two receptors are indistinguishable. The confinement, evaluated by the mean confinement factor $\langle u\rangle$ introduced in equation 3.9 in chapter 3, is 0.016 ± 0.006 for the α-toxin receptor trajectories and it is 0.017 ± 0.008 for the ϵ-toxin receptor trajectories. The acquisition time was held constant for all measurements. Again, these values show that both receptors are equally confined.

A discussion of the large standard deviation of the diffusion coefficients is in order. Averaging single molecule trajectories requires some consideration. First, the technique circumvents ensemble averaging, as it is the case in FCS measurements, and can thus provide access to subpopulations in the distribution of a certain measured variable. However, single trajectories and consequently single measured values for a variable from that trajectory might not be representative of the typical behavior of the moving biomolecule. Enough data has to be acquired to sample all subpopulations and to obtain the correct global average. A second point is that, since the motion of a biomolecule is measured on live cells, this creates an additional dispersion in measured values because the cells are not always in the same condition due to many external and internal factors. In the case of the ϵ-toxin receptor, figure 4.2 shows a histogram of inferred diffusion coefficients D_{Inf} for four different days of experiments. Not only are the mean values of each day different, but so are the distributions. In this work, multiple days are only averaged to compare the α-toxin and ϵ-toxin receptors because experiments were not performed on the same days and combining the data of different days increases the statistics. When the origin of confinement will be investigated in the next chapter, experimental data will be considered for each day individually, since the induced changes in cell biology can be better evaluated on a daily basis.

Other than simply considering the average of diffusion coefficients of the two receptors, it is more instructive to compare their respective distributions. The
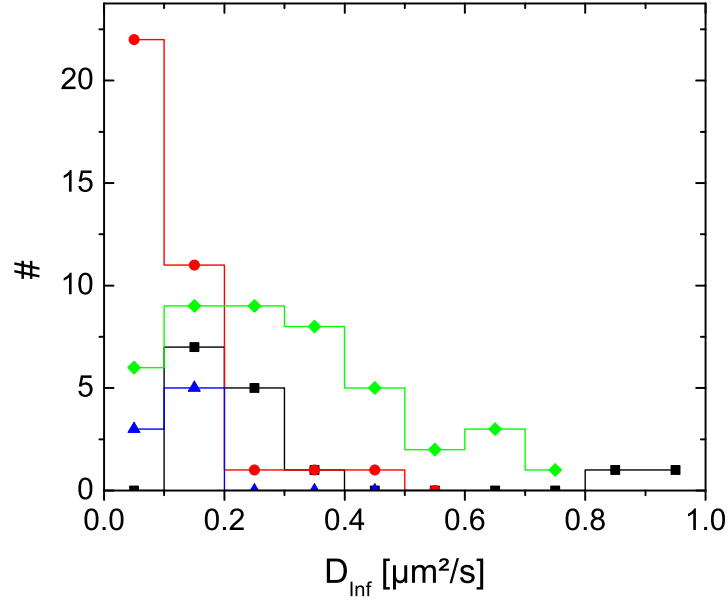
Figure 4.2: Histogram of inferred diffusion coefficients D_{Inf} of the ϵ-toxin receptor at room
temperature on different experimental days. Results from each day are shown with
a different color and symbol. Combining the data from different days increases the
statistics but creates a broader distribution.

combined inferred diffusion coefficients D_{Inf} are shown in figure 4.3 for the two
types of receptors. First, it is useful to consider how many receptors are stationary.
For the α-toxin receptor 65 out of 65 trajectories are moving and fulfill the cri-
terion of having a larger mean displacement per frame than the positioning noise
B_r per frame, i.e. $\langle x(t + \Delta t - x(t)) \rangle > B_r$. For the ϵ-toxin receptor, $2\,\%$ of the
trajectories are immobile. However, for such a small fraction of trajectories, we
cannot exclude the possibility of non-specific binding. For both receptor types, all
of the observed trajectories were confined.

The superimposed histograms show that there is substantial overlap between
the two distributions and that the ϵ-toxin has a few more slower diffusing recep-
tors. A more quantitative technique to evaluate the similarity between two data
sets with low sample size is the two-sample Kolmogorov-Smirnov (KS) test. Here
a cumulative distribution plot is prepared by counting which fraction of the data
set is below the value on the x-axis of the tested variable. The D-value is then
calculated for the point where the difference between the two cumulative distribu-
tion functions is the largest and a P-value, which is the probability of obtaining a
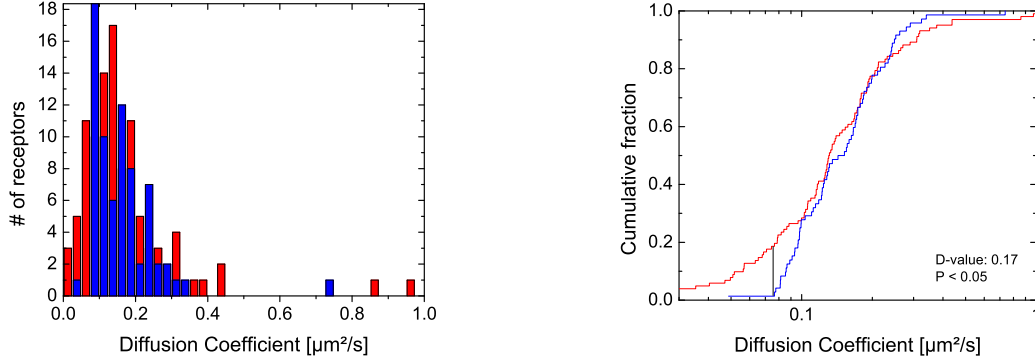
(a) Histogram of D_{Inf} of α- (blue N=72) and ϵ-toxin (red N=101) receptors.

(b) Kolmogorov Smirnov analysis of the two distributions.

Figure 4.3: Histogram of D_{Inf} of α- (blue) and ϵ-toxin (red) receptors. The distribution of measured parameters is more instructive than the measured mean values of $0.16 \pm 0.09 \, \mu m^2/s$ for the α-toxin receptor and $0.16 \pm 0.14 \, \mu m^2/s$ for the ϵ-toxin receptor at 21 °C. The distributions are similar with only a few more slowly diffusion receptors for the ϵ-toxin. This is also visible in the cumulative fraction plot, where the D-value for the two distributions is located with 0.17. The associated P-value is 0.05, which is equal, but not below the threshold P-value and thus both distributions are similar. There is no detectable difference in diffusion coefficients between the two types of receptors.

test statistic at least as extreme as the one that was observed, can be associated to it via the Kolmogorov distribution. This test is sensitive to differences in the location and the shape of the empirical cumulative distribution function. However, a P-value between two distributions is not helpful unless a threshold P-value is defined. If the measured P-value is below the threshold value, the two distributions are deemed different. This threshold is estimated in this work from a Monte Carlo simulation with 10000 steps, that combines both data sets and randomly splits this set into two separate sets of sizes equal to those of the real data sets. These two artificial sets are no longer from different distributions because they data has been mixed. The two sets are then compared to each other in a KS-test giving a D-value and P-value. The threshold P-value is here defined to be more than one standard deviation smaller than the mean P-value from all the Monte Carlo iterations.

The cumulative distribution plots for the two receptor types are shown in figure 4.3 b). The function shows that there are indeed more ϵ-toxin receptors with lower diffusion coefficients. It is also at low diffusion coefficients that the D-value of 0.17 is found. The associated P-value is 0.05, which is not smaller than the threshold

P-value of 0.05 for these two data sets. It is thus not possible to clearly distinguish the two distributions. This means in biological terms that both receptor types diffuse with the same diffusion coefficients. This is not surprising considering that the size of a GPI-anchored receptor, to which the α-toxin binds (38 kDa, recombinant folate receptor) [185, 186], is typically of similar size to that of the ϵ-toxin receptor, which has a molecular weight of 34 kDa [170, 187].

Given that the diffusion coefficients are similar, the question arises if the two toxin receptors are located in the same domain type. To this end, we will now analyze the domain area. The histogram of the distributions are given in figure 4.4 for receptors at room temperature. As explained above, the domain size is defined to be the area that comprises 95 % of the locations visited by the receptor. Again, the measured domain area A is given in blue for the receptor of the α-toxin and in red for the receptor of the ϵ-toxin. Similarly to the mean values, the two distributions do not differ according to the KS test. This implies that both receptors may be confined in the same type of domain and that the mechanism of confinement is the same.
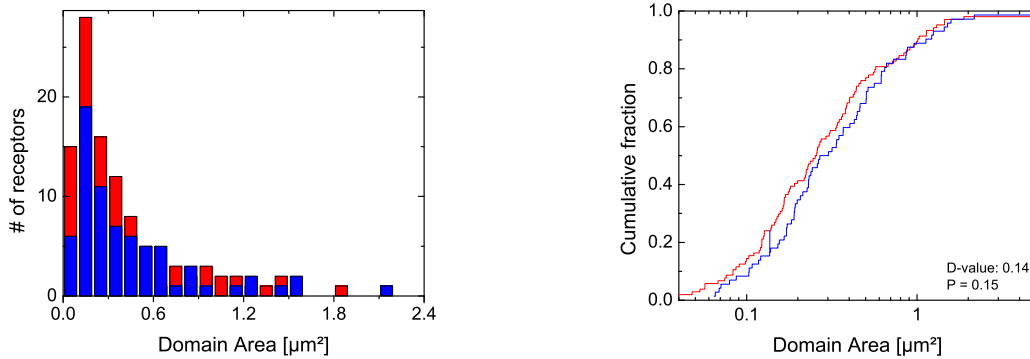
(a) Histogram of the domain area A for α- (blue, N=72) and ϵ-toxin (red, N=101) receptors.

(b) Kolmogorov Smirnov analysis of the two distributions.

Figure 4.4: Histogram of the domain area A of α- (blue) and ϵ-toxin (red) receptors. The measured mean values are $0.4 \pm 0.4 \, \mu m^2$ for both receptor types. The distributions are very similar. This is also visible in the cumulative fraction plot, where the D-value is found to be 0.14. The associated P-value is 0.15, which is not below the threshold P-value. There is no detectable difference in domain area between the two receptor types.

Overall, the values for the diffusion constant of the α-toxin receptor, which is a GPI-anchored membrane protein, and of the ϵ-toxin receptor are comparable to

values found in the literature for membrane proteins exhibiting confined motion. The average diffusion coefficient $\langle D_{Inf} \rangle$ of $0.16 \pm 0.09\,\mu m^2/s$ found here is comparable to the values of $0.33 \pm 0.3\,\mu m^2/s$, determined by Umemura et al. that use a high-speed acquisition to determine the movement of a membrane protein in small domains attributed to the picket and fence model [153]. De Brabander et al. also suspect the cytoskeleton to be the reason of confinement of their GPI-anchored protein and found a value of $0.1\,\mu m^2/s$ [154]. Sheets et al., who attribute the confinement of their GPI-anchored proteins to lipid rafts found a diffusion coefficient of $0.0035 - 0.081\,\mu m^2/s$ [125]. The GPI-anchored receptor in the work by Pinaud et al. is transiently localized in GM1-rich zones that also contain caveolin [166]. The diffusion coefficient is $0.038\,\mu m^2/s$ [166]. Another experiment by Nishimura et al. and Vrljic et al. found a diffusion coefficient of $0.16 \pm 1.1\,\mu m^2/s$ [160, 161]. However, the localization that they observe is not strong and the cited coefficient corresponds to receptors that undergo fast anomalous diffusion.

The sizes of the confining domains of the α-toxin receptor are larger than most values found by other groups. The determined values for GPI-anchored proteins range from 0.0011 to $0.33\,\mu m^2$ [153,166]. De Brabander et al., however, determined their confining domains to have a size of 1 to $4\,\mu m^2$ [154].

The residence time in a confining domain of a few minutes found in our measurements is also much longer than that found by other groups for their GPI-anchored proteins [153, 166]. However, signaling platforms are believed to be stable over longer period of times and some GPI-anchored proteins have been in their confinement zone for many minutes [126].

4.2   The inferred confining potential

The inference technique introduced in chapter 3 for confined receptors also provides access to the confining potential. As previously explained, the forces acting on the receptor can be extracted in a mesh. Here a force is inferred for each mesh point individually and is used to obtain the force maps. A second approach directly infers the parameters of a model potential. Here the forces in the mesh are no longer independent, but are governed by the parameters of the potential. This approach is chosen when the potential map is shown in this chapter.

Figure 4.5 shows the trajectories of a single ϵ-toxin receptor, with the corresponding inferred force map. The inferred diffusion coefficient D_{Inf} is $0.076 \pm 0.003\,\mu m^2/s$. The trajectory is 1500-frames long and is confined to an area of $0.15\,\mu m^2$. The level of confinement u for this receptor is 0.017. Forces, acting on the receptor have a mean value of $0.16 \pm 0.11\,pN$ and are as strong as $0.5 \pm 0.2\,pN$.

The next task is to find a model potential that can describe the single-molecule trajectory of the confined toxin receptor in a satisfactory manner. We will start with a very general description of the attractive potential by a high-order polynomial. Of course, a higher-order polynomial description of the potential with more degrees of freedom will always better match the data than an expression with less parameters. However, according to Occam's razor principle [221], we will now drop unnecessary higher orders of the polynomial description of the potential so that only a physically relevant expression is left in order to find a meaningful description of the potential. To this end, the potential is inferred via a polynomial of various orders for the same experimental trajectory. Because it is the nature of the experimental potential that is unknown, we have to resort to using experimental data rather than numerical trajectories. By comparing the performance of the various orders, it is possible to eliminate unneeded higher orders by observing the minimal required polynomial order that still precisely models the experimental confining potential. Figure 4.6 shows the inferred potential for a second-order polynomial with black squares, while the result of a fourth-order polynomial is shown by red circles for the same ϵ-toxin trajectory at $21\,°\mathrm{C}$. The difference between the two extracted potentials is given in blue. It turns out that a second-order polynomial is accurate enough to model the confining potential as can be seen from the calculated difference in blue. Large deviations only occur at the border of the potential, where the width of the posteriori probability distribution and consequently the error is large. The coefficients of the x^2 and y^2 terms only change by $10\,\%$ when reducing the order from 4 to 2. Furthermore, the linear-term contributions are less than $1\,\%$ compared to the quadratic term contributions, which leads to the conclusion that the linear terms can be dropped in the description of the experimental potential. Overall, the confining potential of both toxin receptors can be classified as spring like. The inferred potentials can now easily be compared to each other via the radial spring constant k_r, which is calculated from the inferred coefficients of the independent x^2 and y^2 terms: $k_r = \sqrt{k_x^2 + k_y^2}$.

Histograms of the inferred spring constants k_r are shown in figure 4.7. The distribution for the α-toxin receptor is given in blue (N=72), while the distribution for the ϵ-toxin receptor is displayed in red (N=101). The mean values and standard deviation are $0.3 \pm 0.2\,\mathrm{pN/\mu m}$ for the α-toxin receptor and $0.6 \pm 0.7\,\mathrm{pN/\mu m}$ for the ϵ-toxin receptors at $21\,°\mathrm{C}$. The KS analysis of the cumulative fraction plot gives a D-value of 0.20, located at the high spring-constant end. The associated P-value is 0.01, which is below the threshold P-value of 0.05. This confirms that the ϵ-toxin receptors show more cases of higher confinement. The difference in k_r can stem from the fact that the two toxins couple to different receptors which, despite their similar molecular weight and confinement in domains of equal size, experience the confinement differently possibly due to the receptor's molecular structure or inter-
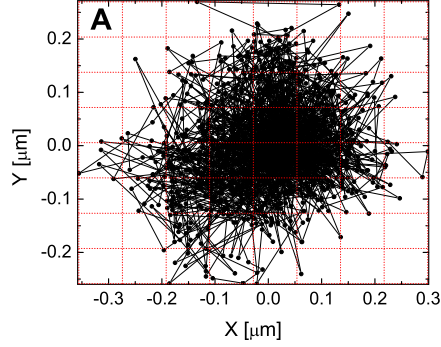
(a) Trajectory of an ϵ-toxin receptor
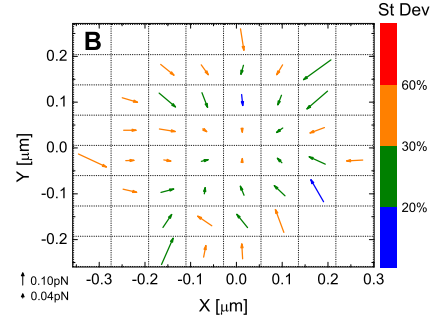
(b) Corresponding force map color-coded for the standard deviations.
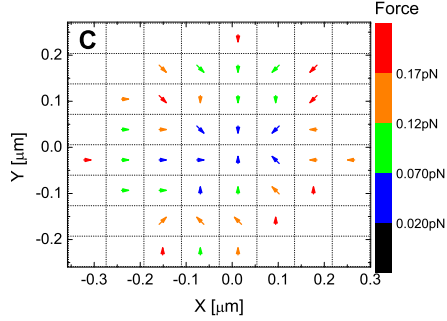
(c) Corresponding force map color-coded for the force values.
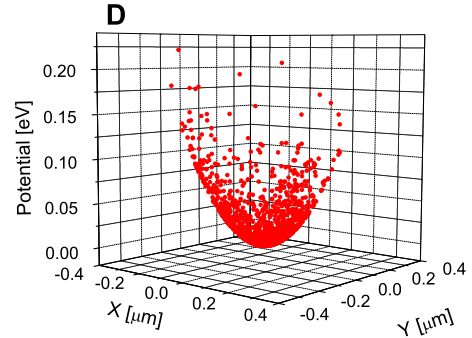
(d) Inferred confining potential.

Figure 4.5: Trajectory, inferred force map and confining potential of a single ϵ-toxin receptor at 21 °C. The inferred diffusion coefficient D_{Inf} is $0.076 \pm 0.003\,\text{µm}^2/\text{s}$. The trajectory is 1500-frames long and is confined to an area of $0.15\,\text{µm}^2$. The level of confinement u for this receptor is 0.017. Forces, acting on the receptor have a mean of $0.13 \pm 0.06\,\text{pN}$ and are as strong as $0.28 \pm 0.08\,\text{pN}$. The forces in the mesh are inferred independently, while the potential is inferred directly via optimizing the polynomial model's parameters and not by fitting the independent forces of the force map.
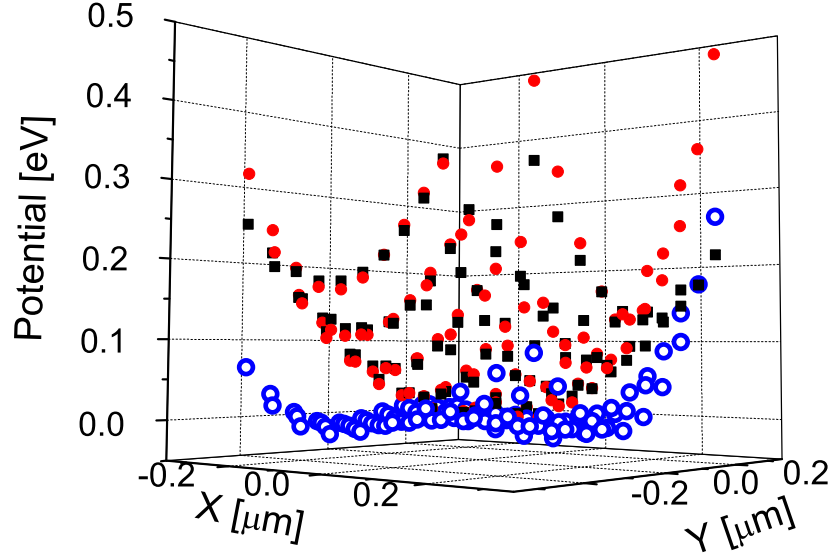
Figure 4.6: Polynomial 2nd (black) vs. 4th order (red) description of the confining potential. Their difference is shown in blue. Occam's razor principle can be used to minimize the order of the model polynomial potential inferred from experimental trajectories to show that the confining potential is parabolic. This allows for a simple description of the potential by a radial spring constant k_r.

action with other molecules.

Overall, the magnitude of the inferred spring constants is lower by a factor of 10 than that obtained for transmembrane proteins, which are thought to be attached to the cytoskeleton: $2.6 \pm 0.8 \, \text{pN/µm}$ for the CFTR Cl^- transmembrane receptor [86], $2.4 - 8.4 \, \text{pN/µm}$ for the LFA-1 adhesion protein after binding to ICAM-1 ligand [69] and $10 \, \text{pN/µm}$ for the δ-receptor in the membrane of Escherichia coli bacteria [71]. This leads us to think that α- and ϵ-toxin receptors are not attached to the cytoskeleton.
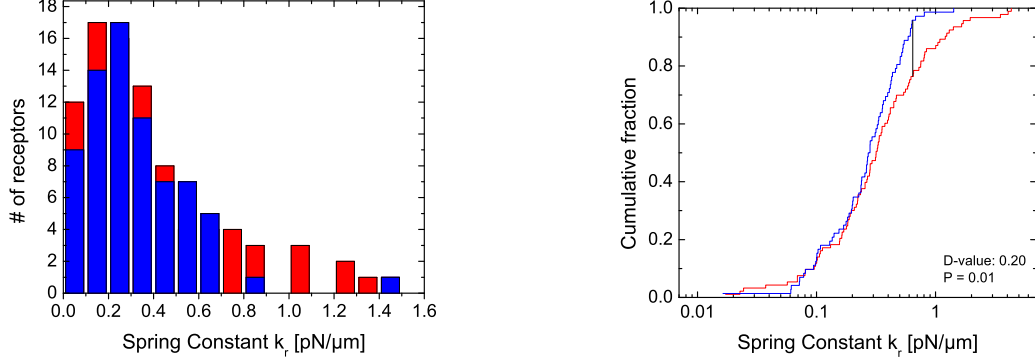
(a) Histograms of inferred spring constants k_r for α- (blue N=72) and ϵ-toxin (red N=101) receptors.

(b) Kolmogorov Smirnov analysis of the two distributions.

Figure 4.7: Histograms of inferred spring constants k_r of α (blue) and ϵ-toxin (red) receptors. The mean values and standard deviation are 0.3 ± 0.2 pN/µm for the α-toxin receptor and 0.6 ± 0.7 pN/µm for the ϵ-toxin receptor. The KS analysis of the cumulative fraction plot gives a D-value of 0.20. The associated P-value is 0.01, which is below the threshold P-value. ϵ-toxin receptors show more cases of higher confinement.

4.3 The radial density distribution (RDD)

A different approach that has been used to investigate spring-like potentials in single-molecule data is the analysis of the radial density distribution (RDD) of a trajectory's data points [86]. For this technique the radial density distribution $d(r)$ is calculated by

$$d(r) = N(r)/\pi \left[(r + \Delta r/2)^2 - (r - \Delta r/2)^2 \right] \tag{4.1}$$

This distribution can be understood as a density measure of the number of points $N(r)$ that fall within a circular zone $\left[r - \frac{\Delta r}{2}; r + \frac{\Delta r}{2} \right]$ around the origin of the confinement domain. The distribution is then fitted, assuming Boltzmann statistics, by the following equation

$$d(r) = d(0) \, exp \left[\frac{-V(r)}{k_b T} \right] \tag{4.2}$$

$$V(r) = k_r^{RDD} \, r^2 \tag{4.3}$$

where the potential $V(r)$ is assumed to be spring-like with radial spring constant k_r^{RDD}. This technique provides an alternative method to test what kind of potential best describes a confined trajectory, by substituting different types of potentials for equation 4.3. However, in their work, the authors average 65 experimental trajectories of CFTR Cl^- transmembrane receptors to obtain a better estimate of the spring constant [86]. Here, trajectories are analyzed individually, which is possible due to the large frame number made possible by the photostability of the europium-doped nanoparticles. The spring constants of the individual trajectories k_r^{RDD} are then compared to the previously inferred spring constants k_r.
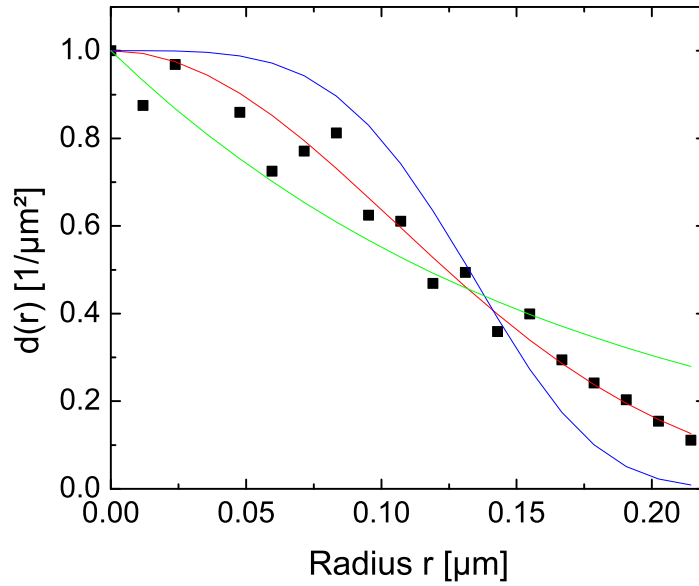
Figure 4.8: Radial density distribution analysis of the single α-toxin receptor from figure 4.1. The fit for the cone potential ($V \propto r$) is shown in green, the fit with a ($V \propto r^4$) potential is plotted in blue. The spring potential ($V \propto r^2$) in red best fits the radial density distribution and gives a value for the spring constant that is comparable to the value obtained with the inference technique.

The radial density distribution for the α-toxin receptor of figure 4.1 is shown in figure 4.8 along with the fits for various potentials. A $V(r) \propto r$ type potential is given in green, while a $V(r) \propto r^4$ type potential is shown in blue. The red spring potential, $V(r) \propto r^2$, gives the best fit and confirms the conclusion of the previous section 4.2. The spring constant obtained from the RDD analysis k_r^{RDD},

is 0.2 ± 0.1 pN/µm, while the inferred spring constant k_r for this trajectory is stiffer with 0.45 ± 0.05 pN/µm. However, overall, the averages for the spring constants determined by both techniques agree, since $\left\langle k_r^{RDD}(\alpha - toxin)\right\rangle = 0.2\pm0.2$ pN/µm and $\left\langle k_r(\alpha - toxin)\right\rangle = 0.3 \pm 0.2$ pN/µm. The mean values and standard deviation for the ϵ-toxin receptors are $\left\langle k_r^{RDD}(\epsilon - prototoxin)\right\rangle = 0.4 \pm 0.7$ pN/µm and $\left\langle k_r(\epsilon - prototoxin)\right\rangle = 0.6 \pm 0.7$ pN/µm. Thus, the analysis of the radial density distribution of single receptor trajectories confirms the findings of the inference method.

4.4 The diffusion coefficient is constant within its domain

The choice of inferring the diffusion coefficient D_{Inf} as a global parameter that does not vary over the trajectory has to be justified. The inference technique allows the extraction of independent local diffusion coefficients, just like the forces in the mesh. It is thus possible to detect fluctuations in diffusion coefficients within a single confining domain. This can be a useful tool to detect biological processes that depend on a local change in diffusion coefficient.

Figure 4.9 shows the inferred local diffusion coefficients for the ϵ-toxin receptor trajectory of figure 4.5. The blue surface is the value of the globally inferred diffusion coefficient of 0.076 ± 0.003 µm^2/s, while the local values are indicated by the black squares. Values do vary within the mesh and show greater variations at the border of the domain due to the lower density of trajectory points, but their overall mean is 0.077 ± 0.014 µm^2/s and the mean and maximal deviation from the globally inferred diffusion coefficient are only 13 % and 39 %, respectively. This result shows that there is no significant change in diffusion coefficient within the membrane domain and it is justified to simply infer a global diffusion coefficient, which will be more accurate due to the larger amount of data points.

4.5 Motion of the confining domain

All measurements that have been and will be shown are collected from receptors, moving in stationary membrane domains. However, the entire domain can also be seen to move. Furthermore, the receptor can leave its confinement domain. These hopping events are rare, while the drifting of the domain is observed more often. This section will show that, although hopping and drift events are observed, they are difficult to interpret. It is therefore important to first investigate the reason
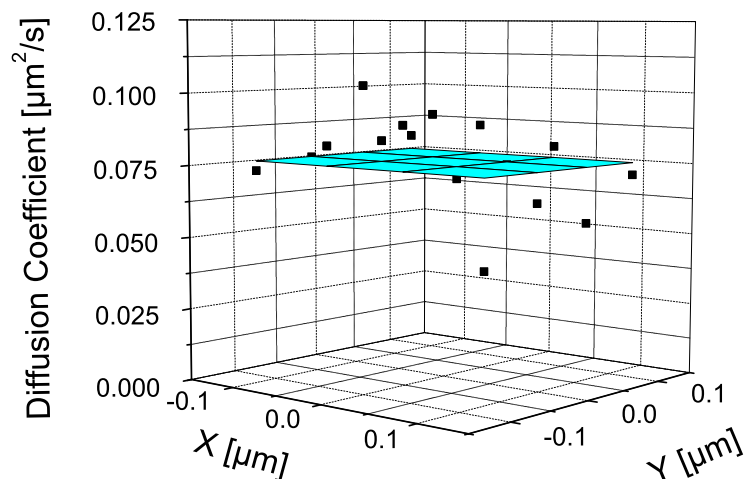
Figure 4.9: Comparison of D_{global} vs. D_{local} for the trajectory of an ϵ-toxin receptor at 21 °C. Inferring diffusion coefficients locally in a mesh can be used to show that the diffusion coefficient does not change significantly within the confining domain. The mean and maximal deviation from the globally inferred diffusion coefficient (blue surface) are only 13 % and 39 %, respectively.

for the confinement, which will be done in chapter 5.

4.5.1 Drift of the confining domain

Domains that form confining boundaries have been shown to diffuse on the membrane in the case of lipid rafts [113, 126] and protein aggregates [150, 152]. Moreover, the apparent motion of the confining domain is also possible during temporal restructuring of the cytoskeleton [89, 92]. However, there are also many mechanisms postulated that can tie a lipid raft or a protein cluster to the cytoskeleton and thus fix it either by bending of the membrane in the case of caveolae [107] or by interactions with transmembrane proteins, which are directly attached to the cytoskeleton [89].

During this study, drift of confining domains was observed for many trajectories. Evidence for the movement of an entire confining domain rather than movement of only the tracked molecule can be obtained from the MSD plot of the receptor motion. Figure 4.10 shows a receptor that is still confined in a domain, as can be seen by the plateau in the MSD plot in figure 4.10 b). The fact

that the plateau is not flat but inclined indicates the motion of the entire domain. The MSD plot can be understood as the sum of two processes, the typical plot of confined motion with a flat plateau, where each point is shifted by a movement of the domain with diffusion coefficient D_{MSD}^{Domain} of $0.0070 \pm 0.0001\,\mu m^2/s$ (Fig. 4.10 d). The drift-independent diffusion coefficient of the receptor inside the domain is $0.18 \pm 0.01\mu m^2/s$ and the domain area is $0.50\,\mu m^2$. The total distance of the domain drift during the acquisition of 77 seconds is $0.8\,\mu m$, which can be measured in figure 4.10 a). The drift velocity, obtained from the slope in figure 4.10 d) increases as a function of time and thus the speed does not remain constant.
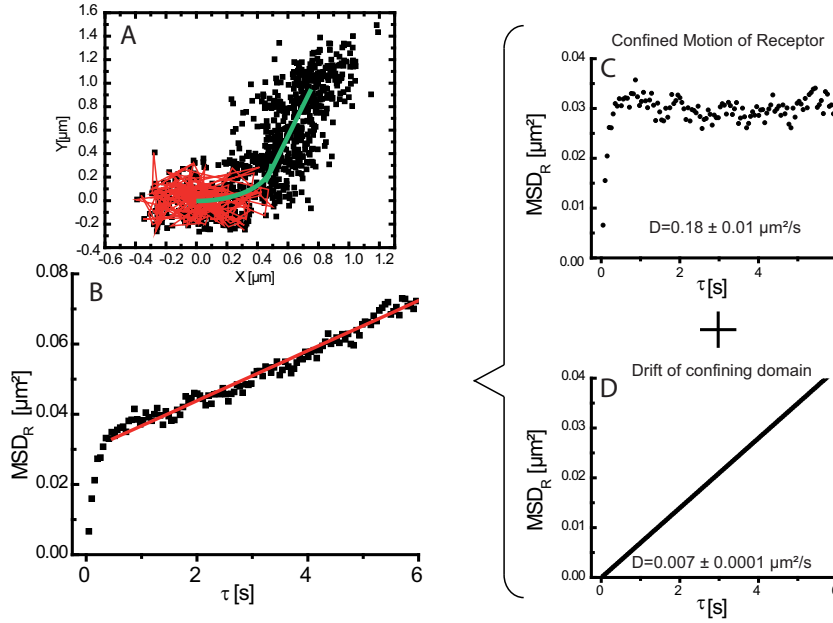
Figure 4.10: The drift of an entire confining domain can be observed, without the escape of the labeled receptor a). The MSD plot of the combined motion b) can be understood as the sum of two processes: First the typical plot of confined motion with a flat plateau in c), where each point is shifted due to the second process, which is the movement of the entire domain d). Because of the low diffusion speed of the membrane domains, it is difficult to assess from a single drifting domain, if the motion is guided or Brownian.

It is important to realize that, due to the low diffusion speed of the membrane domains, it is difficult to assess if the motion is guided or Brownian from a single drifting domain. However, motion of multiple domains in the same direction, as often observed in experiments with the toxin receptors, is an indication of directed motion of the membrane domains. The apparent directed motion may be only due to the motion of the entire membrane, which drags the embedded confining domains along as in references [210, 222]. This issue will revisited in chapter 6.

An indication that the observed drift is not a drift of the domains, but a drift of the entire membrane and cell is given by its speed. Active transport, as for the transport of neuronal antigens to the leading edge of the growth cones takes place at a speed of $1 - 2\,\mu m/s$, which is much faster than the drift observed here [223]. All measurements that have been and will be shown are collected from receptors, moving in stationary membrane domains.

4.5.2 Hopping

The toxin targets receptors that move within a small domain to concentrate itself and to increase the probability of pore formation due to oligomerization. Nevertheless, the receptor is observed to hop out of one domain into an adjacent domain. Hopping effects have been described for receptors that are confined by the cytoskeleton [39, 53, 65, 157, 158] and for receptors that are confined in lipid rafts and protein aggregates [149, 224], where hopping is referred to recruitment and escape of proteins into and from rafts. However, the hopping probability is generally lower for receptors confined in rafts and clusters compared to the probability in cytoskeleton corrals.

For the toxin receptors of both α- and ϵ-toxin, hopping events are observed. Distinction between hopping and domain drift can be made due to the speed of displacement, which is much higher in the case of hopping, or better by the observation of a change in diffusion mode. Presumably, once a receptor escapes from a confining domain, it is no longer confined and its mode of displacement will be closer to free Brownian motion. Such an event can be seen in figure 4.11. Here, the receptor undergoes confined motion in two different domains, which are colored in black and blue. The MSD plot, (black) for the motion in the first domain, shows the typical plateau behavior for confined motion. The MSD plot (blue) for the motion in the second domain shows the same behavior with a difference in plateau level and thus domain size. The receptor changes from one domain into the other via a small segment where it undergoes free Brownian diffusion for 2 seconds. This can be seen from the linear shape of the MSD plot, shown in red in figure 4.11 (the orange line is a linear fit). The MSD plot for the first domain is added in black to highlight the difference. After the short Brownian walk, the receptor is recaptured into the blue domain.

Additional evidence that the receptor left its initial domain and is recaptured into a different domain is given by the change in diffusion coefficient from $0.24 \pm 0.02\,\mu m^2/s$ in the first domain to $0.29 \pm 0.01\,\mu m^2/s$. Furthermore, the area of the confining domain changes from initially $1.2\,\mu m^2$ to $1.7\,\mu m^2$. This change in domain size is also visible in the height of the final plateau in the MSD plot for the two domains. The diffusion coefficient of the free motion is $0.25 \pm 0.07\,\mu m^2/s$,

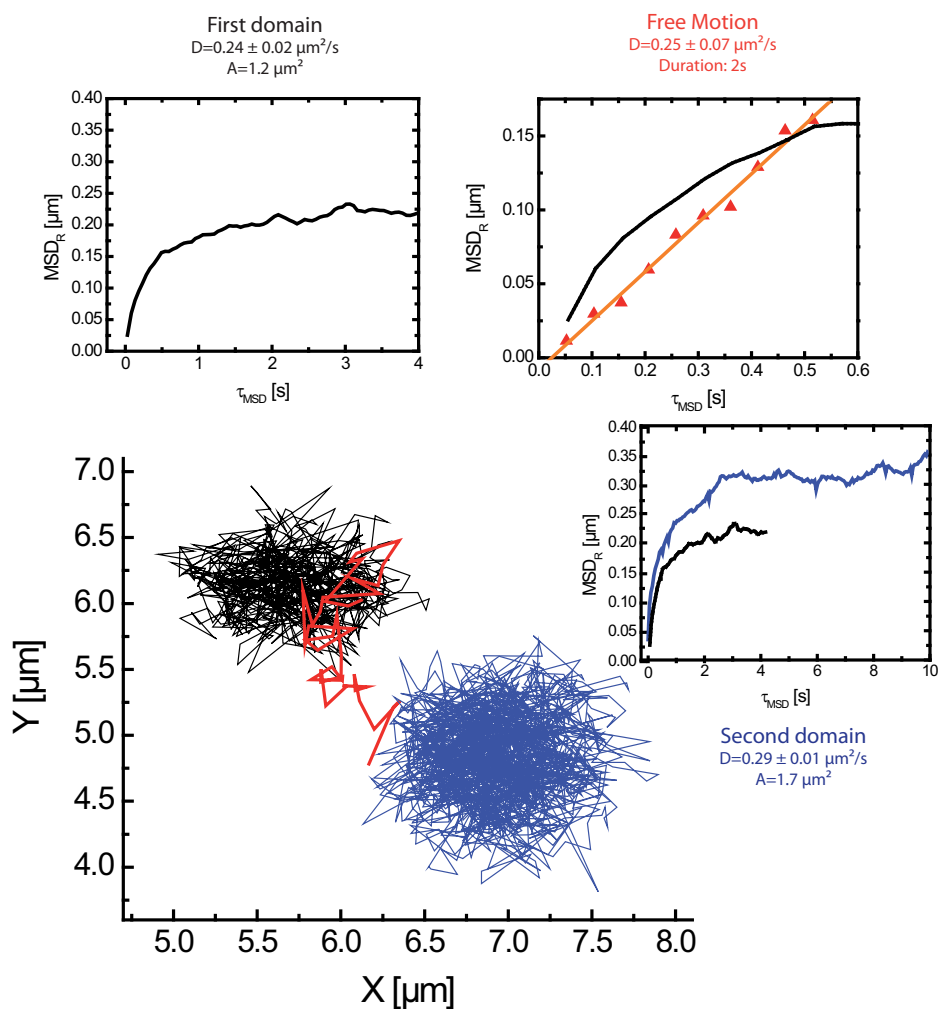Figure 4.11: Hopping event of a single toxin receptor. The receptor escapes from the black
confinement zone, moves across the membrane in a Brownian fashion as visible
from the linear MSD plot in red and is finally recaptured into the blue confining
domain. Additional evidence that the receptor is hopping is given by the change in
diffusion coefficient and domain area from one domain to the other.

which is comparable to the diffusion coefficient inside of the domains. The total displacement during the short Brownian walk across the membrane is 1.8 µm. There is however a chance that the confining domain quickly moved inside the membrane and deformed, which would also explain the change in area and the relatively similar values of diffusion coefficients before, during and after the hop.

Figure 4.12 shows further hopping events, where the receptor explores multiple domains. Overall, hopping events are observed in 2 % of the α-toxin receptor trajectories and in 7 % of the ϵ-toxin receptor trajectories at 21 °C, which have an average duration of 150 s. At the higher temperature of 37 °C, the hopping probability increases slightly to 6 % for the α-toxin receptor trajectories and remains constant for the ϵ-toxin receptor at 6 %. But not many hopping incidents are as clear as the example given in 4.11. The domains in figure 4.12 lie very closely together and are of similar size. Here, the domain could have simply hopped from one point to the next.

| (a) | (b) | (c) |
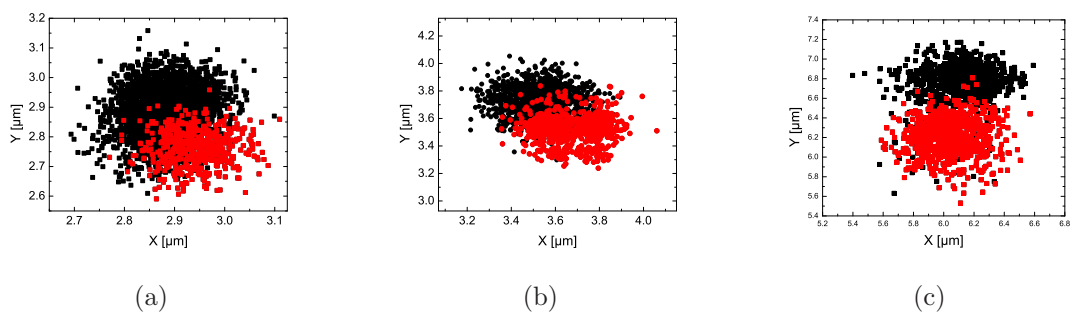
Figure 4.12: Trajectories that display hopping events. The target confinement zone is colored red. The difference to the drifting cases discussed in section 4.5.1 is the speed of displacement. However, diffusion coefficient and domain size do not differ much before and after the hopping event. In some cases, it is thus not clear if the entire domain is shifting or if only the receptor is hopping.

Hopping events, where the receptor is displaced quickly over a large distance are rare compared to the rate observed for hopping events of a G-Protein-Coupled and FcϵRI receptor, which reside in their domains for only $0.76-1.6$ s, that are thought to be confined by the actin boundaries [158, 159]. The hopping rate observed here is more comparable to values reported by groups attributing the localization to lipid rafts or protein aggregates [149, 166, 224]. In one case, stable domains have even been seen to be maintained during cell division [225].

Overall, the drift and the hopping characteristics like drift speed and escape time show similarities with experiments where confinement is attributed to lipid

rafts.

4.6   Discussion and summary

Experimental trajectories of α- & ϵ-toxin receptors are confined to small zones in the apical surface of MDCK cells. It is through this effect that the toxin increases its toxicity. By targeting receptors that are already pre-clustered or in close proximity to each other, the monomers drastically increase the probability of oligomerization and pore formation.

Diffusion coefficients of the two toxin receptors at $21\,°C$ were shown to be similar via a two-sample Kolmogorov-Smirnov (KS) test in figures 4.3 & 4.4. These observations suggest that the nature of confinement is the same for both receptors, since the diffusion coefficient depends on the type of receptor and the environment in which it diffuses. With respect to results from other groups, we find a comparable value for the mean diffusion coefficient but a larger size for the confining domains. The diffusion coefficient does not change significantly over the domain.

Confining potentials and force maps were inferred from the trajectory via the newly introduced inference technique for both receptor types, as shown in figure 4.5. Furthermore, the confining potential was shown to be spring-like by eliminating unneeded terms, as shown in figure 4.6. The determined spring constant was a factor 10 smaller than previously determined spring constants for transmembrane proteins tethered to the cytoskeleton, which is not surprising given that a GPI-anchor is not tied directly to the actin network [226]. The spring-like nature of the potential and the obtained mean spring constants were confirmed by fitting the radial density distribution in figure 4.8. A KS test on the distribution of spring constants showed that the confinement domains tend to create stiffer potentials for the ϵ-toxin receptor (see figure 4.7). This difference might stem from a difference in the strength of interaction with other membrane molecules or from a difference in molecular structure between the receptors.

The often observed drift of the confining domains shown in figure 4.10 is most likely due to the membrane dragging the zones along, rather than active transport, due to the low speed and the constant direction over one cell. Hopping of the receptor out of a domain into another was observed, however not frequently. Cases can be shown where the receptor clearly changes confinement domain, as in figure 4.11. However, other cases are much less clear because free Brownian motion of the receptor is not always observable during the fast hop and it could be the entire domain that is shifting.

The receptor of the α-toxin receptor is a GPI-anchored receptor. This receptor class has been shown to localize into lipid rafts [102, 121–123]. Since the α- and ϵ-toxin receptors show similar results with respect to confinement, domain size and diffusion coefficient, we have some evidence that the reason for confinement

of both toxin receptors are lipid rafts.

These results show that it is necessary to understand the nature of the domains. More importantly, we need to address the question of how the spring-like potential is created and how the forces are relayed to a receptor that only moves in the outer leaflet of the lipid bilayer, as is the case for the GPI-anchored α-toxin receptor. This is the topic of the next chapter.

Chapter 5

Origin of the Confining Potentials

The goal of the work presented in this chapter is to determine why the α- and ϵ-toxin receptors are confined in the apical membrane of MDCK cells. As we have seen in chapter 4, both toxin receptors undergo diffusion with similar diffusion coefficients with a mean value and standard deviation of $0.16 \pm 0.14\,\mu\mathrm{m}^2/\mathrm{s}$ in a spring-like potential with a spring constant of $0.45\,\mathrm{pN/\mu m}$. The typical area of these domains is around $0.5\,\mu\mathrm{m}^2$.

To distinguish between different confinement scenarios, the cells were treated with biochemical reagents, which modify specific biological aspects. With the correct drugs and enough precision in the measured variables, it is possible to determine which model best describes the confinement. Here we will mainly test for the picket and fence model and the lipid raft theory by first disrupting the actin cytoskeleton and then by disaggregating lipid domains. If the confinement is lost for one of these cases the reason for confinement can be inferred. However, we will not test for crowding effects, since reducing the number of proteins in the cell membrane is not possible. Experiments that test for this model have been performed and rely on extracting membrane blebs that can be protein de-enriched [162]. Furthermore we do not consider the case of a direct tethering, since the α-toxin receptors are not transmembrane proteins.

This chapter proposes two approaches towards understanding the origin of confinement. The first consists of observing changes directly at the molecular level by single-molecule tracking and another by observing the net effect of the changes induced by the drugs on the toxicity of the toxin on a cell culture. The second ensemble approach can make up for the limited number of observed single molecule trajectories. The changes that are monitored for the single-molecule experiments are those of the diffusion coefficient D_{Inf}, the domain area A of the confinement zone, and the radial spring constant k_r of the confining potential. They are compared to each other before and after treatment with the Kolmogorov-Smirnov (KS) test that was introduced in chapter 4 and which is explained in section B.4. To

increase the precision of parameters before and after treatment, we use only data that is recorded during a single day of experiments. As we have seen in the previous chapter, there is a large spread in measured values on different days. Combining this variability with the variability of responses to the biochemical reagents, would further smear out the distribution.

5.1   Disrupting the actin skeleton

This section investigates the effect of the depolymerization of the actin cytoskeleton on the mode of motion of the toxin receptors to determine whether the confinement is due to the cytoskeleton.

5.1.1   Action of Latrunculin B
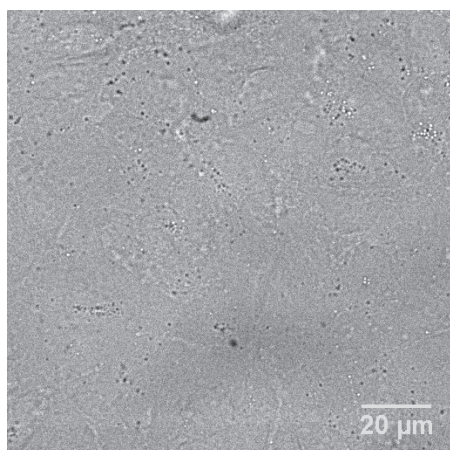
(a) MDCK cells before treatment.
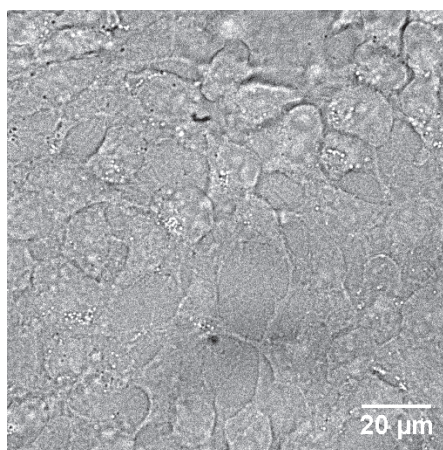
(b) MDCK cells after Latrunculin B treatment.

Figure 5.1: Actin depolymerization with Latrunculin B in MDCK cells. The cells were treated with 5 μM Latrunculin B at 21 °C for 30 minutes in a medium without serum. The disruption of the cytoskeleton causes the cells to contract.

There exist two groups of compounds that affect the actin cytoskeleton. The group of Jasplakinolides and Phallotoxins are potent filament stabilizers and decrease the pool of monomeric actin, whereas the families of Latrunculins and Cytochlasins either sequester actin monomers or cap barbed ends of actin filaments and thus inhibit further polymerization [227]. Eight different forms of Latrunculins have been found and are isolated from different marine sponges. They inhibit

actin polymerization by binding within the ATP-binding cleft of monomeric actin. Since the actin cytoskeleton constantly assembles and disassembles, this blocking of monomers leads to a reduction in polymerization rate and a net depolymerization of the cytoskeleton. The compound chosen for the disruption of the actin filaments is Latrunculin B, which is isolated from *N. magnifica* [228]. As already mentioned, this compound reduces the actin binding rate, it therefore must stay present in solution during the experiment because once removed, the rate returns to its normal state. To depolymerize the actin network, cells were incubated for 20 minutes with 500 nM Latrunculin B (Calbiochem) in HBSS + 10 mM HEPES. Successful depolymerization was easily confirmed by eye as shown in figure 5.1.

5.1.2 The α-toxin receptor after actin disruption

To determine whether the disruption of the actin cytoskeleton has an effect on the confinement, we track single toxin receptors before and after the treatment with 5 µM Latrunculin B at 21 °C for 30 minutes in a medium without serum. If a change in confinement is detected, it suggests that the cytoskeleton plays a role in the observed confinement.

The mean values and standard deviation of the inferred diffusion coefficients are 0.18 ± 0.06 µm^2/s (N=58) for the α-toxin receptor before and 0.17 ± 0.07 µm^2/s (N=38) after the actin depolymerization at 21 °C. Again, we exploit the full distribution of measured values that is obtained by single-molecule tracking, which contains more information than just the mean value. The histogram for D_{Inf} before and after treatment is given in blue and red, respectively, in figure 5.6. The cumulative fraction plot of the two distributions is very similar. A KS-test determines a P-value of above 0.2, which does not lie below the threshold value of 0.05 for a detectable difference. The threshold value was obtained from simulations as explained in appendix B.4. Thus, the actin depolymerization does not change the diffusion coefficient of the α-toxin receptor.

Histograms for domain areas of the confinement zone are also shown in figure 5.6, where the data before treatment are shown in blue and those after treatment in red. The measured confinement areas before and after treatment with Latrunculin B are 0.44 ± 0.35 µm^2 and 0.34 ± 0.23 µm^2, respectively. They did not change beyond the error of the measurement. The KS analysis confirms that the distribution did not change.

The shape of the confining potential does not change either due to the depolymerization of the actin cytoskeleton. The determined spring constants before and after the treatment are given in the histogram in figure 5.6. The mean spring constant of the blue histogram before treatment is 0.28 ± 0.17 pN/µm. The mean value

for the red distribution after cytoskeleton depolymerization is 0.34 ± 0.27 pN/µm. The KS test shows that there is no detectable induced change in the spring constant distribution.

Overall, the depolymerization of the actin cytoskeleton by Latrunculin B does not induce a change in inferred diffusion coefficient D_{Inf}, domain area A and radial spring constant k_r, although the cells show a clear change in morphology as a response to the treatment.

5.1.3 The ϵ-toxin receptor after actin disruption

The behavior of the ϵ-toxin receptor with respect to the depolymerization of the cytoskeleton by 5 µM Latrunculin B at 21 °C for 30 minutes is summarized in figure 5.7. All trajectories were recorded on the same day to minimize a broadening of the variable distributions due to biological factors. Cytoskeleton depolymerization also does not affect the mode of motion and the receptors are still confined.

The mean value for the diffusion coefficient of the ϵ-prototoxin receptor before actin depolymerization is 0.18 ± 0.08 µm^2/s (N=42). After treatment the determined mean value is 0.16 ± 0.06 µm^2/s (N=65). The change in mean value is within the standard deviation. The KS test for the two distributions also confirms that there is no change due to the treatment. The measured P-value is larger than 0.2 and is not below the threshold P-value of 0.05.

The domain area before treatment is 0.37 ± 0.31 µm^2 and 0.38 ± 0.28 µm^2 after treatment with Latrunculin B. The distribution of measured areas is very similar, as the good overlap of the cumulative fraction plots indicates. The KS analysis gives a P-value of 0.15, which is above the threshold value of 0.1.

The confining potential is still of spring type and the measured spring constants before and after Latrunculin treatment are 0.32 ± 0.21 pN/µm and 0.34 ± 0.28 pN/µm, respectively. Again, a KS analysis shows that the distribution does not change with depolymerization. The P-value of the two distributions is larger than 0.2, which is above the threshold value of 0.05, indicating that there is no significant difference between the distributions.

Overall, the depolymerization of the actin cytoskeleton by Latrunculin B did not induce a change in inferred diffusion coefficient D_{Inf}, domain area A and radial spring constant k_r for the ϵ-prototoxin receptor, although the cells showed a clear change in morphology as a response to the treatment. A milder treatment with a Latrunculin B concentration of 500 nM gave the same result.

5.2 Lipid raft destabilization

This section investigates the effect of the lipid raft disaggregation on the mode of motion of the toxin receptors to determine whether the confinement is due to lipid domains. As mentioned in the introduction, saturated lipids can be more tightly packed and ordered than polyunsaturated lipids.

5.2.1 Cholesterol oxidase oxidizes cholesterol

Lipid rafts are considered to be clusters of certain types of lipids, that can be more densely packed, to form an ordered phase [79, 107, 229]. The packing is facilitated by cholesterol. When the membrane is depleted of its cholesterol, the small clusters have been shown to disassociate [74, 123]. Cholesterol is an abundant steroid metabolite that can be found in all eukaryotic cells. Cholesterol oxidase is an enzyme that catalyzes the chemical reaction of its substrates, which are cholesterol and oxygen. The products of the reaction are hydrogen peroxide and 4-Cholesten-3-one. Although the cholesterol is only oxidized it can be considered as extracted since it loses its ability to tightly pack lipids. The treatment of the whole cell does not cause the consumption of intracellular sterol pools. However, about 90 % of the cell's sterol is in the plasma membrane [230].

The action of the enzyme is not readily visible as in the case of the treatment with Latrunculin because treated cells do not undergo morphological changes. Thus, a calibration curve was recorded with a cholesterol quantization kit to verify the action of the cholesterol oxidase and quantify the amount of oxidized cholesterol. The results for different experimental conditions are given in Appendix A.6. For the work presented here, $27 \pm 2\,\%$ of the total cell cholesterol, accessible by cholesterol oxidase, was oxidized with an enzyme concentration of $20\,\text{U/mL}$ and an incubation time of 30 minutes at $21\,°\text{C}$. However, not all of the cholesterol is equally accessible to the enzyme for oxidation as a study by Patzer et al. showed [229]. This work demonstrated that much less cholesterol can be oxidized in artificial vesicles made up from cholesterol and either sphingomyelin, phosphatidylcholine or phosphatidylethanolamine, mimicking lipid rafts, when compared to oxidation in vesicles made up of cholesterol and phosphatidylserine, mimicking the unordered lipid phase. This implies that, although cholesterol is oxidized, it is not oxidized at the same rate or percentage from the different lipid phases of the membrane, i.e. cholesterol oxidation in lipid rafts in the cell membrane is slower than oxidation in the unordered phase. This means that the oxidized cholesterol in the lipid raft phase is most probably lower than $27\,\%$. Additionally, it should be noted that the product of the enzymatic reaction, cholestenone, has been shown to actually strongly inhibit domain formation in model membranes [231].

5.2.2   The α-toxin receptor after cholesterol depletion

The most striking effect of the cholesterol depletion is that, for many receptors, the confinement is reduced and even disappears. Taking advantage of the single-molecule technique, we can monitor a single receptor during the extraction of cholesterol from the membrane. Figure 5.2 shows the trajectory of the *same* α-toxin receptor before incubation with cholesterol oxidase in blue and after a 10-minute incubation in red. The zoom into the trajectory reveals that the receptor confinement zone has drastically increased after 10 minutes of incubation.
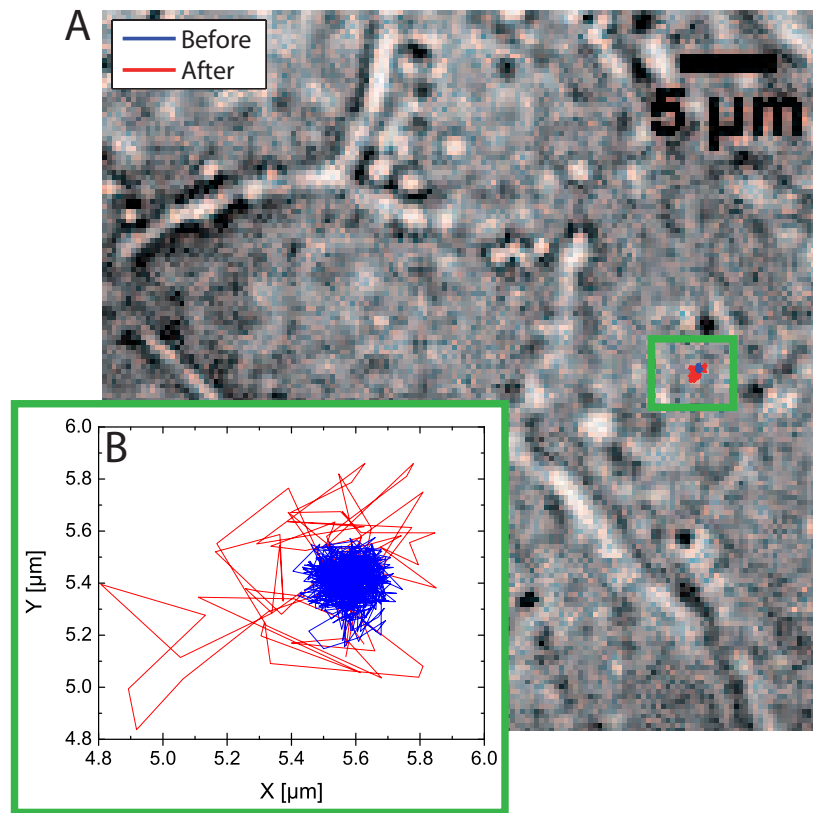
Figure 5.2: Trajectory of a single α-toxin receptor during incubation with cholesterol oxidase. The blue trajectory is the motion of the receptor before the incubation and the red trajectory was recorded 10 minutes after the beginning of the incubation. In the white light image the cell contours of the confluent MDCK cells are visible along with some organelles (circular objects). The zoom into the trajectory in b) shows that the area explored by the receptor increased dramatically from $0.04\,\mu m^2$ to $1.04\,\mu m^2$. After 5 minutes of incubation the domain area is $0.14\,\mu m^2$.

The mode of motion of the receptor can be deduced from the MSD plot shown in figure 5.3. The blue plot is the MSD curve from figure 5.2 before the incubation and the red plot was recorded ten minutes after the incubation start. The black

trace shows the MSD plot after 5 minutes of incubation. The blue and black curves are scaled up by a factor of 10 to compare them more easily on the same graph to the MSD curve after 10 minutes. The MSD plots of the receptor trajectory before and after 5 minutes of incubation show the characteristic plateau for motion in a confined zone. After 10 minutes, the plateau has disappeared and the motion appears to be lightly subdiffusive. This demonstrates that there is a transition in the receptor's mode of motion from confined to Brownian or subdiffusive due to cholesterol oxidation.
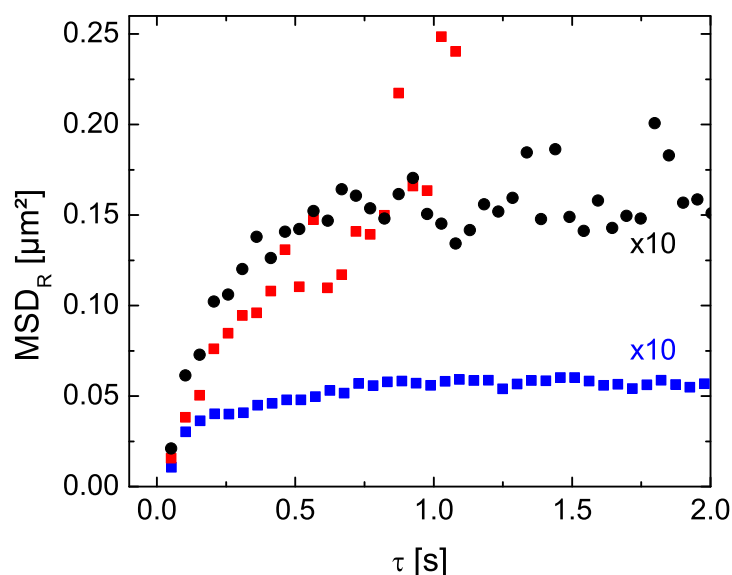
Figure 5.3: MSD plot corresponding to a single α-toxin receptor trajectory during cholesterol oxidation. The blue plot is the MSD plot of the receptor trajectory in figure 5.2 before the incubation and the red plot was recorded ten minutes after the beginning of the incubation. The black trace shows the MSD plot of the receptor trajectory after 5 minutes of incubation. These two curves are scaled up by a factor of 10 to compare them more easily to the MSD curve after 10 minutes. The mode of motion of the receptor before and after 5 minutes of incubation show the characteristic plateau for motion in a confined zone. After 10 minutes, the plateau has disappeared and the motion appears to be Brownian or lightly subdiffusive.

The diffusion coefficient increases with the level of extracted cholesterol. The inferred diffusion coefficients for 0, 5 and 10 minutes of incubation with cholesterol oxidase are $0.087 \pm 0.006 \mu\mathrm{m}^2/\mathrm{s}$, $0.09 \pm 0.01 \mu\mathrm{m}^2/\mathrm{s}$ and $0.21 \pm 0.05 \mu\mathrm{m}^2/\mathrm{s}$, respectively. Furthermore, the posteriori probabilities for the diffusion coefficient D_{Inf} before and after 10 minutes of incubation do not overlap as can be seen in

figure 5.4 a). The confinement factor u decreased from 0.1 to 0.01 even though the diffusion coefficient increased. This means that the change in the area of the confining zone was more drastic. The inferred potentials reveal that the spring constant decreased from $1.2 \pm 0.2\,\text{pN/µm}$ to only $0.08 \pm 0.05\,\text{pN/µm}$. The more strongly confined receptors after cholesterol oxidation were determined to still be spring-like, but the potential of the fraction that is exhibiting almost Brownian motion is more difficult to classify and no potential might exist.
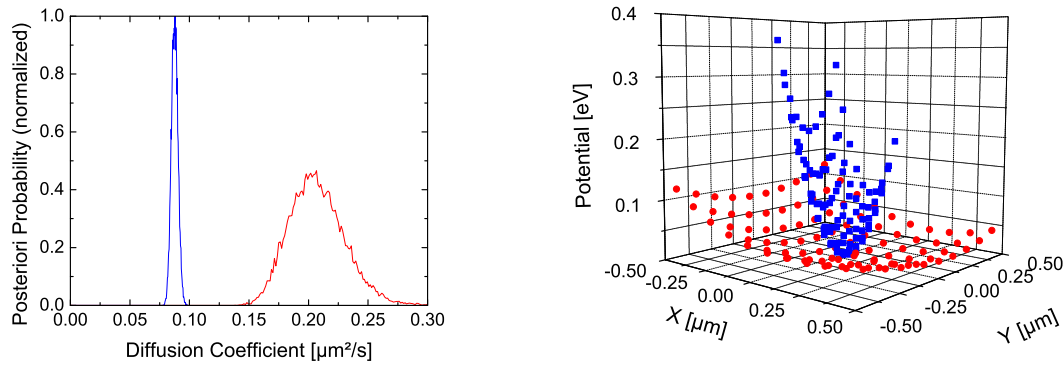
(a) Posteriori probability for the diffusion coefficient D_{Inf} before and after 10 minutes of cholesterol extraction.

(b) Confining potential before (blue) and after 10 minutes of cholesterol oxidation (red).

Figure 5.4: Effects of cholesterol oxidation on D_{inf} and on the confining potential of a single α-toxin receptor. Blue indicates the properties before and red after 10 minutes of incubation with $20\,\text{U/mL}$ cholesterol oxidase. The posteriori probabilities for D_{Inf} of the same receptor before and after cholesterol oxidation do not overlap and the maximum value has increases from $0.087 \pm 0.006\,\text{µm}^2/\text{s}$ to $0.21 \pm 0.05\,\text{µm}^2/\text{s}$ after incubation. The confining potential is much weaker after incubation. The spring constant decreases from $1.2 \pm 0.2\,\text{pN/µm}$ to only $0.08 \pm 0.05\,\text{pN/µm}$.

The same decrease in confinement was observed for the entire distribution of measured receptors as summarized in figure 5.8. The measured mean diffusion coefficient D_{Inf} of α-toxin receptors is $0.15 \pm 0.12\,\text{µm}^2/\text{s}$ (N=32) before cholesterol extraction. This value agrees with the value determined for the same receptor before treatment with latrunculin B. After oxidation of $27 \pm 2\,\%$ of the cell's cholesterol by adding $20\,\text{U/mL}$ cholesterol oxidase for 30 minutes, the mean diffusion coefficient is $0.16 \pm 0.08\,\text{µm}^2/\text{s}$ (N=42). The cumulative fraction plot of the two distributions shows, just like the histogram, that there are more receptors with higher diffusion coefficients, while other receptors still show diffusion values as before extraction. The P-value of 0.01 of the KS analysis is below the threshold

P-value, which means that, although the mean values are similar, the distribution of values has changed.

The mean domain area increases with treatment from $0.45 \pm 0.49\,\mu m^2$ to $0.71 \pm 0.86\,\mu m^2$. The form of the distribution does not change much, however, it is shifted to larger domain areas after cholesterol oxidation. The KS analysis gives a P-value of 0.01, which is below the threshold P-value of 0.05. The average increase in domain area is 37 %.

Much like the diffusion coefficient, the inferred k_r values for the spring-like confining potential show the presence of receptors that are much less confined after cholesterol extraction. There is still a fraction that is confined just as before treatment. The mean values and standard deviation of the distribution, before and after cholesterol extraction, are $0.38 \pm 0.28\,pN/\mu m$ and $0.24 \pm 0.16\,pN/\mu m$, respectively. The average decrease in the spring constant is 37 %. The new less confined fraction leads to a P-value of much less than 0.01, which is well below the threshold P-value of 0.05. The confining potential of the GPI-anchored α-toxin receptor is thus cholesterol dependent. This result is in agreement with the observation that GPI-anchored proteins have been found in lipid rafts [102, 121–123], which are stabilized by cholesterol.

5.2.3   The ϵ-toxin receptor after cholesterol depletion

The behavior of the ϵ-toxin receptor also changes due to the extraction of cholesterol by cholesterol oxidase on the single molecule level. Figure 5.5 shows the same receptor before and during an incubation with $20\,U/mL$ cholesterol oxidase at $21\,°C$. The diffusion coefficient increases from $0.189 \pm 0.006\,\mu m^2/s$ to $0.256 \pm 0.009\,\mu m^2/s$ after 5 minutes and to $0.275 \pm 0.009\,\mu m^2/s$ after 10 minutes. The area increases from $0.89\,\mu m^2$ to $11.94\,\mu m^2$ after 10 minutes. The spring constant decreases from initially $0.11 \pm 0.01\,pN/\mu m$ to $0.021 \pm 0.004\,pN/\mu m$ after 10 minutes of cholesterol extraction. Note that there is a surprising difference in response speed to the treatment between diffusion coefficient and domain area. The diffusion coefficient has already increased after five minutes, while the receptor is still confined to the small domain. The domain size increases only after 10 minutes.

Overall, the inferred diffusion coefficient D_{Inf} was measured to be $0.29 \pm 0.27\,\mu m^2/s$ and $0.38 \pm 0.41\,\mu m^2/s$ before and after extraction, respectively, of 27 ± 2 % of the cell's cholesterol. The histogram of the measured values is given in figure 5.9. The cumulative fraction plot shows a few faster diffusing receptors, but the KS analysis reveals that the difference between the two distributions is not large enough to be significant.
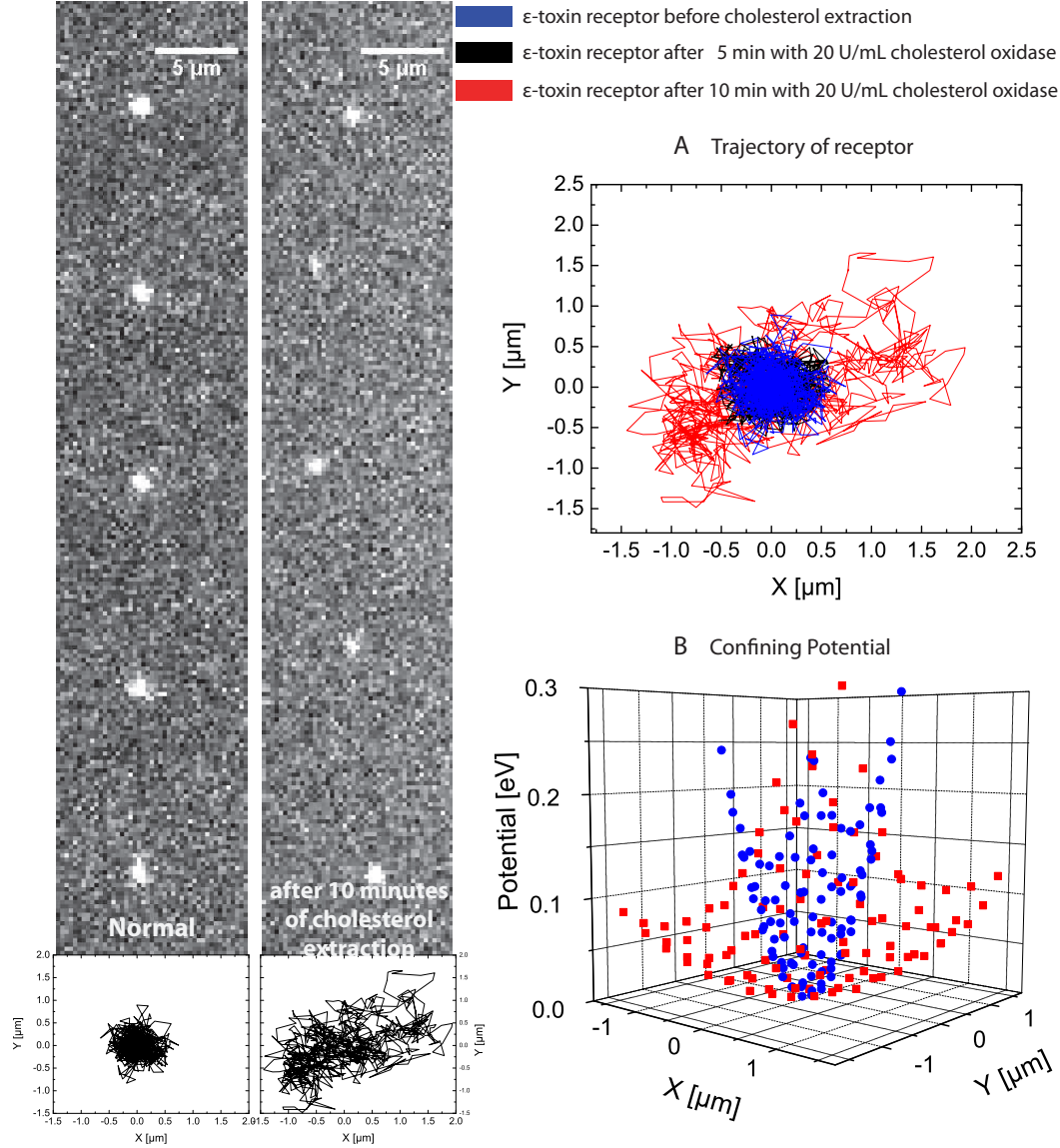
Figure 5.5: Effect of cholesterol extraction on a single ϵ-toxin receptor. The figure shows on the left a series of raw images of the labeled receptor together with the determined trajectories. The difference in confinement area A is clearly visible after 10 minutes of incubation. The area increases from $0.89\,\mu m^2$ to $11.94\,\mu m^2$. The diffusion coefficient increases from $0.189 \pm 0.006\,\mu m^2/s$ to $0.256 \pm 0.009\,\mu m^2/s$ after 5 minutes and to $0.275 \pm 0.009\,\mu m^2/s$ after 10 minutes. The spring constant k_r decreases from initially $0.11 \pm 0.01\,pN/\mu m$ to $0.021 \pm 0.004\,pN/\mu m$ after 10 minutes of cholesterol extraction. The motion of the receptor is dependent on the amount of cholesterol in the membrane.

The average area of confinement however increases by 57 % from $0.36\pm0.45\,\mathrm{\mu m}^2$ to $0.83 \pm 0.42\,\mathrm{\mu m}^2$ after cholesterol extraction. The increase is due to a shift in the entire distribution of measured values and not only to the appearance of more receptors that diffuse in larger domains. The KS analysis gives a P-value of less than 0.01, which is well below the threshold P-value of 0.05 and thus significant.

Confinement potentials show the most drastic change. The average spring constant decreases from $0.25 \pm 0.16\,\mathrm{pN/\mu m}$ to $0.10 \pm 0.07\,\mathrm{pN/\mu m}$ after the cholesterol is extracted. While some strongly confined receptors remain, most receptors are now confined very weakly. The KS analysis gives a P-value of much less than 0.01, which is below the threshold value of 0.05.

Both the α- and the ϵ-toxin receptors show a reduction in confinement and an increase in diffusion coefficient after the treatment with cholesterol oxidase. As mentioned above, the response to the treatment for the α-toxin is consistent with the literature since GPI-anchored receptors have been shown to localize into lipid rafts [102,121–123]. In chapter 4 we have seen that the α- and ϵ-toxin receptors are confined to domains of similar size and diffuse with a similar diffusion coefficient and we invoked that both toxin receptors might be confined to the same confining domain type. Together with the observed reduction in confinement after cholesterol oxidase treatment, we have further evidence that the ϵ-toxin is also confined into cholesterol stabilized raft domains as is the α-toxin GPI-anchored receptor.
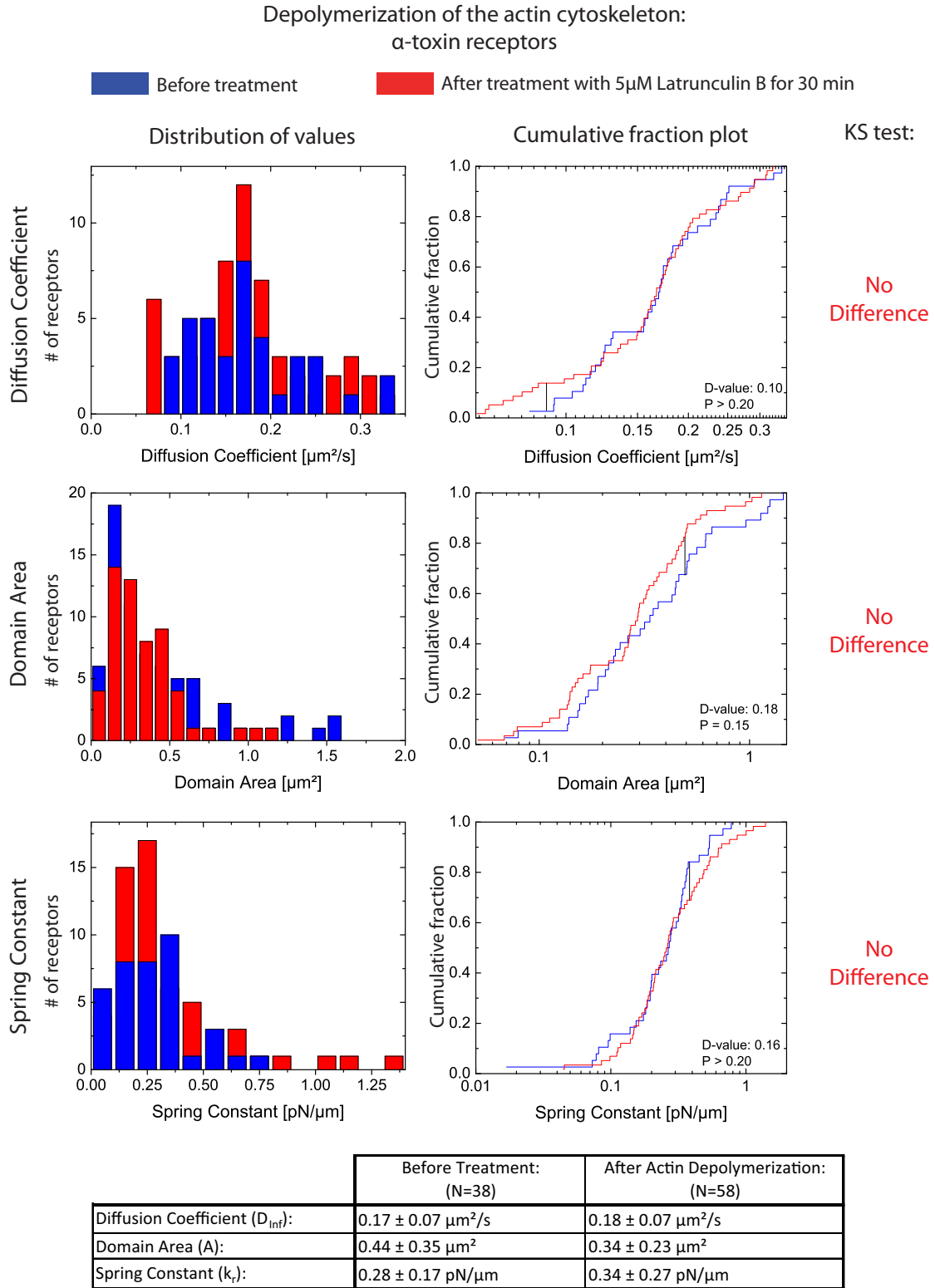
Figure 5.6: Effect of actin depolymerization on the motion of α-toxin receptors. Cells were treated with 5 µM Latrunculin B at 21 °C for 30 minutes. No significant differences are observed in diffusion coefficient, domain area and spring constant before and after treatment.
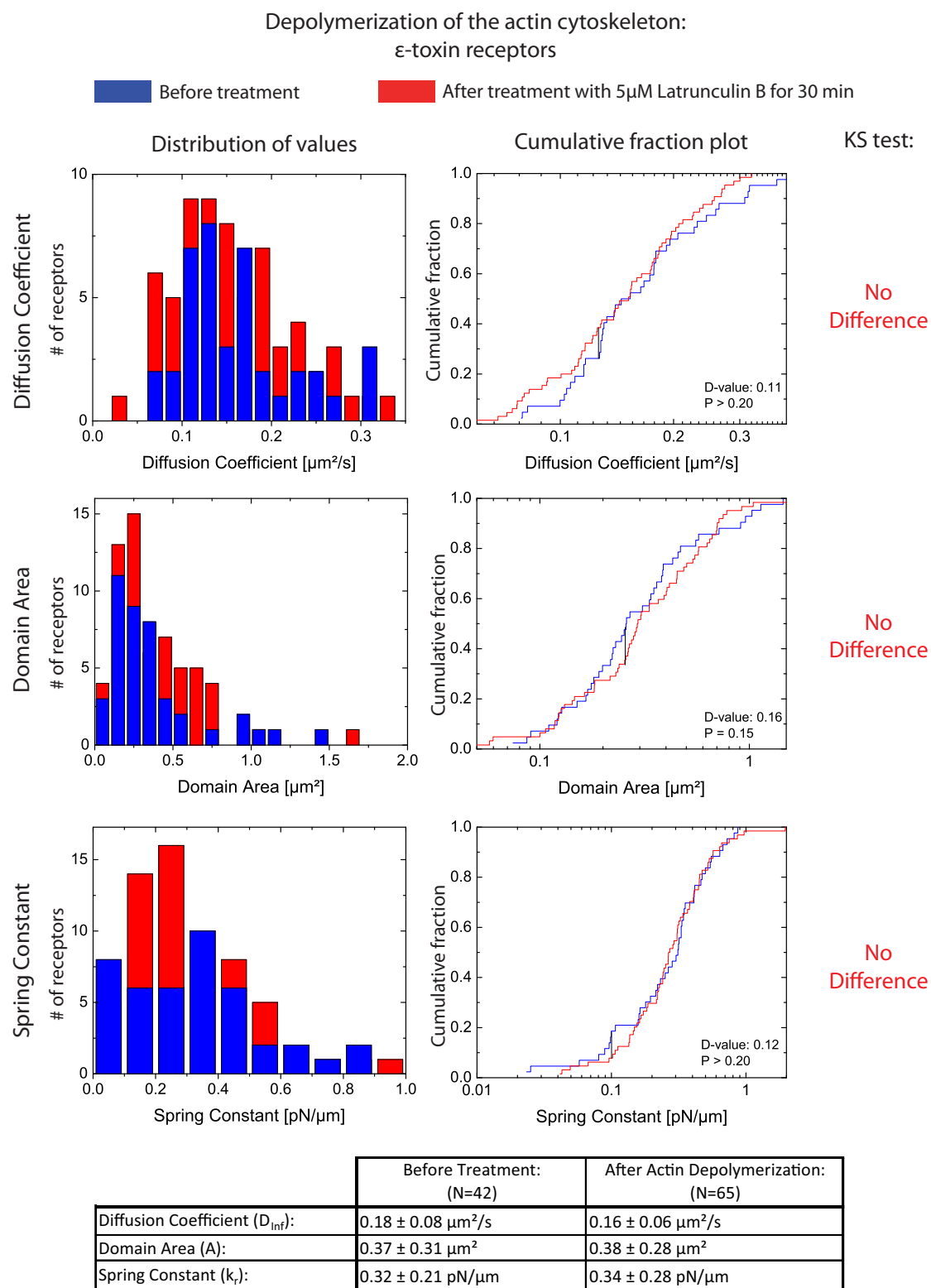
Figure 5.7: Effect of actin depolymerization on the motion of ϵ-toxin receptors. Cells were treated with 5 µM Latrunculin B at 21 °C for 30 minutes. No significant differences are observed in diffusion coefficient, domain area and spring constant before and after treatment.
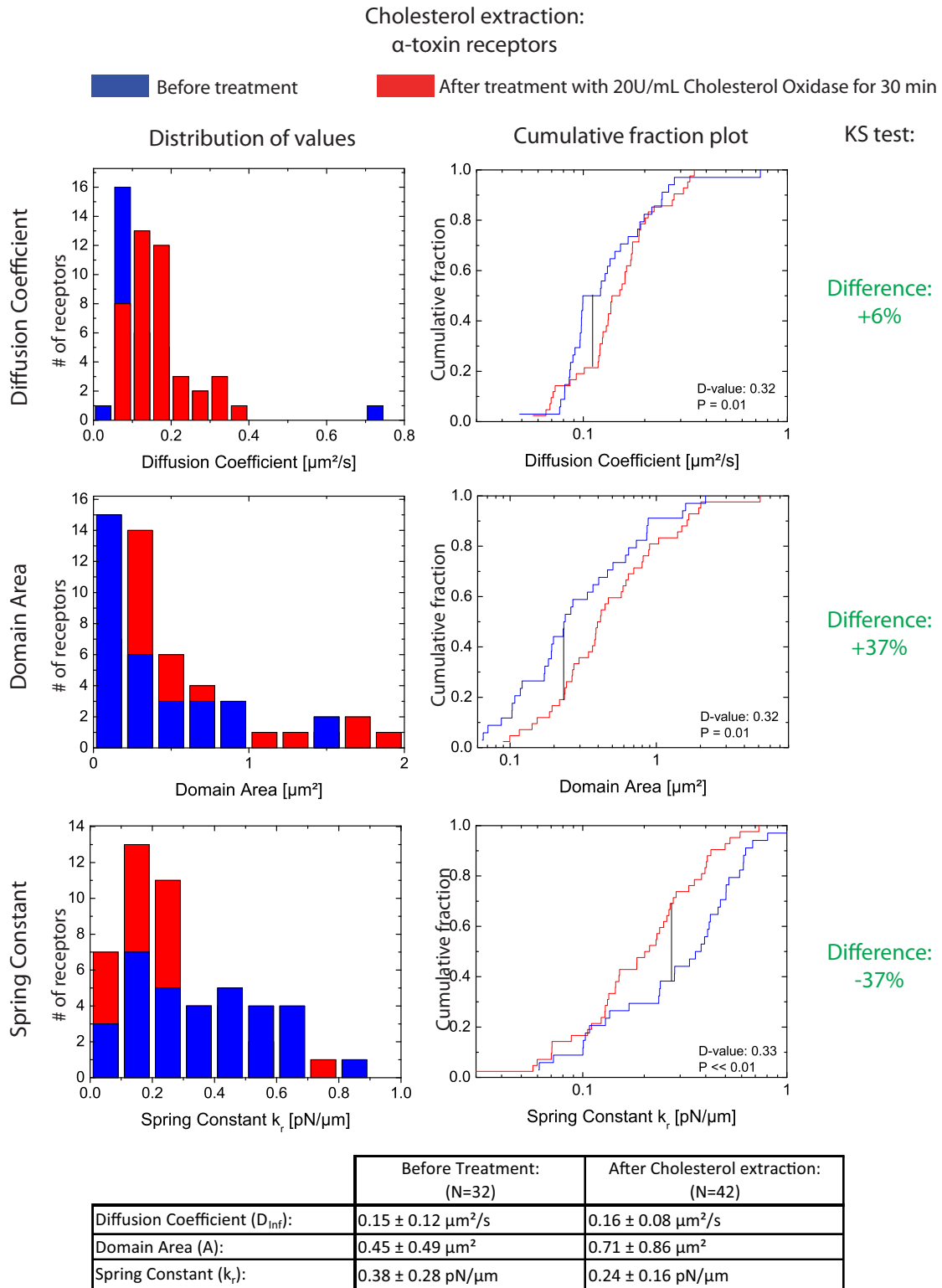
Figure 5.8: Effect of cholesterol extraction on the motion of α-toxin receptors. Cells were treated with $20\,\mathrm{U/mL}$ cholesterol oxidase at $21\,^\circ\mathrm{C}$ for 30 minutes to oxidize $27 \pm 2\,\%$ of the cell's cholesterol. Significant differences are observed in diffusion coefficient, domain area and spring constant before and after treatment.
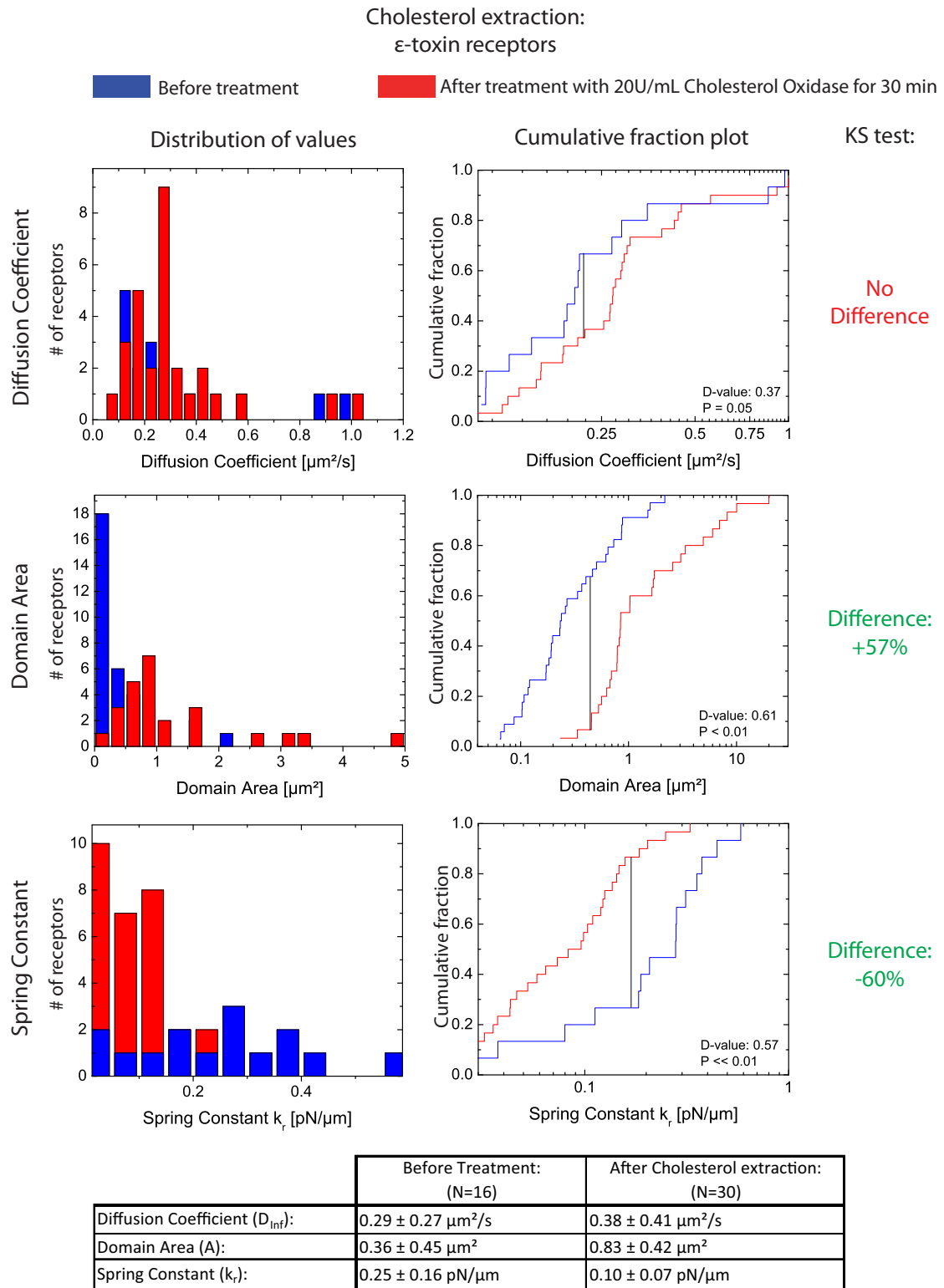
Figure 5.9: Effect of cholesterol extraction on the motion of ϵ-toxin receptors. Cells were treated with $20\,\mathrm{U/mL}$ cholesterol oxidase at $21\,^\circ\mathrm{C}$ for 30 minutes to oxidize $27 \pm 2\,\%$ of the cell's cholesterol. Significant differences are observed in domain area and spring constant before and after treatment.

5.3   Effects of drugs on toxicity

Single-molecule experiments have shown that the localization of single α- and ϵ-toxin receptors is cholesterol dependent. This section will examine the effects of both actin depolymerization and cholesterol extraction on the toxicity of the toxin. The toxicity is a measure of the behavior of many toxin receptors and is thus an ensemble measurement. It is a complementary experiment that can confirm the tendencies observed in single-molecule data where the statistics is necessarily limited.

Figure 5.10 shows the results of an MTT assay for the toxicity of non labeled α- and ϵ-toxin on an MDCK cell culture after a 30-minute incubation with the toxin. The green line represents the toxicity of the toxin after actin depolymerization due to prior treatment with 500 nM Latrunculin B for 30 minutes. The blue and red curves show the toxicity after cholesterol extraction after a prior 30-minute incubation with 1 or 20 U/mL cholesterol oxidase, respectively. The toxicity is compared to that for cells that were not treated by any drug previously (data shown in black).
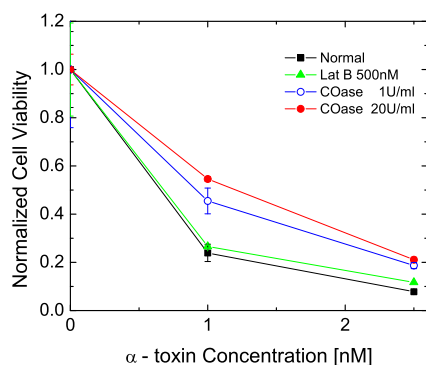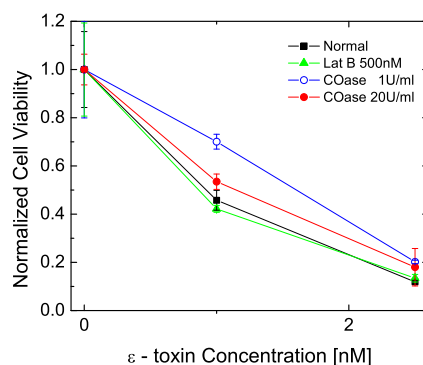
(a) MTT assay for the toxicity of α-toxin.   (b) MTT assay for the toxicity of ϵ-toxin.

Figure 5.10: MTT assay for the toxicity after biochemical treatment of MDCK cells. Non-treated cells are shown in black for reference. The toxicity after actin depolymerization by 500 nM Latrunculin B is given in green. The blue and red curves show the toxicity measured after a 30-minute incubation with 1 or 20 U/mL cholesterol oxidase, respectively. Cells were incubated with the toxin for 30 minutes after the prior drug treatment.

As expected, the data show that less cells survive as the toxin concentration increases. Prior treatment with Latrunculin B to depolymerize the actin cytoskeleton does not alter the toxicity of the toxin at any concentration. This observation is consistent with the results from single-receptor tracking. There, actin depoly-

merization did not alter the behavior of the receptor motion. Prior cholesterol extraction of $27 \pm 2\,\%$ of the cell's cholesterol leads to a decrease in toxicity for both the α- and ϵ-toxin. This bulk observation confirms the changes due to cholesterol extraction that were observed at the single-molecule level. Less confinement will decrease the probability of pore assembly from toxin monomers and thus decrease toxicity. The decrease in toxicity due to cholesterol extraction has also been observed in MTT assays by others [232].

5.4   Temperature effects

5.4.1   Temperature influences the diffusion coefficient

The temperature of a system influences its energy. The Einstein relation gives the relation between temperature T and diffusion coefficient D

$$D = k_B T b \tag{5.1}$$

where k_B is Boltzmann's constant and b the mobility. For a sphere in an unbounded fluid, this equation transforms into the well known Stokes-Einstein formula

$$D = \frac{k_B T}{6\pi\eta R_h} \tag{5.2}$$

where R_h is the hydrodynamic radius of the diffusing molecule and η is the viscosity of the membrane domain [233]. A more adapted equation to explain the diffusion coefficient of transmembrane proteins in a thin membrane is the Saffman-Delbrück equation [234]. However, in both equations, the Einstein relation holds and as the temperature increases, so should the diffusion coefficient. Diffusion coefficients of membrane proteins in live cells have been shown to increase with temperature [163]. Other results are in sharp contrast and show that diffusion coefficients are not affected by temperature under normal conditions [160, 161].

5.4.2 Temperature can influence the state of raft aggregation

We have already determined that the confinement of the α- and ϵ-toxin receptors is cholesterol dependent. In a steady-state view, these domains are formed due to interactions between lipids, cholesterol and proteins and also depend on the temperature. Several groups have studied the formation of lipid ordered phases in model membrane systems [25, 110, 113, 116]. Phase diagrams have been recorded for ternary systems of multi-lamellar vesicles containing palmitoylsphingomyelin (PSM), palmitoyloleoylphosphatidylcholine (POPC) and cholesterol [108]. The study shows the spontaneous formation of lipid ordered phases with a disordered phase above $0\,°C$ and for a PSM concentration within a certain range. Both phases can be in a liquid-liquid coexistence. Increasing the temperature above $\sim 35°C$ shows that the ordered phase is lost. In such a picture, the increase in temperature could alter the architecture of the membrane and the confinement of the receptor. A reduction in confinement domain sizes with temperature has been observed in muscle cells [36]. Another study suggests a transition temperature between $25 - 37\,°C$ in MDCK cells, for the percolation threshold crossing to occur [193, 235]. Below $25\,°C$, an isolated non-raft phase is dispersed in a raft phase. Above the percolation threshold, the raft phase is dispersed in the non-raft phase. Raft-associated proteins that cannot leave rafts would be confined above the percolation threshold.

In s dynamic picture where cell membranes are not at thermal equilibrium, the natural phase separation into ordered and unordered phase is likely to be modulated by the presence of proteins and their state of clustering as well as by the continuous trafficking of lipids to and from the plasma membrane and by the membrane asymmetry [99, 111].

5.4.3 The α-toxin receptor at different temperatures

To investigate the influence of the temperature on our system experiments were performed at $21\,°C$ and $37\,°C$. The diffusion coefficients of the α-toxin receptor were measured on different days. Receptors are still confined at $37\,°C$ and the results for the extracted diffusion coefficients, domain areas and spring constants can be found in figure 5.11. The mean diffusion coefficient does not change after the increase in temperature from $21\,°C$ to $37\,°C$. The mean diffusion coefficient is $0.16 \pm 0.09\,\mu m^2/s$ at room temperature and $0.18 \pm 0.07\,\mu m^2/s$ at $37\,°C$. A KS-test shows that the distribution of values is not altered. The same is observed for the domain area. The receptor is confined to zones of $0.4 \pm 0.4\,\mu m^2$ at $21\,°C$ and to zones of $0.4 \pm 0.3\,\mu m^2$ at $37\,°C$. The average spring constant of the spring-like confining potential is $0.3 \pm 0.2\,pN/\mu m$ for both temperatures.

5.4.4 The ϵ-toxin receptor at different temperatures

The increase in temperature from 21 °C to 37 °C does not alter the confined motion of the ϵ-toxin receptor, as shown in figure 5.12, except for the stiffness of the confining potential. The diffusion coefficients at room temperature (21 °C) and at 37 °C are $0.16 \pm 0.14 \, \mu m^2/s$ and $0.13 \pm 0.05 \, \mu m^2/s$, respectively. The KS analysis shows no significant change in the distribution of the measured values. The domain area does not change as a function of temperature and is measured to be $0.4 \pm 0.4 \, \mu m^2$ and $0.4 \pm 0.3 \, \mu m^2$ for low and high temperature, respectively. The average value of the spring constant, however, shows a decrease of 50 % from $0.6 \pm 0.7 \, pN/\mu m$ at 21 °C to $0.3 \pm 0.2 \, pN/\mu m$ at 37 °C. The shift, which is confirmed by the KS analysis, is due to a reduction in very strongly confined receptors. No receptor is confined in a potential with spring constant higher than $0.8 \, pN/\mu m$ at 37 °C, as can be seen in the histogram in figure 5.12.

The diffusion coefficient of neither the α- nor the ϵ-toxin receptor is altered by the increase in temperature, although the Einstein relation (eqn. 5.1) predicts a drop in diffusion coefficient by $\sim 40\%$. This observation is in conflict with those made for a H-Ras membrane-anchor in the cytoplasmic leaflet of the cell membrane in reference [163], but it agrees with findings in references [160, 161]. The latter authors argue that the lipid ordered phase does not condense further as the temperature is decreased due to the presence of cholesterol.

The receptor confinement persists at the physiological temperature of 37 °C. The confinement domain area does not depend on temperature, in contrast to what was reported in reference [36]. Furthermore, we did not observe an inversion from a distribution of rafts in a non-raft phase to a distribution of a disordered phase in a raft phase for the temperature range investigated here in contrast to what was reported in references [193, 235]. Possible reasons for this disagreement may be that the disassociation of the raft domains confining the toxin receptors occurs at higher temperatures or that the rafts are not in thermal equilibrium, as suggested in [99, 111].
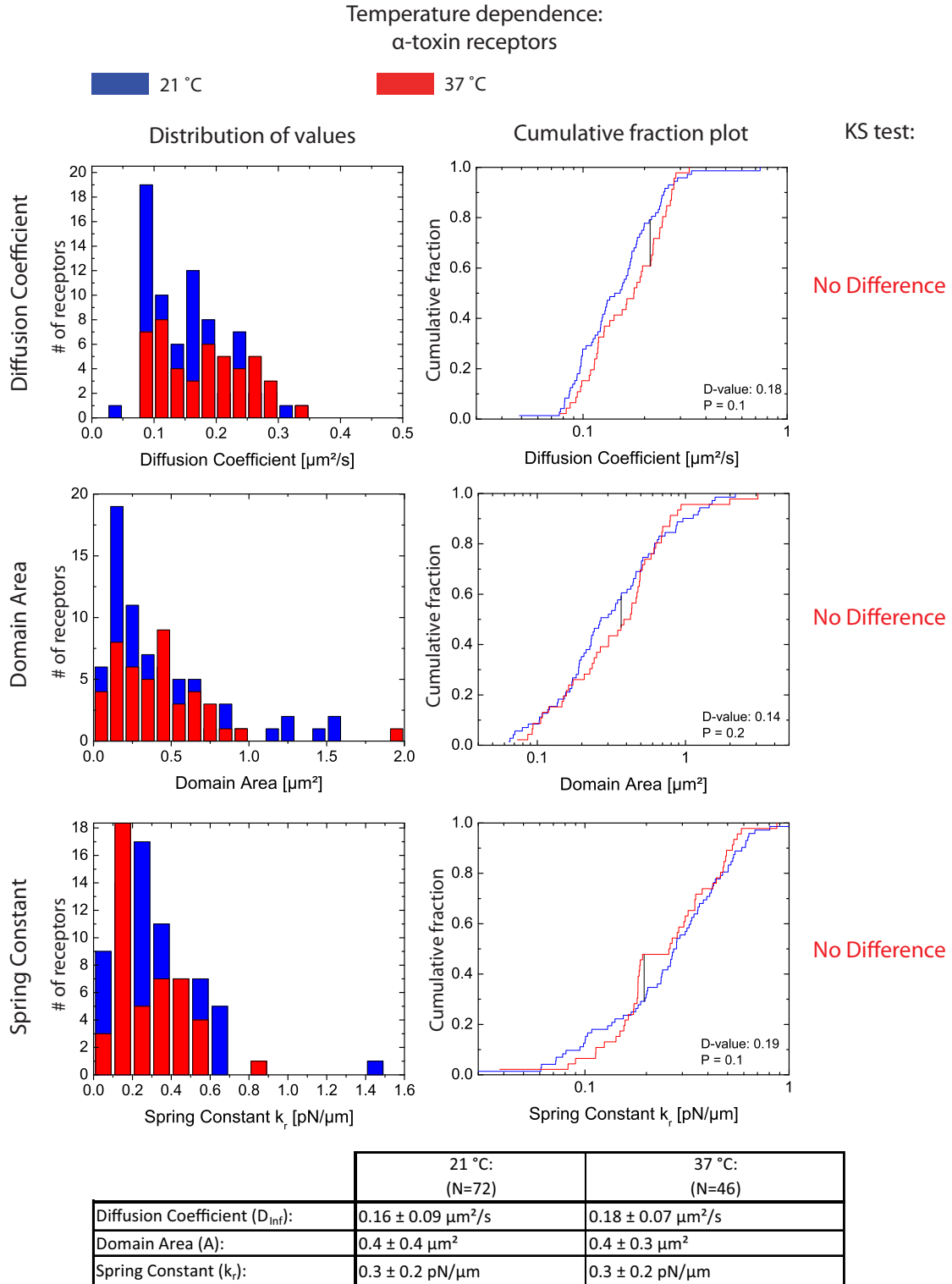
Figure 5.11: Effect of temperature on the motion of α-toxin receptors. Trajectories were recorded at 21 °C (blue) and 37 °C (red).
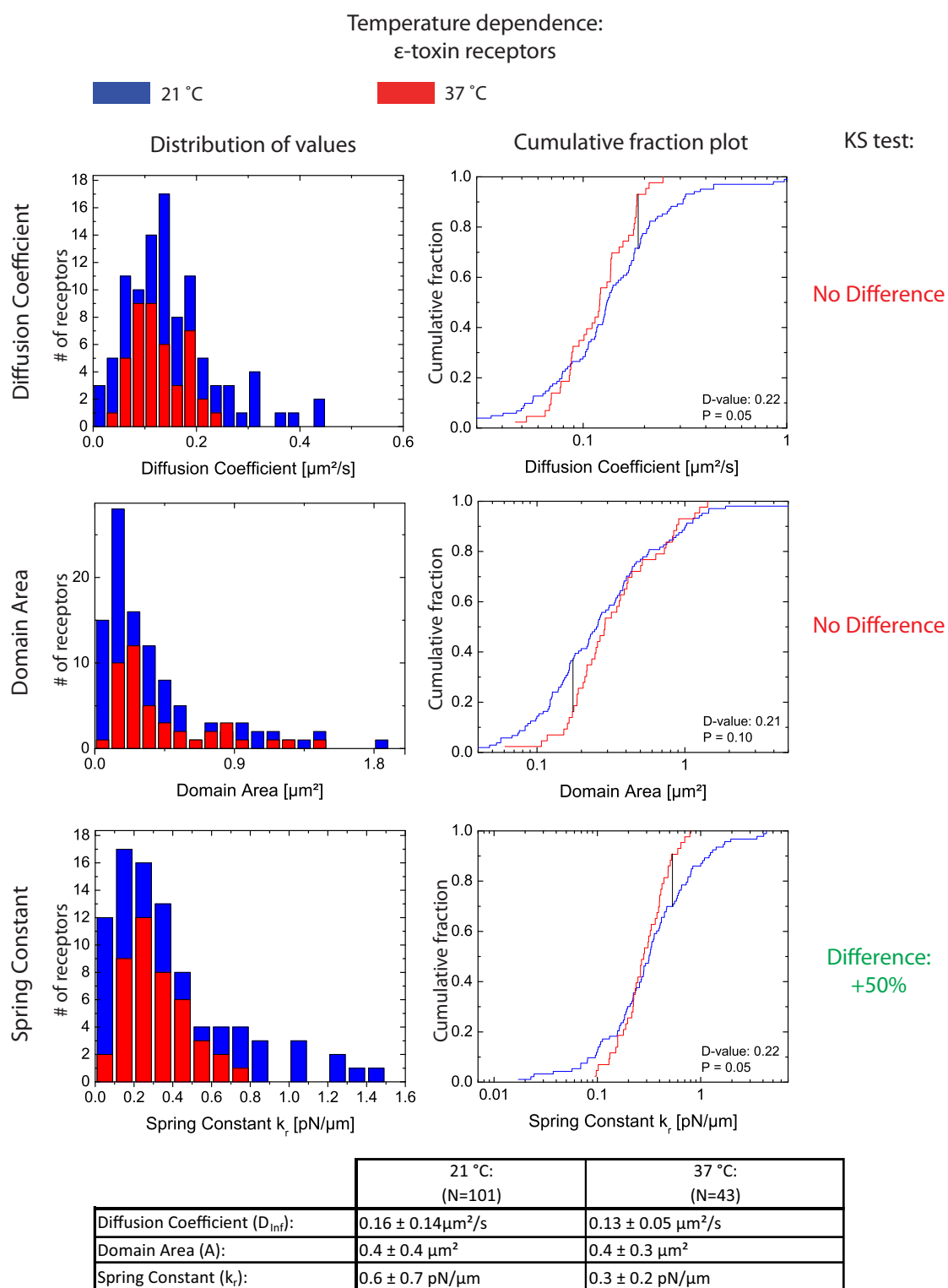
Figure 5.12: Effect of temperature on the motion of ϵ-toxin receptors. Trajectories were recorded at 21 °C (blue) and 37 °C (red).

5.5   A model for the confinement

A model that can explain the confinement in cholesterol stabilized raft domains
can now be built from the observed evidence:

- Both toxin receptors are confined in domains of equal size, that exert a
  spring-like potential on the receptor.

- GPI-anchored proteins have been shown to localize into lipid rafts [102, 118,
  121–123, 127, 128].

- The diffusion coefficient of both receptors within the domain does not vary
  significantly.

- The diffusion coefficient of both receptors is similar to each other.

- Receptors do not leave the confining zones, except for some rare hopping
  events.

- The domains drift in the membrane, but based on their speed, they are not
  actively transported.

- Domains do not undergo random motion, but are dragged along by the cell
  membrane.

- The actin cytoskeleton does not seem to be directly confining the receptors.

- Cholesterol depletion of the membrane decreases the confinement of both
  receptors.

- Toxicity is reduced after cholesterol depletion but not after actin depolymer-
  ization.

- A change in temperature does not alter the diffusion coefficient or the mode
  of motion, which is still confined at $37\,^{\circ}$C.

- The area of the confining domains does not depend on temperature.

- In the case of the ϵ-toxin receptor, there are less potentials with strong spring
  constants at $37\,^{\circ}$C.

The observations show that receptors are confined due to either a special lipid
phase or a protein cluster that is stabilized by cholesterol. The cytoskeleton does
not seem important in stabilizing the confining zone or potential. This implies
that the observed spring-like confining potential is caused by the lipid phase or
protein cluster. A confining spring potential has been observed before for a protein
that was directly linked to the cytoskeleton [86], however this is not the case for

the receptor of the α-toxin.

The non-random motion of these domains and the fact they are often dragged along with the bulk movement of the membrane indicates some interaction with the cytoskeleton or fixed protein clusters in the membrane that act as barriers. The observation that treatment with Latrunculin B did not lead to free motion of the entire domain does not exclude direct domain interactions with the cytoskeleton, since certainly not all actin was depolymerized. Lipid rafts have been shown to contain cytoskeletal and adhesion proteins. Identified proteins include actin, myosin, vinculin, cofilin, cadherin, filamin and ezrin [236–240]. Such proteins, if colocalized with the toxin receptor domain could pin-down the confining domain to the cytoskeleton.

The single-molecule tracking experiments with actin depolymerization and cholesterol extraction lead to the conclusion that the confinement is aided by cholesterol which, in terms of membrane models that were introduced in chapter 1, is consistent with the lipid raft model and the protein cluster model. However, because both receptors behave similarly and because the α-toxin receptor is known to be localized in lipid rafts, we assume that the confining domains are lipid rafts. We prefer to use refer to them as cholesterol stabilized domains or rafts because the difference between protein clusters and lipid rafts is not clearly defined and the clustering of proteins also depends on their interaction with surrounding lipids. Proteins that cluster can be surrounded by a thin shell of an ordered lipid phase and cholesterol due to surface tension [111, 134–136, 241, 242]. Extraction of cholesterol could destabilize this shell and lead to the disaggregation of the protein cluster. A change in confinement with cholesterol extraction is not predicted by the picket and fence model, nor by crowding effects. Tetraspanin complexes, which are complexes of multiple tetraspanin proteins with their partner proteins, are also resistant to cholesterol extraction [243, 244] ruling out a tetraspanin-web as reason for confinement. The results of the MTT assay on toxicity further underline the fact that the confining domains are either a cholesterol-stabilized lipid phase or a protein cluster that is stabilized by cholesterol.

However, the long residence time and the large size of these domains is inconsistent with the lipid raft model. As cited before, lipid rafts are thought to be small ($10 - 200\,\mathrm{nm}$) and temporally short lived [26, 111, 245]. Nevertheless, small rafts are believed to coalesce to form larger, more stable domains upon ligand binding [?, ?, 123, 144]. Such stabilized rafts are thought to function as signaling platforms [139, 246, 247]. Considering that we label the receptor with a toxin that binds to its receptor, it is very plausible that the imaged confining domain is actually induced by the ligand binding, rendering the domain size and long term stability consistent with the lipid raft model. Such long residence times in the

confining domains and their large sizes are also consistent with protein clusters. The domains attributed to the picket and fence model are smaller and much lower residence times are involved, which is inconsistent with our data [96, 153, 158, 248]. However, we cannot exclude that picket and fence type domains exist inside our cholesterol-stabilized domains involving residence times shorter than the acquisition time.

The hypothesis that the aggregated confining lipid domains or protein clsuters are actively maintained by the cell can also explain the absence of change in confinement following a change in temperature. Domain characteristics should depend on temperature if in thermal equilibrium, however, this does not hold for a cell far from equilibrium that is actively maintaining the domains [99].

We have thus determined that the confining domain is a raft of lipids or a protein cluster mediated by cholesterol. However, an explanation for the spring-like potential still remains to be found. Besides binding to the cytoskeleton, another mechanism can create a force field: line tension, which is a force that exists at the boundary of two phases, which could be a lipid ordered and unordered phase. It is a measure of the energy required to create the phase boundary. This force is one of the driving forces for spontaneous lipid raft formation [110, 111]. The hydrophobicity of a protein is determined by its chemical structure and it is important how large the hydrophobic patch is. The larger the hydrophobic mismatch, and thus the larger the difference in membrane thickness between the ordered and the disordered phase, the greater the line tension [112]. The line tension, which is also the cost of energy required to maintain the phase separation, can be lowered by bending or tilting of the lipids that are close to the boundary [110]. Furthermore, a lipid gradient could exist in cell membranes to gradually reduce the hydrophobic mismatch between ordered and unordered phase. The following facts speak in favour of this hypothesis: Phospholipids harboring two saturated fatty acyl chains, which are generally thought to make up the lipid ordered phase, are normally low in concentration ($< 10 \, \text{mol\%}$) in cells and not enough to make up all the lipids in lipid rafts [111, 249, 250]. In addition, the plasma membrane of living eukaryotic cells consists of up to 500 different lipid species [99–101, 111]. Finally, lipidomic studies have shown that most lipids in rafts contain at least one unacylated chain [249, 250]. Based on this, a hydrophobic gradient can exist in large rafts that contain many different lipid species due to variations in thickness and composition.

To demonstrate this, I performed a simulation, containing three types of lipids or proteins that have different hydrophobic mismatch with respect to the matrix species in which they are embedded (Figure 5.13). The matrix species is represented in blue, while the green, yellow and red species have increasing hydrophobic

mismatch with the blue matrix species. If the randomly dispersed species, as shown in figure 5.13 a), are left to reorganize in order to minimize the energy of the system, clusters appear as in image 5.13 b). Further optimization then causes the clusters to rearrange and to display a radial gradient in species with the particles of highest hydrophobic mismatch (red) in the center, surrounded by particles with decreasing mismatch, as can be seen in figure 5.13 c). The mismatch between matrix species and the other species does not have to be hydrophobic, but it could also be a difference in thickness of the hydrophobic patch of the species. Species with a long hydrophobic patch will try to be next to species that also have a long hydrophobic patch. Overall, species with a longer hydrophobic spot tend to be larger. It has been observed that a difference in hydrophobicity changes the thickness of the bilayer [112].

(a) Randomly positioned lipids.

(b) Initial clusters form.

(c) Clusters display gradients.
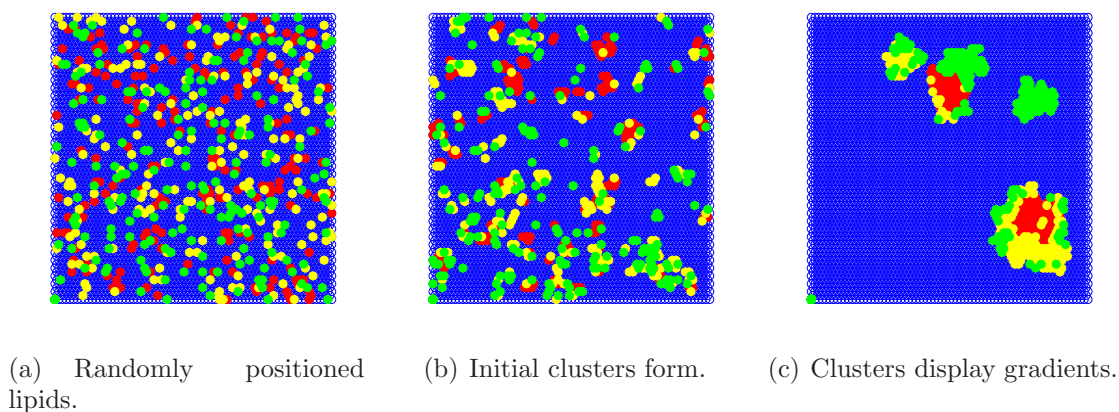
Figure 5.13: Clustering due to hydrodynamic mismatch. The blue particles are the matrix. The hydrophobicity mismatch of the other three species is indicated by their color, from green (least) to red (highest) mismatch. When the system is allowed to lower its energy, clustering occurs along with sorting of the particles. The sorting creates a radially decreasing profile in hydrophobicity mismatch in the clusters.

Difference in the hydrophobicity of the lipid molecules changes the bilayer thickness, where a larger difference in hydrophobicity leads to a larger height difference between the lipid ordered and unordered phase as reported in [112]. Let us assume that a confined receptor has the same hydrophobicity mismatch with the matrix, as the species in the center of the clusters. If the receptor leaves from the center into a zone where there are predominantly other species than those in the center of the domain, there will be a relative hydrophobicity mismatch between the receptor and the bilayer. It has been proposed that a membrane protein is in hydrophobic coupling with the bilayer, which implies that lipids and proteins interact due to their hydrophobicity [251–253]. This coupling can induce a deformation, compression and change in thickness of the membrane in close proximity ($\sim 1\,\mathrm{nm}$), but

also a change in conformation and function of the protein [252]. Furthermore, a change in bilayer elasticity has been shown to regulate the function of a sodium channel [251]. The hydrophobic coupling dictates that the hydrophobic length of a protein and the bilayer thickness in the vicinity of the protein should match to minimize the energy penalty. This can lead to recruitment of lipid shells around proteins and recruitment of proteins into lipid rafts [101]. If there is a mismatch in length, the bilayer will deform. It is the bilayer that deforms, rather than the protein, since the bilayer is about $100 - 1000$ times softer than the protein structure [252].

The deformation of the bilayer changes the energy of the system G_{def}^0 as described for a cylindrical protein of radius r_0 by

$$\Delta G_{def}^0 = \int_{r0}^{\infty} \left[K_a \left(2u_{bl}/d_0 \right)^2 + K_c \left(\nabla^2 u_{bl} - c_0 \right)^2 \right] \cdot \pi r \, dr - \int_{r_0}^{\infty} K_c c_0^2 \cdot \pi r \, dr \tag{5.3}$$

The expression has three terms, where the first represents the change in energy due to the compression or expansion of the membrane with compression-expansion modulus K_a and $u_{bl}(r)$ defined as half the change in local bilayer thickness d with respect to the normal thickness d_0 ($u_{bl} = (d_0 - d)/2$). The second term is the energy due to the monolayer bending with curvature c_0 and its modulus is the splay-distortion modulus K_c [252]. The last term is the curvature frustration energy, which exists in the unperturbed bilayer because the lipids are forced into the shape of the lipid bilayer.

As done in references [251,254,255], equation 5.3 can be rewritten in biquadratic form as

$$\Delta G_{def}^0 = H_B(d_0 - l)^2 + H_X(d_0 - l)c_0 + H_C c_0^2 \tag{5.4}$$

where H_B, H_X & H_C can be seen as spring constants that are determined by the parameters, K_a, K_c, r_0 and d_0 and l is the hydrophobic length of the inclusion. If the protein moves in the membrane from a region of thickness d_1 to a region of thickness d_2 and assume that its hydrophobic length l does not change, then the change in energy is given by

$$\Delta\Delta G_{def}^{d_1 \to d_2} = H_B(d_2 - d_1)(d_2 + d_1 - 2l) + H_X(d_2 - d_1)c_0 \tag{5.5}$$

This expression for the energy change of the system leads to a simple expression for the force that is applied on a protein due to a change of mismatch in hydrophobic length following a displacement in direction perpendicular to the membrane x_{displ}, which determines the change in membrane thickness $d_2 - d_1 = f(x_{displ})$:

$$F = - \left(-\frac{\partial \Delta\Delta G_{def}^{d_1 \to d_2}}{\partial(x_{displ})} \right) = \frac{\partial \Delta\Delta G_{def}^{d_1 \to d_2}}{\partial(d_2 - d_1)} \frac{\partial(d_2 - d_1)}{\partial(x_{displ})} \tag{5.6}$$

Due to the bending of the membrane, the force is perpendicular with respect to the surface of the lipids that are in contact with the protein. There is thus a component of the force in the bilayer plane, which will tend to move the protein inside the plane.

If the protein is assumed to match the membrane thickness in the center of the membrane domain, then d_1 is equal to l. If the molecule leaves the center and enters a zone of different lipid composition with a different height d_2, the change in energy will create a force back towards the center where the hydrodynamic mismatch is weaker. A larger mismatch will create a larger force. Assuming that the change in bilayer thickness is between $0.2 - 1.5$ nm [256], the bilayer spring constant H_B is $1 - 30 \, k_B T$ nm^2 [255] and neglecting a change in monolayer bending, the in-plane component of the generated force can readily create the measured spring constants for the toxin receptors. The plot on the right of figure 5.14 shows the line profile of the hydrophobicity or membrane thickness (red) across the cluster shown on the left that was obtained from the simulations of figure 5.13. If more species with a more gradual difference in hydrophobicity were contained in the raft, the potential on a receptor with hydrophobic length matched to that of the innermost species would be smooth, as shown in blue in figure 5.14.

In summary, if larger lipid rafts or protein clusters are made up of different species with different membrane heights or hydrophobic properties, then these will arrange in such a way that a radial gradient in hydrophobicity or height will be set up between the center and the border. A protein that best matches the properties of the innermost species will experience a force directed towards the center when it moves into a zone of different composition further out. This force is due to the hydrophobic coupling between the protein and the lipid bilayer around the protein. Recently, studies have shown that the lateral diffusion of proteins and lipids in artificial bilayers is indeed influenced by the matrix composition [257, 258]. These experimental results would also suggest an increase in diffusion coefficient as the protein leaves the central region of the raft or clusters if there is a radial gradient
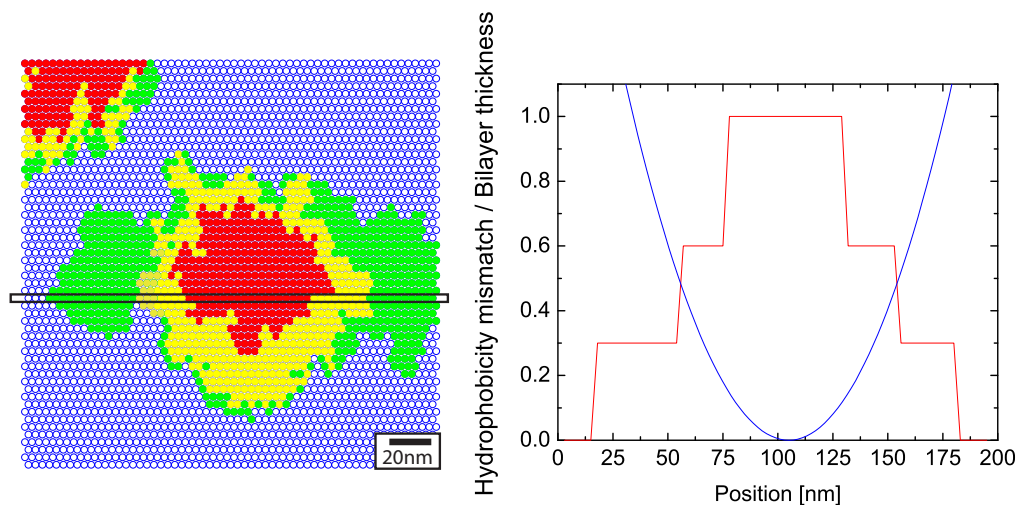
Figure 5.14: Profile of a cluster that contains different species with different hydrophobicity (left). The matrix species is given in blue, while the green, yellow and red species have increasing hydrophobic mismatch with the blue matrix species. On the right, the plot in red shows the hydrophobicity mismatch with respect to the matrix species across the highlighted black line profile, where the maximum mismatch is normalized to 1. A receptor that has the same hydrophobicity mismatch as species in the center would be subjected to the blue potential, in the case of a large number of differen species with more gradual differences in hydrophobicity.

in hydrophobicity or height. However, the expected increase in diffusion coefficient is at the maximum 50 %, which is not detectable by our measurements due to the limited number of data points in a trajectory and thus related accuracy of inferred values.

5.6   Summary

In this chapter the origin of the confining potential of the toxin receptors is investigated. Single-molecule tracking of the receptors reveals that the depolymerization of the actin cytoskeleton by Latrunculin B does not alter the confinement or diffusion coefficient. However, cholesterol extraction from the membrane with cholesterol oxidase leads to a drastic reduction in confinement strength k_r and an increase in the mean area of the confining zone A due to the appearance of trajectories that are not confined. These results are summarized in figures 5.6 to 5.9.

A MTT assay on the toxicity of the toxin on MDCK cells in culture after actin depolymerization or cholesterol extraction shows a reduction in toxicity for the

case of cholesterol extraction, while toxicity remains at its normal level after actin depolymerization. The assay confirms the finding of single-molecule experiments that confinement is cholesterol dependent.

Receptor trajectories, recorded at $21\,°C$ or $37\,°C$ show the same size of confinement domains and diffusion coefficient, except for a reduction in spring constant k_r for the ϵ-toxin receptor, as summarized in figures 5.11 and 5.12. These results indicate that the confining domains are not formed in thermal equilibrium but are actively maintained by the cell.

In the light of the observations discussed in chapter 4 and the current chapter, I have developed a model that can explain the observations: The receptors are confined in clusters of lipids (lipid rafts) and/or proteins that are held together by cholesterol. We refer to them as cholesterol stabilized domains or rafts. A radial gradient in species can explain the confining potential through hydrophobic coupling and mismatch.

Chapter 6

Receptor Tracking in Non-Equilibrium Conditions

6.1 Receptors under external force

Until now we have studied the toxin receptor subjected to the intrinsic potential that is created by the cell membrane architecture. However, it is possible to generate an additional external force on the receptor to gain further insight about the architecture of the membrane or the receptor itself.

By applying a force on the studied toxin receptors, we can test if the cholesterol-stabilized confining domains are floating freely in the lipid bilayer or if they are interacting with the cytoskeleton. Earlier results, presented in chapter 4.5.1, on the drift of these domains indicate that they tend to get pulled along in the membrane but nothing further is known. If the domains are free, it should be possible to drag them along long distances across the cell membrane.

Another valuable information about a receptor is its interaction strength with a ligand or drug, which is quantified by the dissociation constant. This constant is a measure of the natural tendency of the reversible process of unbinding of the ligand (L) from a receptor (R) to happen. The two-state reaction for a ligand-receptor complex (C) is given by:

$$C \rightleftharpoons R + L \tag{6.1}$$

$$K_D = \frac{[R][L]}{[C]} = \frac{k_{off}}{k_{on}} \tag{6.2}$$

The dissociation constant K_D is then defined as the ratio of the concentrations of products over reactants of the chemical disassociation reaction or as the ratio of reaction rates k_{off} and k_{on}, as in equation 6.2. A larger disassociation constant indicates a weak interaction between a drug and a receptor, for example.

The dissociation constant can be measured by the surface plasmon resonance (SPM) technique. This label-free technique measures the association and disassociation rate k_{on} and k_{off} of an analyte and an immobilized prey receptor. The binding of an analyte to the prey receptor changes the dielectric constant of the surface, which is probed by surface electromagnetic waves [259, 260]. A change in the dielectric constant of the surface will change the angle of the reflected light that creates the surface plasmon wave. The technique has recently been implemented for prey receptors that are embedded in a lipid bilayer [261]. However, this method only works on especially prepared surfaces. Another issue is that the sensitivity of the method depends on the concentration of bound analyte. This implies that it is necessarily an ensemble technique.

Optical tweezers are a method for applying a force directly on the bond between a receptor and a ligand or on the receptor in its environment. The idea to exert a force by radiation pressure on beads was first proposed in 1970 [262, 263] and a technique with a single laser beam was first proposed in 1978 [264]. First experimental results on biological applications followed on trapping Escherichia coli bacteria and tobacco mosaic viruses [265]. The next step was trapping the two ends of single macroscopic molecules like DNA with two beams [266]. Many experiments with optical tweezers take advantage of a fluid flow to prepare the sample, the force is exerted via the optical or magnetical tweezers [267–272]. However, two papers in particular used either optical tweezers or a micropipette to pin down a single strand of DNA on one side, while a force was exerted on the strand via a liquid flow [270, 273]. These groups determined that the hydrodynamic coupling within the DNA chain is important, even at long extensions. This experiment was designed to investigate forces that act within a single DNA chain and is thus an intra-molecular experiment.

Optical tweezers have also been used in single-molecule tracking experiments to measure the effects of deforming the cytoskeleton on tracked diffusing species [65]. Alternatively, the optical trap can also apply a force directly on the observed membrane molecule to measure the distance along which it can be dragged without encountering a barrier (barrier-free path) [66–68, 88, 126]. A limitation of the optical tweezers technique is the low amount of sampled molecules, since the optical tweezers have to pull on each measured molecule. However, advances with multiple traps that are created by holographic techniques could overcome this problem [274–276].

The interaction between a ligand and a receptor can also be directly probed by attaching the ligand to the tip of an atomic force microscope (AFM) and by scanning it over a surface or cell [277, 278]. This technique has been used to measure the unbinding force of a single ligand-receptor pair and demonstrated that the inter-molecular binding forces are smaller than the intra-molecular forces [279]. As with optical tweezers, this technique is a single molecule technique and only one molecule can be investigated at a time. An advantage is the sampling rate and the fact that the same receptor-ligand pair can be re-measured many times, when the AFM tip is oscillating at high frequencies. The biomembrane force probe approach is based on the same concept as the functionalized AFM tip. In this approach a lipid vesicle held by a micropipette is brought in contact with a functionalized surface [280, 281]. The ligand-receptor pair is formed between the surface and the vesicle. A variable force can be applied by modifying the tension of the vesicle by adjusting the pressure in the pipette.

To overcome the bottleneck of low sample statistics, Halvorsen et al. implemented massively parallel single-molecule manipulation using centrifugal forces [282]. Here, a microscope is mounted on an arm of a rotary stage. The coverslip surface is perpendicular to the arm and a centrifugal force is exerted on beads on the coverslip. This force will stretch a molecule that is attached with one end on the coverslip and with the other on the bead that is forced off the coverslip by the centrifugal force. Such a set-up is custom built and not easily transferable to other laboratories but it is efficient at determining the rate k_{off}.

Here we propose a new technique that can create a force on a membrane receptor or between two molecular species in general, which is borrowed from single cell parasites. Trypanosomatids are protozoa parasites with only one flagellum that can cause major diseases in humans, such as sleeping sickness, cagas disease and leishmaniasis [283]. The parasite $Trypanosoma\,brucei$ is known for its ability to evade the human immune system partly by clearance of surface-bound antibodies [284]. Engstler et al. showed that the parasite clears GPI-anchored variant surface glycoproteins labeled by an IgG antibody to the flagella pocket, where the antibody is endocytosed [285]. Without exposed antibodies, the immune system cannot act on the parasite. The clearance is due to the hydrodynamic resistance of the antibody and the resulting drag force towards the rear of the cell when the parasite swims. The antibody acts as a parachute and pulls the attached membrane receptors towards the flagella pocket.

The same concept can be used to create a force on membrane receptors in single molecule tracking experiments. A flow of liquid across the cell membrane creates a drag force that scales with the hydrodynamic radius of the part of the receptor that sticks out of the membrane. For unlabeled receptors this force is negligible,

but coupled nanoparticle labels act as parachutes and amplify the drag force [286].

The advantage of this technique is that, although it is a single-molecule technique, many receptors can be observed at the same time. Furthermore, it is much easier and cheaper to implement than an optical tweezers set-up. In fact, the technique does not even require a laser. A further advantage is that a luminescent nanoparticle attached to a biomolecule can serve both as a force amplifier and as a label to visualize the localization of the biomolecule. In the optical tweezers approach two different particles are typically used to apply and visualize the biomolecule position. The set-up allows for the investigation of molecular interactions, but also interactions of ligands and life cells.

6.2   Calculation of the hydrodynamic drag force

The nanoparticle acts as a parachute and increases the hydrodynamic interaction with the fluid as shown in figure 6.1. When the fluid flow is generated inside a microfluidic channel, viscous forces are more important than inertial force, which leads to a small Reynolds number. The Reynolds number is a dimensionless number that describes the ratio of inertial forces to viscous forces. When a flow is applied, a small spherical particle in solution experiences a drag force. In the small Reynolds regime, the drag force on a spherical particle can be described by

$$\mathbf{F}_d = 6\pi\eta r \mathbf{v}_{flow} \qquad (6.3)$$

where the drag force $\mathbf{F}_d$ depends on the fluid viscosity η, the hydrodynamic radius r of the nanoparticle and the velocity $\mathbf{v}_{flow}$ of the fluid.

To implement this concept for applying a force, besides the material properties η and r, the velocity is the only parameter that needs to be known to calculate the applied force. Furthermore, the flow of the liquid should be laminar, i.e. without turbulence, in order to easily control the force on the receptor. A microfluidic channel provides adequate conditions, since the flow within the channel is laminar and its velocity can be calculated at any point based on the Navier-Stokes equation. The solution is a Poiseuille flow, for an incompressible fluid with a flow direction along a channel, which is assumed to be much longer than wide and constant in size. If a rectangular channel is much wider than high and if it is driven by a syringe pump (constant flow rate) or by a constant pressure, then the flow velocity only varies along the position z across the height h and not in the flow direction.

(a) Concept for applying a force to a receptor.

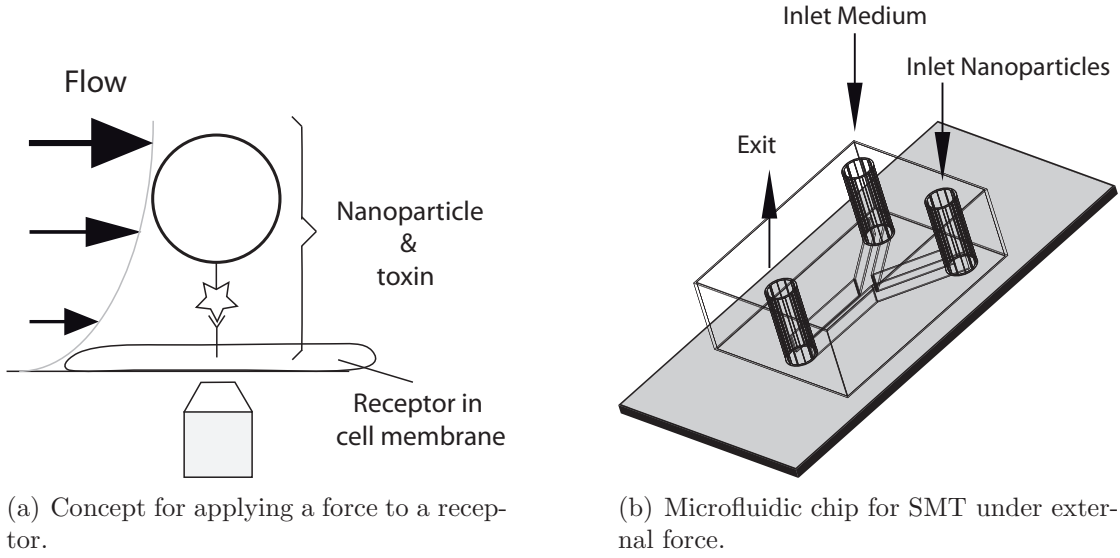(b) Microfluidic chip for SMT under external force.

Figure 6.1: A force can be applied onto a single receptor or molecule by relaying a drag force from an attached nanoparticle label in a moving fluid.

$$v_{flow}(z) = \ v_{max}\left[1 - \tfrac{4}{h^2}\left(z - \tfrac{h}{2}\right)^2\right] \qquad (6.4)$$

$$v_{max} = \qquad v_{z=h/2} = \tfrac{3U}{2Lh} \qquad (6.5)$$

This velocity profile is a parabola with a maximal flow speed v_{max} half way between the bottom and the top of the channel, which depends on the length L and height h of the channel, as well as on the flow rate U. The flow speed at the boundary is zero.

In summary, the drag force that is relayed from the nanoparticle to the receptor can be calculated from the dimensions of the microfluidic system, the flow rate U, the size of the nanoparticle and the position z of the nanoparticle in the channel via equations 6.4 and 6.3. However, the cells complicate the simple Poiseuille flow scenario. They change the height of the channel h and they invalidate the initial simplifications that lead to the simple expression for Poiseuille flow because the flow is no longer parallel to the walls and the no-slip condition might no longer be true at the cell-water interface. It has been proposed that the lipid bilayer possesses fluidity and hence flows under imposed shear stress [287]. Nevertheless, the cell surface is often treated as a no-slip boundary and we will follow this assumption [288].

A simple way to partly remove this complication is by assuring that the cells form a confluent surface with a known height. The height h in the equation for flow velocity 6.4 then is replaced by the channel height $h_{channel}$ minus the height of the cells h_{cells}. Another complication is the proximity of the particle to the cell membrane. If the distance to a boundary becomes comparable to the size of the nanoparticle, the simple equation for the drag force 6.3 is no longer valid since the velocity field around the particle is modified. In the concept presented here for applying a force on a biomolecule that is fixed on a surface, the distance between nanoparticle and surface will always be comparable to the diameter of the nanoparticle and often much smaller. These so-called wall effects have been investigated for the case of a no-slip boundary [289] and for the case of proximity to a wall with slip [290]. In both cases, the problem is solved by the approximate and iterative technique named method of reflections. Here, the particle is first assumed to be in an infinite flow field, very far away from the wall. This field, however, violates the boundary conditions at the wall. To correct this, an additional flow field, or so called reflection, is added to correct the boundary condition at the wall. This reflection however violates the boundary condition at the particle surface, which is corrected for by introducing a second reflection that will again violate the boundary condition at the wall and so on.

Given these complications, it is preferable to directly measure the flow velocity around the nanoparticle by the means of particle image velocimetry (PIV) techniques to avoid assumptions that are difficult to verify [291–295].

6.3 Measuring k_{off} under external force

As already introduced in equation 6.2, the reaction rate k_{off} is a measure of the interaction strength between two molecules. Due to the added hydrodynamic drag of the nanoparticle, the force that can be applied between the two molecules can be relatively large and can be controlled as described in the previous section. In the absence of force, the interaction between the ligand and the receptor when the two interacting molecules are a complex can be modeled by a particle that is trapped in a potential. In this model, the molecules become unbound when the particle escapes from the potential. The rate at which the particle escapes the potential is the rate k_{off} is related to the thermal energy ($k_B T$) and the energy barrier ΔE of the system [219]:

$$k_{off}(0) = w_0 \, exp\left(-\Delta E / k_B T\right) \tag{6.6}$$

An external force, which acts on the molecule complex, will introduce an extra term in equation 6.6 [296]. The new rate equation contains a second term that lowers the energy barrier due to the applied force F over the distance a.

$$k_{off}(F) = w_0 \, exp\left(-\Delta E/k_B T\right) \, exp\left(-Fa/k_B T\right) = k_{off}(0) \, exp\left(-Fa/k_B T\right) \quad (6.7)$$

It then becomes possible to calculate $k_{off}(0)$ at zero force by measuring the rate $k_{off}(F)$ at different forces, without having to know the distance a, which depends on the molecular pair. However, it has been shown that the unbinding of the complex does not only depend on the external force, but also on the load rate r_{load} [280, 297]. The $k_{off}(F, r_{load})$ rate is thus linearly dependent on the load rate r_{load} and exponentially proportional to the force F for a single energy barrier [279].

6.4   Experimental set-up

To guarantee a laminar Poiseuille flow, we use polydimethylsiloxane (PDMS) microchannels that are closed by a glass microscope coverslip on one side, as shown in figure 6.1 b). PDMS is a cheap, flexible material that can be easily molded using the dry film photoresist soft lithography technique [298]. The master mold was etched into Eternal Laminar E8020 negative films of thickness $49 \pm 2\,\mu m$. The photoresist layers for the master mold were laminated onto a clean glass slide using an office laminator at $100\,°C$ until the desired channel height of the main channel was reached ($50\,\mu m$). The photoresist film was exposed to UV light through a photo mask with the desired channel architecture. The photoresist is developed by immersion in an aqueous bath of carbonate potassium at $1\,\%$ mass concentration. PDMS (Dow Corning SYLGARD 184, 1/10 ratio of curing agent to bulk material) is then poured over the master mold and cured for $3\,hours$ at $70\,°C$. After peeling-off the cured PDMS, it is sealed by plasma bonding with the microscope glass coverslip.

Culture medium (CM) (DMEM, $10\,\%$ fetal calf serum (FCS), $1\,\%$ penicillin-streptomycin) is injected into the channel one day prior to cell injection and the channel is incubated overnight at $37\,°C$ to remove gas from the PDMS that would interfere with the growth of cells by forming bubbles in the channel. Suspended MDCK cells in CM are injected at high concentration ($\sim 8 \times 10^7\,cells/ml$) into the channel and incubated overnight at $37\,°C$. This method for cell growth in microchannels is not optimal and the yield of microfluidic chips that contain healthy cells is limited due to the poor circulation of medium during the growth phase of cells. To improve this we suggest to grow cells under a small flow or to implement

the molecular sticker method, where cells are first grown normally on a glass coverslip and the PDMS chip is added just before the experiment [299].

For the experiment, the microfluidic chip is mounted on a wide-field inverted microscope (Zeiss Axiovert 100) equipped with a 63x, NA = 1.4 oil immersion objective. Two syringe pumps are attached to the two inputs of the chip, one pumping observation medium (OM) (HBSS + 10 mM HEPES) and the other with a solution of ϵ-prototoxin coupled nanoparticles at a concentration of 0.05 mM in vanadate ions. Care has to be taken to avoid any bubble formation in the tubing or the channel, when the chip is connected. The surface tension force of the air-medium interface will tear off all cells if a bubble passes through the channel. First the channel is rinsed at a flow of 1 µl/min with OM through the first input. Nanoparticles are then injected through the second input and incubated with the cells for 30 minutes. After the incubation, the channel is rinsed with OM through the first input at a low flow rate of 1 µl/min to remove unbound nanoparticles. The channel design with two inputs provide an easy system to remove unbound nanoparticles that would increase the background fluorescence.

The tracking experiments under external force are performed in the same experimental conditions as without force: Images of the receptors are recorded with an EM-CCD (Roper Scientific QuantEM:512SC). The nanoparticles are excited with an Ar^+-ion laser using the 465.8 nm line. The emission of the NPs is collected through a 617/8M filter (Chroma). We record images at frame rates down to 20 Hz and an excitation intensity of 0.25 kW/cm^2 at room temperature or 37 °C. The motion of the receptor is first recorded without flow to check if the receptor behaves normally, then the motion is tracked under external force, by applying a flow through the syringe pump with OM.

The velocity of the solution at the nanoparticle position can be calculated assuming an ideal Poiseuille flow. For a more precise determination, the velocity can be measured by tracking the speed of passing objects in solution at the height of the investigated nanoparticles. Alternatively, fluorescent beads can be introduced into the solution and the speed can be obtained from their motion. To overcome the difficulties introduced by the Poiseuille flow velocity profile, the fluid can be moved by electrophoresis, which generates a flat velocity profile [300, 301].

6.5   Results

The goal of the work presented here is the investigation of the motion of the ϵ-toxin receptor under external force, and not a measure of the k_{off} for the receptor and the toxin complex. First, two control experiments were designed to verify that the

flow does not displace the cells, results of the motion of the ϵ-toxin receptor are reported. The experiments were done in collaboration with Jean-Marc Allain from the Laboratoire de mécanique des solides at Ecole Polytechnique. Furthermore, two undergraduate students, Violaine Randrian and Ryan Luersen, contributed to this work in the framework of a *stage*. The work lead to an application for a patent [286].

6.5.1   Control experiments

If we track toxin receptors under moderate external force, we expect small displacements perhaps on the order of the domain size or multiple domain sizes. It is thus important to verify that the observed displacement is indeed due to the flow-induced drag force acting on the nanoparticle and not due to the displacement of the entire cell due to the induced shear stress. To verify this, two experiments were designed: observation of the microtubule skeleton of cells that are subjected to flow and observation of fluorophore-labeled GM1 receptors in the cell membrane.

Microtubules define the shape of cells and cell deformation will lead to deformation of the microtubules. Microtubules grow outwards starting at the centrosome and bend once they reach the cell membrane. To observe microtubules, MDCK cells were transfected to express end-binding protein 3 (EB3)- green fluorescent protein (GFP) (EB3-GFP), which bind to the growth end of the microtubule. All reagents for the transfection along with support was provided by Cedric Bouzigues. The protocol for transfection can be found in appendix A.6. To visualize the GFP-labeled microtubules under flow, the cells are grown and transfected in microchannels and observed on a wide-field microscope (Zeiss Axio Observer D1) equipped with a 63x, NA = 1.4 oil immersion objective. The GFP fluorophores are excited by a mercury arc lamp with an excitation filter (Zeiss BP475/30). The emission is filtered by an emission filter (Chroma, ET525/50m) and recorded by a digital CCD camera (QImaging, Retiga-4000R) with an acquisition time of 30 s per image.

Figure 6.2 shows the labeled microtubules of two cells without fluid flow in red and during flow of 50 µL/min in green. This flow rate is the maximal flow rate used during single molecule experiments. The maximal observed displacement of the microtubules is 0.6 ± 0.1 µm and 0.15 ± 0.06 µm for the two cells, shown in figure 6.2 a) and b), respectively. These values were determined by averaging 10 independent displacement measurements for each cell.

The second control experiment monitors the surface of the cell membrane rather than the shape of the entire cell. Monosialotetrahexosylganglioside (GM1) is a membrane molecule that is known to be recruited into lipid rafts [116, 246, 302]. These raft markers can be cross-linked with cholera toxin, which binds up to five GM1 receptors [303, 304]. Visualizing the position of these labeled rafts can be
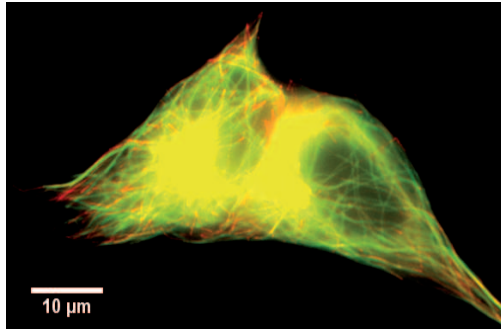
(a) Maximal displacement of microtubules is $0.6 \pm 0.1\,\mu m$.
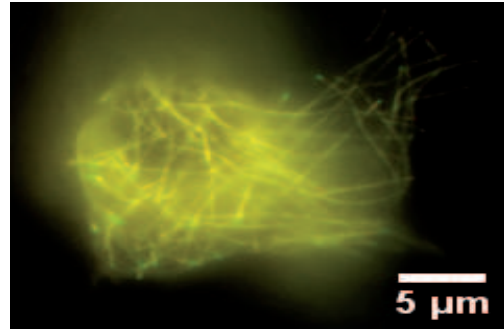
(b) Maximal displacement of microtubules is $0.15 \pm 0.06\,\mu m$.

Figure 6.2: Cells with EB3-GFP fluorescently labeled microtubules show that cells do not deform under flow. Microtubules without flow are shown in red and with a flow of $50\,\mu L/min$ in green.

used to measure the displacement of the cell membrane under flow.

MDCK cells are grown in microchannels as described above and in appendix A.6. The GM1 receptors are labeled by injecting $100\,\mu L$ of a $20\,\mu g/\mu L$ solution of cholera toxin subunit B coupled to Alexa488 (CT-B-Alexa488) (Molecular Probes) and incubating for 15 minutes at $37\,°C$. The cells are rinsed to remove excess unbound CT-B.

To image the labeled GM1 clusters under flow, the microchannels are mounted on a wide-field microscope (Zeiss Axio Observer D1) equipped with a 63x, NA = 1.4 oil immersion objective. The Alexa488 fluorophores are excited by a mercury arc lamp with an excitation filter (Zeiss BP475/30). The emission is filtered by an emission filter (Chroma, ET525/50m) and recorded by a digital CCD camera (QImaging, Retiga-4000R).

The fluorescently labeled GM1 clusters are shown in figure 6.3. The red image was recorded without flow and the green image shows the cell under a flow of $2.5\,\mu L/min$. Thresholding the image reveals that the maximal displacement of the GM1 clusters is $0.24 \pm 0.06\,\mu m$.

Overall, the two control experiments show that cells move slightly due to the liquid flow, but the maximal observed displacement is only $0.6 \pm 0.1\,\mu m$, which is comparable to the average confinement domain diameter of the toxin receptors, which is $0.7\,\mu m$.

(a) Overlay of GM1 domains before (red) and during a flow of 2.5 µL/min (green).

(b) By thresholding the image, the maximal displacement of GM1 clusters is determined to be 0.24 ± 0.06 µm.
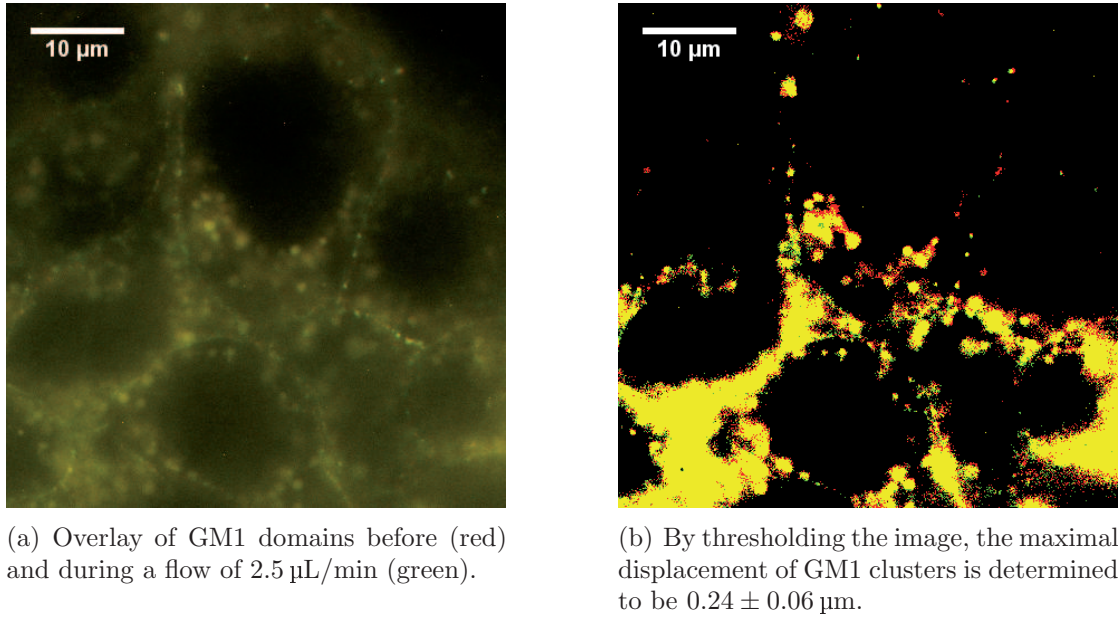
Figure 6.3: GM1 clusters marked by cholera toxin subunit B coupled to Alexa488 (CT-B-Alexa488) under a flow of 2.5 µL/min. The maximal displacement of the clusters is 0.24 ± 0.06 µm.

6.5.2 ϵ-toxin receptor

The control experiments established that the hydrodynamic drag shifts the cells by a negligible distance. However, it easily displaces a nanoparticle-labeled ϵ-toxin receptor at a flow rate of 7.5 µL/min, as can be seen in figure 6.4. The receptor-nanoparticle complex is displaced by 2.1 ± 0.3 µm in the flow direction. The displacement is calculated by averaging all positions of the receptor before the flow started and then subtracting the average position during flow. From the speed of the displacement $v_{displacement}$ due to the flow and the displacement distance L, we can calculate the Péclet number Pe of the system, which is the ratio of the rate of advection due to the flow to the diffusion of the particle D:

$$Pe = Lv_{displacement}/D \tag{6.8}$$

The measured Péclet number of 7 indicates that the receptor is indeed displaced by the hydrodynamic drag of the flow and not due to the Brownian motion. Furthermore, the displacement is much larger than the small displacement of 0.6 ± 0.1 µm observed for cells under flow in the control experiments presented

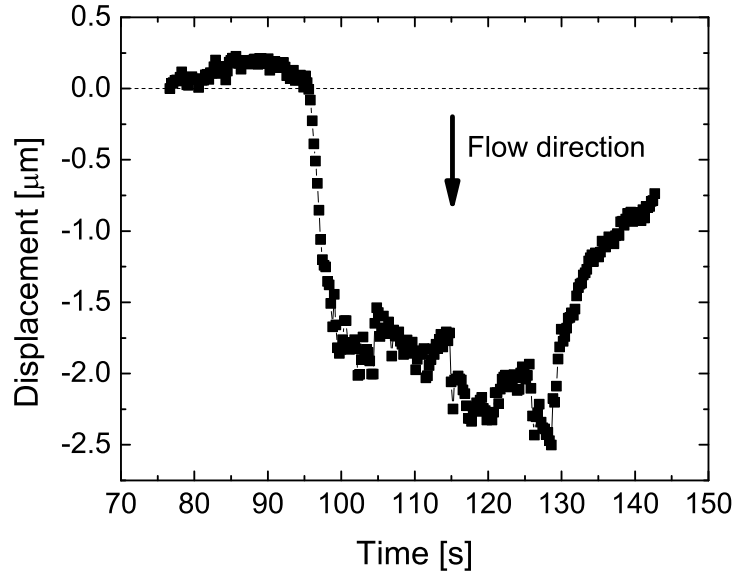in the previous section. This indicates that the receptor is moving within the membrane and due to the flow.

Figure 6.4: Displacement of a receptor under a flow of 7.5 µL/min due a drag force enhanced by its nanoparticle label. The flow is applied at $t \approx 96\,$s and switched to zero at $t \approx 129\,$s. The flow direction is indicated by the arrow and the initial position is indicated by the dashed line for reference. The hydrodynamic drag force due to the nanoparticle is large enough to displace the receptor significantly with respect to the displacement that is caused by Brownian diffusion and the movement of the cell under flow.

After an initial phase of displacement with a velocity $v_{displacement}$ of $0.52 \pm 0.03\,$µm/s, the complex reaches an equilibrium position. Once the flow is stopped at $t \approx 129\,$s, the labeled receptor returns close to its initial position. The displacement is thus due to an elastic, reversible process accompanied by a small plastic deformation that manifests itself in the small shift between the initial position before flow and the final position after the flow has been stopped of $0.5 \pm 0.2\,$µm. The displacements over which the receptor returns back to its initial position surprisingly are large. For the flow of $20\,$µL/min, it returns over $9.6 \pm 0.7\,$µm back to its initial position, after the flow is stopped. This distance is more than ten times the average diameter of the confining domains. The return of the receptor close to its initial position implies that the equilibrium position reached under flow corresponds to a position where the hydrodynamic drag force is equal to the force that tends to bring the receptor back to its initial position.

There are two populations of tracked receptors. The first is displaced under flow, while a smaller population is not displaced. It is more difficult to track receptors on cells in microchannels due to a lower signal to noise ratio. During one day of experiments, 9 out of 32 nanoparticles could be tracked and analyzed.

Given that the displacement is reversible, the same receptor can be pulled at different flow rates to investigate the relationship between drag force and displacement. First, a convention on measuring the displacement is introduced in figure 6.5. The displacement of the receptor can be measured with respect to the initial position (black), with respect to the previous position without flow (blue) and with respect to the position the receptor will relax to after the flow is stopped (red). If the distance shown in red is smaller than that shown in blue, this means that the structure underlying the receptor and determining its position has undergone plastic deformation.
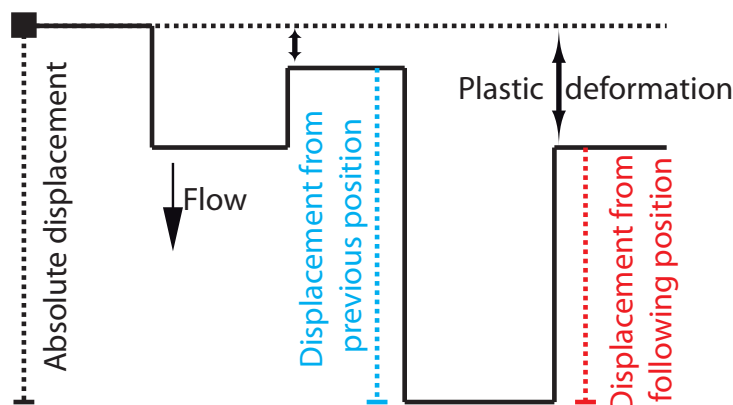

Figure 6.5: Measuring convention for the receptor displacement measurements. The displacement can be measured with respect to the initial position (black), with respect to the previous position without flow (blue) and with respect to the position where the receptor will relax to after the flow is stopped (red). The plastic deformation is the shift in position after one or more cycles of switching the flow on and off. A difference between the blue and red measurement indicates a plastic deformation.

An experiment series is shown in figure 6.6 for flow rates ranging from 2.5 to 50 µL/min. Four different behaviors can be identified: elastic deformation of the structure underlying the receptor linearly dependent on drag force, encountering of boundaries in the cell membrane and plastic deformation of the underlying structure. Finally, at high flow rates, ripping off of the receptors.
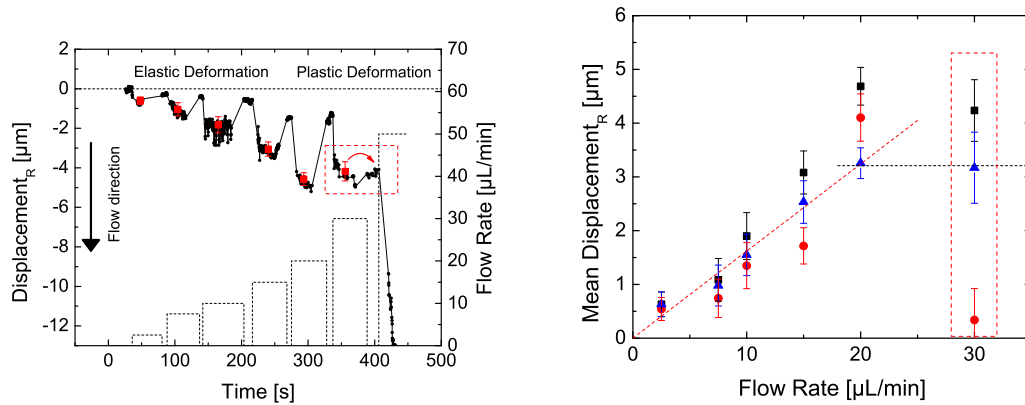
(a) Position of the ϵ-toxin receptor for a series of flow cycles indicated by the dashed line. The flow direction is indicated by the arrow. The red squares indicate the mean equilibrium position for each flow. When the flow rate is increased to 50 µL/min, the receptor is ripped off.

(b) Mean displacement of the receptor as a function of flow rates. Three measurements are recorded for each flow according to the convention in figure 6.5. Black squares indicate absolute displacement, whereas the blue triangles show the displacement with respect to the previous resting position. Red squares show the mean displacement with respect to the position where the receptor comes to rest after switching off the flow. A linear fit shows that the displacement follows Hooke's law for flow rates from 2.5 to 20 µL/min. The receptor is not displaced further than 3.21 ± 0.06 µm for a flow rate of 30 µL/min, indicating the presence of a boundary. When the receptor is forced past this boundary, the underlying structure it undergoes a large plastic deformation (red box).

Figure 6.6: Displacements of the same receptor for flow rates ranging from 2.5 to 50 µL/min. The general trend up to a flow rate of 20 µL/min is that a higher flow rate and thus higher resulting drag force cause a larger elastic displacement.

6.5.3   Elastic linear deformation

As the flow rate increases, the hydrodynamic drag force that acts on the receptor increases linearly as given by equation 6.3. A higher drag force causes a larger elastic displacement of the receptor in the cell membrane up to a flow rate of $20\,\mu L/min$, as shown in figure 6.6. This relationship suggests that Hooke's law can be applied to the trajectory of the receptor. This means that the equilibrium position under flow is reached when the displacement Δx satisfies:

$$F_{drag} = F_{Hooke} \tag{6.9}$$
$$\mathbf{F}_d = 6\pi\eta r \mathbf{v}_{flow} = k\Delta\mathbf{x} \tag{6.10}$$

This spring-like behavior can be explained by the interaction of the confining raft with the cytoskeleton. As mentioned before, rafts have been shown to contain many cytoskeletal and adhesion proteins, such as actin, myosin, vinculin, cofilin, cadherin, filamin and ezrin [236–240]. Such an interaction can explain why the confining domains of the toxin receptors were not observed to diffuse freely in the membrane. The flow speed was not measured, but calculated using equation 6.4. Assuming a flow speed v_{flow} of $0.23\,mm/s$ (no-slip boundary, $30\,nm$ above cells) at the nanoparticle position and using equation 6.3, the drag force F_d on the receptor at a flow rate of $20\,\mu L/min$ is $0.15 \pm 0.06\,pN$. Using this conversion of flow rate to drag force, the spring constant obtained from the inverse of the slope of the linear fit in figure 6.6 a) is $0.04 \pm 0.02\,pN/\mu m$. This value is in the range of the spring constants measured for the confining potential of the toxin receptors without flow. However, this is probably coincidence. Indeed, we do not think that the confining potential of the raft can extend that far, because the average confinement domain size is only $0.7\,\mu m$. Other groups have measured the spring constant for proteins attached to actin filaments and cite values in the range of $2.6 \pm 0.8\,pN/\mu m$ for the CFTR Cl$^-$ transmembrane receptor [86], $2.4 - 8.4\,pN/\mu m$ for the LFA-1 adhesion protein after binding to ICAM-1 ligand [69] and $10\,pN/\mu m$ for the δ-receptor in the membrane of *Escherichia coli* bacteria [71]. These values concern proteins directly tethered to the actin cytoskeleton, which is not the case for the α-toxin receptors. However, the confining raft of the receptor can be tethered to the cytoskeleton via proteins that interact with the cytoskeleton [236–240]. Dragging of the transferrin receptor subpopulation that is not tethered to the cytoskeleton with optical tweezers has shown that the receptor is confined by actin fences [66]. If the receptor is dragged with a drag force of $0.25\,pN$, the fences can be deformed and stretched and the measured spring constant is $3 \pm 2\,pN/\mu m$. However, we think that our cholesterol stabilized confinement domains are directly tethered to the cytoskeleton because the elastic deformation can reach very large distances

and not only the length of the diameter of the confining domain as in reference [66].

Because that drag force on the nanoparticle that we determine is very low, we suggest measuring the flow speed by PIV techniques to check the obtained results.

6.5.4 Boundaries in the cell membrane

At a flow rate of 30 µL/min, the receptor in figure 6.6 is not displaced any further than it was displaced for a flow of 20 µl/min. This indicates either the presence of some boundary at this distance of 3.21 ± 0.06 µm or that the spring has reached its maximum extension. The boundary is marked by the black dashed line in figure 6.6 b). Figure 6.7 shows another trajectory that shows two boundaries at 2.11 ± 0.07 µm and 8.1 ± 0.6 µm, marked by the two dashed lines in figure 6.7 b). Boundaries have been described when a receptor is assumed to be moving in domains according to the picket and fence model [66]. In this work, the boundary spacing was equal to the size of the confining domain diameter of 0.7 µm and are thought to be elastic actin fences, over which the receptors can diffuse by hop-diffusion. In the picket and fence model, on average, a receptor cannot be on average displaced by more than half of the domain size L without encountering a boundary. Once the boundary is cleared, the receptor will encounter the next barrier at $3L/2$. In our case, however, the average domain diameter is also 0.7 µm, but the first boundary is encountered not at half the domain length, but almost at three times the domain diameter. We thus attribute the observed boundaries to randomly dispersed obstacles in the membrane. Image 6.7 c) shows that the two boundaries in the trajectory of the displaced receptor coincide with cellular features, such as the nucleus, that might deform the membrane, create a stronger interaction of the cytoskeleton with the lipid bilayer and thereby create a boundary. However, it is not always possible to attribute a visible cellular feature to the boundary due to the limitations of the light microscope.

6.5.5 Plastic deformation and rip-off

When the receptor is displaced past a boundary, it either undergoes a large plastic deformation and does not return back to its initial position after the flow is stopped, or it is ripped off. The difference in mean displacement between the blue (with respect to initial position) and the red (with respect to final position) value indicates plastic deformation and is visible for the flow rate of 30 µL/min in figure 6.6 b).The plastic deformation can be explained by considering that the receptor or the entire domain jumped over a boundary, which is defined by the cytoskeleton.
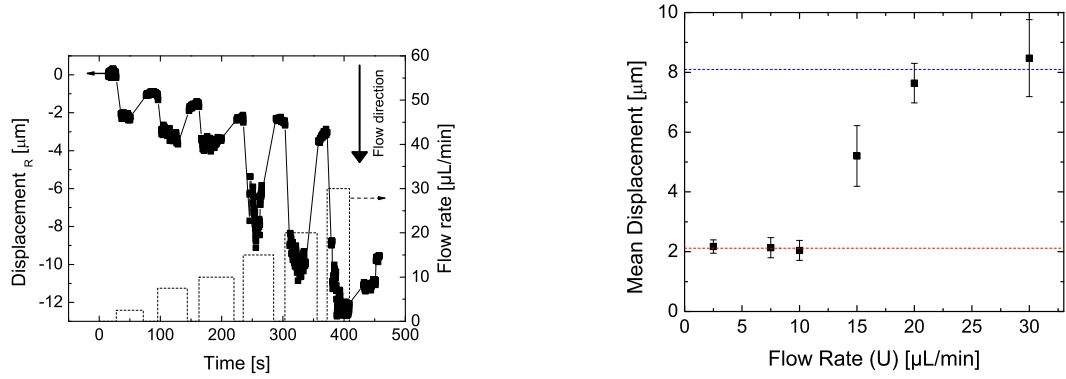
(a) Position of the ϵ-toxin receptor for a series of flow rates indicated by the dashed line. The flow direction is indicated by the arrow.

(b) Mean displacement of the receptor for the flow rates shown in a). Two plateaus, indicated by the red and blue dashed line indicate boundaries at $2.11 \pm 0.07\,\mu m$ and $8.1 \pm 0.6\,\mu m$, respectively. When the drag force is large enough, the receptor can be dragged over the boundary.
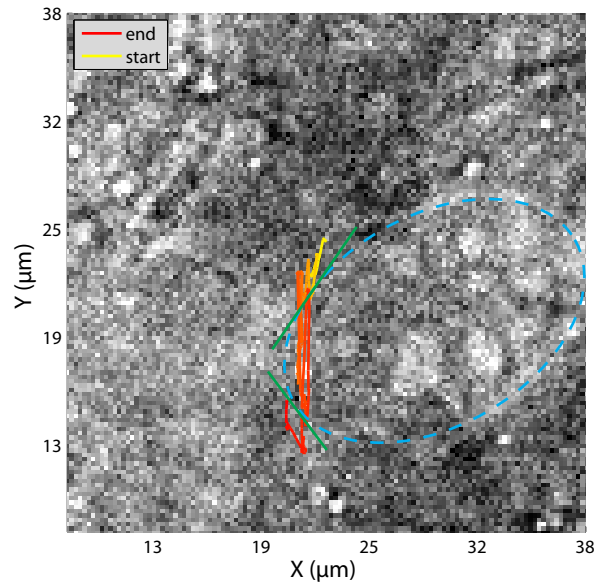
(c) Trajectory of the ϵ-toxin receptor superimposed on a white light image of the MDCK cell. The receptor trajectory is shown by the solid line, color-coded for time with yellow being the beginning and red the end. The nucleus is marked by the dashed blue ellipse. The boundaries highlighted in b) colocalize with the positions where the trajectory meets the nucleus, which is indicated by the green tangents. The nucleus might deform the membrane at these positions and hinder the displacement.

Figure 6.7: Position of an ϵ-toxin receptor for a series of flow rates. This trajectory shows two obstacles that colocalize with the position of the nucleus.

The receptor can be ripped out of the membrane at high flow rates and thus high drag forces. Such a process can be seen in figure 6.6 b) for a flow rate of $50\,\mu\text{L/min}$. It is not clear whether the nanoparticle-labeled toxin detaches from its receptor or if the entire receptor is ripped out of the membrane because only the toxin is labeled. Both, the toxin and the receptor would have to be labeled to distinguish between the two scenarios. However, the energy required to rip the entire toxin receptor out of the membrane is probably larger than that required to detach the toxin from its receptor. The first scenario is therefore more probable. If the toxin is indeed separated from its receptor, such measurements can be used to calculate k_{off}, as explained in section 6.3. The binding force of anti-sendai antibodies to sendai-epitopes fused into bacteriorhodopsin molecules from purple membranes was detected to have an interaction strength of 70 to $170\,\text{pN}$ by AFM studies [279]. To break such bonds, higher drag forces have to be generated by using larger nanoparticles or more viscous fluids.

6.6   Summary

This chapter introduced a new method that can easily apply a force on a single receptor in the cell membrane or more generally between two interacting molecules. A nanoparticle, which is attached to one of the interacting molecules, amplifies the hydrodynamic drag force of a passing liquid flow and relays the force to the bond between the two molecules.

By conducting the experiment in a microfluidic channel, where the liquid flow is laminar, the force that is relayed to the molecule can be calculated from the flow speed and the size of the nanoparticle.

This technique can be used to determine the k_{off} rate and more generally, for all experiments requiring generation of a force in a multiplexed, easier to implement and cheaper fashion than AFM or optical tweezers experiments.

We grew MDCK cells in PDMS microchannels to track ϵ-toxin receptors under an external force using this new technique. The amplification of the drag force is large enough to displace the receptor in the cell membrane. Control experiments, analyzing the structure of the cell, show that the receptor moves within the membrane whereas the cell structure is modified only minimally. Pushing on the receptor with different flow rates ranging from 2.5 to $50\,\mu\text{L/min}$ reveals four regimes: elastic linear deformation of the structure determining the receptor position, hindrance by boundaries, plastic deformation and finally ripping off of the receptors.

We interpret this behavior with an interaction between the cytoskeleton and the confining cholesterol stabilized domains. In this framework, the linear regime, which can be modeled by Hooke's law, corresponds to the stretching of the cytoskeleton. Boundaries are regions where cell structures or the cytoskeleton act as

a barrier and restrict further movement of the confining domain over this boundary unless the force is increased. Once the barrier is overcome, the confining domain does not return to its initial position when the external drag force is switched off.

To our knowledge, this is the first experimental single-molecule evidence that lipid rafts are attached to the cytoskeleton. Previous work, has put forward this hypothesis [236–240].

6.7 Outlook

An important issue is to accurately determine the drag force by measuring flow speed around the nanoparticles. Alternatively, a flow created by electrophoresis could be advantageous because it simplifies the flow profile.

To draw further conclusions from the recorded data on the ϵ-toxin receptor, experiments should be done in the presence of Latrunculin B, which depolymerizes the actin cytoskeleton. Such experiments can provide further insight into the nature of the observed boundaries and could help verify the origin of the elastic displacement. Experiments with cells where cholesterol has been extracted from the membrane by cholesterol oxidase can furthermore verify our current conclusions because the receptor can be freed from the the confining domain and it can be tested if it still interacts with the cytoskeleton. Based on the data obtained so far, we expect that the receptor will not return to its initial position after both treatments.

Moreover, we propose to use this new technique to determine the k_{off} rate of an interacting molecular pair. To provide such a measure, a microfluidic chip surface can be coupled to a molecule, while nanoparticles are functionalized with the molecule's interacting partner. For a demonstration experiment, a well known pair should be chosen so that the experimental findings can be compared to the literature. After incubation with the nanoparticles, the number of molecules remaining bound to their interaction partners with respect to the number of initially bound molecules can be measured for various drag forces to obtain values for k_{off}. The technique can then be used to measure the k_{off} rate of a molecular pair that is more difficult to measure by conventional techniques.

Conclusion & Outlook

In this thesis I presented my work on the cell membrane architecture. To probe the architecture, we investigated the motion of two membrane receptors that are exploited by bacterial toxins. Toxin receptor trajectories are obtained by single-molecule tracking with $Y_{0.6}Eu_{0.4}VO_4$ luminescent nanoparticles, which are coupled to the toxins which in turn bind to their receptors. We chose two members of pore-forming toxin family: the ϵ-toxin of *C. Perfringens* which is the virulent toxin of the family and the α-toxin of *C. Septicum*. The α-toxin of, which is known to target a GPI-anchored receptor and provides thus a good foundation to explain experimental observations.

We introduce the most commonly used fluorescence techniques to study the cell membrane along with the current models of the cell membrane architecture in chapter 1. The presented models are tethering to the cytoskeleton, the picket-and-fence model, crowding effects, protein clusters and lipid rafts.

The second chapter introduces the α- and ϵ-toxins and highlights their function. These pore-forming toxins couple to the membrane as monomers and then oligomerize. Once a heptamer has formed, the toxin forms a pore by piercing the cell membrane with a β-barrel. An important fact is that these toxins are extremely lethal and that the monomers exploit the cell membrane architecture to concentrate themselves in order to increase the probability of oligomerization. Experimental trajectories show that the receptors are confined to small domains within the apical membrane of the MDCK cells. The second chapter furthermore introduces the wide field microscopy set-up, properties of the nanoparticle labels, experimental conditions and numerical studies on the limits of our single-molecule tracking experiment and image analysis algorithm.

We use a new method based on Bayesian inference to extract more information from our single-molecule trajectories showing confined motion. The main advantages with respect to the mean-square displacement (MSD) analysis is that our method starts with fewer assumptions. An extra term that allows the confining potential to take an arbitrary form makes this model less restricting in terms of assumptions. In fact, the technique can be applied to other cases of motion, where

the receptor is not confined by replacing the Langevin equation of motion by a different equation that would contain terms for active transport or drift, for example. Using performance tests we adapt the analysis algorithm to our experimental conditions and can thus be confident in the inferred values for diffusion coefficient and confining potential. The performance of the method is then compared to the MSD analysis and the residence time method. It is important to point out that our inference approach exploits the full information stored in the trajectory whereas all other approaches exploit only a subset of this information.

The fourth chapter shows experimental trajectories for both toxins and compares them. Both receptors undergo confined diffusion with a diffusion coefficient of $0.16\pm0.14\,\mu m^2/s$ in a spring-like potential with a spring constant of $0.45\,pN/\mu m$. The typical domain area is $0.5\,\mu m^2$. Due to their similar behavior, we conclude that the confinement domains of both receptors must be similar and that the confinement mechanism is the same.

The next task was to determine the reason for confinement. Chapter 5 explains how we used different biochemical reagents to disrupt the actin cytoskeleton and lipid rafts. We found that the disruption of the cytoskeleton does not change the confinement, while the partial disaggregation of confining domains leads to a large increase in diffusion coefficient, domain size and a large decrease in spring constant of the confining potential and, in some cases, to the complete suppression of confinement. We then built a model on the collected observations that makes hydrophobic interaction between the receptor and the lipid bilayer responsible for the confinement. We propose that lipid rafts are made up of many different lipids that arrange according to their hydrodphobicity mismatch with respect to the constituents of the lipid disordered phase to create a gradient of hydrophobicity mismatch. Such a raft composition can then lead to a spring-like potential for a receptor that is recruited into it due to hydrophobic interactions.

To further investigate the cell membrane architecture, we introduced a method to easily apply a force on a single receptor (chapter 6) and applied for a patent. This scheme is borrowed from parasites that evade the host immune system by taking advantage of hydrodynamic interactions between the host's antibodies that are attached to membrane receptors and the blood flow around the parasite to clear them to a flagella pocket where they are endocytosed. We thus take advantage of the hydrodynamic interaction of nanoparticles labeling receptors with a controlled fluid flow within a microfluidic channel to apply a force on the receptors. The nanoparticle label acts as a parachute and increases the hydrodynamic interaction with the fluid, so that the drag induced by convection becomes important. Tracking receptors in an induced external force field that distorts the thermal equilibrium shows that the confining lipid raft is interacting with the cytoskele-

ton. To our knowledge, this is the first experimental single-molecule evidence that lipid rafts are attached to the cytoskeleton. Previous work, has put forward this hypothesis [236–240].

In conclusion, this work has shown that the studied toxin receptors are confined within cholesterol stabilized rafts. Implementation of a new concept to apply an external force amplified by a nanoparticle label demonstrates that these rafts interact with the cytoskeleton. The recorded receptor trajectories were analyzed with a novel approach based on bayesian inferences. This technique exploiting the full information stored in the trajectory extracted a spring-like confining potential inside the rafts. The data was interpreted in terms of confinement governed by hydrophobic interaction between the receptor and the surrounding bilayer lipids, which create the inferred confining potential. This work is an example of how research at the interface between different disciplines based on the expertise of multiple collaborating teams can lead to novel experimental and theoretical results and open the way for research in new directions.

Further research opportunities that lie within the scope of our lab are the application of the inference approach to different modes of motion, such as directed motion and hopping. Here again, the inference approach can extract new information on the biological systems. For example, it is not clear if it is the receptor that hops from domain to domain or if it is the entire confining domain that hops over a boundary. It would thus be useful to infer the potential of the confining domain before and after the hopping event and to compare them. The advantage is that in addition to the diffusion coefficient, which might not change in a different domain, data is now available that describes the confining domain in more detail than just its dimension.

Furthermore, it would be useful to genetically label the GPI-anchored receptor of the α-toxin. Monitoring the distribution of the receptors prior to and after toxin incubation may answer the open question of the origin of the large confining rafts. Simultaneous dual-color imaging of receptors and labeled toxins can clarify this. So far, the receptor-toxin complex has been monitored and the binding of the toxin might induce and stabilize the raft that is exploited by the toxin monomers to locally concentrate themselves. Indeed, it has been proposed that large lipid rafts are somehow stabilized by the cell and act as signaling platforms. It is also interesting to study the oligomerization dynamics of the toxins in these platforms.

For the single-molecule tracking under applied force, improvements should be made in culturing cells in microfluidic chips by either using a small flow during culturing or using a sticker technology, where the chip is bonded onto a coverslip full of normally cultured cells just before the experiments. Such improvements will

greatly increase the number of trajectories and provide the statistics necessary to study the interaction between confining zones and the cytoskeleton. Furthermore, experiments in the presence of Latruculin B, which depolymerizes the actin skeleton and cholesterol oxidase, which extracts cell cholesterol are necessary to confirm the current interpretations. Actin depolymerization should increase the displacement of a given domain under the same force, and could suppress the return to the initial position upon switching off of the drag force. It should also reduce the amount of encountered boundaries. Disaggregation of lipid rafts should also remove the elastic deformation because the toxin receptor only interacts with the cytoskeleton through its confining domain and not directly by itself. To make quantitative measurements, the velocity of the flow has to be known at the position of the nanoparticle. To this end, we suggest fluorescent labels to measure it directly during the experiment using unbound fluorescent labels.

Another interesting application of the introduced method of hydrodynamic drag force amplification would be a measurement of k_{off} rate for an interacting molecular pair. First, the results should be tested by using a well studied molecular pair with known interaction strength. The method can then be extended to a pair that is more difficult to measure by conventional techniques.

Appendix A

Protocols

A.1 Synthesis and functionalization of nanoparticles

$Y_{0.6}Eu_{0.4}VO_4$ nanoparticles were prepared as described in [57,202,205,305]. Briefly, the nanoparticles were prepared from an aqueous solution of sodium orthovanadate by drop-wise adding an aqueous solution of yttrium and europium nitrate with the desired europium content ($[Y^{3+}] + [Eu^{3+}] = [VO_4^-]$). The solution was then purified by dialysis against pure water. The particles were coated by a thin silica layer by absorption of silicate (SiO_2^-) ions onto the surface from an added tetramethylammonium silicate solution. The nanoparticles were then functionalized with a silicon alkoxysilane bearing amino groups (3-aminopropyltriethoxysilane, APTES), which is polymerized around the particles through a hydrolysis / condensation reaction. The final thickness of the amino silane shell is about 2.6 nm, with 1.4 reactive amino groups per nm^2.

We then coupled the APTES-coated europium-doped nanoparticles to α- and ϵ-toxins produced by the *C. septicum* and *C. perfringens* bacteria, respectively, via the amine-reactive cross-linker bis (sulfosuccinimidyl) suberate (BS_3) [205]. First, the NPs are size selected and aggregates are removed. The APTES-coated NPs are not stable in water and are therefore transferred into ultra pure DMSO. The NP-BS_3 coupling reaction is achieved in 2 ml DMSO under argon atmosphere, at 60 °C with 30 mg BS_3 (in large excess with respect to NPs) and 4 µL triethylamine (TEA). The reaction takes place for 7 days and is stopped by removing excess BS_3 and the TEA by centrifugation. The NPs are then incubated with the toxins in a phosphate buffer solution at pH 7.4 for 1 h at 37 °C in a shaker. After removing excess unbound toxins by centrifugation, the NP-toxin complexes were stored at −80 °C. The NP-protein coupling ratio can be adjusted by varying the ratio of the toxin concentration to the nanoparticle concentration. To speed up the reaction, high nanoparticle concentrations are used. We used a toxin concentration of 1 µM

in vanadate ions for a nanoparticle concentration of 8 mM. A BCA test showed that we have achieved a coupling ratio of $1:1$ for the ϵ-toxin to nanoparticles [202]. Since the distribution is Poissonian peaked at one, the fraction of NPs bound to zero, one and two or more toxins are 37 %, 37 %, and 26 %, respectively. Nanoparticles with- out toxins do not bind to the cells and are rinsed away. Given the size of the NPs, it is improbable that more than one toxin is present on the same area of the NP surface allowing simultaneous binding to more than one receptor. Furthermore, the binding ability of a fraction of the toxins may be impaired by the coupling to the NPs. We therefore estimate that the fraction of NPs bound to more than one receptor is less than 10 %.

A.2 MDCK cell culture and sample preparation

Madin-Darby canine kidney (MDCK) cells were cultured in culture medium (CM) (DMEM, 10 % fetal calf serum (FCS), 1 % penicillin-streptomycin) at 37 °C. For tracking experiments, cells were trypsinated two days before an experiment and transferred onto acid bath treated glass coverslips and grown until confluent. The medium was replaced by an observation medium (OM) (HBSS + 10 mM HEPES, 1 % FCS) just before the tracking experiment. Cells were not used for longer than 10 weeks for culture and not longer than 1.5 hours for experiments.

A.3 Single-molecule tracking experiments

Tracking experiments were performed with a wide-field inverted microscope (Zeiss Axiovert 100) equipped with a 63x, NA = 1.4 oil immersion objective. Images were recorded with an EM-CCD (Roper Scientific QuantEM:512SC, EM Gain: 750). The nanoparticles were excited with an Ar^+-ion laser using the 465.8 nm line. The emission of the NPs was collected through a 617/8M filter (Chroma). Confluent cells on coverslips were incubated with 0.04 nM labeled α- or ϵ-toxin (which can form oligomers) or ϵ-prototoxin (which cannot form oligomers) for 20 minutes at room temperature. The sample was then rinsed three times with OM to remove non bound nanoparticles. We recorded images at a frame rate of 20 Hz and an excitation intensity of 0.25 kW/cm^2 at room temperature or 37 °C.

A.4 Nanoparticle size determination

Given that the nanoparticles are not single emitters, but are made up of multiple emitters, it is possible to relate their size to their fluorescence intensity, as described in reference [306]. The radius R of the nanoparticle is related to the number of emitted photons via:

$$R = \left(\frac{3\, N_{ph}\, V_{Unit\,cell}}{16\, \pi\, x\, Q\, \omega\, n_{col}}\, t_{acq} \right)^{1/3} \tag{A.1}$$

The number of emitted photons N_{ph} during the acquisition time t_{acq} is obtained from the volume under the Gaussian fit to the image. The volume of the first 10 images is averaged and then divided by the camera gain factor (258.6 counts/photon for the settings: 5MHz, standard gain 3x and EM gain 750 x) to calculate the number of photons from the number of recorded counts. The size of the Eu nanoparticle unit cell $V_{Unitcell}$ is $0.323\,\text{nm}^3$. The doping concentration x of the nanoparticles used for tracking is $40\,\%$ and their quantum efficiency Q is $4\,\%$. ω is a parameter that contains the absorption cross-section σ of the nanoparticles at the excitation wavelength, which is $2.82 \times 10^{-21}\,\text{cm}^{-2}$, multiplied by the excitation intensity I_{Inc}, divided by the energy of the excitation photon, which is $2.66\,\text{eV}$. The excitation intensity I_{Inc} depends on the position of the nanoparticle on the coverslip. This dependence is modeled by a Gaussian fit of the imaged laser beam on a clean glass coverslip, which is taken before each experiment. The fraction of collected photons n_{col} includes the solid angle collected by the objective, transmission through the optical elements and the quantum efficiency of the camera. The acquisition time t_{acq} is normally $50\,\text{ms}$ and the typical number of detected photons for this period is 50.

A.5   Lifetime measurements of a colloidal solution

Lifetime measurements were performed in a $90°$ detection scheme, as shown in figure A.1 a). The sample is excited by the Ar^+-ion laser using the $465.8\,\text{nm}$ line. The beam is focused onto the chopper to reduce the time it takes to chop the beam. For low chopping rates, a commercial chopper (Princeton Applied Research Model 197) was sufficient and for higher rates we used a homemade chopper. The emission was gathered by two lenses and filtered by a 617/8M emission filter (Chroma). The signal was recorded by a photomultiplier tube (PMT) (Hamamatsu $\text{R}636-10$) and a digital oscilloscope, averaging 264 cycles.

A.6   Spectral measurements of a colloidal solution

The spectrum of a colloidal nanoparticle solution was measured in a $90°$ detection scheme, as shown in figure A.1 b). The sample is excited by the Ar^+-ion laser using

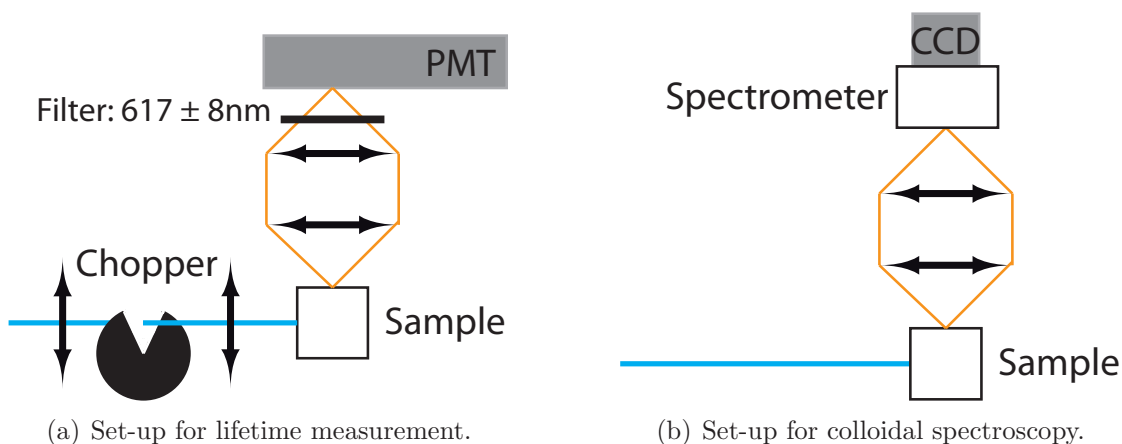(a) Set-up for lifetime measurement.   (b) Set-up for colloidal spectroscopy.

Figure A.1: Set-up for colloidal measurements. The blue beam depicts the excitation light and the orange light represents the emitted fluorescence.

the 465.8 nm line. The emission was gathered and focused by two lenses onto the entrance slit of the spectrometer. The Spectrum is recorded with a liquid-nitrogen cooled CCD camera (Princeton Instruments LN/CCD-400-PB 400x1340 pixels, back-illuminated).

Disruption of actin filaments

Cells were incubated for 20 minutes with 500 nM Latrunculin B (Calbiochem) in HBSS + 10 mM HEPES to depolymerize the actin network. Successful depolymerization was confirmed by eye. Latrunculin B was kept in the solution during experiments.

Cholesterol extraction

Cells were incubated for 30 minutes with 20 U/mL Cholesterol Oxidase (Calbiochem) in HBSS + 10 mM HEPES. Quantification of the extracted cholesterol by the Amplex red cholesterol assay kit (Invitrogen) revealed the extraction of $27 \pm 2\%$ of total cholesterol in our experimental conditions A.2.
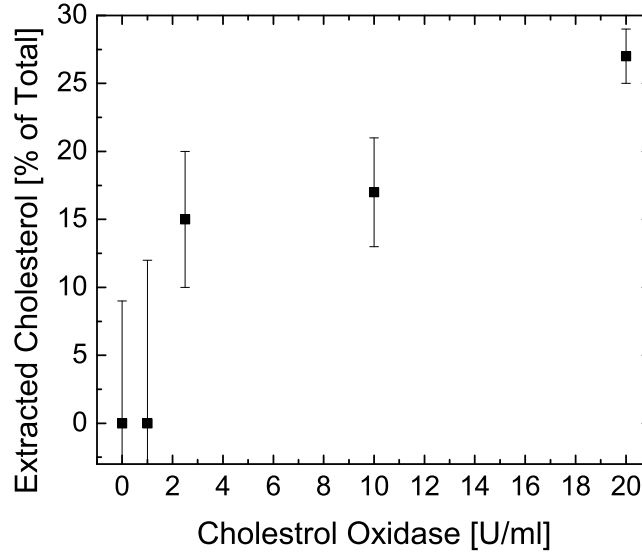
Figure A.2: Extracted Cholesterol percentage with respect to the total cell cholesterol by choles-
terol oxidase treatment at 37 °C and an incubation time of 30 minutes.

Mitochondrial viability (MTT) assay

We used a mitochondrial viability assay (MTT assay Sigma) to determine the tox-
icity of nanoparticles and to measure the toxicity of toxins after Latrunculin B and
cholesterol oxidase treatment. Here, MDCK cells were grown in 24 wells in normal
culture medium (DMEM, 10 % FCS, 1 % penicillin-streptomycin) until confluent.
The medium was replaced by observation medium (HBSS + 10 mM HEPES, 1 %
FCS). Cells were incubated with toxins or nanoparticles for 1 hour. After rinsing
of the wells, we added 250 µl PBS with 25 µl MTT agent (5 mg/ml) to each well
and incubated for 3 hours at 37 °C. Cells were then lysed and incubated over night
at 37 °C. Cell viability was tested by comparing the absorption at 530 nm to the
absorption at 650 nm according to the manufacturer's protocol.

Preparation of PDMS microchannels

The polydimethylsiloxane (PDMS) is molded using the dry film photoresist soft
lithography technique [298]. The master mold of thickness 49 ± 2 µm was etched
into Eternal Laminar E8020 negative films. The photoresist layers for the master
mold were laminated onto a clean glass slide using an office laminator at 100 °C

until the desired channel height of the main channel was reached. The photoresist film was exposed to UV light through a photo mask with the desired channel architecture. The photoresist is developed by immersion in an aqueous bath of carbonate potassium at 1% mass concentration. PDMS (Dow Corning SYLGARD 184, 1/10 ratio of curing agent to bulk material) is then poured over the master mold and cured for 3 hours at $70\,°C$. After peeling-off, the cured PDMS is sealed by plasma bonding onto a microscope glass coverslip.

Growth of MDCK cells in PDMS microchannels

Culture medium (CM) (DMEM, 10% fetal calf serum (FCS), 1% penicillin - streptomycin) is injected into the channel one day prior to cell injection and the channel is incubated overnight at $37\,°C$ to remove gas from the PDMS that would interfere with the growth of cells by forming bubbles in the channel. Cells were trypsinated and resuspended in CM. After concentrating the cells by centrifugation to a high concentration ($\sim 8 \times 10^7$ cells/ml), they are injected into the channel and incubated overnight at $37\,°C$. Cells are used the next day for experiments. This method for cell growth in microchannels is not optimal and the yield of microfluidic chips that contain healthy cells is limited due to the poor circulation of medium during the growth phase of cells. To improve this we suggest to grow cells under a small flow or to implement the molecular sticker method, where cells are first grown normally on a glass coverslip and the PDMS chip is added just before the experiment [299].

Tracking of receptors in microfluidic chips

For the tracking experiment, the microfluidic chip is mounted on a wide-field inverted microscope (Zeiss Axiovert 100) equipped with a 63x, NA = 1.4 oil immersion objective. Two syringe pumps are attached to the two inputs of the chip, one contains observation medium (OM) (HBSS + $10\,mM$ HEPES, 1% FCS) and the other contains a solution of ϵ-prototoxin functionalized nanoparticles at a concentration of $0.05\,mM$ in vanadate ions. First, the channel is rinsed with OM through the first input with a low flow rate of $\sim 1\,µL/min$. Nanoparticles are then injected through the second input and incubated with the cells for 30 minutes. The channel is rinsed with OM through the first input at a low flow rate of $1\,µL/min$ to remove unbound nanoparticles. The channel design with two inputs provides an easy system to remove unbound nanoparticles that would increase the background fluorescence.

For tracking experiments under external force, images of the receptors are recorded with an EM-CCD (Roper Scientific QuantEM:512SC). The nanoparticles are excited with an Ar^+-ion laser using the 465.8 nm line. The emission of the NPs is collected through a 617/8M filter (Chroma). We record images at frame rates down to 20 Hz and an excitation intensity of $0.25 \, \text{kW/cm}^2$ at room temperature or 37 °C. The motion of the receptor is first recorded without flow to check if it behaves normally, then its motion is tracked under external force, by applying a flow through the syringe pump containing OM.

Transfection with end-binding protein 3-green fluorescent protein (EB3-GFP)

First a stock solution of EB3-GFP DNA in phosphate buffer (PBS) is prepared at a concentration of 0.1 g/L. 3 µL *Fugene* is diluted in 90 µl PBS and added to 10 µL of the EB3-GFP DNA solution and incubated for 20 minutes. The solution is added to 750 µL of culture medium and added to the cells for 5 hours. After replacing the solution with culture medium, the cells are incubated for 24 hours to give them time to express the protein. All reagents for the transfection along with support was provided by Cedric Bouzigues.

Labeling GM1 molecules with cholera toxin subunit B-Alexa488 (CT-B-Alexa488)

Monosialotetrahexosylgangliosides (GM1) are membrane molecules that are considered to be recruited into lipid rafts [116, 246, 302]. These raft markers can be cross-linked with cholera toxin, which binds up to five GM1 receptors [303, 304]. The GM1 receptors are labeled by adding 100 µL of a $10 - 100 \, \text{µg/µL}$ solution of cholera toxin subunit B coupled to Alexa488 (CT-B-Alexa488, Molecular Probes) and incubating for 15 minutes at 37 °C. The cells are rinsed to remove excess CT-B.

Appendix B

Algorithms

B.1   Mean square displacement (MSD) analysis

The mean-squares-displacement (MSD) analysis was performed according to references [72, 73, 213]. The MSD was evaluated in X, Y and R using equation B.1, however, only values as a function of R were considered for this work. MSD points were calculated for time lags τ shorter than the total trajectory length divided by 5 to avoid fitting data points with too large of an error. The diffusion coefficient (D_{MSD}) was extracted from a linear fit of the first 3 points, while the positioning error was obtained from the offset of the liner fit. The complete MSD curve was then fitted with equation B.2 to obtain the domain size (L_{MSD}).

$$MSD(n\delta t) =$$
$$\frac{1}{N-1-n}\sum_{j=1}^{N-1-n}[x(j\delta t + n\delta t) - x(j\delta t)]^2 + [y(j\delta t + n\delta t) - y(j\delta t)]^2 \quad (B.1)$$

$$MSD(n\delta t) = \frac{L_{MSD}^2}{3} - \frac{32L_{MSD}^2}{\pi^4}\sum_{n=1(odd)}^{\infty}\frac{1}{n^4}exp\left\{-\frac{1}{2}\left(\frac{n\pi}{L_{MSD}}\right)^2 2Dt\right\} \quad (B.2)$$

$$D_{MSD} = slope\,(\tau_{1-3})/4 \quad (B.3)$$

B.2   Broyden-Fletcher-Goldfarb-Shanno (BFGS) Algorithm

The Broyden-Fletcher-Goldfarb-Shanno (BFGS) Algorithm is a *quasi-Newton* or *variable metric* method in multiple dimensions that accumulates information from successive minimizations so that many such minimizations lead to the exact minimum of the function. It was implemented as presented in reference [307]. It is

assumed that the function $f(x)$ that is to be minimized can be approximated as a quadratic function,

$$f(x) \approx c - b \cdot x + \frac{1}{2}x \cdot A \cdot x \qquad (B.4)$$

where b and A contain the free parameters of the function.

The idea of the BFGS algorithm is to build up, iteratively, a good approximation to the inverse Hessian matrix A^{-1}. To this end, the method builds a sequence of matrices H_i, such that

$$lim_{i \to \infty} H_i = A^{-1} \qquad (B.5)$$

Near the current position x_i , the value of the function $f(x)$ can be approximated by

$$f(x) = f(x_i) + (x - x_i) \cdot \nabla f(x_i) + \frac{1}{2}(x - x_i) \cdot A \cdot (x - x_i) \qquad (B.6)$$

where

$$\nabla f(x) = \nabla f(x_i) + A \cdot (x - x_i) \qquad (B.7)$$

To determine the next iteration point, we set $\nabla f(x) = 0$:

$$x - x_i = -A^{-1} \cdot \nabla f(x_i) \qquad (B.8)$$

where $x - x_i$ is the Newton step that needs to be taken to minimize the function. The quality of the evaluated step size thus depends on the approximation of A^{-1}. To further improve the minimization, backtracking is often used, because if the function is too far from its minimum, the whole Newton step $x - x_i$ would be too large. To this end, a new position x_{new} is determined from the previous position x_{old} and from the Newton step $p = x - x_i$ as follows:

$$x_{new} = x_{old} + \lambda p \qquad (0 < \lambda \leq 1) \qquad (B.9)$$

The goal is to find λ such that $f(x_{old} + \lambda p)$ has decreased sufficiently.

After one iteration with a Newton step p, the next Hessian matrix H_{i+1} is calculated using the previous matrix H_i plus a correction that includes the two vectors $x_{i+1} - x_i$ and $\nabla f_{i+1} - \nabla f_i$ via

$$H_{i+1} = H_i + \frac{(x_{i+1}-x_i) \otimes (x_{i+1}-x_i)}{(x_{i+1}-x_i) \cdot (\nabla f_{i+1} - \nabla f_i)}$$
$$- \frac{[H_i \cdot (\nabla f_{i+1} - \nabla f_i)] \otimes [H_i \cdot (\nabla f_{i+1} - \nabla f_i)]}{(\nabla f_{i+1} - \nabla f_i) \cdot H_i \cdot (\nabla f_{i+1} - \nabla f_i)}$$
$$+ \; [(\nabla f_{i+1} - \nabla f_i) \cdot H_i \cdot (\nabla f_{i+1} - \nabla f_i)] \; u \otimes u \qquad \text{(B.10)}$$

where $\otimes$ is the outer product of the two vectors and u is defined as

$$u \equiv \frac{(x_{i+1} - x_i)}{(x_{i+1} - x_i) \cdot (\nabla f_{i+1} - \nabla f_i)} - \frac{H_i \cdot (\nabla f_{i+1} - \nabla f_i)}{(\nabla f_{i+1} - \nabla f_i) \cdot H_i \cdot (\nabla f_{i+1} - \nabla f_i)} \quad \text{(B.11)}$$

B.3 Monte Carlo optimization

The Monte Carlo optimization shifts all variables x by a random amount and computes the value of the function $f(x)$ at the new point. We use this technique after the previously introduced BFGS algorithm to further minimize the function and determine the error on the calculated variables. We use $N = 50000$ iterations in our algorithm and the maximal amplitude of variation is $15\,\%$ for the forces and $15\,\%$ for the diffusion coefficient. If the change in variables yields a better value of the function $f(x)$, the Monte Carlo step is accepted and it is rejected if the new parameters do not yield a better value. The optimal final value is then the mean of all visited values and given by

$$\langle f \rangle = \frac{1}{N} \sum_i f(x_i) \qquad \text{(B.12)}$$

while the standard deviation of the value is given by

$$\langle \sigma_f \rangle = \left[\left(\frac{1}{N} \sum_i f(x_i)^2 \right) - \langle f \rangle^2 \right]^{1/2} \qquad \text{(B.13)}$$

Figure B.1 shows the influence of the number of iterations N of the Monte Carlo optimization. The inferred diffusion coefficient bias is shown for four different N with respect to the confinement factor u. 50000 iterations are shown in black, 50 iterations (red), 500000 (blue), 5 (green) for numerical trajectories with fixed diffusion coefficient of $0.075\,\mu\text{m}^2/\text{s}$, $51.3\,\text{ms}$ acquisition time, 1000 points and a spring constant that is varied from 0.002 to 0.5 pN. 50000 iterations are enough to give an accurate result. In fact, 50 iterations also provide the correct inferred value, however, the error on the value is larger because it is related to the number of Monte Carlo iterations.
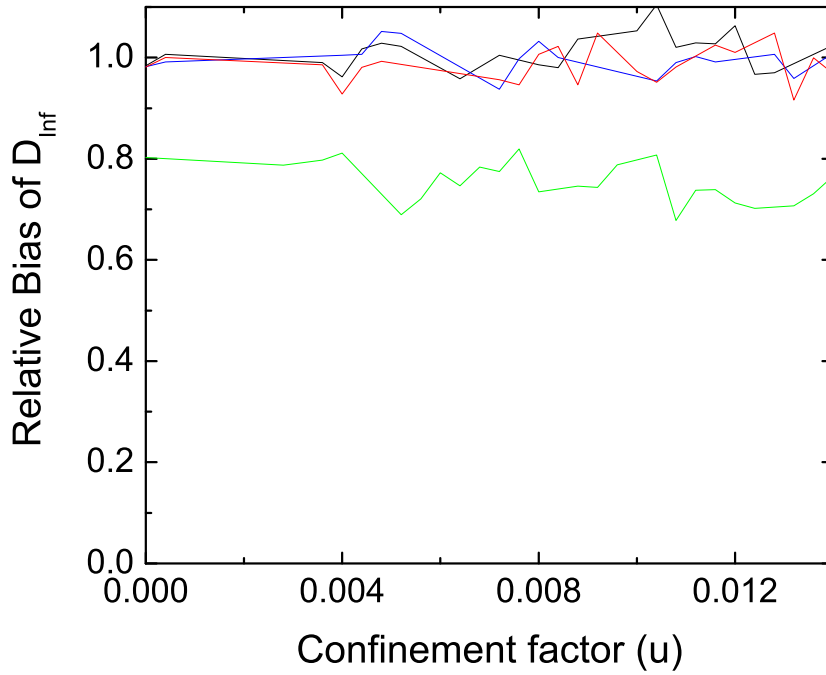
Figure B.1: The inferred diffusion coefficient bias is shown for four different iterations N with respect to the confinement factor u. 50000 iterations are shown in black, 50 iterations (red), 500000 (blue), 5 (green) for numerical trajectories with fixed diffusion coefficient of $0.075\,\mu\mathrm{m}^2/\mathrm{s}$, $51.3\,\mathrm{ms}$ acquisition time, 1000 points and a spring constant that is varied from 0.002 to $0.5\,\mathrm{pN}$. 50000 iterations are enough to give an accurate result. In fact, 50 iterations also provide the correct inferred value, however, the error on the value is larger because it is related to the number of Monte Carlo iterations.

B.4   Kolmogorov-Smirnov (KS) test

The Kolmogorov-Smirnov test (KS-test) tries to determine if two data sets differ significantly. The advantage of the KS-test is that it makes no assumption about the distribution of the data, i.e. it is nonparametric [308].

A cumulative distribution plot is prepared by counting which fraction of the data set is below the value on the x-axis of the tested variable. The D-value is then calculated for the point where the difference between the two cumulative distribution functions is the largest and a P-value can be associated to it via the Kolmogorov distribution. The P-value is the probability of obtaining a test statistic as the one that was observed. This test is sensitive to differences in the location and the shape of the empirical cumulative distribution function. However, a P-value between two distributions is not helpful unless a threshold P-value is defined. If the measured P-value is below the threshold value, the two distributions are deemed different. This threshold was estimated in this work from a

Monte Carlo simulation with 10000 steps, that combines both data sets that are compared and randomly splits this set into two separate sets of sizes equal to those of the real data sets. These two artificial sets are no longer from different distributions because the data has been mixed. The two sets are then compared to each other in a KS-test giving a D-value and P-value. The threshold P-value is here defined to be more than one standard deviation smaller than the mean P-value from all the Monte Carlo iterations.

List of Figures

Bibliography

[1] J.-B. Masson, D. Casanova, S. Türkcan, G. Voisinne, M. R. Popoff, M. Vergassola, and A. Alexandrou: *Inferring Maps of Forces inside Cell Membrane Microdomains.* Physical Review Letters **102**, 48103 (2009).

[2] B. Alberts, D. Bray, J. Lewis, M. Raff, K. Roberts, and J. Watson: *Molecular biology of the cell.* Garland Publ., New York, 1994.

[3] L. Wolpert: *How we live and why we die: the secret lives of cells.* Norton, 2009.

[4] S. L. Miller: *A production of amino acids under possible primitive earth conditions.* Science **117**, 528 (1953).

[5] A. Bangham and R. Horne: *Negative staining of phospholipids and their structural modification by surface-active agents as observed in the electron microscope.* Journal of Molecular Biology **8**, 660 (1964).

[6] J. Loeb: *The Recent Development of Biology.* Science **20**, 777 (1904).

[7] E. Gorter and F. Grendel: *On bimolecular layers of lipoids on the chromocytes of the blood.* Journal of Experimental Medicine **41**, 439 (1925).

[8] L. Frye and M. Edidin: *The rapid intermixing of cell surface antigens after formation of mouse-human heterokaryons.* Journal of cell science **7**, 319 (1970).

[9] R. CONE: *Rotational diffusion of rhodopsin in the visual receptor membrane.* Nature **236**, 39 (1972).

[10] M. Edidin: *Lipids on the frontier: a century of cell-membrane bilayers.* Nature Reviews Molecular Cell Biology **4**, 414 (2003).

[11] S. Singer and G. Nicolson: *The fluid mosaic model of the structure of cell membranes.* Science **175**, 720 (1972).

[12] D. Chalfie, M. Tu, Y. Euskirchen, G. Ward, W.W. Prasher: *Green fluorescent protein as a marker gene expression.* Science **263**, 802 (1994).

[13] D. Axelrod, D. Koppel, J. Schlessinger, E. Elson, and W. Webb: *Mobility measurement by analysis of fluorescence photobleaching recovery kinetics.* Biophysical Journal **16**, 1055 (1976).

[14] B. Sprague, R. Pego, D. Stavreva, and J. McNally: *Analysis of binding reactions by fluorescence recovery after photobleaching.* Biophysical Journal **86**, 3473 (2004).

[15] D. Magde, E. Elson, and W. Webb: *Thermodynamic fluctuations in a reacting systemmeasurement by fluorescence correlation spectroscopy.* Physical Review Letters **29**, 705 (1972).

[16] D. S. Banks and C. Fradin: *Anomalous diffusion of proteins due to molecular crowding.* Biophysical Journal **89**, 2960 (2005).

[17] P. Sengupta, K. Garai, J. Balaji, N. Periasamy, and S. Maiti: *Measuring Size Distribution in Highly Heterogeneous Systems with Fluorescence Correlation Spectroscopy.* Biophysical Journal **84**, 1977 (2003).

[18] R. H. Köhler, P. Schwille, W. W. Webb, and M. R. Hanson: *Active protein transport through plastid tubules: velocity quantified by fluorescence correlation spectroscopy.* Journal of cell science **113**, 3921 (2000).

[19] D. Magde, E. Elson, and W. Webb: *Fluorescence correlation spectroscopy. II. An experimental realization.* Biopolymers **13**, 29 (1974).

[20] T. Förster: *Zwischenmolekulare energiewanderung und fluoreszenz.* Annalen der Physik **437**, 55 (1948).

[21] D. L. Andrews and D. S. Bradshaw: *Virtual photons, dipole fields and energy transfer: a quantum electrodynamical approach.* European journal of physics **845**, 845 (2004).

[22] A. Salam: *Resonant transfer of excitation between two molecules using Maxwell fields.* The Journal of chemical physics **122**, 044113 (2005).

[23] A. Salam: *A general formula for the rate of resonant transfer of energy between two electric multipole moments of arbitrary order using molecular quantum electrodynamics.* The Journal of chemical physics **122**, 044112 (2005).

[24] Y. Sako, S. Minoghchi, and T. Yanagida: *Single-molecule imaging of EGFR signalling on the surface of living cells.* Nature cell biology **2**, 168 (2000).

[25] J. R. Silvius and I. R. Nabi: *Fluorescence-quenching and resonance energy transfer studies of lipid microdomains in model and biological membranes.* Molecular membrane biology **23**, 5 (2006).

[26] C. Eggeling, C. Ringemann, R. Medda, G. Schwarzmann, K. Sandhoff, S. Polyakova, V. N. Belov, B. Hein, C. von Middendorff, A. Schönle, and S. W. Hell: *Direct observation of the nanoscale dynamics of membrane lipids in a living cell.* Nature **457**, 1159 (2009).

[27] L. S. Barak and W. W. Webb: *Diffusion of low density lipoprotein-receptor complex on human fibroblasts.* The Journal of cell biology **95**, 846 (1982).

[28] M. De Brabander, G. Geuens, R. Nuydens, M. Moeremans, and J. De Mey: *Probing microtubule-dependent intracellular motility with nanometre particle video ultramicroscopy (nanovid ultramicroscopy).* Cytobios **43**, 273 (1985).

[29] B. Schnapp, J. Gelles, and M. Sheetz: *Nanometer-scale measurements using video light microscopy.* Cell Motility and the Cytoskeleton **10**, 47 (1988).

[30] B. Schnapp, J. Gelles, and M. Sheetz: *Tracking kinesin-driven movements with nanometre-scale precision.* Nature **331**, 450 (1988).

[31] K. Mortensen, L. Churchman, J. Spudich, and H. Flyvbjerg: *Optimized localization analysis for single-molecule tracking and super-resolution microscopy.* Nature Methods **7**, 377 (2010).

[32] Y. Zhang, M. So, A. Loening, H. Yao, S. Gambhir, and J. Rao: *HaloTag protein-mediated site-specific conjugation of bioluminescent proteins to quantum dots.* Angewandte Chemie **118**, 5058 (2006).

[33] A. Gautier, A. Juillerat, C. Heinis, I. R. Corrêa, M. Kindermann, F. Beaufils, and K. Johnsson: *An engineered protein tag for multiprotein labeling in living cells.* Chemistry & biology **15**, 128 (2008).

[34] M. Howarth, W. Liu, P. Sujiet, Y. Zheng, L. F. Marshall, M. M. Schmidt, K. D. Wittrup, M. G. Bawendi, and A. Y. Ting: *Monovalent, reduced-size quantum dots for imaging receptors on living cells.* Nature Methods **5**, 397 (2008).

[35] T. Pons, H. T. Uyeda, I. L. Medintz, and H. Mattoussi: *Hydrodynamic dimensions, electrophoretic mobility, and stability of hydrophilic quantum dots.* J. Phys. Chem. B **110**, 20308 (2006).

[36] G. J. Schütz, G. Kada, V. P. Pastushenko, and H. Schindler: *Properties of lipid microdomains in a muscle cell membrane visualized by single molecule microscopy.* The EMBO journal **19**, 892 (2000).

[37] R. Iino, I. Koyama, and A. Kusumi: *Single Molecule Imaging of Green Fluorescent Proteins in Living Cells: E-Cadherin Forms Oligomers on the Free Cell Surface.* Biophysical Journal **80**, 2667 (2001).

[38] G. Harms, L. Cognet, P. Lommerse, G. Blab, H. Kahr, R. Gamsjäger, H. Spaink, N. Soldatov, C. Romanin, and T. Schmidt: *Single-Molecule Imaging of L-Type Ca^{2+} Channels in Live Cells.* Biophysical Journal **81**, 2639 (2001).

[39] R. Iino and A. Kusumi: *Single-Fluorophore Dynamic Imaging in Living Cells.* Journal of Fluorescence **11**, 187 (2001).

[40] J. Vogelsang, R. Kasper, C. Steinhauer, B. Person, M. Heilemann, M. Sauer, and P. Tinnefeld: *A reducing and oxidizing system minimizes photobleaching and blinking of fluorescent dyes.* Angewandte Chemie International Edition **47**, 5465 (2008).

[41] A. Alivisatos: *Semiconductor clusters, nanocrystals, and quantum dots.* Science **271**, 933 (1996).

[42] M. Dahan, T. Laurence, F. Pinaud, D. S. Chemla, a. P. Alivisatos, M. Sauer, and S. Weiss: *Time-gated biological imaging by use of colloidal quantum dots.* Optics letters **26**, 825 (2001).

[43] P. Reiss, J. Bleuse, and A. Pron: *Highly Luminescent CdSe/ZnSe Core/Shell Nanocrystals of Low Size Dispersion.* Nano Letters **2**, 781 (2002).

[44] M. Dahan, S. Lévi, C. Luccardini, P. Rostaing, B. Riveau, and A. Triller: *Diffusion dynamics of glycine receptors revealed by single-quantum dot tracking.* Science **302**, 442 (2003).

[45] M. Nirmal, B. Dabbousi, M. Bawendi, J. Macklin, J. Trautman, T. Harris, and L. Brus: *Fluorescence intermittency in single cadmium selenide nanocrystals* **383**, 802 (1996).

[46] B. Mahler, P. Spinicelli, S. Buil, X. Quelin, J.-P. Hermier, and B. Dubertret: *Towards non-blinking colloidal quantum dots.* Nature materials **7**, 659 (2008).

[47] X. Wang, X. Ren, K. Kahen, M. a. Hahn, M. Rajeswaran, S. Maccagnano-Zacher, J. Silcox, G. E. Cragg, A. L. Efros, and T. D. Krauss: *Non-blinking semiconductor nanocrystals.* Nature **459**, 5 (2009).

[48] D. R. Larson, W. R. Zipfel, R. M. Williams, S. W. Clark, M. P. Bruchez, F. W. Wise, and W. W. Webb: *Water-soluble quantum dots for multiphoton fluorescence imaging in vivo.* Science **300**, 1434 (2003).

[49] X. Michalet, F. F. Pinaud, L. a. Bentolila, J. M. Tsay, S. Doose, J. J. Li, G. Sundaresan, a. M. Wu, S. S. Gambhir, and S. Weiss: *Quantum dots for live cells, in vivo imaging, and diagnostics.* Science **307**, 538 (2005).

[50] M. De Brabander, H. Geerts, R. Nuyens, R. Nuydens, and F. Cornelissen: *Nanovid microscopy: imaging and quantification of colloidal gold labels in living cells.* Electronic Light Microscopy: Techniques in Modern Biomedical Microscopy 141–155 (1993).

[51] M. J. Saxton and K. Jacobson: *Single-particle tracking: applications to membrane dynamics.* Annual review of biophysics and biomolecular structure **26**, 373 (1997).

[52] A. Kusumi, H. Ike, C. Nakada, K. Murase, and T. Fujiwara: *Single-molecule tracking of membrane molecules: plasma membrane compartmentalization and dynamic assembly of raft-philic signaling molecules.* Seminars in immunology **17**, 3 (2005).

[53] K. Murase, T. Fujiwara, Y. Umemura, K. Suzuki, R. Iino, H. Yamashita, M. Saito, H. Murakoshi, K. Ritchie, and A. Kusumi: *Ultrafine Membrane Compartments for Molecular Diffusion as Revealed by Single Molecule Techniques* **86**, 4075 (2004).

[54] M. Lippitz, M. A. van Dijk, and M. Orrit: *Third-harmonic generation from single gold nanoparticles.* Nano letters **5**, 799 (2005).

[55] V. Jacobsen, P. Stoller, C. Brunner, V. Vogel, and V. Sandoghdar: *Interferometric optical detection and tracking of very small gold nanoparticles at a water-glass interface.* Optics express **14**, 405 (2006).

[56] D. Lasne, G. A. Blab, S. Berciaud, M. Heine, L. Groc, D. Choquet, L. Cognet, and B. Lounis: *Single nanoparticle photothermal tracking (SNaPT) of 5-nm gold beads in live cells.* Biophysical Journal **91**, 4598 (2006).

[57] E. Beaurepaire, B. V., M. Sauviat, D. Giaume, K. Lahlil, A. Mercuri, D. Casanova, A. Huignard, J. Martin, T. Gacoin, J. Boilot, and A. Alexandrou: *Functionalized Fluorescent Oxide Nanoparticles: Artificial Toxins for Sodium Channel Targeting and Imaging at the Single-Molecule Level.* Nano Letters **4**, 2079 (2004).

[58] Y. I. Park, J. H. Kim, K. T. Lee, K.-S. Jeon, H. B. Na, J. H. Yu, H. M. Kim, N. Lee, S. H. Choi, S.-I. Baik, H. Kim, S. P. Park, B.-J. Park, Y. W. Kim, S. H. Lee, S.-Y. Yoon, I. C. Song, W. K. Moon, Y. D. Suh, and T. Hyeon: *Nonblinking and Nonbleaching Upconverting Nanoparticles as an Optical Imaging Nanoprobe and T1 Magnetic Resonance Imaging Contrast Agent.* Advanced Materials **21**, 4467 (2009).

[59] S. Wu, G. Han, D. J. Milliron, S. Aloni, V. Altoe, D. V. Talapin, B. E. Cohen, and P. J. Schuck: *Non-blinking and photostable upconverted luminescence from single lanthanide-doped nanocrystals.* PNAS **106**, 10917 (2009).

[60] G. Mialon, S. Türkcan, G. Dantelle, D. P. Collins, M. Hadjipanayi, R. A. Taylor, T. Gacoin, A. Alexandrou, and J.-P. Boilot: *High up-conversion efficiencies of YVO$_4$:Yb,Er nanoparticles in water down to the single-particle level.* J. Phys. Chem. C **114**, 22449 (2010).

[61] L. Wang, C. Yang, and W. Tan: *Dual-luminophore-doped silica nanoparticles for multiplexed signaling.* Nano letters **5**, 37 (2005).

[62] H. Ow, D. R. Larson, M. Srivastava, B. A. Baird, W. W. Webb, and U. Wiesner: *Bright and stable core-shell fluorescent silica nanoparticles.* Nano letters **5**, 113 (2005).

[63] O. Faklaris, D. Garrot, V. Joshi, F. Druon, J. Boudou, T. Sauvage, P. Georges, P. Curmi, and F. Treussart: *Detection of single photoluminescent diamond nanoparticles in cells and study of the internalization pathway.* Small **4**, 2236 (2008).

[64] O. Faklaris, V. Joshi, T. Irinopoulou, P. Tauc, M. Sennour, H. Girard, J.-C. Arnault, A. Thorel, J.-P. Boudou, P. A. Curmi, and F. Treussart: *Photoluminescent diamond nanoparticles for cell labeling: study of the uptake mechanism in mammalian cells.* ACS nano **3**, 3955 (2009).

[65] M. Tomishige and A. Kusumi: *Compartmentalization of the Erythrocyte Membrane by the Membrane Skeleton: Intercompartmental Hop Diffusion of Band 3.* Molecular Biology of the Cell **10**, 2475 (1999).

[66] Y. Sako and A. Kusumi: *Barriers for lateral diffusion of transferrin receptor in the plasma membrane as characterized by receptor dragging by laser tweezers: fence versus tether.* The Journal of cell biology **129**, 1559 (1995).

[67] Y. Sako, A. Nagafuchi, S. Tsukita, and M. Takeichi: *Movement of E-cadherin on the free cell surface as studied by optical tweezers and single particle tracking: corralling and tethering by the membrane skeleton.* The Journal of cell biology **140**, 1227 (1998).

[68] M. Edidin, S. C. Kuo, and M. P. Sheetz: *Lateral movements of membrane glycoproteins restricted by dynamic cytoplasmic barriers.* Science **254**, 1379 (1991).

[69] I. Peters, Y. van Kooyk, S. van Vliet, B. de Grooth, C. Figdor, and J. Greve: *3D single-particle tracking and optical trap measurements on adhesion proteins.* Cytometry Part A **36**, 189 (1999).

[70] K. Suzuki, R. Sterba, and M. Sheetz: *Outer membrane monolayer domains from two-dimensional surface scanning resistance measurements.* Biophysical Journal **79**, 448 (2000).

[71] L. Oddershede, J. K. Dreyer, S. Grego, S. Brown, and K. Berg-Sørensen: *The Motion of a Single Molecule, the lambda -Receptor, in the Bacterial Outer Membrane.* Biophysical Journal **83**, 3152 (2002).

[72] J. Fourier and A. Freeman: *The analytical theory of heat.* The University Press, 1878.

[73] A. Kusumi, Y. Sako, and M. Yamamoto: *Confined lateral diffusion of membrane receptors as studied by single particle tracking (nanovid microscopy). Effects of calcium-induced differentiation in cultured epithelial cells.* Biophysical Journal **65**, 2021 (1993).

[74] R. Varma and S. Mayor: *GPI-anchored proteins are organized in submicron domains at the cell surface.* Nature **394**, 798 (1998).

[75] T. Feder, I. Brustmascher, J. Slattery, B. Baird, and W. Webb: *Constrained diffusion or immobile fraction on cell surfaces: a new interpretation.* Biophysical Journal **70**, 2767 (1996).

[76] C. M. Anderson, G. N. Georgiou, I. E. Morrison, G. V. Stevenson, and R. J. Cherry: *Tracking of cell surface receptors by fluorescence digital imaging microscopy using a charge-coupled device camera. Low-density lipoprotein and influenza virus receptor mobility at $4°C$.* Journal of cell science **101**, 415 (1992).

[77] R. Simson, E. Sheets, and K. Jacobson: *Detection of temporary lateral confinement of membrane proteins using single-particle tracking analysis.* Biophysical Journal **69**, 989 (1995).

[78] M. Karnovsky, A. Kleinfeld, R. Hoover, and R. Klausner: *The concept of lipid domains in membranes.* The Journal of cell biology **94**, 1 (1982).

[79] K. Simons and E. Ikonen: *Functional rafts in cell membranes.* Nature **387**, 569 (1997).

[80] T. Harder and K. Simons: *Caveolae, DIGs, and the dynamics of sphingolipid-cholesterol microdomains.* Current opinion in cell biology **9**, 534 (1997).

[81] M. Schaaf, W. Koopmans, T. Meckel, J. van Noort, B. Snaar-Jagalska, T. Schmidt, and H. Spaink: *Single-molecule microscopy reveals membrane microdomain organization of cells in a living vertebrate.* Biophysical Journal **97**, 1206 (2009).

[82] D. Marguet, P.-F. Lenne, H. Rigneault, and H.-T. He: *Dynamics in the plasma membrane: how to combine fluidity and order.* The EMBO journal **25**, 3446 (2006).

[83] P. Lenne, L. Wawrezinieck, F. Conchonaud, O. Wurtz, A. Boned, X. Guo, H. Rigneault, H. He, and D. Marguet: *Dynamic molecular confinement in the plasma membrane by microdomains and the cytoskeleton meshwork.* The EMBO Journal **25**, 3245 (2006).

[84] F. Gittes, B. Mickey, J. Nettleton, and J. Howard: *Flexural rigidity of microtubules and actin filaments measured from thermal fluctuations in shape.* The Journal of cell biology **120**, 923 (1993).

[85] J. Podolski and T. Steck: *Distribution of F-actin in Dictyostelium discoideum.* Journal of Biological Chemistry **265**, 1312 (1990).

[86] S. Jin, P. M. Haggie, and A. S. Verkman: *Single-particle tracking of membrane protein diffusion in a potential: simulation, detection, and application to confined diffusion of CFTR Cl- channels.* Biophysical Journal **93**, 1079 (2007).

[87] Y. Sako and A. Kusumi: *Compartmentalized structure of the plasma membrane for receptor movements as revealed by a nanometer-level motion analysis.* The Journal of cell biology **125**, 1251 (1994).

[88] J. Dai and M. Sheetz: *Mechanical properties of neuronal growth cone membranes studied by tether formation with laser optical tweezers.* Biophysical Journal **68**, 988 (1995).

[89] A. Kusumi and Y. Sako: *Cell surface organization by the membrane skeleton.* Current opinion in cell biology **8**, 566 (1996).

[90] A. Tsuji and S. Ohnishi: *Restriction of the lateral motion of band 3 in the erythrocyte membrane by the cytoskeletal network: dependence on spectrin association state.* Biochemistry **25**, 6133 (1986).

[91] M. Saxton: *The membrane skeleton of erythrocytes. A percolation model.* Biophysical Journal **57**, 1167 (1990).

[92] E. D. Sheets, R. Simson, and K. Jacobson: *New insights into membrane dynamics from the analysis of cell surface interactions by physical methods.* Current opinion in cell biology **7**, 707 (1995).

[93] K. Jacobson, E. D. Sheets, and R. Simson: *Revisiting the fluid mosaic model of membranes.* Science **268**, 1441 (1995).

[94] D. Boal and S. Boey: *Barrier-free paths of directed protein motion in the erythrocyte plasma membrane.* Biophysical Journal **69**, 372 (1995).

[95] C. Nakada, K. Ritchie, Y. Oba, M. Nakamura, Y. Hotta, R. Iino, R. S. Kasai, K. Yamaguchi, T. Fujiwara, and A. Kusumi: *Accumulation of anchored proteins forms membrane diffusion barriers during neuronal polarization.* Nature cell biology **5**, 626 (2003).

[96] A. Kusumi, C. Nakada, K. Ritchie, K. Murase, K. Suzuki, H. Murakoshi, R. S. Kasai, J. Kondo, and T. Fujiwara: *Paradigm shift of the plasma membrane concept from the two-dimensional continuum fluid to the partitioned fluid: high-speed single-molecule tracking of membrane molecules.* Annual review of biophysics and biomolecular structure **34**, 351 (2005).

[97] J. A. Dix and A. S. Verkman: *Crowding effects on diffusion in solutions and cells.* Annual review of biophysics **37**, 247 (2008).

[98] J. Bouchaud and A. Georges: *Anomalous diffusion in disordered media: statistical mechanisms, models and physical applications.* Physics reports **195**, 127 (1990).

[99] S. Mayor and M. Rao: *Rafts: scale-dependent, active lipid organization at the cell surface.* Traffic **5**, 231 (2004).

[100] W. Griffiths, A. Jonsson, S. Liu, D. Rai, and Y. Wang: *Electrospray and tandem mass spectrometry in biochemistry.* Biochem J **355**, 545 (2001).

[101] J. Benting, A. Rietveld, I. Ansorge, and K. Simons: *Acyl and alkyl chain length of GPI-anchors is critical for raft association in vitro.* FEBS letters **462**, 47 (1999).

[102] D. Brown and J. Rose: *Sorting of GPI-anchored proteins to glycolipid-enriched membrane subdomains during transport to the apical cell surface.* Cell **68**, 533 (1992).

[103] G. Van Meer, D. Voelker, and G. Feigenson: *Membrane lipids: where they are and how they behave.* Nature reviews molecular cell biology **9**, 112 (2008).

[104] A. G. Lee, N. J. Birdsall, J. C. Metcalfe, P. A. Toon, and G. B. Warren: *Clusters in lipid bilayers and the interpretation of thermal effects in biological membranes.* Biochemistry **13**, 3699 (1974).

[105] F. Wunderlich, W. Kreutz, P. Mahler, a. Ronai, and G. Heppeler: *Thermotropic fluid goes to ordered "discontinuous" phase separation in microsomal lipids of Tetrahymena. An X-ray diffraction study.* Biochemistry **17**, 2005 (1978).

[106] B. Lentz, D. Barrow, and M. Hoechli: *Cholesterol-phosphatidylcholine interactions in multilamellar vesicles.* Biochemistry **19**, 1943 (1980).

[107] T. Kurzchalia and R. Parton: *Membrane microdomains and caveolae.* Current opinion in cell biology **11**, 424 (1999).

[108] R. De Almeida, A. Fedorov, and M. Prieto: *Sphingomyelin/Phosphatidylcholine/Cholesterol Phase Diagram: Boundaries and Composition of Lipid Rafts.* Biophysical Journal **85**, 2406 (2003).

[109] S. Veatch and S. Keller: *Miscibility phase diagrams of giant vesicles containing sphingomyelin.* Physical review letters **94**, 148101 (2005).

[110] T. Baumgart, S. T. Hess, and W. W. Webb: *Imaging coexisting fluid domains in biomembrane models coupling curvature and line tension.* Nature **425**, 821 (2003).

[111] L. J. Pike: *The challenge of lipid rafts.* Journal of lipid research **50 Suppl**, S323 (2009).

[112] A. García-Sáez, S. Chiantia, and P. Schwille: *Effect of line tension on the lateral organization of lipid membranes.* Journal of Biological Chemistry **282**, 33537 (2007).

[113] C. Dietrich: *Lipid Rafts Reconstituted in Model Membranes.* Biophysical Journal **80**, 1417 (2001).

[114] R. de Almeida, L. Loura, A. Fedorov, and M. Prieto: *Lipid rafts have different sizes depending on membrane composition: a time-resolved fluorescence resonance energy transfer study.* Journal of molecular biology **346**, 1109 (2005).

[115] Y. Hsueh, K. Gilbert, C. Trandum, M. Zuckermann, and J. Thewalt: *The effect of ergosterol on dipalmitoylphosphatidylcholine bilayers: a deuterium NMR and calorimetric study.* Biophysical Journal **88**, 1799 (2005).

[116] C. Dietrich, Z. N. Volovyk, M. Levi, N. L. Thompson, and K. Jacobson: *Partitioning of Thy-1, GM1, and cross-linked phospholipid analogs into lipid rafts reconstituted in supported model membrane monolayers.* PNAS **98**, 10642 (2001).

[117] K. Jacobson, O. G. Mouritsen, and R. G. W. Anderson: *Lipid rafts: at a crossroad between cell biology and physics.* Nature cell biology **9**, 7 (2007).

[118] K. Rothberg, Y. Ying, B. Kamen, and R. Anderson: *Cholesterol controls the clustering of the glycophospholipid-anchored membrane receptor for 5-methyltetrahydrofolate.* The Journal of cell biology **111**, 2931 (1990).

[119] P. Casey: *Protein lipidation in cell signaling.* Science **268**, 221 (1995).

[120] A. Kenworthy and M. Edidin: *Distribution of a glycosylphosphatidylinositol-anchored protein at the apical surface of MDCK cells examined at a resolution of¡ 100 Å using imaging fluorescence resonance energy transfer.* The Journal of cell biology **142**, 69 (1998).

[121] S. Mayor, K. G. Rothberg, and F. R. Maxfield: *Sequestration of GPI-anchored proteins in caveolae triggered by cross-linking.* Science **264**, 1948 (1994).

[122] P. Keller, D. Toomre, E. Díaz, J. White, and K. Simons: *Multicolour imaging of post-Golgi sorting and trafficking in live cells.* Nature cell biology **3**, 140 (2001).

[123] T. Friedrichson and T. V. Kurzchalia: *Microdomains of GPI-anchored proteins in living cells revealed by crosslinking.* Nature **394**, 802 (1998).

[124] T. Harder, P. Scheiffele, P. Verkade, and K. Simons: *Lipid domain structure of the plasma membrane revealed by patching of membrane components.* J. Cell Biol **141**, 929 (1998).

[125] E. D. Sheets, G. M. Lee, R. Simson, and K. Jacobson: *Transient confinement of a glycosylphosphatidylinositol-anchored protein in the plasma membrane.* Biochemistry **36**, 12449 (1997).

[126] A. Pralle, P. Keller, K. Simons, E. L. Florin, and J. K. H. Hörber: *Sphingolipid–cholesterol Rafts Diffuse as Small Entities in the Plasma Membrane of Mammalian Cells.* The Journal of Cell Biology **148**, 997 (2000).

[127] P. Sharma, R. Varma, R. Sarasij, Ira, K. Gousset, G. Krishnamoorthy, M. Rao, and S. Mayor: *Nanoscale organization of multiple GPI-anchored proteins in living cell membranes.* Cell **116**, 577 (2004).

[128] T. van Zanten, A. Cambi, M. Koopman, B. Joosten, C. Figdor, and M. Garcia-Parajo: *Hotspots of GPI-anchored proteins and integrin nanoclusters function as nucleation sites for cell adhesion.* Proceedings of the National Academy of Sciences **106**, 18557 (2009).

[129] K. Suzuki, T. Fujiwara, F. Sanematsu, R. Iino, M. Edidin, and A. Kusumi: *GPI-anchored receptor clusters transiently recruit Lyn and Gα for temporary cluster immobilization and Lyn activation: single-molecule tracking study 1.* The Journal of Cell Biology **177**, 717 (2007).

[130] R. Lasserre, X. Guo, F. Conchonaud, Y. Hamon, O. Hawchar, A. Bernard, S. Soudja, P. Lenne, H. Rigneault, D. Olive, *et al.*: *Raft nanodomains contribute to Akt/PKB plasma membrane recruitment and activation.* Nature chemical biology **4**, 538 (2008).

[131] P. Sengupta, A. Hammond, D. Holowka, and B. Baird: *Structural determinants for partitioning of lipids and proteins between coexisting fluid phases in giant plasma membrane vesicles.* Biochimica et Biophysica Acta (BBA)-Biomembranes **1778**, 20 (2008).

[132] H. Kaiser, D. Lingwood, I. Levental, J. Sampaio, L. Kalvodova, L. Rajendran, and K. Simons: *Order of lipid phases in model and plasma membranes.* Proceedings of the National Academy of Sciences **106**, 16645 (2009).

[133] D. Lingwood, J. Ries, P. Schwille, and K. Simons: *Plasma membranes are poised for activation of raft phase coalescence at physiological temperature.* Proceedings of the National Academy of Sciences **105**, 10005 (2008).

[134] S. Akimov, V. Frolov, P. Kuzmin, J. Zimmerberg, Y. Chizmadzhev, and F. Cohen: *Domain formation in membranes caused by lipid wetting of protein.* Physical Review E **77**, 051901 (2008).

[135] M. Allende and R. Proia: *Lubricating cell signaling pathways with gangliosides.* Current opinion in structural biology **12**, 587 (2002).

[136] R. G. W. Anderson and K. Jacobson: *A role for lipid shells in targeting proteins to caveolae, rafts, and other lipid domains.* Science **296**, 1821 (2002).

[137] B. Brügger, B. Glass, P. Haberkant, I. Leibrecht, F. T. Wieland, and H.-G. Kräusslich: *The HIV lipidome: a raft with an unusual composition.* PNAS **103**, 2641 (2006).

[138] A. Ono and E. Freed: *Role of Lipid Rafts in Virus Replication.* Advances in Virus Research **64**, 311 (2005).

[139] K. Jacobson and C. Dietrich: *Looking at lipid rafts?* Trends in cell biology **9**, 87 (1999).

[140] H. Heerklotz, H. Szadkowska, T. Anderson, and J. Seelig: *The Sensitivity of Lipid Domains to Small Perturbations Demonstrated by the Effect of Triton.* Journal of Molecular Biology **329**, 793 (2003).

[141] S. Schuck, M. Honsho, K. Ekroos, A. Shevchenko, and K. Simons: *Resistance of cell membranes to different detergents.* PNAS **100**, 5795 (2003).

[142] B. Brügger, C. Graham, I. Leibrecht, E. Mombelli, A. Jen, F. Wieland, and R. Morris: *The membrane domains occupied by glycosylphosphatidylinositol-anchored prion protein and Thy-1 differ in lipid composition.* The Journal of biological chemistry **279**, 7530 (2004).

[143] H. Ewers, W. Römer, A. Smith, K. Bacia, S. Dmitrieff, W. Chai, R. Mancini, J. Kartenbeck, V. Chambon, L. Berland, *et al.*: *GM1 structure determines SV40-induced membrane invagination and infection.* Nature cell biology **12**, 11 (2009).

[144] W. Römer, L. Berland, V. Chambon, K. Gaus, B. Windschiegl, D. Tenza, M. Aly, V. Fraisier, J. Florent, D. Perrais, *et al.*: *Shiga toxin induces tubular membrane invaginations for its uptake into cells.* Nature **450**, 670 (2007).

[145] N. Destainville and L. Foret: *Thermodynamics of nanocluster phases: A unifying theory.* Physical Review E **77**, 1 (2008).

[146] N. Destainville: *Cluster phases of membrane proteins.* Physical Review E **77**, 3 (2008).

[147] J. J. Sieber, K. I. Willig, R. Heintzmann, S. W. Hell, and T. Lang: *The SNARE motif is essential for the formation of syntaxin clusters in the plasma membrane.* Biophysical Journal **90**, 2843 (2006).

[148] T. Gulik-Krzywicki, M. Seigneuret, and J. Rigaud: *Monomer-oligomer equilibrium of bacteriorhodopsin in reconstituted proteoliposomes. A freeze-fracture electron microscope study.* Journal of Biological Chemistry **262**, 15580 (1987).

[149] A. Weigel, M. Tamkun, and D. Krapf: *Single Molecule Kv2. 1 Channel Dynamics in Live Mammalian Cells.* In: *APS Meeting Abstracts*, 10012. 2010.

[150] K. D. Mossman, G. Campi, J. T. Groves, and M. L. Dustin: *Altered TCR signaling from geometrically repatterned immunological synapses.* Science **310**, 1191 (2005).

[151] B. Lillemeier, M. Mörtelmaier, M. Forstner, J. Huppa, J. Groves, and M. Davis: *TCR and Lat are expressed on separate protein islands on T cell membranes and concatenate during activation.* Nature Immunology **11**, 90 (2009).

[152] K. Salaita, P. M. Nair, R. S. Petit, R. M. Neve, D. Das, J. W. Gray, and J. T. Groves: *Restriction of receptor movement alters cellular response: physical force sensing by EphA2.* Science **327**, 1380 (2010).

[153] Y. M. Umemura, M. Vrljic, S. Y. Nishimura, T. K. Fujiwara, K. G. N. Suzuki, and A. Kusumi: *Both MHC class II and its GPI-anchored form undergo hop diffusion as observed by single-molecule tracking.* Biophysical Journal **95**, 435 (2008).

[154] M. de Brabander, R. Nuydens, A. Ishihara, B. Holifield, K. Jacobson, and H. Geerts: *Lateral diffusion and retrograde movements of individual cell surface components on single motile cells observed with Nanovid microscopy.* The Journal of cell biology **112**, 111 (1991).

[155] A. Kenworthy, B. Nichols, C. Remmert, G. Hendrix, M. Kumar, J. Zimmerberg, and J. Lippincott-Schwartz: *Dynamics of putative raft-associated proteins at the cell surface.* The Journal of cell biology **165**, 735 (2004).

[156] K. M. Wilson, I. E. Morrison, P. R. Smith, N. Fernandez, and R. J. Cherry: *Single particle tracking of cell-surface HLA-DR molecules using R-phycoerythrin labeled monoclonal antibodies and fluorescence digital imaging.* Journal of cell science **109**, 2101 (1996).

[157] K. Ritchie, X.-Y. Shan, J. Kondo, K. Iwasawa, T. Fujiwara, and A. Kusumi: *Detection of non-Brownian diffusion in the cell membrane in single molecule tracking.* Biophysical Journal **88**, 2266 (2005).

[158] K. Suzuki, K. Ritchie, E. Kajikawa, T. Fujiwara, and A. Kusumi: *Rapid Hop Diffusion of a G-Protein-Coupled Receptor in the Plasma Membrane as Revealed by Single-Molecule Techniques.* Biophysical Journal **88**, 3659 (2005).

[159] N. L. Andrews, K. A. Lidke, J. R. Pfeiffer, A. R. Burns, B. S. Wilson, J. M. Oliver, and D. S. Lidke: *Actin restricts FcepsilonRI diffusion and facilitates antigen-induced receptor immobilization.* Nature cell biology **10**, 955 (2008).

[160] S. Y. Nishimura, M. Vrljic, L. O. Klein, H. M. McConnell, and W. E. Moerner: *Cholesterol depletion induces solid-like regions in the plasma membrane.* Biophysical Journal **90**, 927 (2006).

[161] M. Vrljic, S. Y. Nishimura, W. E. Moerner, and H. M. McConnell: *Cholesterol depletion suppresses the translational diffusion of class II major histocompatibility complex proteins in the plasma membrane.* Biophysical Journal **88**, 334 (2005).

[162] J. M. Crane and A. S. Verkman: *Long-range nonanomalous diffusion of quantum dot-labeled aquaporin-1 water channels in the cell plasma membrane.* Biophysical Journal **94**, 702 (2008).

[163] P. H. M. Lommerse, G. A. Blab, L. Cognet, G. S. Harms, B. E. Snaar-jagalska, H. P. Spaink, and T. Schmidt: *Single-Molecule Imaging of the H-Ras Membrane-Anchor Reveals Domains in the Cytoplasmic Leaflet of the Cell Membrane.* Biophysical Journal **86**, 609 (2004).

[164] P. H. M. Lommerse, K. Vastenhoud, N. J. Pirinen, A. I. Magee, H. P. Spaink, and T. Schmidt: *Single-molecule diffusion reveals similar mobility for the Lck, H-ras, and K-ras membrane anchors.* Biophysical Journal **91**, 1090 (2006).

[165] K. Magnusson, M. Gustafsson, K. Holmgren, and B. Johansson: *Small intestinal differentiation in human colon carcinoma HT29 cells has distinct effects on the lateral diffusion of lipids (ganglioside GM1) and proteins (HLA class 1, HLA class 2, and neoplastic epithelial antigens) in the apical cell membrane.* Journal of cellular physiology **143**, 381 (1990).

[166] F. Pinaud, X. Michalet, G. Iyer, E. Margeat, H.-P. Moore, and S. Weiss: *Dynamic partitioning of a glycosyl-phosphatidylinositol-anchored protein in glycosphingolipid-rich microdomains imaged by single-quantum dot tracking.* Traffic **10**, 691 (2009).

[167] H. Tada, H. Higuchi, T. M. Wanatabe, and N. Ohuchi: *In vivo real-time tracking of single quantum dots conjugated with monoclonal anti-HER2 antibody in tumors of mice.* Cancer research **67**, 1138 (2007).

[168] J. Ballard, A. Bryant, D. Stevens, and R. K. Tweten: *Purification and characterization of the lethal toxin (alpha-toxin) of Clostridium septicum.* Infection and immunity **60**, 784 (1992).

[169] R. K. Tweten: *Clostridium perfringens beta toxin and Clostridium septicum alpha toxin: their mechanisms and possible role in pathogenesis.* Veterinary microbiology **82**, 1 (2001).

[170] L. Petit, M. Gibert, D. Gillet, C. Laurent-Winter, P. Boquet, and M. R. Popoff: *Clostridium perfringens Epsilon-Toxin Acts on MDCK Cells by Forming a Large Membrane Complex.* Journal of bacteriology **179**, 6480 (1997).

[171] J. L. McDonel: *Clostridium perfringens toxins (type A, B, C, D, E).* Pharmacology & Therapeutics **10**, 617 (1980).

[172] M. M. Garcia and K. A. McKay: *On the Growth and Survival of Clostridium septicum in Soil.* J. appl. Bact. **32**, 362 (1969).

[173] M. Kahn: *Anaerobic spore-bearing bacteria of the human intestine in health and in certain diseases.* The Journal of Infectious Diseases **35**, 423 (1924).

[174] J. D. Maclennan: *The histotoxic clostridial infections of man.* Bacteriological reviews **26**, 177 (1962).

[175] J. G. Songer: *Clostridial enteric diseases of domestic animals.* Clinical microbiology reviews **9**, 216 (1996).

[176] G. Saunders: *Diagnosing braxy in calves and lambs.* Vet. Med **81**, 1050 (1986).

[177] B. A. W. Bernheimer: *Parallelism in the lethal and heamolytic activity of the toxin of clostridium septicum.* Exp. Med. **80**, 309 (1944).

[178] L. Smith: *The pathogenic anaerobic bacteria.* Springfield, Ill (1975).

[179] M. E. Fernandez-Miyakawa, B. H. Jost, S. J. Billington, and F. A. Uzal: *Lethal effects of Clostridium perfringens epsilon toxin are potentiated by alpha and perfringolysin-O toxins in a mouse model.* Vet Microbiol **127**, 379 (2008).

[180] A. R. Cole, M. Gibert, M. Popoff, D. S. Moss, R. W. Titball, and A. K. Basak: *Clostridium perfringens epsilon-toxin shows structural similarity to the pore-forming toxin aerolysin.* Nature structural & molecular biology **11**, 797 (2004).

[181] J. A. Melton-Witt, L. M. Bentsen, and R. K. Tweten: *Identification of functional domains of Clostridium septicum alpha toxin.* Biochemistry **45**, 14347 (2006).

[182] L. Song, M. Hobaugh, C. Shustak, S. Cheley, H. Bayley, and J. Gouaux: *Structure of staphylococcal alpha-hemolysin, a heptameric transmembrane pore.* Science **274**, 1859 (1996).

[183] S. J. Tilley and H. R. Saibil: *The mechanism of pore formation by bacterial toxins.* Current opinion in structural biology **16**, 230 (2006).

[184] S. Miyata, O. Matsushita, J. Minami, S. Katayama, S. Shimamoto, and a. Okabe: *Cleavage of a C-terminal peptide is essential for heptamerization of Clostridium perfringens epsilon-toxin in the synaptosomal membrane.* The Journal of biological chemistry **276**, 13778 (2001).

[185] V. M. Gordon, K. L. Nelson, J. T. Buckley, V. L. Stevens, R. K. Tweten, P. C. Elwood, and S. H. Leppla: *Clostridium septicum alpha toxin uses glycosylphosphatidylinositol-anchored protein receptors.* The Journal of biological chemistry **274**, 27274 (1999).

[186] M. J. Wichroski, J. A. Melton, C. G. Donahue, R. K. Tweten, and G. E. Ward: *Clostridium septicum Alpha-Toxin Is Active against the Parasitic Protozoan Toxoplasma gondii and Targets Members of the SAG Family of Glycosylphosphatidylinositol-Anchored Surface Proteins.* Infection and Immunity **70**, 4353 (2002).

[187] M. R. Popoff: *Personal Communication* (2010).

[188] S. Miyata, J. Minami, E. Tamai, O. Matsushita, S. Shimamoto, and A. Okabe: *Clostridium perfringens epsilon-toxin forms a heptameric pore within the detergent-insoluble microdomains of Madin-Darby canine kidney cells and rat synaptosomes.* The Journal of biological chemistry **277**, 39463 (2002).

[189] B. R. Sellman, B. L. Kagan, and R. K. Tweten: *Generation of a membrane-bound, oligomerized pre-pore complex is necessary for pore formation by Clostridium septicum alpha toxin.* Molecular microbiology **23**, 551 (1997).

[190] S. Mayor and H. Riezman: *Sorting GPI-anchored proteins.* Nature reviews. Molecular cell biology **5**, 110 (2004).

[191] A. Soler-Jover, J. Blasi, I. Gómez de Aranda, P. Navarro, M. Gibert, M. R. Popoff, and M. Martín-Satué: *Effect of epsilon toxin-GFP on MDCK cells and renal tubules in vivo.* The journal of histochemistry and cytochemistry: official journal of the Histochemistry Society **52**, 931 (2004).

[192] J. Reinhardt, N. Golenhofen, O. Pongs, H. Oberleithner, and A. Schwab: *Migrating transformed MDCK cells are able to structurally polarize a voltage-activated K+ channel.* PNAS **95**, 5378 (1998).

[193] O. V. Vieira, K. Gaus, P. Verkade, J. Fullekrug, W. L. C. Vaz, and K. Simons: *FAPP2, cilium formation, and compartmentalization of the apical membrane in polarized Madin Darby canine kidney (MDCK) cells.* PNAS **103**, 18556 (2006).

[194] K. Matter and I. Mellman: *Mechanisms of cell polarity: in epithelial cells.* Current Opinion in Cell Biology **6**, 545 (1994).

[195] W. J. Nelson: *Adaptation of core mechanisms to generate cell polarity.* Nature **422**, 766 (2003).

[196] C. Yeaman, K. K. Grindstaff, and W. J. Nelson: *New perspectives on mechanisms involved in generating epithelial cell polarity.* Physiological reviews **79**, 73 (1999).

[197] B. Hicks and K. Angelides: *Tracking movements of lipids and Thy1 molecules in the plasmalemma of living fibroblasts by fluorescence video microscopy with nanometer scale precision.* Journal of Membrane Biology **144**, 231 (1995).

[198] L. S. Barak and W. W. Webb: *Fluorescent low density lipoprotein for observation of dynamics of individual receptor complexes on cultured human fibroblasts.* The Journal of cell biology **90**, 595 (1981).

[199] G. Mialon: *Monocristaux YVO$_4$:LN à l'échelle nanométrique: Méchanismes de fluorescence et upconversion.* Ph.D. thesis, Ecole Polytechnique, France (2009).

[200] D. Casanova: *Nanoparticules d'oxyde: développements et applications comme sondes biologiques.* Ph.D. thesis, Ecole Polytechnique, France (2008).

[201] G. Mialon, S. Türkcan, A. Alexandrou, T. Gacoin, and J. Boilot: *New Insights into Size Effects in Luminescent Oxide Nanocrystals.* The Journal of Physical Chemistry C **113**, 18699 (2009).

[202] D. Giaume, M. Poggi, D. Casanova, G. Mialon, K. Lahlil, A. Alexandrou, T. Gacoin, and J.-P. Boilot: *Organic functionalization of luminescent oxide nanoparticles toward their application as biological probes.* Langmuir : the ACS journal of surfaces and colloids **24**, 11018 (2008).

[203] G. Mialon, M. Gohin, T. Gacoin, and J. Boilot: *High Temperature Strategy for Oxide Nanoparticle Synthesis.* ACS Nano **2**, 2505 (2008).

[204] A. Huignard, T. Gacoin, and J.-P. Boilot: *Synthesis and Luminescence Properties of Colloidal YVO 4 :Eu Phosphors.* Chemistry of Materials **12**, 1090 (2000).

[205] D. Casanova, D. Giaume, J.-L. Martin, T. Gacoin, J.-P. Boilot, and A. Alexandrou: *Counting the Number of Proteins Coupled to Single Nanoparticles.* J. Am. Chem. Soc **129**, 12592 (2007).

[206] H. Baker: *The microscope made easy.* Science Heritage, 1742.

[207] A. J. North: *Seeing is believing? A beginners' guide to practical pitfalls in image acquisition.* The Journal of cell biology **172**, 9 (2006).

[208] K. Tanaka, K. Suzuki, Y. Shirai, S. Shibutani, M. Miyahara, H. Tsuboi, M. Yahara, A. Yoshimura, S. Mayor, T. Fujiwara, *et al.*: *Membrane molecules mobile even after chemical fixation.* Nature Methods (2010).

[209] G. M. Lee, B. Johnstone, K. Jacobson, and B. Caterson: *The dynamic structure of the pericellular matrix on living cells.* The Journal of cell biology **123**, 1899 (1993).

[210] G. M. Lee, F. Zhang, A. Ishihara, C. L. McNeil, and K. A. Jacobson: *Unconfined lateral diffusion and an estimate of pericellular matrix viscosity revealed by measuring the mobility of gold-tagged lipids.* The Journal of cell biology **120**, 25 (1993).

[211] R. E. Thompson, D. R. Larson, and W. W. Webb: *Precise nanometer localization analysis for individual fluorescent probes.* Biophysical Journal **82**, 2775 (2002).

[212] F. Daumas, N. Destainville, C. Millot, A. Lopez, D. Dean, and L. Salome: *Confined Diffusion Without Fences of a G-Protein-Coupled Receptor as Revealed by Single Particle Tracking.* Biophysical Journal **84**, 356 (2003).

[213] H. Qian, M. P. Sheetz, and E. L. Elson: *Single particle tracking. Analysis of diffusion and flow in two-dimensional systems.* Biophysical Journal **60**, 910 (1991).

[214] A. Kusumi, Y. Sako, and M. Yamamoto: *Confined Lateral Diffusion of Membrane Receptors as Studied by Single Particle Tracking (Nanovid Microscopy). Effects of Calcium-Induced Differentiation in Cultured Epithelial Cells.* Biophysical Journal **65**, 2021 (1993).

[215] G. Voisinne, A. Alexandrou, and J.-B. Masson: *Quantifying biomolecule diffusivity using an optimal Bayesian method.* Biophysical Journal **98**, 596 (2010).

[216] H. Risken: *The Fokker-Planck equation: Methods of solution and applications.* Springer Verlag, 1996.

[217] T. Cover and J. Thomas: *Elements of Information Theory.* Wiley-Interscience, Hoboken, NJ., 2006.

[218] D. Montiel, H. Cang, and H. Yang.: *2006. Quantitative characterization of changes in dynamical behavior for single-particle tracking studies.* J. Phys. Chem. B. **110**, 1976319770 (2006).

[219] H. A. Kramers: *Brownian motion in a field of force and the diffusion model of chemical reactions.* Physica **7**, 284 (1940).

[220] V. M. Gordon, K. L. Nelson, J. T. Buckley, V. L. Stevens, R. K. Tweten, P. C. Elwood, and S. H. Leppla: *Clostridium septicum alpha toxin uses glycosylphosphatidylinositol-anchored protein receptors.* The Journal of biological chemistry **274**, 27274 (1999).

[221] R. Ariew: *Ockham's razor: A historical and philosophical analysis of Ockham's principle of parsimony.* Ph.D. thesis, University of Illinois at Urbana-Champaign (1976).

[222] J. Lee, M. Gustafsson, K.-E. Magnusson, and K. Jacobson: *The Direction Membrane Locomoting of Lipid Flow Polymorphonuclear Leukocytes.* Science **247**, 1229 (1990).

[223] M. Sheetz, N. Baumrind, D. Wayne, and A. Pearlman: *Concentration of membrane antigens by forward transport and trapping in neuronal growth cones.* Cell **61**, 231 (1990).

[224] C. Dietrich, B. Yang, T. Fujiwara, A. Kusumi, and K. Jacobson: *Relationship of Lipid Rafts to Transient Confinement Zones Detected by Single Particle Tracking.* Biophysical Journal **82**, 274 (2002).

[225] S. Reinsch and E. Karsenti: *Orientation of spindle axis and distribution of plasma membrane proteins during cell division in polarized MDCKII cells.* The Journal of cell biology **126**, 1509 (1994).

[226] K. C. Kirkbride, B. N. Ray, and G. C. Blobe: *Cell-surface co-receptors: emerging roles in signaling and human disease.* Trends in biochemical sciences **30**, 611 (2005).

[227] G. Kustermans, J. Piette, and S. Legrand-Poels: *Actin-targeting natural compounds as tools to study the role of actin cytoskeleton in signal transduction.* Biochemical pharmacology **76**, 1310 (2008).

[228] J. S. Allingham, V. A. Klenchin, and I. Rayment: *Actin-targeting natural products: structures, properties and mechanisms of action.* Cellular and molecular life sciences : CMLS **63**, 2119 (2006).

[229] E. Patzer, R. Wagner, and Y. Barenholz: *Cholesterol oxidase as a probe for studying membrane organisation.* Nature **274**, 394 (1978).

[230] Y. Lange: *Tracking cell cholesterol with cholesterol oxidase.* Journal of lipid research **33**, 315 (1992).

[231] X. Xu and E. London: *The effect of sterol structure on membrane lipid domains reveals how cholesterol can induce lipid domain formation.* Biochemistry **39**, 843 (2000).

[232] S. Miyata, J. Minami, E. Tamai, O. Matsushita, S. Shimamoto, and A. Okabe: *Clostridium perfringens epsilon-toxin forms a heptameric pore within the detergent-insoluble microdomains of Madin-Darby canine kidney cells and rat synaptosomes.* J. Biol. Chem. **277**, 39463 (2002).

[233] E. A. Reits and J. J. Neefjes: *From fixed to FRAP: measuring protein mobility and activity in living cells.* Nature cell biology **3**, E145 (2001).

[234] P. G. Saffman and M. Delbrück: *Brownian motion in biological membranes.* PNAS **72**, 3111 (1975).

[235] D. Meder, M. J. Moreno, P. Verkade, W. L. C. Vaz, and K. Simons: *Phase coexistence and connectivity in the apical membrane of polarized epithelial cells.* PNAS **103**, 329 (2006).

[236] L. J. Foster, C. L. De Hoog, and M. Mann: *Unbiased quantitative proteomics of lipid rafts reveals high specificity for signaling factors.* PNAS **100**, 5813 (2003).

[237] R. R. Sprenger, D. Speijer, J. W. Back, C. G. De Koster, H. Pannekoek, and A. J. G. Horrevoets: *Comparative proteomics of human endothelial cell caveolae and rafts using two-dimensional gel electrophoresis and mass spectrometry.* Electrophoresis **25**, 156 (2004).

[238] K.-A. McMahon, M. Zhu, S. W. Kwon, P. Liu, Y. Zhao, and R. G. W. Anderson: *Detergent-free caveolae proteome suggests an interaction with ER and mitochondria.* Proteomics **6**, 143 (2006).

[239] L. Bini, S. Pacini, S. Liberatori, S. Valensin, M. Pellegrini, R. Raggiaschi, V. Pallini, and C. T. Baldari: *Extensive temporally regulated reorganization of the lipid raft proteome following T-cell antigen receptor triggering.* Biochemical Journal **369**, 301 (2003).

[240] D. L. MacLellan, H. Steen, R. M. Adam, M. Garlick, D. Zurakowski, S. P. Gygi, M. R. Freeman, and K. R. Solomon: *A quantitative proteomic analysis of growth factor-induced compositional changes in lipid rafts of human smooth muscle cells.* Proteomics **5**, 4733 (2005).

[241] J. Fantini: *Cellular and Molecular Life Sciences Visions & Reflections How sphingolipids bind and shape proteins : molecular basis of lipid-protein interactions in lipid shells , rafts and related biomembrane domains.* Cellular and Molecular Life Sciences **60**, 1027 (2003).

[242] A. Lee: *Lipid-protein interactions in biological membranes: a structural perspective.* Biochimica et Biophysica Acta (BBA) - Biomembranes **1612**, 1 (2003).

[243] C. Espenel, E. Margeat, P. Dosset, C. Arduise, C. Le Grimellec, C. A. Royer, C. Boucheix, E. Rubinstein, and P.-E. Milhiet: *Single-molecule analysis of CD9 dynamics and partitioning reveals multiple modes of interaction in the tetraspanin web.* The Journal of cell biology **182**, 765 (2008).

[244] S. Charrin, F. le Naour, O. Silvie, P.-E. Milhiet, C. Boucheix, and E. Rubinstein: *Lateral organization of membrane proteins: tetraspanins spin their web.* The Biochemical journal **420**, 133 (2009).

[245] N. Bertaux, D. Marguet, and A. Serge: *Dynamic multiple-target tracing to probe spatiotemporal cartography of cell membranes.* Nature Methods **5**, 687 (2008).

[246] D. A. Brown and E. London: *Structure and function of sphingolipid- and cholesterol-rich membrane rafts.* The Journal of biological chemistry **275**, 17221 (2000).

[247] D. Lingwood and K. Simons: *Lipid rafts as a membrane-organizing principle.* Science **327**, 46 (2010).

[248] T. Fujiwara, K. Ritchie, H. Murakoshi, K. Jacobson, and A. Kusumi: *Phospholipids undergo hop diffusion in compartmentalized cell membrane.* The Journal of cell biology **157**, 1071 (2002).

[249] E. K. Fridriksson, P. A. Shipkova, E. D. Sheets, D. Holowka, B. Baird, and F. W. McLafferty: *Quantitative analysis of phospholipids in functionally important membrane domains from RBL-2H3 mast cells using tandem high-resolution mass spectrometry.* Biochemistry **38**, 8056 (1999).

[250] L. J. Pike, X. Han, K.-N. Chung, and R. W. Gross: *Lipid rafts are enriched in arachidonic acid and plasmenylethanolamine and their composition is independent of caveolin-1 expression: a quantitative electrospray ionization/mass spectrometric analysis.* Biochemistry **41**, 2075 (2002).

[251] J. a. Lundbaek, P. Birn, A. J. Hansen, R. Sø gaard, C. Nielsen, J. Girshman, M. J. Bruno, S. E. Tape, J. Egebjerg, D. V. Greathouse, G. L. Mattice, R. E. Koeppe, and O. S. Andersen: *Regulation of sodium channel function by bilayer elasticity: the importance of hydrophobic coupling. Effects of Micelle-forming amphiphiles and cholesterol.* The Journal of general physiology **123**, 599 (2004).

[252] O. S. Andersen and R. E. Koeppe: *Bilayer thickness and membrane protein function: an energetic perspective.* Annual review of biophysics and biomolecular structure **36**, 107 (2007).

[253] F. N. R. Petersen, I. Laursen, H. Bohr, and C. H. Nielsen: *Protein-induced bilayer perturbations: Lipid ordering and hydrophobic coupling.* Biochemical and biophysical research communications **387**, 760 (2009).

[254] C. Nielsen, M. Goulian, and O. Andersen: *Energetics of Inclusion-Induced Bilayer Deformations.* Biophysical Journal **74**, 1966 (1998).

[255] C. Nielsen: *Inclusion-Induced Bilayer Deformations: Effects of Monolayer Equilibrium Curvature.* Biophysical Journal **79**, 2583 (2000).

[256] A. J. García-Sáez, S. Chiantia, and P. Schwille: *Effect of line tension on the lateral organization of lipid membranes.* The Journal of biological chemistry **282**, 33537 (2007).

[257] S. Ramadurai, R. Duurkens, V. V. Krasnikov, and B. Poolman: *Lateral diffusion of membrane proteins: consequences of hydrophobic mismatch and lipid composition.* Biophysical Journal **99**, 1482 (2010).

[258] S. Ramadurai, A. Holt, L. V. Schäfer, V. V. Krasnikov, D. T. S. Rijkers, S. J. Marrink, J. A. Killian, and B. Poolman: *Influence of hydrophobic mismatch and amino Acid composition on the lateral diffusion of transmembrane peptides.* Biophysical Journal **99**, 1447 (2010).

[259] J. Piehler: *New methodologies for measuring protein interactions in vivo and in vitro.* Current opinion in structural biology **15**, 4 (2005).

[260] M. A. Cooper: *Label-free screening of bio-molecular interactions.* Analytical and bioanalytical chemistry **377**, 834 (2003).

[261] M. A. Cooper: *Advances in membrane receptor screening and analysis.* Journal of molecular recognition : JMR **17**, 286 (2004).

[262] A. Ashkin: *Acceleration and trapping of particles by radiation pressure.* Physical Review Letters **24**, 156 (1970).

[263] A. Ashkin: *Atomic-Beam Deflection by Resonance-Radiation Pressure.* Physical Review Letters **25**, 1321 (1970).

[264] A. Ashkin: *Trapping of Atoms by Resonance Radiation Pressure.* Physical Review Letters **40**, 729 (1978).

[265] A. Ashkin and J. M. Dziedzic: *Trapping and Manipulation of Viruses and Bacteria.* Science **235**, 1517 (1987).

[266] S. Chu and S. Kron: Int. Quantum Electronics Conf. Tech. Digest (Optical Soc. of Am., Washington, D.C.) 202 (1990).

[267] S. B. Smith, L. Finzi, and C. Bustamante: *Direct mechanical measurements of the elasticity of single DNA molecules by using magnetic beads.* Science **258**, 1122 (1992).

[268] M. Wang, H. Yin, R. Landick, J. Gelles, and S. Block: *Stretching DNA with optical tweezers.* Biophysical Journal **72**, 1335 (1997).

[269] C. Baumann, V. Bloomfield, S. Smith, C. Bustamante, M. Wang, and S. Block: *Stretching of Single Collapsed DNA Molecules.* Biophysical Journal **78**, 1965 (2000).

[270] M. L. Bennink, S. H. Leuba, G. H. Leno, J. Zlatanova, B. G. de Grooth, and J. Greve: *Unfolding individual nucleosomes by stretching single chromatin fibers with optical tweezers.* Nature structural biology **8**, 606 (2001).

[271] J. Liphardt, B. Onoa, S. B. Smith, I. Tinoco, and C. Bustamante: *Reversible unfolding of single RNA molecules by mechanical force.* Science **292**, 733 (2001).

[272] J. Zlatanova and S. H. Leuba: *Stretching and imaging single DNA molecules and chromatin.* Journal of muscle research and cell motility **23**, 377 (2002).

[273] T. Perkins, D. Smith, R. Larson, and S. Chu: *Stretching of a single tethered polymer in a uniform flow.* Science **268**, 83 (1995).

[274] E. Dufresne and D. Grier: *Optical tweezer arrays and optical substrates created with diffractive optics.* Review of Scientific Instruments **69**, 1974 (1998).

[275] J. E. Curtis, B. A. Koss, and D. G. Grier: *Dynamic holographic optical tweezers.* Optics Communications **207**, 169 (2002).

[276] D. G. Grier: *A revolution in optical manipulation.* Nature **424**, 810 (2003).

[277] V. Moy, E. Florin, and H. Gaub: *Intermolecular forces and energies between ligands and receptors.* Science **266**, 257 (1994).

[278] P. Hinterdorfer, W. Baumgartner, H. J. Gruber, K. Schilcher, and H. Schindler: *Detection and localization of individual antibody-antigen recognition events by atomic force microscopy.* PNAS **93**, 3477 (1996).

[279] F. Kienberger, G. Kada, H. Mueller, and P. Hinterdorfer: *Single molecule studies of antibody-antigen interaction strength versus intra-molecular antigen stability.* Journal of molecular biology **347**, 597 (2005).

[280] R. Merkel, P. Nassoy, a. Leung, K. Ritchie, and E. Evans: *Energy landscapes of receptor-ligand bonds explored with dynamic force spectroscopy.* Nature **397**, 50 (1999).

[281] E. Evans, K. Ritchie, and R. Merkel: *Sensitive force technique to probe molecular adhesion and structural linkages at biological interfaces.* Biophysical Journal **68**, 2580 (1995).

[282] K. Halvorsen and W. P. Wong: *Massively parallel single-molecule manipulation using centrifugal force.* Biophysical Journal **98**, L53 (2010).

[283] A. G. B. Simpson, J. R. Stevens, and J. Lukes: *The evolution and diversity of kinetoplastid flagellates.* Trends in parasitology **22**, 168 (2006).

[284] L. McLintock, C. Turner, and K. Vickerman: *Comparison of the effects of immune killing mechanisms on Trypanosoma brucei parasites of slender and stumpy morphology.* Parasite immunology **15**, 475 (1993).

[285] M. Engstler, T. Pfohl, S. Herminghaus, M. Boshart, G. Wiegertjes, N. Heddergott, and P. Overath: *Hydrodynamic flow-mediated protein sorting on the cell surface of trypanosomes.* Cell **131**, 505 (2007).

[286] S. Türkcan, J.-M. Allain, and A. Alexandrou: *Procédé et dispositif d'analyse d'interactions moléculaires, et utilisations.* FR1055940 (2010).

[287] R. Probstein: *Physicochemical hydrodynamics: an introduction.* Wiley-Interscience, 1994.

[288] G. Schmid-Schönbein and D. Granger: *Molecular basis for microcirculatory disorders.* Springer France Editions, 2003.

[289] J. Happel and H. Brenner: *Low Reynolds number hydrodynamics: with special applications to particulate media.* Kluwer Academic Print on Demand, 1991.

[290] E. Lauga and T. M. Squires: *Brownian motion near a partial-slip boundary: A local probe of the no-slip condition.* Physics of Fluids **17**, 103102 (2005).

[291] R. Lindken and W. Merzkirch: *Velocity measurements of liquid and gaseous phase for a system of bubbles rising in water.* Experiments in Fluids **29**, S194 (2000).

[292] R. Lindken and W. Merzkirch: *A novel PIV technique for measurements in multiphase flows and its application to two-phase bubbly flows.* Experiments in Fluids **33**, 814 (2002).

[293] J. Westerweel, P. Geelhoed, and R. Lindken: *Single-pixel resolution ensemble correlation for micro-PIV applications.* Experiments in Fluids **37**, 375 (2004).

[294] R. Lindken, J. Westerweel, and B. Wieneke: *Stereoscopic micro particle image velocimetry.* Experiments in Fluids **41**, 161 (2006).

[295] P. Vennemann, K. T. Kiger, R. Lindken, B. C. W. Groenendijk, S. Stekelenburg-de Vos, T. L. M. ten Hagen, N. T. C. Ursem, R. E. Poelmann, J. Westerweel, and B. P. Hierck: *In vivo micro particle image velocimetry measurements of blood-plasma in the embryonic avian heart.* Journal of biomechanics **39**, 1191 (2006).

[296] G. I. Bell: *Models for the specific adhesion of cells to cells.* Science **200**, 618 (1978).

[297] E. Evans and K. Ritchie: *Dynamic strength of molecular adhesion bonds.* Biophysical Journal **72**, 1541 (1997).

[298] D. Duffy, J. McDonald, O. Schueller, and GM: *Rapid prototyping of microfluidic systems in poly (dimethylsiloxane).* Anal. Chem **70**, 4974 (1998).

[299] M. Morel, D. Bartolo, J. Galas, M. Dahan, and V. Studer: *Microfluidic stickers for cell-and tissue-based assays in microchannels.* Lab on a Chip **9**, 1011 (2009).

[300] P. Tabeling: *introduction à la microfluidique, collection échelles.* Belin, 2003.

[301] T. M. Squires and M. Z. Bazant: *Induced-charge electro-osmosis.* Journal of Fluid Mechanics **509**, 217 (2004).

[302] L. Rajendran and K. Simons: *Lipid rafts and membrane dynamics.* Journal of cell science **118**, 1099 (2005).

[303] B. D. Spangler: *Structure and function of cholera toxin and the related Escherichia coli heat-labile enterotoxin.* Microbiological Reviews **56**, 622 (1992).

[304] Y. Fujinaga, A. A. Wolf, C. Rodighiero, H. Wheeler, B. Tsai, L. Allen, M. G. Jobling, T. Rapoport, R. K. Holmes, and W. I. Lencer: *Gangliosides that associate with lipid rafts mediate transport of cholera and related toxins from the plasma membrane to endoplasmic reticulm.* Molecular Biology of the Cell **14**, 4783 (2003).

[305] R. Ropp: *Luminescence and the solid state.* Elsevier Science Ltd, 1991.

[306] D. Casanova, D. Giaume, E. Beaurepaire, T. Gacoin, J.-P. Boilot, and A. Alexandrou: *Optical in situ size determination of single lanthanide-ion doped oxide nanoparticles.* Applied Physics Letters **89**, 253103 (2006).

[307] W. Press, W. Vetterling, S. Teukolsky, and B. Flannery: *Numerical recipes in C++: the art of scientific computing.* Cambridge University Press New York, NY, USA, 2001.

[308] H. Lilliefors: *On the Kolmogorov-Smirnov test for normality with mean and variance unknown.* Journal of the American Statistical Association **62**, 399 (1967).

Abstract

The cellular membrane is a vital part of the cell, which plays a crucial role in many cellular processes, such as, signaling and trafficking, and pathologies. This thesis aims to investigate the architecture of the cell membrane. The study uses the motion of two membrane receptors that are exploited by bacterial toxins to probe the architecture. Advances in light microscopy techniques have shown that many membrane receptors do not diffuse freely in the membrane, but undergo confined or anomalous diffusion. Currently a few models compete to explain the confinement of the receptors, such as the Picket-Fence model, lipid rafts and protein aggregates.

To investigate the membrane, lanthanide doped nanoparticles ($Y_{0.6}Eu_{0.4}VO_4$) are coupled to two different peptidic pore-forming toxins, the α-toxin of *C. septicum* and the ϵ-toxin of *C. perfingens*. Single molecule tracking of receptor bound labeled toxins in the apical membrane of MDCK cells in a wide-field microscope reveals the receptor motion with sub-diffraction resolution of down to $10\,\text{nm}$. The α & ϵ-toxin receptors both undergo confined diffusion with similar diffusion coefficients of $0.16 \pm 0.14\,\mu\text{m}^2/\text{s}$ in temporaly stable domains of $0.5\,\mu\text{m}^2$. To analyze the receptor trajectories, we introduced a novel approach based on an inference method. Our only assumption is that the receptor moves according to the Langevin equation of motion. This method exploits the information of the ensemble of the trajectory and the quality of the extracted values is verified through simulations. Both receptors are confined in a spring-like potential with a spring constant of $0.45\,\text{pN}/\mu\text{m}$. Tracking after cholesterol depletion by cholesterol oxidase and cytoskeleton depolymerization by Latrunculin B, shows that confinement of single receptors is cholesterol dependent and actin depolymerization does not influence the confinement. Using the nanoparticle labels as a hydrodynamic force amplifier in a liquid flow, tests the response of the receptor to an external force and indicates attachment of the confining domains to the cytoskeleton. Finally, a model for the confinement of the receptor is proposed, based on the hydrophobic coupling of the receptor and the surrounding bilayer which can explain the spring-like potential of the confining domain.

Keywords: Single molecule Tracking (SMT), Toxins, Receptor, Membrane architecture, Microscopy, Fluorescence, Lipid rafts, Protein complexes, Hydrophobic coupling

Abstract

La membrane cellulaire est une partie vitale de la cellule dont l'architecture joue un rôle crucial dans de nombreux processus cellulaires, comme la signalisation et le trafic, et dans diverses pathologies. Cette thèse vise à sonder l'architecture membranaire via le mouvement de deux récepteurs membranaires qui sont exploités par des toxines bactériennes. Les progrès récents des techniques de microscopie optique ont montré que certains récepteurs membranaires ne diffusent pas librement dans la membrane, mais sont confinés ou diffusent de façon anomale. Actuellement, plusieurs modèles concourent pour expliquer le confinement des récepteurs, tel que le modè le Picket-Fence, les radeaux lipidiques et les agrégats de protéines.

Pour sonder la membrane, des nanoparticules ($Y_{0.6}Eu_{0.4}VO_4$) dopées avec des lanthanides sont couplées à deux toxines peptidiques différentes formant des pores dans la membrane, la toxine α de *C. septicum* et la toxine ϵ de *C. perfingens*. Le suivi de récepteurs individuels sur lesquels sont fixées des toxines marquées dans la membrane apicale de cellules MDCK avec un microscope à champ large permet de détecter le mouvement du récepteur avec une résolution meilleure que la limite de diffraction. Les récepteurs de la toxine α et ϵ montrent une diffusion confinée avec des coefficients de diffusion similaires de $0.16 \pm 0.14\,\mu m^2/s$ dans des domaines stables de $0.5\,\mu m^2$. Pour analyser les trajectoires des récepteurs, nous avons mis en œuvre une nouvelle technique basée sur une méthode d'inférence. Notre seule hypothèse est que le récepteur se déplace selon l'équation de Langevin. Cette méthode exploite l'ensemble de l'information stockée dans la trajectoire et la qualité des valeurs extraites est vérifiée par des simulations. Les deux récepteurs sont confinés dans un potentiel de type ressort avec une raideur de $0.45\,pN/\mu m$. Des expériences après déplétion du cholestérol par la cholestérol oxydase et après la dépolymérisation du cytosquelette par latrunculin B montrent que le confinement des récepteurs individuels dépend du taux de cholestérol et que la dépolymérisation de l'actine n'influence pas le confinement. En utilisant la nanoparticule couplée aux toxines comme un amplificateur de la force hydrodynamique appliqueé par un flux liquide, nous avons mesuré la réponse du récepteur à une force extérieure. Les résultats indiquent une fixation des domaines de confinement sur le cytosquelette. Enfin, un modèle pour le confinement du récepteur est proposé, basé sur le couplage hydrophobe entre le récepteur et la bicouche lipidique qui l'entoure. Ce modèle permet d'expliquer le potentiel de type ressort à l'intérieur du domaine de confinement.

Mots-clés: Suivi de molécules uniques (SMT), toxines, récepteur, architecture membranaire, microscopie, fluorescence, suivi de particules uniques (SPT), microscopie vidéo, radeaux lipidiques, agrégats de protéines, couplage hydrophobe